Sources, chemistry, and transport of urban aerosols and oxidized mercury: An analysis combining aircraft and surface observations with a chemical transport model

Viral Pinakin Shah

A dissertation

submitted in partial fulfillment of the

requirements for the degree of

Doctor of Philosophy

University of Washington

2018

Reading Committee:

Lyatt Jaeglé, Chair

Daniel Jaffe

Joel A. Thornton

Program Authorized to Offer Degree:

Department of Atmospheric Sciences

University of Washington

Abstract

Sources, chemistry, and transport of urban aerosols and oxidized mercury:
An analysis combining aircraft and surface observations
with a chemical transport model

Viral Pinakin Shah

Chair of the Supervisory Committee:
Professor Lyatt Jaeglé
Department of Atmospheric Sciences

I examine of the sources, chemistry, and transport of aerosol particles and oxidized mercury compounds in the atmosphere using aircraft- and ground-based observations and a global chemical transport model.

In Chapter 2, I use extensive airborne observations of atmospheric composition over the eastern U.S. from the 2015 Wintertime Investigation of Transport, Emissions, and Reactivity (WINTER) campaign, ground-based observations, and the GEOS-Chem chemical transport model, to determine the controls on winter SO_4^{2-} and NO_3^-. The model reproduces observed concentrations of total SO_4^{2-}-NO_3^--NH_4^+ particulates (2.45 μg sm^{-3}) and their composition (SO_4^{2-}: 47%, NO_3^-: 32%, NH_4^+: 21%) during WINTER. I find that the wintertime oxidation efficiency of SO_2 to SO_4^{2-} in the eastern U.S. is limited by low [H_2O_2] and [OH]. Relatively acidic fine

particulates (pH~1.3) allow 45% of the total nitrate to partition to the particle phase. Between the 2007 and 2015 simulations, SO_2 emissions decreased by 58%, but simulated [H_2O_2] remained constant, causing an increase in the simulated SO_2 oxidation efficiency to SO_4^{2-}. Simulated NOx emissions decreased by 35%, but the NO_3^- particle fraction increased as fine particle acidity decreased. These feedbacks resulted in a 40% decrease of [SO_4^{2-}] and no change in [NO_3^-]. [SO_4^{2-}] and [NO_3^-] will change slowly between 2015 and 2023, unless SO_2 and NOx emissions decrease faster in the future than in the recent past.

In Chapter 3, I analyze the wintertime emissions and secondary formation of organic aerosols (OA) over the northeastern U.S. with observations from the WINTER aircraft campaign and ground-based monitoring sites, and three OA modeling approaches in GEOS-Chem. The observed OA concentrations below 1 km during WINTER were 1.48 μg sm^{-3}. Factor analysis of the observations indicate that secondary OA (SOA) contributed 60% and primary OA (POA) 40%. I reproduce the WINTER OA, POA, and SOA observations using an empirical parameterization for SOA from urban emissions and POA emissions from the National Emissions Inventory (NEI) reduced by half, suggesting that the NEI overestimates primary wintertime OA emissions. The simulation captures the observed OA growth from the photochemical formation of SOA, and reproduces ground-based OA measurements. The traditional approach, which includes SOA from oxidation of C_6-C_8 aromatics, predicts almost no SOA. The approach that includes SOA from the oxidation of low-volatility gases emitted initially as POA underestimates POA by a factor of 5. I find that OA are regionally distributed and account for 35% of the fine particulates over the NE US during WINTER. Wintertime OA over the region is overwhelmingly anthropogenic, with 23% from residential wood combustion emissions and 63% from secondary sources.

In Chapter 4, I use the GEOS-Chem model to quantify how surface deposition of Hg(II) is influenced by oxidized mercury (Hg(II)) production at different atmospheric heights. GEOS-Chem reproduces ground- and aircraft-based observations of Hg(II) reasonably well. Hg(II) produced above 750 hPa constitutes 91% of the tropospheric mass of Hg(II) and 77% of the global Hg(II) deposition flux. This is because of fast chemical production and slow loss of Hg(II) at these altitudes. I assess the effects of the main sources of model uncertainty (oxidant concentrations, oxidation pathways, and emissions speciation) with additional simulations, and find similarly large contribution of Hg(II) produced above 750 hPa to the tropospheric Hg(II) mass (78–90%) and to the global Hg(II) surface deposition flux (57–76%). I find that 55% of the spatial variation of Hg wet deposition flux observed at the ground-based sites in the U.S. is explained by the combined variation of precipitation and Hg(II) produced above 750 hPa. Hg(II) present in the subtropical anticyclones accounts for 74% of Hg(II) at 500 hPa and about 60% at the surface over the continental U.S. Hg(II) produced in the upper and middle troposphere subsides in the anticyclones, where the dry conditions inhibit the loss of Hg(II), which make these anticyclones important for Hg cycling in the atmosphere.

TABLE OF CONTENTS

LIST OF FIGURES

LIST OF TABLES

ACKNOWLEDGEMENTS

I thank Lyatt Jaeglé, my advisor and mentor, for teaching me the craft of scientific research and about the culture and values of our research community. I thank her for advocating for me throughout the past six years. I thank Becky Alexander, Dan Jaffe, Joel Thornton, and Ulrich Hetmaniuk for generously devoting their time to serve on my thesis committee, for guiding me and encouraging me in my research.

I am grateful to Felipe Lopez-Hilfiker, Ben Lee, Jason Schroder, Pedro Campuzano-Jost, Jose Jimenez, Hongyu Guo, Amy Sullivan, Rodney Weber, Jaime Green, Marc Fiddler, Solomon Bililign, Teresa Campos, Mike Reeves, Meghan Stell, Andy Weinheimer, Denise Montzka, Steve Brown, Eric Apel, Rebecca Hornbrook, Andy Hills, and Nicola Blake for collaboration on the WINTER campaign; Lynne Gratz and Jesse Ambrose for collaboration on the NOMADSS campaign, Xinrong Ren and Steve Brooks for sharing their mercury measurements, and all operators and organizations running the Chemical Speciation Network, the Interagency Monitoring of Protected Visual Environments, the Clean Air Status and Trends Network, the Mercury Deposition Network, the Atmospheric Mercury Network, and the European Monitoring and Evaluation Programme for collecting and sharing their measurements.

Chapter 1. INTRODUCTION

This is a study of the sources, chemistry, and transport of aerosol particles and oxidized mercury compounds in the atmosphere. Aerosols and mercury affect human health and impact the Earth's physical and biological systems. Both are present naturally in the Earth's atmosphere, but emissions from human activities have considerably altered their natural abundance and composition. Both aerosols and mercury have become global environmental problems and have been the focus of mitigation policies at the international, national, and sub-national levels. These policies are undergirded by our scientific understanding of the atmospheric processes of the origin and fate of these pollutants. My motivation in doing this work is to contribute to the understanding of some of the underlying processes that affect these pollutants in the atmosphere. Specifically, I will analyze the characteristics of aerosols during the winter season over urbanized areas focusing on the eastern U.S. (Chapters 2 and 3), and I examine the areas in the atmosphere where the oxidation of mercury and its transport occurs. I begin with a brief introduction to atmospheric aerosols and mercury.

1.1 ATMOSPHERIC AEROSOLS

Atmospheric aerosols, also known as particulate matter (PM), are tiny solid or liquid particles suspended in air. These particles are a complex mixture of numerous chemical species and biological material. Atmospheric aerosols have diameters between a few nanometers and about 100 μm. Aerosols with a diameter smaller than 2.5 μm are known as $PM_{2.5}$. $PM_{2.5}$ is a pervasive air pollutant; its inhalation is harmful to human health. The small $PM_{2.5}$ particles penetrate deep into the lungs and can enter the bloodstream affecting various vital organs. They cause damage to

the respiratory and cardiovascular systems and lead to premature death and non-fatal effects like heart attack, asthma, and decreased lung function (Dominici et al., 2006; Pope and Dockery, 2006; Zanobetti and Schwartz, 2009). Young children, older adults, and people with existing health conditions like asthma are most susceptible to these effects. They are also linked to adverse reproductive outcomes and impaired brain function (Ailshire and Crimmins, 2014; Slama et al., 2008). Atmospheric aerosols are responsible for up to 3 million premature deaths per year globally (Cohen et al., 2017; Lelieveld et al., 2015; World Health Organization, 2016), and 59–130 thousand deaths in the U.S. alone (Anenberg et al., 2010; Cohen et al., 2017; Fann et al., 2012). $PM_{2.5}$ affect human well-being by reducing visibility by forming haze and by damaging buildings, statues, and monuments by depositing on their surfaces. This has led to the enactment of emissions regulations and establishment of air quality standards for $PM_{2.5}$, such as the National Ambient Air Quality Standards (NAAQS) in the U.S., to protect human health and enhance human well-being.

Atmospheric aerosols have important climatic and biogeochemical impacts, as illustrated in Fig. 1.1. Aerosols absorb and scatter solar and longwave radiation and affect the Earth's climate (direct radiative effect). In addition, aerosols interact with clouds, producing an indirect radiative effect on the Earth's climate. The radiative forcing of aerosols is not well-constrained and is a major source of uncertainty in climate science (Boucher et al., 2013). Absorbing aerosols can deposit on snow and ice surfaces, reduce surface albedo, and affect the Earth's radiation budget. When deposited on to land and ocean ecosystems, they supply nutrients like carbon, nitrogen, phosphorous, and iron, but can also lead to eutrophication and acidification of the ecosystems (Mahowald et al., 2011). In addition, they are sites for heterogeneous and multiphase chemical reactions and thus affect the trace-gas composition of the atmosphere.

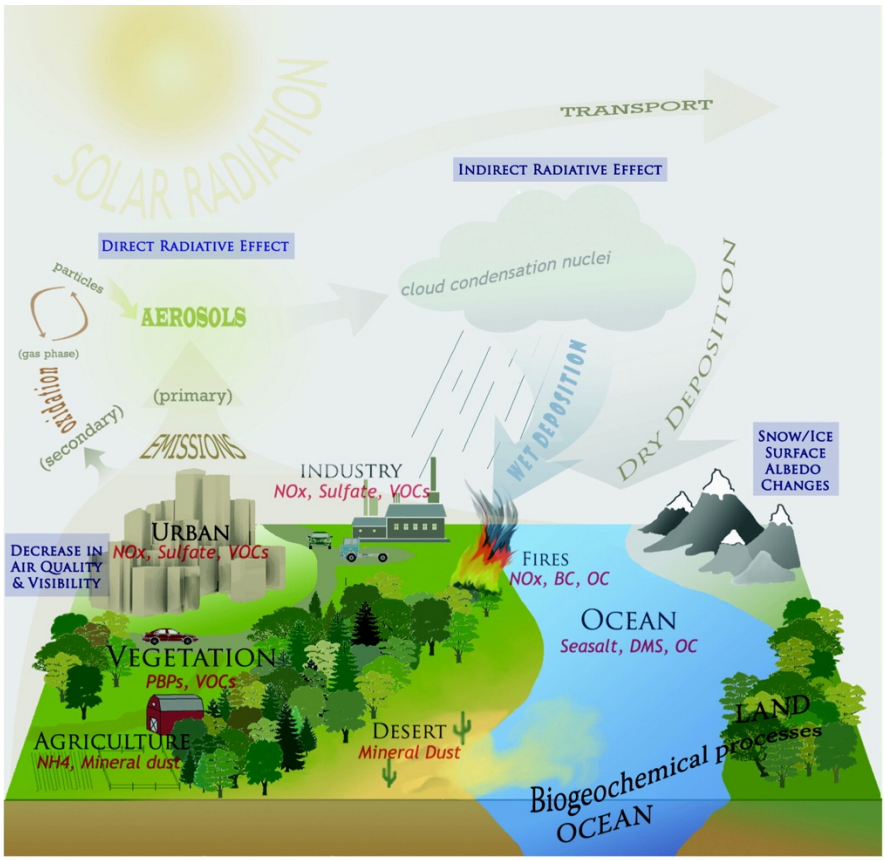

Mahowald N, et al. 2011.
Annu Rev. Environ. Resour. 36:45–74

Figure 1.1: Illustration of the sources, fate, and impacts of atmospheric aerosols (Mahowald et al., 2011). Reproduced with permission from Annual Reviews.

1.1.1 *Sources and fate of aerosols*

Tropospheric aerosols are composed of sulfate (SO_4^{2-}), nitrate (NO_3^-), ammonium (NH_4^+), organic carbon (OA), black carbon, sea salt particles, mineral dust, and primary biological particles (PBP) (Fig. 1.1). They also contain water, but the composition of dry aerosols is studied more often because it is an indicator of the aerosol sources. Aerosols are released into the atmosphere by direct emissions from various anthropogenic and natural sources (primary emissions), or are formed in the atmosphere through chemical processing of gas-phase precursors (secondary

formation) from anthropogenic and natural sources. Primary anthropogenic sources of aerosols include incomplete fossil-fuel and biofuel burning and fires, which mostly emit OA (known as primary organic aerosols, POA) and black carbon (BC), and dust from human activities. Natural sources of primary aerosols include the suspension of mineral dust, sea salt aerosols, and biological particles.

SO_4^{2-}, NO_3^-, and NH_4^+ aerosols are largely formed through secondary processes. SO_4^{2-} is formed from the oxidation of sulfur dioxide (SO_2), which is mostly emitted from coal combustion, volcanic sources, or forms from the oxidation of biogenic dimethyl sulfide (DMS) emitted by marine phytoplankton. NO_3^- is formed from the oxidation of nitrogen oxides (NOx), which are emitted during fossil fuel combustion and biomass burning, and from soils and lightning. NH_4^+ is the main cation associated with SO_4^{2-} and NO_3^-. It forms from ammonia (NH_3), which is emitted mainly from agriculture sources. Secondary organic aerosols (SOA) are formed from the oxidation of volatile organic compounds (VOC) emitted from anthropogenic and biogenic sources.

Aerosols are removed from the atmosphere by rain and snow (wet deposition) or by turbulence-driven collisions or gravitational settling of the particles to the Earth's surface (dry deposition). The efficiency of removal by these processes depends on the local meteorological conditions, land surface type, and the size distribution and composition of the aerosols. The lifetime of aerosols in the atmosphere is typically between a few hours and a few weeks. The irregular distribution of the aerosols sources and sinks leads to large variability in the concentration and composition of aerosols in space and time.

1.1.2 *Global observations and modeling of aerosols*

Near-ground aerosols concentrations over most of the continents are close to 10 μg m^{-3}, but concentrations higher than 100 μg m^{-3} are common over Asia and Africa (Fig. 1.2). Mineral dust is the largest aerosol constituent in PM_{10} (PM smaller than 10 μm diameter) in Asia and Africa, but also in Europe and parts of South America, accounting for about 35% or more of the aerosol mass there. Its contribution over North America is small.

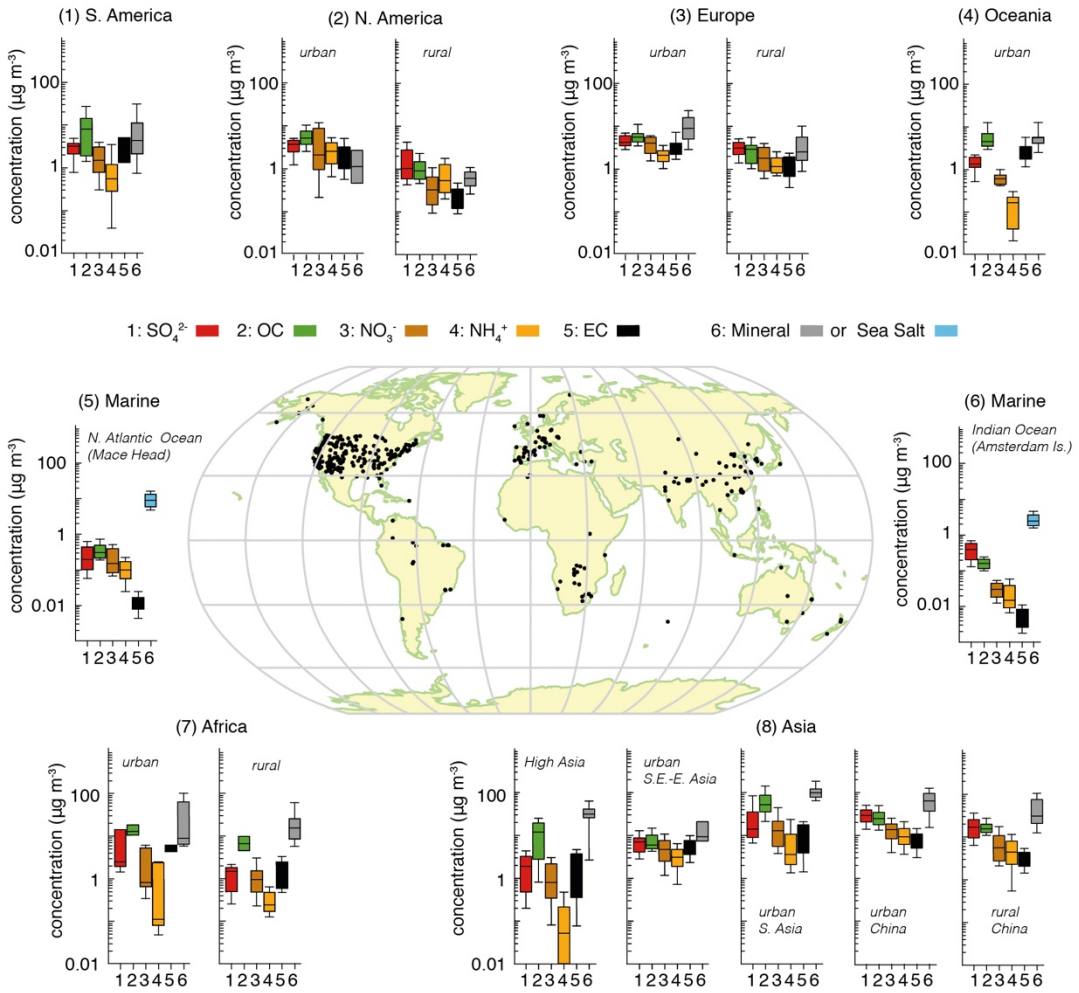

Figure 1.2: Observed concentrations of the main aerosol constituents in PM_{10} (PM smaller than 10 μm diameter) at surface sites worldwide (Boucher et al., 2013). Reproduced with permission.

Much of the mineral dust is present on coarse particles that larger than 2.5 μm. OA and SO_4^{2-} are typically the most abundant species in $PM_{2.5}$ over land, each contributing 10–30% to the aerosol mass depending on the region. The aerosol composition in urban and rural areas is not too different in most continents, except in North America. Urban areas here have larger amounts of OA and NO_3^-, while rural areas have larger amounts of SO_4^{2-}, reflecting spatial differences in the sources of aerosols and their precursors. The influence of anthropogenic sources reduces far from land, and sea salt particles begin to dominate the aerosol mass over the ocean. Sea salt aerosols account for about 80% of the aerosol mass over marine areas.

The observed aerosol concentrations and composition are a product of numerous underlying physical and chemical processes that cannot be observed directly. Thus, to interpret these observations we often rely on mathematical models of these processes. Three-dimensional chemical transport models (CTMs) use numerical algorithms to simulate the processes of emissions, chemistry, transport, and deposition and produce spatially and temporally varying concentrations of atmospheric aerosols and trace gases. CTMs are often used to study the effect of human activities on the composition of Earth's atmosphere. As such, they are important tools in the development of effective emissions regulations to improve air quality and to mitigate the climatic effect of aerosols. Moreover, by enabling the examination of properties and processes not directly observable, CTMs are one of the driving factors advancing our scientific understanding of atmospheric aerosols and trace gases.

Table 1.1 shows the global sources and burden of main constituents of atmospheric aerosols simulated by an ensemble of models. We see that the natural sources of mineral dust and sea salt aerosols (2400–10800 Tg a^{-1}) far exceed the sources of all other aerosol species (180–581 Tg a^{-1}). Thus, the simulated global mass of atmospheric aerosols is dominated by mineral dust and

sea salt aerosols, and explains the spatial patterns seen in the surface observations (Fig. 1.2). Of the remaining species, SO_4^{2-} and OA tend to be more abundant (~35% each) than NO_3^-, NH_4^+, and BC, which is consistent with the surface observations.

Table 1.1:Multi-model estimate of the atmospheric mass of the main aerosol constituents (Bian et al., 2017; Boucher et al., 2013; Kinne et al., 2006; Tsigaridis et al., 2014).

Species	Sources (Tg a^{-1}) median (range)	Burden (Tg) median (range)
SO_4^{2-}	139 (107 – 198)	1.6 (0.8 – 3.3)
NO_3^-	47 (7 – 125)	0.6 (0.1 – 1.9)
NH_4^+	31 (23 – 38)	0.3 (0.2 – 0.8)
OA	100 (50 – 220)	1.4 (0.7 – 3.7)
BC	11 (8 – 19)	0.2 (0.05 – 0.5)
Sea salt aerosols	1400 – 6800	6.4 (2.5 – 13)
Mineral dust	1000 – 4000	21 (4.5 – 30)

Models are imperfect representations of real world. This is because of gaps in our fundamental understanding of the relevant natural processes and because of the simplifying assumptions used by models to be computationally viable. Different models make different assumptions which results in significant variation in the results of the simulations. Table 1.1 illustrates the spread in the modelled sources and burdens of the main aerosol constituents. We see a factor of 2–4 variation in the magnitude of the sources of the aerosol species among the models. Similarly, there is at least a factor of 4 variation in the simulated burden of the aerosol species, and it is almost a factor of 20 for NO_3^-. This spread among the models represents the uncertainty in our understanding the processes governing the sources, sinks, and transport of atmospheric aerosols.

In situ observations are indispensable for reducing this uncertainty. They are benchmarks against which models are tested and the use of a particular model for a given problem depends on

how well it reproduces the relevant observations. Ground-based monitoring sites, such as those shown in Fig. 1.2, provide continuous measurements over extended periods of time, but are limited in their spatial and chemical resolution. Aircraft-based field intensive campaigns, on the other hand, collect measurements with larger horizontal and vertical extent and higher time resolution, but over short periods. Moreover, aircraft-based campaigns typically deploy a suite of advanced instruments to simultaneously measure gas-phase species important in the chemistry of aerosols. Thus, aircraft-based campaigns provide a detailed snapshot of the chemical composition of the atmosphere over a region that is needed to constrain CTMs.

1.1.3 *Overview of thesis work*

In my Ph.D. research, I leverage the complementarity of aircraft-based observations, ground-based observations, and a three-dimension chemical transport model to study the sources and chemistry of aerosols during the winter season over the eastern U.S. The eastern U.S. is the most densely populated area of the country. It encompasses the Northeast Urban Corridor stretching from Washington D.C. to Boston, and the Ohio River Valley extending over parts of Pennsylvania, West Virginia, Ohio, Indiana, and Kentucky. These two regions are the largest source regions for anthropogenic pollution in the country. The annual average $PM_{2.5}$ concentrations near these regions ranged from 10 to 13 μg m^{-3} for the 2012-2014 period (U.S. Environmental Protection Agency, 2015b), which, despite recent reductions in emissions, is higher than the WHO guideline of 10 μg m^{-3} (World Health Organization, 2016). For the 2012-2014 period, 4 counties in the Northeast U.S. exceeded the $PM_{2.5}$ NAAQS standard (U.S. Environmental Protection Agency, 2015b).

The summer season has traditionally been the focus of air pollution research over the eastern U.S. This is because of vigorous sun-driven photochemistry in the summer, leading to the faster production of secondary aerosols and gaseous pollutants like ozone (O_3). Many of the past aircraft-based field intensives and modeling studies have been carried out during the summer season, and the wintertime atmospheric chemistry over polluted regions like the eastern U.S. remain under-studied (Thornton et al., 2014). This led to the recent Wintertime INvestigation of Transport, Emissions, and Reactivity (WINTER) aircraft campaign. The NSF/NCAR C-130 aircraft was used to make aerosol and trace gas measurements over the eastern U.S between 1 February and 15 March 2015. During my Ph.D. work, I participated as a flight planner during the measurements phase and have subsequently used the WINTER observations and the GEOS-Chem CTM to analyze the wintertime sources and chemistry of aerosols over the eastern U.S.

This work is divided into two chapters. In Chapter 2, we determine the controls on the formation of SO_4^{2-}, NO_3^-, and NH_4^+ aerosols during the WINTER campaign, and on the basis of that explain changes in SO_4^{2-}, NO_3^-, and NH_4^+ aerosols concentrations in response to SO_2 and NOx emissions reduction in the recent past (2007–2015) and projected for the near future (2015–2023). I show that feedbacks associated with oxidant concentrations and particle acidity lower the efficacy of emissions reductions slowing down the decrease in wintertime $PM_{2.5}$. In Chapter 3, we focus on the primary and secondary sources of OA over the northeastern US during WINTER. I use the WINTER observations, and concurrent surface observations, to evaluate three approaches to model OA in GEOS-Chem. Using the approach that yields results most consistent with the observations, we analyze the simulated spatial distribution of OA and its contribution to fine particulate matter over the eastern U.S. in winter.

1.2 ATMOSPHERIC MERCURY

Mercury (Hg) is detrimental to human and ecosystem health. It is a toxin that affects the human nervous and cardiovascular systems (Mergler et al., 2007). In animals, Hg exposure can affect reproductive behavior (Scheuhammer et al., 2007). Hg exposure happens through the consumption of food contaminated with methylmercury. Methylmercury is taken up at the bottom of the food chain, and bioaccumulates to concentrations that are 6–7 orders of magnitude higher at the top of the food chain (Morel et al., 1998). Hg abundance in the environment has increased by factors of 3 to 7 because of anthropogenic emissions (Amos et al., 2013; Selin, 2009; Zhang et al., 2014) making it a major public health concern. An international treaty, known as the Minamata Convention on Mercury, was adopted by about 100 countries in 2013 to protect human and ecosystem health from the above effects by cutting down on global anthropogenic use and emissions of Hg. In the U.S., the Mercury and Air Toxics Standards have been enacted to reduce atmospheric emissions of Hg from power plants among other regulations targeting releases of Hg into air and water from different industries.

1.2.1 *Mercury cycling in the atmosphere*

In the atmosphere, Hg is present as a gaseous element (Hg(0)), or in the oxidized state (Hg(II)), either in the gas-phase or bound to particles. Hg(II) originates predominantly from the oxidation of Hg(0), but the oxidation pathways and the chemical forms of Hg(II) have not been established. In the ocean waters and lakes, mercury is found in the dissolved elemental form, a variety of inorganic oxidized forms, and organic forms that include methylmercury (Fitzgerald et al., 2007).

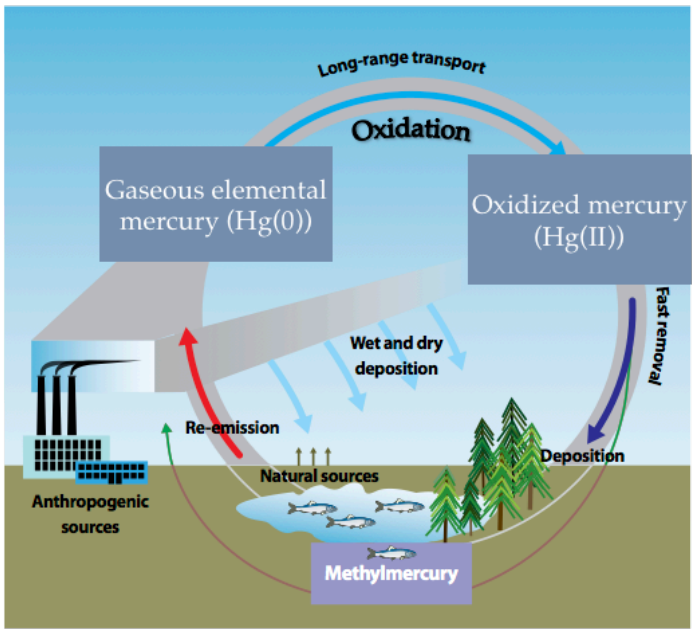

Figure 1.3: Schematic of mercury cycling in the environment. Adapted from UNEP Chemicals Branch (2008).

Hg is released to the atmosphere from the Earth's crust through natural processes such as volcanism, and through human activities such as mining and burning of fossil fuels. In the atmosphere, Hg is transported long distances by winds, cycles between Hg(0) and Hg(II) through oxidation and reduction, and is eventually deposited to the land and ocean surfaces through wet and dry deposition processes (Fig. 1.3). Hg(II) is highly soluble in water, but not Hg(0). Thus, much of the deposition of Hg happens through Hg(II). A small fraction of the deposited Hg is converted to methylmercury, which gets absorbed in the food chain. However, most of the Hg deposited to the oceans is re-volatilized and reemitted to the atmosphere as Hg(0), restarting the cycle. Current Hg emissions from human activities are estimated at about 2000 Mg a^{-1}. The highest primary emissions are from coal burning for power generation and residential heating (45%) followed by artisanal and small-scale gold mining (20%). Metal production, cement production, and waste incineration are other important sectors for Hg emissions. Geogenic emissions are about

90 Mg a^{-1} whereas emissions (natural and reemissions) of Hg from the ocean are estimated at 1900–4200 Mg a^{-1} (Obrist et al., 2018; Pirrone et al., 2010).

The chemistry of Hg in the atmosphere is highly uncertain. Laboratory studies suggest that the gas-phase oxidation of Hg(0) can occur by reaction with a number of atmospheric oxidants: bromine (Br), chlorine (Cl), bromine monoxide (BrO), and nitrate (NO_3) radicals, O_3, and hydroxyl (OH), but the relative importance of these various oxidants is unclear. This is because current instruments for measuring Hg(II) cannot differentiate between the different chemical forms of Hg(II) (Gustin et al., 2015; Jaffe et al., 2014). The Br radical is widely accepted as the dominant oxidant of Hg(0) in the global atmosphere based on field-evidence in a number of different regions and laboratory and theoretical studies (Ebinghaus et al., 2002; Laurier et al., 2003; Donohoue et al., 2006; Obrist et al., 2011; Gratz et al., 2015).

1.2.2 *Observations and modeling of atmospheric mercury*

Observations of Hg concentrations in the atmosphere are scarce. Of the limited number of observations that are available, most are made at ground-based monitoring sites, with some during aircraft- and ship-based campaigns. These observations show that Hg is present in much of the atmosphere at concentrations of 1–2 ng m^{-3}. Hg concentrations are higher in the northern hemisphere, close to source regions, and lower in the southern hemisphere (Sprovieri et al., 2016). Speciated measurements of Hg have shown that almost all of the Hg present at the surface is in the form of Hg(0). Hg(II) concentrations are highly variable because of it is high solubility and has a short lifetime in the atmosphere before it is lost by deposition. Hg(II) concentrations at the surface are typically below 0.05 ng m^{-3}, but can increase to 0.5–1 ng m^{-3} at altitudes close to the tropopause (Lyman and Jaffe, 2012). Hg(II) concentrations are enhanced aloft because of faster oxidation of

Hg(0) and lack of removal. In addition, measurements of Hg concentrations in precipitation are routinely made at several ground-based sites worldwide. These measurements are important in understanding the amounts and spatiotemporal patterns of the emissions and deposition of Hg to and from the atmosphere. As most of the Hg scavenged by precipitation is in the form of Hg(II), these measurements also provide an indirect view into the oxidation of Hg in the atmosphere.

CTMs are used to understand the sources, sinks, and transport of Hg in the atmosphere (e.g. Seigneur et al., 2001; Dastoor and Larocque, 2004; Selin et al., 2007; Jung et al., 2009). However, the physical and chemical processes controlling the fate of Hg in the atmosphere are complex and poorly understood resulting in a large spread in the model results and varying agreement with observations. In a model inter-comparison study of four global CTMs, all models were found to simulate the concentrations of Hg(0) within 20% of each other and within 30% of the surface observations, and Hg wet deposition fluxes were mostly within a factor of 2 of the observations. But considerably poor agreement with the observations was seen for Hg(II) concentrations, with simulated Hg(II) concentrations being a factor of 3 higher for 30–90% of the observations sites (Travnikov et al., 2017). These models used the same anthropogenic emissions, but different reemissions and chemistry. The inter-model differences in simulating the Hg(II) concentrations and deposition fluxes reflect large uncertainties in the chemistry of Hg and the sparsity of speciated Hg measurements, particularly at higher altitudes, to validate the models.

The 2013 Nitrogen, Oxidants, Mercury and Aerosols Distributions, Sources, and Sinks (NOMADSS) campaign was conducted with the goal to characterize the distribution of Hg(II) at different altitudes over a broad region of the U.S. In my master's work, I have analyzed the NOMADSS Hg(II) observations with the GEOS-Chem CTM.

A key finding from my analysis was that higher concentrations of Hg(II) over the southeastern U.S. were associated with dry air masses originating in the subtropical upper troposphere. Hg(II) concentrations of 300–650 pg m^{-3} were observed in air with relative humidity less than 35% and CO lower than 75 ppbv (Shah et al., 2016). I also found that the GEOS-Chem simulation can reproduce the Hg(0) concentrations well, but could not explain the NOMADSS Hg(II) observations at 5–7 km altitude. The GEOS-Chem Hg(II) concentrations were a factor of 2 lower than the observations (Observed mean: 0.19 ng m^{-3}, model mean: 0.1 ng m^{-3}), but the agreement improved when Br concentrations in the model were tripled (model mean Hg(II): 0.16 ng m^{-3}), or when a faster Hg(0)+Br reaction rate was prescribed (model mean Hg(II): 0.18 ng m^{-3}).

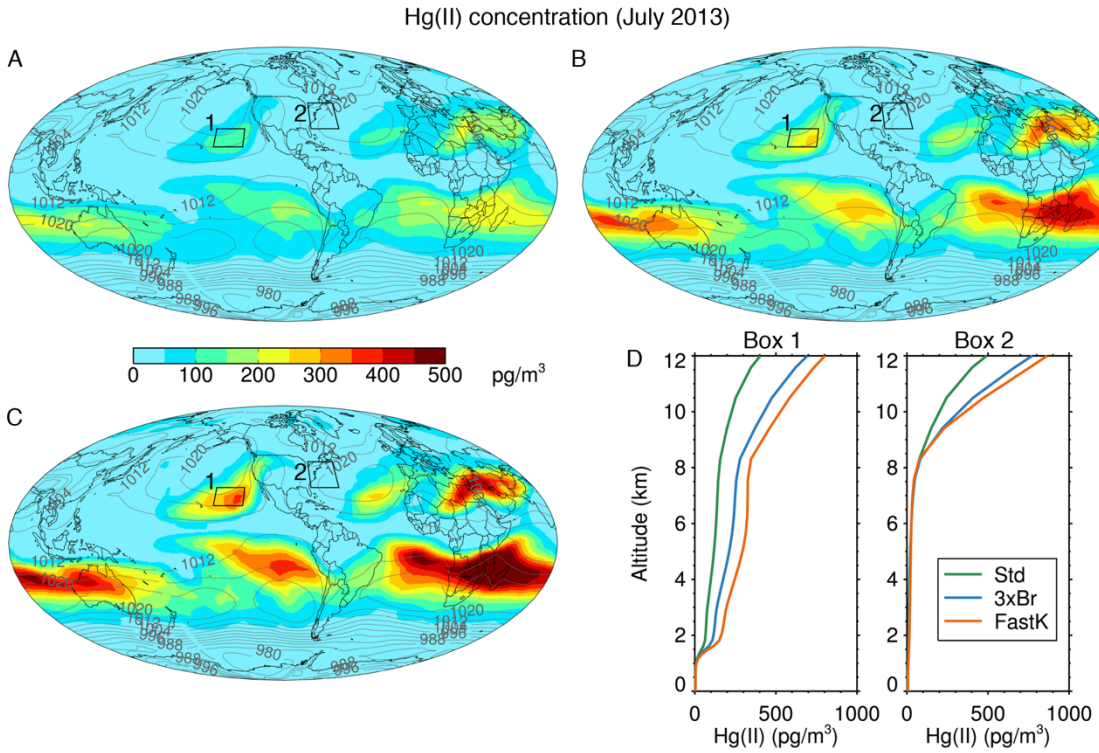

Figure 1.4: Global distribution of Hg(II) at 500 hPa (~6 km altitude) for July 2013 Results from (a) the original GEOS-Chem model (Std), (b) model with tripled Br concentration (3xBr) and (c) with faster Hg(0)+Br reaction rate (FastK). The contours show the sea level pressure (in hPa). The subtropical anticyclones correspond to areas of high pressure. (b) The simulated vertical profile for the two regions marked in panels a–c. (Source: Shah et al. (2016)).

Figure 1.4 shows the global distribution of Hg(II) at 500 hPa from these the three GEOS-Chem simulations for July 2013. In all three simulations, we find that Hg(II) concentrations are enhanced in the subtropical anticyclones throughout most of the troposphere, but the enhancements are higher in simulations with higher Br or a faster oxidation rate. In the North Pacific anticyclone, Hg(II) concentrations at 6–10 km could be an order of magnitude higher (0.2–0.5 ng m^{-3}) than concentrations elsewhere. These results strongly suggest that the production of Hg(II) in upper regions of the troposphere is faster than previously thought, and that the subtropical anticyclones are reservoirs of Hg(II)-rich air. We hypothesized that two processes happening in the subtropical anticyclones could be responsible for the Hg(II) enhancement: the downward transport of Hg(II) produced in the upper regions of the troposphere, and the suppression of cloud formation and precipitation, which suppresses the loss of Hg(II) by wet deposition. These initial results have led to work that I have presented in the second part of my thesis.

1.2.3 *Overview of thesis work*

In Chapter 4, we further investigate the importance of the upper regions of the troposphere and the subtropical anticyclones for the atmospheric concentration and deposition of Hg. We first evaluate the GEOS-Chem simulations against surface- and aircraft-based measurements of Hg(II) concentrations and Hg wet deposition. We then use a modified simulation that tracks where Hg(II) originates to quantify the contribution of Hg(II) formed at different heights in the atmosphere to its global burden and deposition. We also use the results of this simulation to explain the observed variability of Hg(II) concentrations and wet deposition flux at surface sites in the U.S. Finally, I conduct another simulation to infer how much of the Hg(II) is formed or transported in the subtropical anticyclones.

Chapter 2. SULFATE-NITRATE-AMMONIUM AEROSOLS OVER THE NORTHEASTERN U.S. DURING WINTER

This chapter has been submitted for publication and is under review as:
Shah, V., Jaeglé, L., Thornton, J. A., Lopez-Hilfiker, F. D., Lee, B. H., Schroder, J. C., Campuzano-Jost, P., Jimenez, J. L., Guo, H., Sullivan, A. P., Weber, R. J., Green, J. R., Fiddler, M. N., Bililign, S., Campos, T. L., Stell, M., Weinheimer, A. J., Montzka, D. D. and Brown, S. S.: Chemical Feedbacks Weaken The Wintertime Response of Particulate Sulfate And Nitrate To Emissions Reductions Over The Eastern U.S., Proceedings of the National Academy of Sciences, 2018.

2.1 INTRODUCTION

The past decade has seen dramatic reductions of sulfur dioxide (SO_2) and nitrogen oxides (NOx) emissions from power plants and vehicles in the U.S. (U.S. Environmental Protection Agency, 2017d; Krotkov et al., 2016). Thus, hundreds of thousands of deaths and illnesses from exposure to fine particulate matter of aerodynamic diameter less than 2.5 μm ($PM_{2.5}$) have been averted (Cohen et al., 2017). Between 2007 and 2015, SO_2 and NOx emissions have decreased by 58% and 35%, respectively. SO_2 and NOx are precursors of sulfate (SO_4^{2-}) and nitrate (NO_3^-) – two major constituents of $PM_{2.5}$ over the eastern U.S. (Hand et al., 2012). Ground-based observations show that in response to these decreases in precursor emissions, annual average $PM_{2.5}$ concentrations in the eastern U.S. have decreased by a third between 2007 and 2015 (U.S. Environmental Protection Agency, 2017e). However, this decrease in $PM_{2.5}$ has occurred mostly in summer; the decrease in wintertime $PM_{2.5}$ has been half of that in summer (U.S. Environmental Protection Agency, 2017d; Xing et al., 2015). A similar seasonal difference in $PM_{2.5}$ response to emission reductions has occurred over Western Europe (Tørseth et al., 2012; Xing et al., 2015). Severe wintertime $PM_{2.5}$ pollution is prevalent in East China and North India (Huang et al., 2014; Dey and Di Girolamo, 2011), leading to strong mitigation efforts. The design of effective strategies for air quality

improvement in the U.S. and many other countries critically depends on a process-based understanding of the response of wintertime $PM_{2.5}$ to emission reductions.

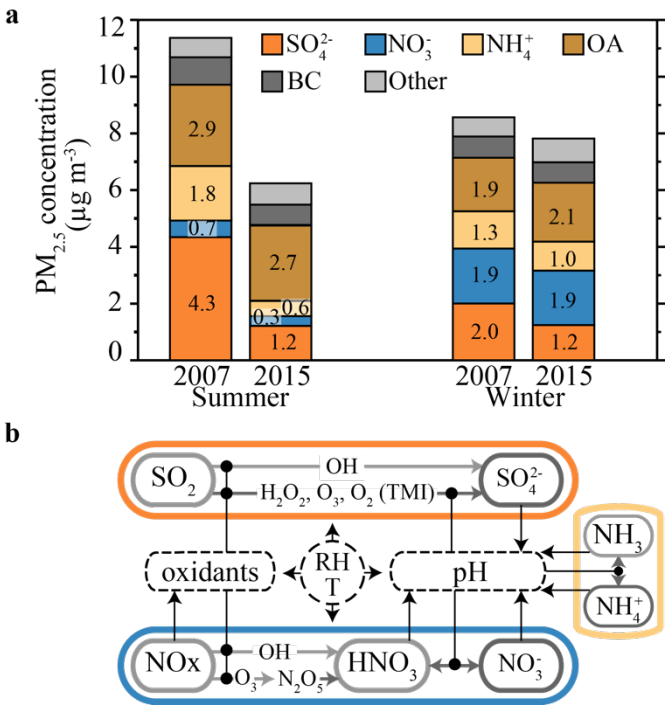

Figure 2.1: Trends and wintertime chemistry of $PM_{2.5}$ (a) Population-weighted $PM_{2.5}$ concentration and composition observed over the eastern U.S. for summer (July, August, and September) and winter (January, February, and March) of 2007 and 2015. The $PM_{2.5}$ composition is separated into sulfate (SO_4^{2-}), nitrate (NO_3^-), ammonium (NH_4^+), organic aerosol (OA), black carbon (BC), and sea-salt and crustal material (other). $PM_{2.5}$ observations are from the U.S. EPA $PM_{2.5}$ monitoring network and include 59 stations shown in Fig. 2A.1 (U.S. Environmental Protection Agency, 2015a). Between 2007 and 2015, SO_2 and NOx emissions decreased by 58% and 35%, respectively. (b) A representation of the important interactions in the wintertime chemistry of SO_4^{2-}, NO_3^-, NH_4^+ and their precursors.

A closer examination of the $PM_{2.5}$ composition observed at U.S. Environmental Protection Agency (EPA) ground-based monitoring sites in the eastern U.S. illustrates the stark seasonal differences in $[SO_4^{2-}]$ and $[NO_3^-]$ changes between 2007 and 2015 (Fig. 2.1a, 2A.1). (The eastern U.S. is defined here as 31˚N–43˚N, 67˚W–86.5˚W, Fig. 2A.1a, and [..] denotes atmospheric mass

concentrations.) During this time, average summertime [SO_4^{2-}] and [NO_3^-] decreased by 72% and 50%, respectively, with an associated 67% decrease in ammonium concentrations ([NH_4^+]). In contrast, wintertime [SO_4^{2-}] decreased by only 40%, [NH_4^+] by 23% and [NO_3^-] did not change (Fig. 2.1a). These wintertime trends in SO_4^{2-}- NO_3^-- NH_4^+ $PM_{2.5}$ have been unfolding since 1990 (Sickles II and Shadwick, 2015).

During winter, formation of SO_4^{2-}- NO_3^-- NH_4^+ $PM_{2.5}$ from emitted precursors is governed by strong feedbacks depending on oxidant availability, cloud water chemistry, and gas-particle partitioning (Fig. 2.1b). With lower photochemical oxidant concentrations during winter, SO_4^{2-} is formed mostly through aqueous-phase oxidation of SO_2, via reactions with hydrogen peroxide (H_2O_2), ozone (O_3), and oxygen (O_2) catalyzed by transition metal ions (TMI). Particulate NO_3^- is in equilibrium with nitric acid (HNO_3) gas, with the former favored at low temperature and high humidity. During winter, HNO_3 formation by hydrolysis of dinitrogen pentoxide (N_2O_5) on aqueous particles becomes more important than by reaction of nitrogen dioxide (NO_2) with hydroxyl radicals (OH) (Alexander et al., 2009a). NOx concentrations themselves, in turn, control oxidant concentrations, which influence SO_2 to SO_4^{2-} oxidation rates. In-cloud SO_2 oxidation by O_3 becomes faster with increasing pH (Pandis and Seinfeld, 1989). Similarly, the fraction of HNO_3 forming particulate NO_3^- (Guo et al., 2016; Weber et al., 2016) increases with increasing fine particle pH. The pH of fine particles and cloud water, in turn, depends on the overall gas and particle composition (Fig. 2.1b).

The state of this chemical system and its feedbacks determine the response of [SO_4^{2-}] and [NO_3^-] to emission reductions. However, reproducing the observed concentrations and trends has been a challenge for current atmospheric chemical transport models. Models are largely unable to

reproduce observed wintertime concentrations, particularly of NO_3^- (Heald et al., 2012; Simon et al., 2012), and fail to capture wintertime trends in $[SO_4^{2-}]$ and $[NO_3^-]$ (Paulot et al., 2017; Xing et al., 2015), resulting in unclear policy guidance. Explanations for the weak response of $[SO_4^{2-}]$ to emission reductions include higher SO_2 oxidation efficiency because of a weakening H_2O_2-limitation on the SO_2–H_2O_2 reaction (Paulot et al., 2017; Tsimpidi et al., 2007), rising cloud water pH (Paulot et al., 2017), and higher [OH] and $[H_2O_2]$ at lower NOx emissions (Holt et al., 2015; Tsimpidi et al., 2007). Some modeling studies have suggested that NO_3^- formation in the eastern U.S. is limited by the availability of ammonia (NH_3), such that $[NO_3^-]$ is weakly sensitive to $[HNO_3]$ but increases as $[SO_4^{2-}]$ is lowered and NH_3 availability increases (Holt et al., 2015; Park et al., 2004; Pinder et al., 2007; Pye et al., 2009; Tsimpidi et al., 2007).

A lack of detailed observations of SO_4^{2-}- NO_3^- - NH_4^+ $PM_{2.5}$ and particularly of their precursors during winter has impeded verification of these various hypotheses. The 2015 Wintertime Investigation of Transport, Emissions, and Reactivity (WINTER) aircraft campaign has produced a unique set of comprehensive wintertime atmospheric composition observations over the eastern U.S. Here, I use the GEOS-Chem chemical transport model, evaluated against airborne WINTER observations and ground-based observations, to show that the formation of SO_4^{2-} and NO_3^- $PM_{2.5}$ in winter is controlled by OH- and H_2O_2-mediated SO_2 oxidation, and by fine particle pH, respectively. I demonstrate that the weakening H_2O_2 limitation and increasing fine particle pH have caused the weak response of $[SO_4^{2-}]$ and $[NO_3^-]$ to emission reductions.

2.2 Observations and Model

Speciated PM_1 composition ($[SO_4^{2-}]$, $[NO_3^-]$, and $[NH_4^+]$) for the WINTER campaign was measured by the HR-ToF-AMS (Canagaratna et al., 2007; DeCarlo et al., 2006; Dunlea et al., 2009; Kimmel

et al., 2011). Air was sampled through a HIMIL inlet (Earth Observing Laboratory, 2018) at a flow rate of 10 L min^{-1} into a pressure controlled inlet operated at 325 torr (Bahreini et al., 2008). The sample passed through an aerodynamic focusing lens into the high-vacuum region of the mass spectrometer, and then to the detection chamber where non-refractory species are flash vaporized at 600°C and then ionized with 70 eV electron impact ionization. The ions are orthogonally extracted and analyzed by time-of-flight mass spectrometry. After applying in-field calibrated relative ionization efficiencies for the different inorganic species, the data was corrected for collection efficiency using the composition dependent algorithm proposed by Middlebrook et al. (2012). Measurements were reported at 1 s and 1 min periods and the latter are used here. Detection limits were 57 ng sm^{-3} (SO_4^{2-}), 30 ng sm^{-3} (NO_3^-), and 5 ng sm^{-3} (NH_4^+), and accuracy was 35% (Bahreini et al., 2009).

CSN, IMPROVE, and CASTNET are ground-based $PM_{2.5}$ monitoring networks (Solomon et al., 2014; U.S. Environmental Protection Agency, 2017f). CSN and IMPROVE report 24-hour mean concentrations every third or sixth day. Given my 6-week long simulation period, I include only sites that report every third day. CASTNET measurements are weekly averages. I exclude sites with less than 70% temporal coverage for Feb. 1–Mar. 15, 2015. The eastern U.S. had 26 such CSN sites in 2015 (21 in 2007), 27 IMPROVE sites in 2015 (26 in 2007), and 26 CASTNET sites in 2015 (33 in 2007). When calculating the 2007–2015 change in $PM_{2.5}$ concentrations, I include only those sites that were operational in both years (CSN: 16, IMPROVE: 23, CASTNET: 23).

GEOS-Chem is driven by assimilated meteorological fields from NASA GMAO's GEOS-5 FP system (Bey et al., 2001; Park et al., 2004; Reinecker et al., 2008). I use GEOS-Chem v10-01 in a nested-grid configuration: 0.5˚ latitude × 0.625˚ longitude resolution over North America

and 4˚×5˚ elsewhere. Simulations were performed for Feb. 1–Mar. 15, with a spin-up period of 15 days for the nested domain. The representation of SO_4^{2-}-NO_3^--NH_4^+ chemistry is similar to previous studies (Jacob, 2000; Park et al., 2004; Evans and Jacob, 2005; Alexander et al., 2005, 2009b; Pye et al., 2009; Heald et al., 2012), except that I update the simulation of HNO_3 production from N_2O_5 hydrolysis with a new parameterization (Bertram and Thornton, 2009), and reduce the surface resistance to uptake of HNO_3 for dry deposition to zero (Wesely and Hicks, 2000). Other minor modifications are described in Appendix 1.1–1.2. Gas-particle equilibrium partitioning for SO_4^{2-}-NO_3^--NH_4^+ PM_1 is calculated with ISORROPIA II (Pye et al., 2009). Anthropogenic emissions of $PM_{2.5}$ and precursor gases over the U.S. are from the U.S. EPA's 2011v6.1 (for 2011) and 2011v6.3 (for 2023) modeling platforms for the 2011 National Emissions Inventory (Travis et al., 2016; U.S. Environmental Protection Agency, 2017b). The 2011 U.S. emissions were scaled to 2015 levels for the WINTER simulation (scaling factors SO_2: 0.72, NOx: 0.80, NH_3: 1.0) based on the U.S. EPA emissions trend report (U.S. Environmental Protection Agency, 2015a) and the Air Markets Program Data (U.S. Environmental Protection Agency, 2017a) (Appendix 1.3). Wintertime livestock NH_3 emissions were recalculated to account for the 2015 meteorology (Appendix 1.4). The 2007 and 2023 SO_2 and NOx emissions were based on the past emissions trend (U.S. Environmental Protection Agency, 2015a) and projected emissions (U.S. Environmental Protection Agency, 2017b) reported by the U.S. EPA (Appendix 1.5). For comparison with observations, the model was sampled at the location and time of the measurements. All 1-second aircraft data were averaged to a period of 1 min, and heavily concentrated plumes (SO_2 or NOx > 10 ppbv) were excluded from the analysis.

2.3 OBSERVATIONS AND SIMULATION RESULTS FOR WINTER 2015

The WINTER campaign consisted of 13 daytime and nighttime flights between Feb. 1 and Mar. 15, 2015 (Fig. 2A.2) on the NSF/NCAR C-130 aircraft equipped with a detailed payload to measure gas and particle concentrations. The majority (71%) of measurements were made below an altitude of 1 km. Concentrations of non-refractory SO_4^{2-}-NO_3^--NH_4^+ PM_1 (PM with aerodynamic diameter < 1 μm) were made with a highly-customized high-resolution time of flight aerosol mass spectrometer (HR-ToF-AMS, Aerodyne Research Inc.) (DeCarlo et al., 2006). SO_2 was measured by pulsed ultraviolet fluorescence (Thermo Electron Corporation), and HNO_3 with the Iodide-adduct high-resolution time of flight chemical ionization mass spectrometer (HRToF-CIMS) (Lee et al., 2014). Other instruments onboard measured carbon monoxide (CO), O_3, reactive nitrogen (NOy), and meteorological variables. These measurements were used to fully evaluate the GEOS-Chem model (Fig. 2A.3).

In the following analysis, I assume that the PM_1 mass composition is representative of that of $PM_{2.5}$ for SO_4^{2-}-NO_3^--NH_4^+ over land, and that the influence of other ions (such as Na^+, K^+, Ca^{2+}, Mg^{2+}, Cl^-) on the chemistry of SO_4^{2-}-NO_3^--NH_4^+ $PM_{2.5}$ is negligible. SO_4^{2-} and NO_3^- are present on coarse (diameter >1 μm) sea-salt and dust particles, but sea-salt and dust are minor components of the $PM_{2.5}$ over the eastern U.S. (Fig. 2.1a, 2A.1a) and, when present, are typically externally-mixed with SO_4^{2-}-NO_3^--NH_4^+ PM_1 (Middlebrook et al., 2003; Murphy et al., 2006). Guo et al. (2016) showed that during WINTER nearly all SO_4^{2-} and NO_3^- over land is present as PM_1, and that excluding the other ions in thermodynamic calculations results in better agreement with the observations. Therefore, hereafter, SO_4^{2-}-NO_3^--NH_4^+, refers to those components in PM_1.

The observed horizontal and vertical distributions of SO_4^{2-}-NO_3^--NH_4^+ are reproduced by the GEOS-Chem model (Fig. 2.2). Below 1 km altitude, mean observed SO_4^{2-}-NO_3^--NH_4^+ during WINTER was 2.45 μg sm^{-3} (1 sm^3 equals 1 m^3 at 273.15 K and 1013.25 hPa), with higher concentrations downwind of the source regions in the Northeast Urban Corridor and in the Ohio River Valley (Fig. 2.2a). GEOS-Chem predicts mean concentrations (2.79 μg sm^{-3}) and spatial patterns consistent with the observations (Fig. 2.2b). Furthermore, the observed composition of SO_4^{2-}-NO_3^--NH_4^+ (47% SO_4^{2-}; 32% NO_3^-; 21% NH_4^+) is reproduced by GEOS-Chem (42% SO_4^{2-}; 34% NO_3^-; 24% NH_4^+). GEOS-Chem results are also in agreement with the ground-based observations at the Chemical Speciation Network (CSN), the Interagency Monitoring of Protected Visual Environments (IMPROVE) network, and the Clean Air Status and Trends Network (CASTNET) for Feb. 1–Mar. 15, 2015 (Fig. 2A.4a, b). Past studies have found that GEOS-Chem simulations overestimate wintertime [NO_3^-] over the eastern U.S. by a factor of 3 (Heald et al., 2012; Holt et al., 2015; Walker et al., 2012; Zhang et al., 2012a) – an issue common to many models (Colette et al., 2011; Simon et al., 2012). The WINTER observations have allowed a detailed analysis of nighttime and daytime NOx chemistry, HNO_3 formation, and HNO_3 dry deposition, leading to improvements in the representation of these processes in GEOS-Chem, and a substantial reduction of the [NO_3^-] overestimate (Appendix 1.1, 1.2). The ability of GEOS-Chem to simulate the wintertime SO_4^{2-}-NO_3^--NH_4^+ over the eastern U.S. is further demonstrated by the agreement between the simulated and observed vertical profiles of [SO_4^{2-}], [NO_3^-], [NH_4^+] (Fig. 2.2c–e), [SO_2] and [HNO_3] (Fig. 2A.5). I find that the extent of agreement with observations remains nearly unchanged when I conduct sensitivity simulations varying oxidant concentrations and fine particle pH (Appendix 2). Having evaluated the consistency of the GEOS-Chem results with the aircraft and ground-based observations, I now explore how wintertime SO_4^{2-} and NO_3^- are formed.

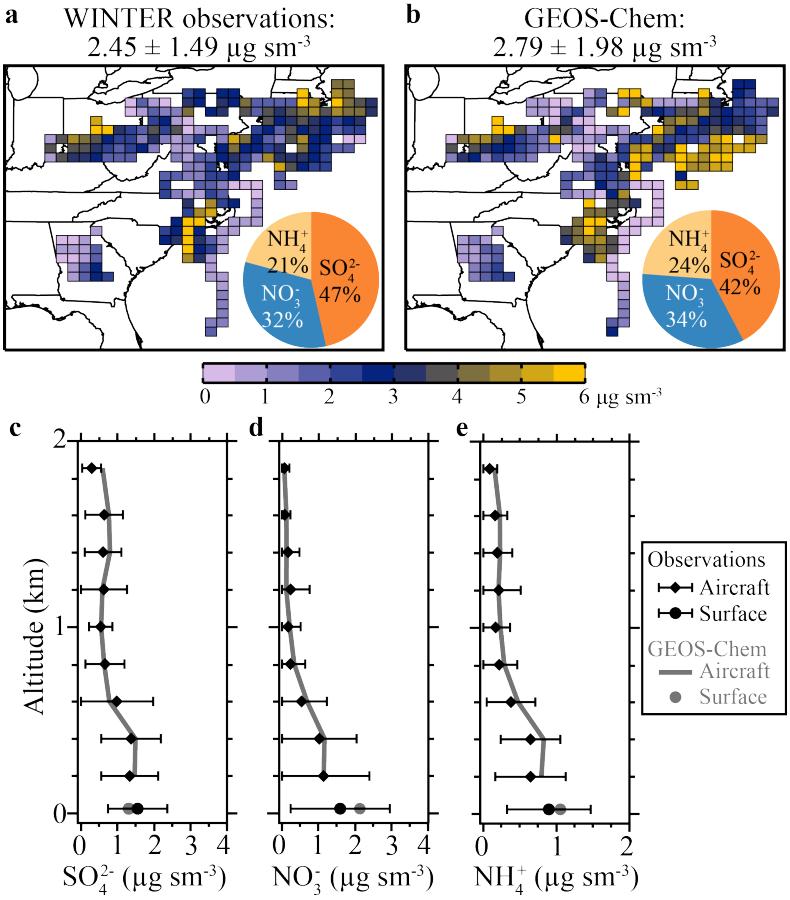

Figure 2.2: Observed and simulated SO_4^{2-}-NO_3^--NH_4^+, during WINTER. Spatial distribution of (a) observed and (b) GEOS-Chem concentrations of SO_4^{2-}-NO_3^--NH_4^+, PM_1 along the WINTER flight paths (Feb. 1–Mar. 15, 2015) below 1 km altitude. The observations are gridded onto the 0.5˚ latitude by 0.625˚ longitude GEOS-Chem grid. The WINTER campaign means ± standard deviations are shown above. The inset pie charts show the average composition of the observed and GEOS-Chem PM1. The lower panels show vertical profiles of observed (black diamonds and error bars: mean ± standard deviation for each altitude bin) and GEOS-Chem (grey line) concentrations of (c) SO_4^{2-}, (d) NO_3^-, (e) NH_4^+ along the WINTER flight tracks. Also shown are the mean observations for the ground-based CSN, IMPROVE, and CASTNET networks (black filled circles with standard deviation) and corresponding model results (grey filled circles) for Feb. 1–Mar. 15, 2015.

2.4 CONTROLS ON THE FORMATION OF SO_4^{2-} AND NO_3^-

Gas-phase and in-cloud oxidation of SO_2 to SO_4^{2-} account for 90% of the SO_4^{2-} source below 2 km altitude in the eastern U.S. during WINTER, with primary anthropogenic emissions of SO_4^{2-} accounting for the remaining 10%. I define the SO_2 to SO_4^{2-} oxidation efficiency (η_{SO42-}) as:

$$\eta_{SO_4^{2-}} = \frac{\text{Mass of } SO_2 \text{ oxidized below 2 km altitude (kg/day)}}{\text{Mass of } SO_2 \text{ emitted (kg/day)}} \quad (2.1)$$

and calculate that over the eastern U.S. during WINTER $\eta_{SO_4^{2-}} = 0.18$. In the model, I find that 46% of SO_2 oxidation in this domain is due to reaction with H_2O_2 in cloud water, 35% due to gas-phase reaction with OH, and the rest comes from the in-cloud SO_2–O_3 and the TMI pathways. The slow winter photochemistry results in low amounts of H_2O_2 (GEOS-Chem winter $[H_2O_2]$ is 0.2 ppbv, 10-fold lower than summer) and OH. While recent work suggests higher oxidant concentrations in winter than previously expected (Thornton et al., 2010; VandenBoer et al., 2013) these oxidant sources are not large enough to shift the relationship between H_2O_2 and SO_2 (Appendix 2). SO_2 oxidation during winter is significantly limited by the availability of H_2O_2, which often gets entirely consumed in the SO_2–H_2O_2 reaction. Figure 2.3a illustrates the relationship between the $[H_2O_2]/[SO_2]$ ratio and the oxidation rate of SO_2 to SO_4^{2-} by reaction with H_2O_2 ($R_{SO_2\text{-}H_2O_2}$) in the model, defined here as:

$$R_{SO_2\text{-}H_2O_2} = \frac{\text{Mass of } SO_2 \text{ oxidized by } H_2O_2 \text{ below 2 km altitude (kg/day)}}{\text{Mass of } SO_2 \text{ below 2 km altitude (kg)}} \quad (2.2)$$

The winter H_2O_2-limitation is demonstrated by the increase of $R_{SO_2\text{-}H_2O_2}$ to around 0.35 day^{-1} as $[H_2O_2]/[SO_2]$ increases to 3, beyond which $R_{SO_2\text{-}H_2O_2}$ becomes independent of this ratio and no longer H_2O_2-limited (Fig. 2.3a). Part of the variability in $R_{SO_2\text{-}H_2O_2}$ is due local variability in cloud liquid water content. The lower troposphere over the land in the eastern U.S. lies in the H_2O_2-limited regime (mean $[H_2O_2]/[SO_2]$: 0.4). The $[H_2O_2]/[SO_2]$ ratio increases over the ocean

as SO_2 concentrations decrease away from source regions and H_2O_2 concentrations increase southward with stronger photochemical production.

Particle-phase NO_3^- is in equilibrium with gas-phase HNO_3 ($HNO_3(g) \leftrightarrow H^+(aq)+NO_3^-(aq)$). This equilibrium shifts to the particle-phase at colder temperatures and at higher particle pH ($pH = -\log_{10} a_{H^+}$, and here a_{H^+}, the activity of H^+, is assumed equal to its molarity (Guo et al., 2016)). Figure 2.3b shows how the GEOS-Chem nitrate particle fraction (ε_{NO3-}, $\varepsilon_{NO_3^-}=\frac{[NO_3^-]}{[HNO_3]+[NO_3^-]}$) varies as a function of PM_1 pH and temperature over the WINTER period below 1 km altitude. The WINTER campaign observations of $\varepsilon_{NO_3^-}$ and PM_1 pH inferred from thermodynamic analysis of observed PM_1 composition (shown as grey circles in Fig. 2.3b) confirm this pattern of increasing $\varepsilon_{NO_3^-}$ with increasing PM_1 pH, as has been reported by Guo et al. (2016).

During WINTER, the GEOS-Chem predicted median PM_1 pH over land below 1 km altitude was 1.29 and $\varepsilon_{NO_3^-}$ was 0.45, in good agreement with those inferred from the measurements (pH = 1.34 and $\varepsilon_{NO_3^-}$ = 0.48 for RH > 40%) (Guo et al., 2016). Local variations in PM_1 pH and temperature influence the spatial distribution of $\varepsilon_{NO_3^-}$ in the model (Fig. 2.3c), with larger $\varepsilon_{NO_3^-}$ (> 0.7) over the colder Midwest with high PM_1 pH (~2) owing to higher NH_3 and lower SO_2 emissions, and smaller $\varepsilon_{NO_3^-}$ (< 0.2) over the warmer ocean with low PM_1 pH. The lower pH of SO_4^{2-}- NO_3^- - NH_4^+ over the ocean is the result of the more rapid decrease of NH_3 away from source regions relative to the more gradual decrease in SO_4^{2-}, which continues to be formed from SO_2 oxidation as air is advected over the ocean. Sea-salt particles are assumed to be externally mixed and NO_3^- present on them is not included in $\varepsilon_{NO_3^-}$(Fig. 2.3c).

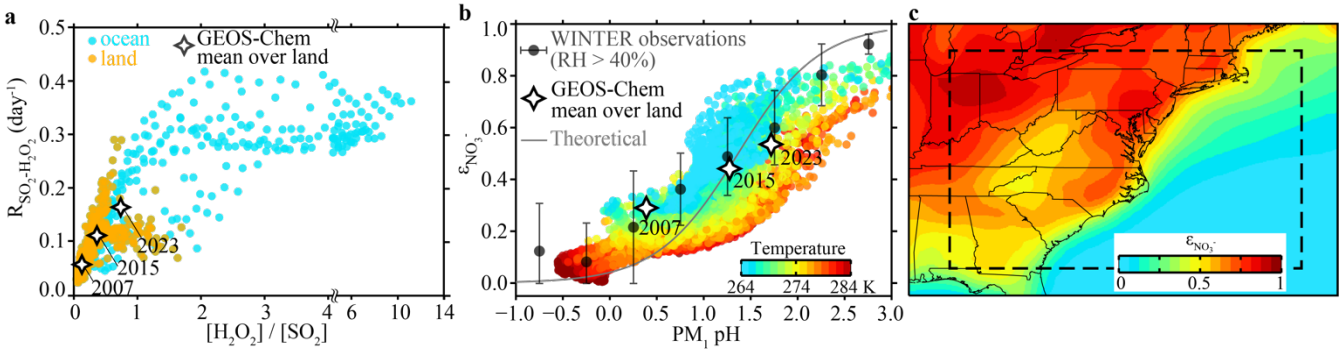

Figure 2.3: Controls on the formation of SO_4^{2-} and NO_3^- during WINTER.(a) GEOS-Chem simulated relationship between the oxidation rate of SO_2 to SO_4^{2-} by reaction with H_2O_2 ($R_{SO_2-H_2O_2}$, see text for definition) and the H_2O_2/SO_2 ratio for Feb. 1–Mar. 15, 2015 in the eastern U.S. (defined as 0-2 km altitude, 31˚N–43˚N, 67˚W–86.5˚W, shown in panel c). (b) GEOS-Chem simulated fraction of nitrate in the particle phase ($\varepsilon_{NO_3^-}$, see text for definition) as function of PM_1 pH and temperature in the bottom 1 km over the eastern U.S. Overlaid (in grey circles) are the measured $\varepsilon_{NO_3^-}$ (means ± standard deviation for each bin) as a function of the measurement-inferred PM_1 pH for the WINTER observations within 1 km of the surface (Guo et al., 2016). Only observations with relative humidity greater than 40% are considered. The black stars represent the mean $\varepsilon_{NO_3^-}$ and PM_1 pH in the bottom 1 km over land in the eastern U.S. for the 2007, 2015, and 2023 simulations. The theoretical relationship between $\varepsilon_{NO_3^-}$ and PM_1 pH for the 2015 mean WINTER conditions is shown with the grey curve. (c) The mean GEOS-Chem $\varepsilon_{NO_3^-}$ (at ground-level) for Feb. 1–Mar. 15, 2015. Note that $\varepsilon_{NO_3^-}$ excludes the contribution of NO_3^- present on sea-salt particles. The dashed black lines enclose the area defined in this study as the eastern U.S.

2.5 Response of $[SO_4^{2-}]$ and $[NO_3^-]$ to Emissions Reductions

I now turn to explaining the weak response of wintertime $[SO_4^{2-}]$ and $[NO_3^-]$ to decreases in SO_2 and NOx emissions between 2007 and 2015, and examining the future response of $[SO_4^{2-}]$ and $[NO_3^-]$ under the 2023 U.S. EPA emissions projections (U.S. Environmental Protection Agency, 2017b). To address these issues, I have performed additional GEOS-Chem simulations for Feb. 1–Mar. 15 with varying U.S. SO_2 and NOx anthropogenic emissions: (i) a simulation with 2007 emissions of SO_2 (15.8 Gg S d^{-1}) and NOx (11.8 Gg N d^{-1}) (U.S. Environmental Protection Agency,

2015a), and (ii) a simulation with 2023 U.S. EPA projected emissions of SO_2 (3.5 Gg S d^{-1}) and NOx (5.8 Gg N d^{-1}) (U.S. Environmental Protection Agency, 2017b). Anthropogenic U.S. emissions of SO_2 and NOx in 2015 were 6.6 Gg S d^{-1} and 7.7 Gg N d^{-1}, respectively (Table 2A.1). Meteorology can affect the interannual variability of $PM_{2.5}$ (Tai et al., 2012), therefore, to isolate the effect of SO_2 and NOx emissions reductions, I have used the same meteorological fields as for my 2015 simulation. Furthermore, I do not consider emission changes for other species, including NH_3 (2007–2015: -2%), CO (-30%), and VOCs (-14%) (U.S. Environmental Protection Agency, 2015a). Despite these simplifying assumptions, the 2007 simulation is consistent with ground-based $PM_{2.5}$ observations for Feb. 1–Mar. 15, 2007 (Fig. 2A.4c, d).

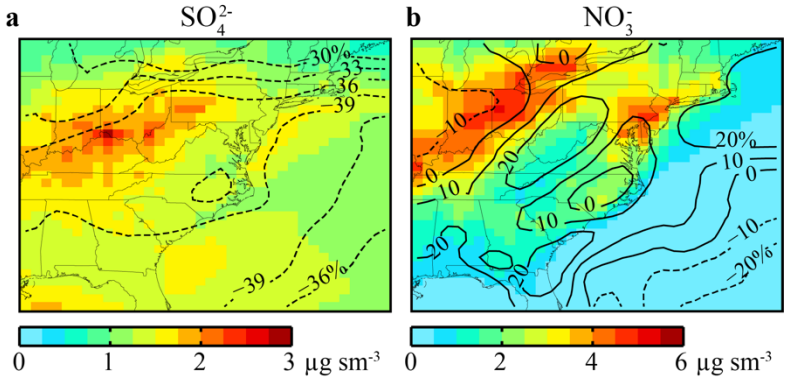

Figure 2.4: GEOS-Chem surface concentrations of SO_4^{2-} (a) and NO_3^- (b) PM_1 for Feb.1–Mar. 15, 2015. The contour lines show the percent change relative to 2007 concentrations (100 ×([2015]-[2007])/[2007]). The 2007–2015 change in SO_2 and NOx emissions is -58% and -35%, respectively.

Simulated surface SO_4^{2-} for Feb. 1–Mar. 15, 2015 show higher concentrations near SO_2 source regions in the Ohio River Valley, but display little spatial variation elsewhere (Fig. 2.4a). The regional extent of SO_4^{2-} pollution reflects the slow oxidation of SO_2 as it is transported downwind of its sources. Between 2007 and 2015, [SO_4^{2-}] decreased everywhere in response to

lower SO_2 emissions, and continues to decrease between 2015 and 2023 (Fig. 2.4a, 2A.6a–c). The 2007–2015 [SO_4^{2-}] decrease observed at surface sites (-0.83 μg sm^{-3}; -31%) is reproduced by GEOS-Chem (-1.06 μg sm^{-3}; -40%). Between 2015 and 2023, the mean modeled [SO_4^{2-}] at surface sites is projected to decrease by another 0.38 μg sm^{-3} (-24%) (Fig. 2.5a).

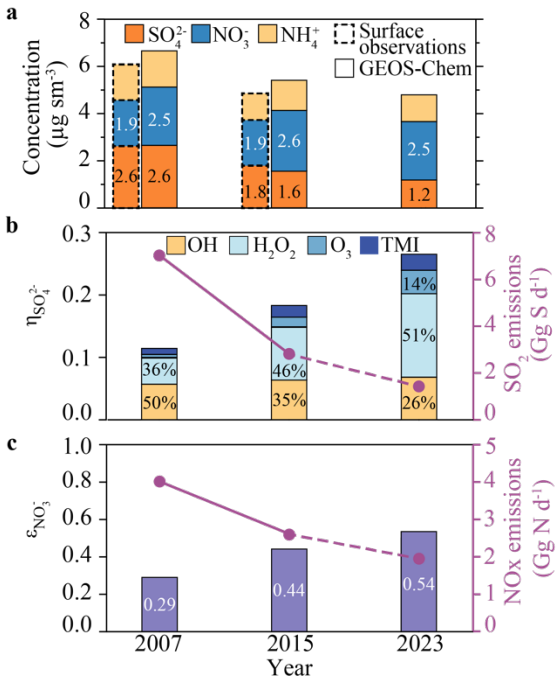

Figure 2.5: Change in SO_4^{2-}-NO_3^--NH_4^+ concentrations and chemical controls from 2007 to 2023.(a) Average surface concentrations of SO_4^{2-}-NO_3^--NH_4^+ $PM_{2.5}$ for the eastern U.S. (31˚N–43˚N, 67˚W–86.5˚W) for Feb.1–Mar. 15, 2007, 2015, and 2023 simulated by GEOS-Chem and observed at the CSN, IMPROVE, and CASTNET ground sites (for 2007 and 2015, bars with dashed lines). (b) SO_2 to SO_4^{2-} oxidation efficiency ($\eta_{SO_4^{2-}}$) over land partitioned by pathway: gas-phase oxidation with OH, aqueous oxidation with H_2O_2, O_3, and O_2 catalyzed by transition metal ions (TMI). SO_2 emissions over the eastern U.S. are shown in purple for the three simulations. (c) Fraction of nitrate in the particle phase ($\varepsilon_{NO_3^-}$) and NOx emissions (in purple) over land in the eastern U.S. for the three simulations.

The relative decrease in modeled [SO_4^{2-}] (2007–2015: -40%, 2015–2023: -24%) is significantly lower than the decrease in U.S. SO_2 emissions (2007–2015: -58%, 2015–2023: -47%). This subdued response to emissions reductions is caused by a corresponding increase in $\eta_{SO_4^{2-}}$, from 0.11 (2007), to 0.18 (2015), and 0.26 (2023) (Fig. 2.5b), which counteracts the effect of reduced SO_2 emissions by allowing a larger fraction of the emissions to be oxidized to SO_4^{2-} on regional and local scales. The increase in $\eta_{SO_4^{2-}}$ is driven by the SO_2–H_2O_2 pathway (Fig. 2.5b): reduced SO_2 concentrations lead to a factor of 2.7 increase in the $[H_2O_2]/[SO_2]$ ratio between 2007 and 2015, and another factor of 2 increase between 2015 and 2023 thereby lowering the degree of H_2O_2-limitation (Fig. 2.3a). The $[H_2O_2]/[SO_2]$ ratio increases mostly because of the decrease in SO_2 concentrations and, to a small extent, because of higher $[H_2O_2]$ at lower NOx emissions. A small increase in $\eta_{SO_4^{2-}}$ is also caused by a faster rate of the SO_2–O_3 aqueous reaction with increasing cloud water pH at lower SO_2 emissions (Fig. 2.5b). In my simulations, mean cloud water pH (weighted by cloud liquid water content) over the eastern U.S. rises from 4.2 (2007) to 4.6 (2023). My results suggest that beyond 2023, $\eta_{SO_4^{2-}}$ will continue to increase with continued relaxation of the H_2O_2-limitation and rise in cloud water pH, further weakening the response of [SO_4^{2-}] to emission reductions.

The model reproduces the observed lack of change in [NO_3^-] over the region between 2007 and 2015, despite a 35% reduction in NOx emissions (Fig. 2.4b, 2.5a, 2A.6d, e). I calculate that the additional 25% decrease in NOx emissions expected by 2023 will not produce much change in [NO_3^-] (Fig. 2.5a, 2A.6f). I find that the formation of total (gas + particle) nitrate decreases linearly with decreasing NOx emissions between 2007 and 2015. But the decrease in nitrate formation is counteracted by an increase in $\varepsilon_{NO_3^-}$ from 0.29 to 0.44, buffering the response of [NO_3^-] (Fig. 2.5c).

In addition, the shift of nitrate to the particle phase increases its lifetime (as NO_3^- deposits more slowly than HNO_3 (Hanson and Lindberg, 1991)) and further offsets its slower formation. Between 2007 and 2023, $\varepsilon_{NO_3^-}$ nearly doubles (0.29 to 0.54), cancelling the effect of NOx emissions reduction. The increase in $\varepsilon_{NO_3^-}$ is the result of an increase in PM_1 pH from 0.39 to 1.7 between 2007 and 2023 (Fig. 2.3b) mainly because of decreasing $[SO_4^{2-}]$ and $[HNO_3]$, but also because of the positive feedback between $\varepsilon_{NO_3^-}$ and PM_1 pH due to the hygroscopicity of NO_3^- (Guo et al., 2017a). There are local differences in the balance between increasing PM_1 pH and decreasing NOx emissions. For example, $[NO_3^-]$ increases downwind of the Ohio River Valley, where the increase in PM_1 pH outpaces the decrease in NOx emissions (Fig. 2.4b, 2A.6d–f).

It is important to note that without a concurrent decrease in NOx emissions, the SO_2 emissions decrease in 2007–2015 would have resulted in a 30% *increase* in $[NO_3^-]$ over the eastern U.S. following the rise in PM_1 pH. It was purely coincidental that the increase in $\varepsilon_{NO_3^-}$ was closely matched by the decrease in NOx emissions, preventing a regional increase in $[NO_3^-]$. My results show that a similar trend is expected to continue until 2023 (Fig. 2.5a, c). At some point beyond 2023, as PM_1 pH increases, $\varepsilon_{NO_3^-}$ will approach 1, and $[NO_3^-]$ will start responding more linearly to NOx emission reductions. My simulations suggest that $[NO_3^-]$ will not decrease much in response to NOx emissions reductions, unless the rate of NOx emission reductions exceeds the rate of increase in $\varepsilon_{NO_3^-}$.

The effectiveness of NOx emissions reductions will be further diminished if emissions of NH_3 were to increase. PM_1 pH is sensitive to NH_3 emissions under present winter conditions over the eastern U.S. (Appendix 2.3) and a pH increase will result in an increase in the conversion of

NOx to NO_3^- (due to $\varepsilon_{NO_3^-}$ increasing with pH). This response of PM_1 pH to NH_3 emissions is not necessarily true in other seasons and locations where both the PM_1 pH and the dependence of $\varepsilon_{NO_3^-}$ on pH may differ (Guo et al., 2017b; Weber et al., 2016).

2.6 CONCLUSION

Wintertime [SO_4^{2-}] and [NO_3^-] in the eastern U.S. have responded weakly to SO_2 and NOx emissions reductions. While previous modeling studies have examined the sensitivity of wintertime [SO_4^{2-}] and [NO_3^-] to emission reductions, the fidelity of these models could not be verified without the constraints of detailed *in situ* observations. In this study, I have presented new aircraft observations of SO_4^{2-}-NO_3^--NH_4^+ PM_1 concentrations and precursor gases that serve as crucial benchmarks for models. I have shown that the GEOS-Chem model simulation of SO_4^{2-}-NO_3^- -NH_4^+ PM_1 concentration and composition is in good agreement with the WINTER campaign observations. GEOS-Chem results for the WINTER campaign showed that 18% of the SO_2 is regionally oxidized to SO_4^{2-} in winter over the eastern U.S., compared to about 35% during summer. SO_2 oxidation happens mostly by H_2O_2 (46%) and OH (35%), and is limited by low wintertime [H_2O_2] and [OH]. The observations and model showed that about 45% of the total nitrate (gas + particle) was in the particle phase during the WINTER campaign period because of low PM_1 pH (~1.3). GEOS-Chem is able to reproduce the weak decrease in [SO_4^{2-}] and [NO_3^-] between 2007 and 2015 observed at ground-based sites. I find that as SO_2 and NOx emissions decrease, the resulting increase in [H_2O_2]/[SO_2] and PM_1 pH leads to more efficient regional formation of SO_4^{2-} and NO_3^- per unit mass of precursor pollutant emitted. I project that these chemical feedbacks will persist into the near future. Between 2015 and 2023, I predict a 24% decrease in [SO_4^{2-}] and little to no change in

[NO_3^-] despite an expected 47% decrease in SO_2 emissions and 25% decrease in NOx emissions. The counteracting chemical feedbacks during the winter necessitate stronger emissions reductions for faster improvements in wintertime air quality.

2.7 APPENDIX 1: EXTENDED DESCRIPTION OF THE GEOS-CHEM SIMULATIONS

GEOS-Chem is a global 3-D model of atmospheric composition (www.geos-chem.org). In this study, I use GEOS-Chem v10-01 driven by assimilated meteorological fields from NASA Global Modeling and Assimilation Office's GEOS-5 Forward Processing (FP) system. The meteorological fields for 2015 have a native horizontal resolution of 0.25° latitude by 0.3125° longitude and have 72 layers (hybrid grid) in the vertical extending to 0.01 hPa. For my study I used the one-way nested-grid configuration with a resolution of 0.5° latitude by 0.625° longitude over North America (130°W–60°W, 10°N–60°N) with initial and boundary conditions from a 4°×5° global simulation (Kim et al., 2015; Wang et al., 2004). There are 47 levels in the vertical in both the North America and the global grids, with typically 8 levels within 1 km of the surface. All simulations were performed for Feb. 1–Mar. 15, with a spin-up period of 15 days for the North America nested simulation, and 6 months for the global simulation.

Transport and deposition

GEOS-Chem simulates the process of advection with a flux-form semi-Lagrangian scheme (Lin and Rood, 1996), boundary layer mixing using a non-local scheme (Lin and McElroy, 2010), and convective transport using archived convective mass fluxes from GEOS-5 FP (Wu et al., 2007). The wet deposition scheme includes scavenging of gases and particles in wet convective updrafts and in large-scale precipitation (Amos et al., 2012; Liu et al., 2001; Wang et al., 2011). The dry deposition scheme is based on the standard resistance-in-series model (Wang et al., 1998; Wesely, 1989; Zhang et al., 2001). I have made a few modifications to these schemes in my simulations.

In the wet deposition calculation, the scavenging rate of a tracer during rainout is inversely proportional to the condensed (ice + water) water content of the precipitating cloud. This is set to a constant value of 1 g m^{-3} in the current scheme (Liu et al., 2001; Wang et al., 2011). However, it is larger than that observed in precipitating in ice clouds (~0.1 g m^{-3}), and results in under-vigorous scavenging at cold temperatures (Croft et al., 2016). I correct for this by setting a temperature dependent value for the condensed water content. I maintain it as 1 g m^{-3} for liquid clouds (T>=268 K), but linearly decrease it to a minimum of 0.1 g m^{-3} for ice clouds (T<=258 K). This change mostly affects the concentrations of soluble gases and particles in the 2–4 km altitude range, where most ice or mixed-phase precipitation is formed. Concentrations below 1 km altitude are not sensitive to this change.

In the dry deposition scheme, the surface resistance to uptake of gases is calculated using Wesely's method (Wesely, 1989). It assumes that dry deposition of gases is extremely slow at low temperatures (T<268K), and applies a temperature-dependent resistance increment to the surface resistance. I have limited this increment in the surface resistance at cold temperatures to a factor of two, following Zhang et al. (2003). Instead of calculating the surface resistance to uptake of HNO_3 online, I assume it to be effectively zero for all surfaces, considering its high solubility (Hanson and Lindberg, 1991; Pryor and Klemm, 2004; Sørensen et al., 2005; Wesely and Hicks, 2000).

Chemistry

I simulate the tropospheric chemistry of SO_4^{2-}-NO_3^--NH_4^+ (Alexander et al., 2009b; Heald et al., 2012; Park et al., 2004; Pye et al., 2009) particles coupled to the gas-phase chemistry of HOx-NOx-VOC-O_3-SO_2-BrOx (Bey et al., 2001; Parrella et al., 2012). SO_2 oxidation takes place in the gas-phase by reaction with OH (Park et al., 2004), in cloud droplets by aqueous-phase reactions

with H_2O_2, O_3 and O_2 catalyzed by Fe(III) and Mn(II), in rainwater by reaction with H_2O_2 and on sea-salt aerosol by reaction with O_3 (Alexander et al., 2009b; Park et al., 2004). Cloud pH for aqueous-phase reactions is calculated in the model based on the concentrations of SO_4^{2-}, total NO_3^-, and total NH_3 (Alexander et al., 2012). The sources of atmospheric Fe and Mn are anthropogenic (via coal combustion) and natural (mineral dust). I follow the work of Alexander et al. (2009b) to simulate Fe(III) and Mn(II) concentrations in GEOS-Chem and their relationship to atmospheric Fe and Mn emissions from mineral dust and coal combustion. I modify the scheme of Alexander et al. (2009b) by introducing a particle-phase anthropogenic Fe tracer (pFe) in the GEOS-Chem model. I assume that pFe is emitted from coal combustion proportionally to primary SO_4^{2-} emissions with an emission ratio of 0.15 kg kg^{-1} (Reff et al., 2009). Deposition of the pFe tracer is assumed to be similar to that of SO_4^{2-}. Anthropogenic Mn concentrations are assumed to be 1/30 times pFe concentrations, based on CSN observations during Feb-Mar 2015.

HNO_3 formation takes place in the gas-phase by OH oxidation of NO_2, oxidation of VOC by NO_3 radical (when proceeding via hydrogen abstraction), and through the hydrolysis of NO_3 radical (reactive uptake coefficient, $\gamma=1\times10^{-4}$) and N_2O_5 (Evans and Jacob, 2005; Jacob, 2000). HNO_3 formation through heterogeneous reaction of NO_2 on aerosol surfaces is slow ($\gamma\approx1\times10^{-6}$) and is excluded from my simulations, assuming that only HNO_2 is produced (Kleffmann et al., 1998). I update the γ for the N_2O_5 heterogeneous reaction using the parameterization of Bertram and Thornton (Bertram and Thornton, 2009) for SO_4^{2-}-NO_3^--NH_4^+ particles, and for organic aerosol particles I assume $\gamma=1\times10^{-4}$ – 1×10^{-3} depending on ambient relative humidity (Badger et al., 2006). The N_2O_5 heterogeneous reaction also results in the formation of $ClNO_2$, which photolyzes to form NO_2. With these updates, I find that about 62% of HNO_3 during WINTER is formed through N_2O_5 hydrolysis, 36% through NO_2+OH, and 2% through the other pathways. These updates to HNO_3

production and dry deposition (described above) were important in reducing the winter bias in $[NO_3^-]$ reported in previous studies.

The gas-particle partitioning of NH_3 and HNO_3 is calculated with ISORROPIA II (Fountoukis and Nenes, 2007; Pye et al., 2009) assuming bulk equilibrium of the gas-phase with SO_4^{2-}-NO_3^--NH_4^+ PM_1. Particles are assumed to be in the liquid-phase, with no solid precipitates, at all relative humidity values. This assumption is suitable in the boundary layer where fluctuations in relative humidity, low aerosol pH and the presence of water soluble organic species often keep particles deliquescent above relative humidity of 20% (Bertram et al., 2011; Heald et al., 2012). Carbonaceous, sea-salt and dust particles are considered externally mixed with SO_4^{2-}-NO_3^--NH_4^+ PM_1 and do not participate in NH_3 and HNO_3 gas-particle partitioning (Hatch et al., 2011a, 2011b; Liu et al., 2003; Middlebrook et al., 2003; Murphy et al., 2006).

Emissions

U.S. anthropogenic emissions are from the U.S. EPA's Emissions Modeling Platform v6.1 (U.S. Environmental Protection Agency, 2017b), which provides spatially (~12 km) and temporally (hourly) resolved emissions fluxes calculated from the U.S. EPA's National Emissions Inventory (NEI) 2011 as implemented in GEOS-Chem by Travis et al. (2016). Emissions are calculated by the Harvard-NASA Emission Component (HEMCO) v1.1 (Keller et al., 2014). The 2011 emissions are scaled to 2015 levels for the Feb. 1–Mar. 15, 2015 simulation (scaling factors for SO_2: 0.72, NOx: 0.80, CO: 0.83, VOCs: 0.9) based on the U.S. EPA emissions trend report (U.S. Environmental Protection Agency, 2015a). The SO_2 emissions scaling factor is higher than that based on the change in annual emissions (0.58) (U.S. Environmental Protection Agency, 2015a) as I also take into account the monthly U.S. EPA's Air Markets Program Data (U.S. Environmental

Protection Agency, 2017a), which shows that SO_2 emissions from power plants for the WINTER period were higher compared to the other months. Emissions totals for Feb. 1–Mar. 15, 2015 are shown in Table 2A.1. According to the U.S. EPA emissions speciation profiles, 2% of anthropogenic sulfur emissions is in the form of SO_4^{2-}. Surface emissions of formaldehyde (HCHO) are scaled by a factor of 5 to match WINTER aircraft observations, and test the sensitivity to this scaling in Appendix 2. Open-fire emissions are from the Global Fire Emissions Database (GFED) version 4 inventory (http://www.globalfiredata.org/data.html). Soil and lightning NOx emissions and oceanic DMS emissions vary with meteorology and are calculated online in the model (Heald et al., 2012; Pye et al., 2009).

NH_3 emissions

The bi-directional surface exchange of NH_3 is represented in GEOS-Chem by emissions and deposition, which are treated independently. Anthropogenic emissions, including from livestock and fertilizer sources, are from the U.S. EPA v6.1 Modeling Platform. Biomass burning emissions are from GFEDv4, and natural emissions from uncultivated soils, wild animals, and oceans are from Bouwman et al. (1997). NH_3 emissions vary with meteorology (Sutton et al., 2013; Willem A. H. Asman et al., 1998), especially temperature, but this variation is not simulated in GEOS-Chem. I account for the dependence of NH_3 livestock emissions on temperature by reallocating annual livestock NH_3 emissions to hourly emissions as a function of the hourly surface temperature: $\log_{10}(NH_3 \text{ emissions}) \sim 0.048 \times \text{temperature (°C)}$ (Aneja et al., 2000). Fertilizer sources of NH_3 are minor during winter in the eastern U.S. and are kept unchanged from the original U.S. EPA emissions. Other anthropogenic NH_3 emissions (e.g. vehicular sources) are also kept unchanged.

Table 2A.2: Emissions of SO_2, NOx and NH_3 for Feb 1–Mar. 15, 2015 over the contiguous U.S. (excludes Alaska and Hawaii) and the eastern U.S. (31˚N–43˚N, 67˚W–86.5˚W). NH_3 emissions for Feb 1–Mar. 15 from the U.S. EPA 2011v1 modeling platform (U.S. Environmental Protection Agency, 2017b) are shown in parenthesis.

Species	Emissions	
	Contiguous U.S.	Eastern U.S.
SO_2 total (Gg S d^{-1})	6.66	2.81
Anthropogenic	6.56	2.90
Biomass burning	0.014	0.003
Volcanic	0.083	0.00
NOx total (Gg N d^{-1})	9.15	2.90
Anthropogenic	7.72	2.69
Biomass burning	0.040	0.008
Soils, fertilizer and lightning	1.38	0.204
NH_3 total (Gg N d^{-1})	4.13 (5.90)	0.806 (1.36)
Anthropogenic	3.86 (5.64)	0.755 (1.31)
Biomass burning	0.053	0.009
Natural	0.210	0.043

The temperature dependence of NH_3 emissions that I use here is based on NH_3 flux measurements from a swine waste storage facility, but for simplicity I consider it as representative of the temperature dependence of NH_3 emissions from all livestock sources (Aneja et al., 2000). There is some uncertainty in the magnitude of the temperature sensitivity of NH_3 emissions. Sutton et al. (2013) analyzed several bottom-up and top-down estimates and found that the temperature sensitivity of NH_3 emissions from terrestrial sources fall in range of a factor of 1.5–3 increase in emissions for a 10˚C increase in temperature. The expression above corresponds to a temperature sensitivity at the upper end of this range, resulting in about a factor of 10 seasonal change in livestock NH_3 emissions. I find that NH_3 emissions for Feb. 1–Mar. 15, 2015 recalculated using my method are 40% lower than U.S. EPA estimate for the same period in 2011 (U.S.

Environmental Protection Agency, 2017b) (Table 2A.1). These lower NH_3 emissions are partly due to cold winter temperatures for 2015 (which were about 5 ºC colder than the climatological mean for the region) and are supported by the agreement between the measured and simulated [NH_4^+] and between the measurement-inferred and GEOS-Chem PM_1 pH for the WINTER campaign.

2007 and 2023 simulations

The simulations for 2007 and 2023 are conducted by scaling U.S. SO_2 and NOx emissions while emissions of other species, non-U.S. emissions, meteorology, and boundary conditions are unchanged from the Feb 1–Mar. 15, 2015 simulation. The scaling factors for 2007 (SO_2: 2.39 and NOx: 1.53, with respect to 2015) are calculated from the U.S. EPA emissions trend report (U.S. Environmental Protection Agency, 2015a). The scaling factors for 2023 (SO_2: 0.53 and NOx: 0.75, with respect to 2015 levels) are calculated from the U.S. EPA emissions projections in the 2011v6.3 (2023el) modeling platform (U.S. Environmental Protection Agency, 2017b). These projections account for changes in activity, fuel types, and national and local regulations that are expected to take effect by 2023. For ease of interpretation, I neglect regional and seasonal differences in the emissions changes for the 2007 and 2023 simulations. Estimates of the state-level differences in SO_2 and NOx emissions changes for Feb. and Mar. for the 2007–2015 and 2015–2023 periods are shown in Fig. 2A.7. The 2007 emissions in Fig. 2A.7 are based on the 2007/2008 v5 Modeling Platform (U.S. Environmental Protection Agency, 2017c) and take into account the effect of the ozone season NOx emission reduction program. The 2023 emissions in Fig. 2A.7 are based on the Feb.–Mar. emissions in the 2011v6.3 (2023el) modeling platform, instead of the annual emissions that were used to calculate the scaling factors. There are considerable variations in the state-level emissions changes, but the average emissions changes for

the eastern U.S. are similar to the national changes. Thus, my simulated changes in [SO_4^{2-}] and [NO_3^-] for 2007–2015 and 2015–2023 are representative of regional scale of the eastern U.S., but do not represent the local changes accurately.

2.8 Appendix 2: Uncertainty in Oxidants and Fine Particle pH

Oxidant concentrations and PM_1 pH are important controls on [SO_4^{2-}] and [NO_3^-] during wintertime (Fig. 2.1b). Here I briefly discuss the sensitivity of my model results to uncertainties in the simulated oxidant sources and PM_1 pH. I determine the model sensitivity to these factors by conducting three additional simulations for Feb.1–Mar. 15, 2015, as described below.

HOx

HCHO is an important anthropogenic source of HOx radicals (HOx=OH+HO_2) during winter over the eastern U.S. It is produced from VOC oxidation and is directly emitted, but its wintertime sources are uncertain (Zhu et al., 2017). In my simulations, I scaled primary HCHO emissions from the NEI inventory by a factor of 5 to be able to capture WINTER aircraft observations of HCHO. I conducted a sensitivity simulation ("Low-HOx" simulation) without this scaling to quantify the uncertainty in HOx and its effect on concentrations of SO_4^{2-}-NO_3^--NH_4^+. In this "Low-HOx" simulation, HOx decreases by 9% in the eastern U.S. (below 1 km), and by up to 16% over the northern states of New York, Ohio, and Pennsylvania. This results in less than a 4% change in the simulated concentrations of SO_4^{2-}-NO_3^--NH_4^+ along the WINTER flight tracks and at ground sites (Fig. 2A.8). This low sensitivity of [SO_4^{2-}] to changes in anthropogenic HOx sources near the surface is because only 35% of the SO_4^{2-} formation takes place through oxidation by OH, and there is little (<3%) change in [H_2O_2] in this simulation. The low sensitivity of [NO_3^-] is because only 36% of HNO_3 formation takes place via the NO_2+OH reaction during winter.

H_2O_2

The SO_2–H_2O_2 aqueous reaction is important for SO_4^{2-} formation during winter over the eastern U.S. This pathway is often limited by low levels of H_2O_2 during winter, and I examine how uncertainty in the GEOS-Chem simulation of H_2O_2 can affects my results. A comparison of GEOS-Chem [H_2O_2] with aircraft observations in the Arctic during spring showed good agreement for the simulations in which aerosol processing of HO_2 does not result in H_2O_2 production (Christian et al., 2017; Mao et al., 2010). The HOx chemistry in my GEOS-Chem simulations is consistent with these previous simulations (Christian et al., 2017). H_2O_2 was not measured during the WINTER campaign, nor is it measured routinely at ground-based sites. However, the agreement between GEOS-Chem and the WINTER campaign observations of HOx precursors and species affecting HOx concentrations (Fig. 2A.3) provide indirect constraints on GEOS-Chem's HOx and H_2O_2 during WINTER. I conduct a sensitivity study in which I increase [H_2O_2] by 50% everywhere ("High H_2O_2" simulation). For simplicity, I increase [H_2O_2] in such a way that the effect of this increase is restricted to SO_2 and SO_4^{2-} chemistry, and there is no direct effect on the broader HOx-NOx-O_3 chemistry. I find that an increase of 50% in [H_2O_2] causes an increase in the campaign-average SO_2–H_2O_2 reaction rate ($R_{SO_2\text{-}H_2O_2}$) of 37%, reflecting the nonlinearities in the reaction. Moreover, the increase in SO_4^{2-} formation by SO_2–H_2O_2 is compensated by a decrease in formation from the other pathways, as SO_2 availability decreases and cloud pH increases from the additional SO_4^{2-}. Total $\eta_{SO_4^{2-}}$ increases by 12%. The resulting increase in [SO_4^{2-}] along the WINTER flight tracks and at ground-based stations is less than 5% (Fig. 2A.8). NO_3^- and NH_4^+ do not change much either, indicating low sensitivity of SO_4^{2-}-NO_3^--NH_4^+ PM_1 to uncertainties in my calculated [H_2O_2].

PM_1 pH

Uncertainty in the simulated PM_1 pH arises in part from uncertainty in the concentrations of the base cations. In my simulations, NH_4^+ is the only base cation in SO_4^{2-}-NO_3^--NH_4^+ PM_1. Sea-salt and dust particles are considered externally mixed, which is supported by observations in the eastern U.S. (Hatch et al., 2011a, 2011b; Liu et al., 2003; Middlebrook et al., 2003; Murphy et al., 2006). $[NH_4^+]$ is a function of NH_3 emissions, which themselves have an uncertainty of about 30% (Sutton et al., 2013). To quantify the uncertainty in PM_1 pH related to concentrations of the base cations, and its effect on SO_4^{2-}-NO_3^--NH_4^+, I conduct a third sensitivity simulation ("Low-pH" simulation) by decreasing domestic NH_3 emissions by 30%. I find that in the "Low-pH" simulation PM_1 pH in the bottom 1 km over land in the eastern U.S. is lower by 0.3 units compared to that in the reference simulation (pH=1.29). This results in a decrease in the fraction of particle nitrate ($\varepsilon_{NO_3^-}$) from 0.45 to 0.37 over the region. $[NO_3^-]$ decreases by 29% along the WINTER flight tracks and by 17% at the surface CSN, IMPROVE, and CASTNET sites (Fig. 2A.8). $[SO_4^{2-}]$ and $[NH_4^+]$ change by <10%. These results indicate that particle pH is sensitive to NH_3 emissions and simulated $[NO_3^-]$ to PM_1 pH during the wintertime over the eastern U.S., unlike other regions or seasons (Guo et al., 2017b; Weber et al., 2016). Despite the sensitivity, the mean simulated $[NO_3^-]$ in the "Low-pH" simulation is within ± 20% of the aircraft and surface observations.

2.9 APPENDIX 3: ADDITIONAL FIGURES FOR CHAPTER 2

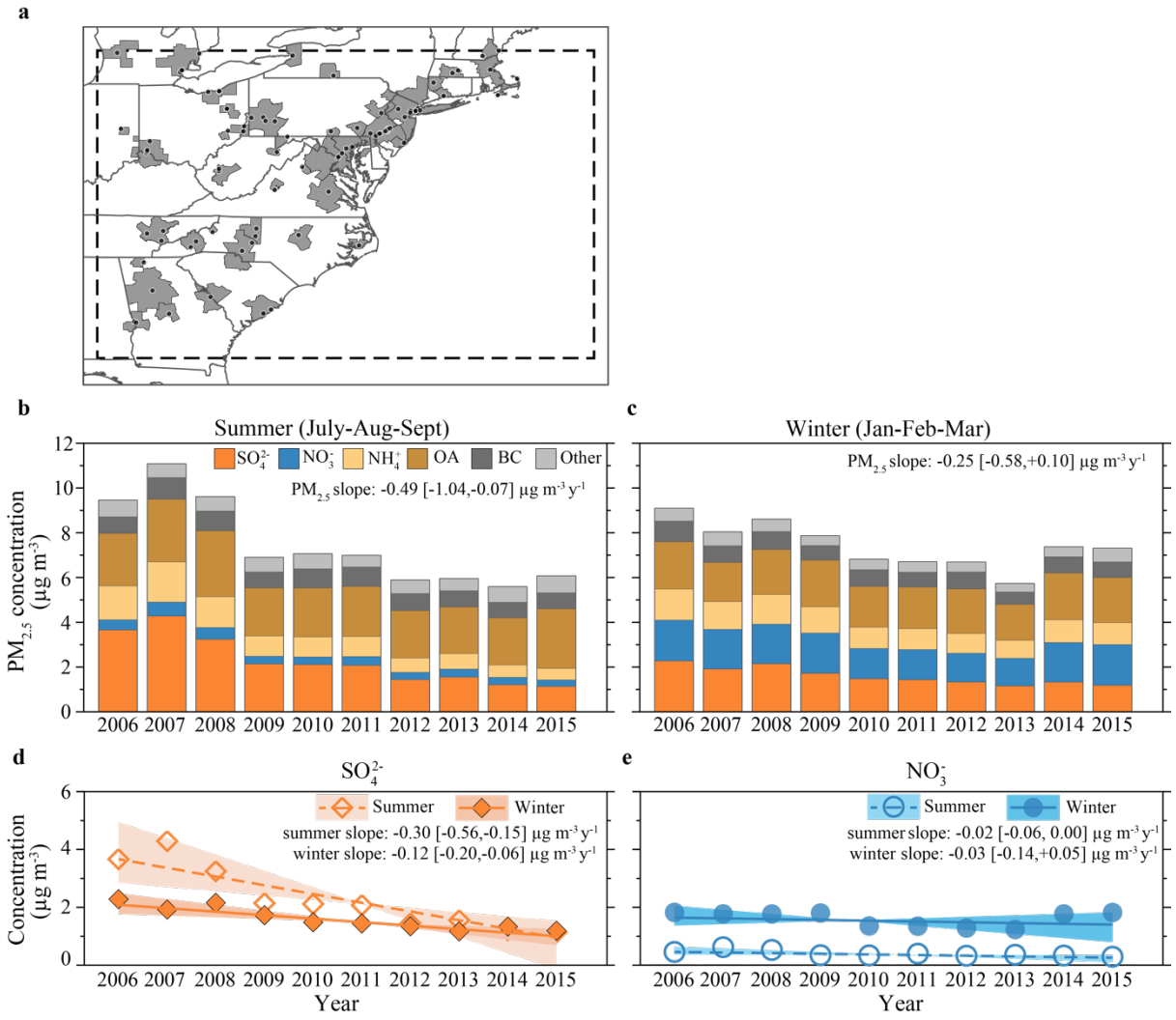

Figure 2A.1: Trends in $PM_{2.5}$ concentrations in the eastern U.S.(a) Locations of the 59 U.S. EPA $PM_{2.5}$ stations used for calculating the population-weighted concentrations shown in Fig. 2.1 (U.S. Environmental Protection Agency, 2017d). The grey shaded regions show the Core Based Statistical Areas or counties associated with each monitor that are used as surrogates to estimate the exposed population. (b) Summer (July-August-September) and (c) winter (January-February-March) population-weighted $PM_{2.5}$ concentrations from 2006 to 2015. 39 stations were in continuous operation in 2006–2015. The $PM_{2.5}$ composition is separated into sulfate (SO_4^{2-}), nitrate (NO_3^-), ammonium (NH_4^+), organic aerosol (OA), black carbon (BC), and sea-salt and crustal material (other). The best-fit rates of concentration change (slopes) and their 95% confidence intervals (in brackets), are calculated with the Kendall-Theil Robust Line method (Helsel and Hirsch, 2002). Population-weighted (d) SO_4^{2-} and (e) NO_3^- concentrations for summer and winter at the surface sites. The best-fit rates of concentration change (solid and dashed lines) and their 95% confidence bands (shaded) are shown.

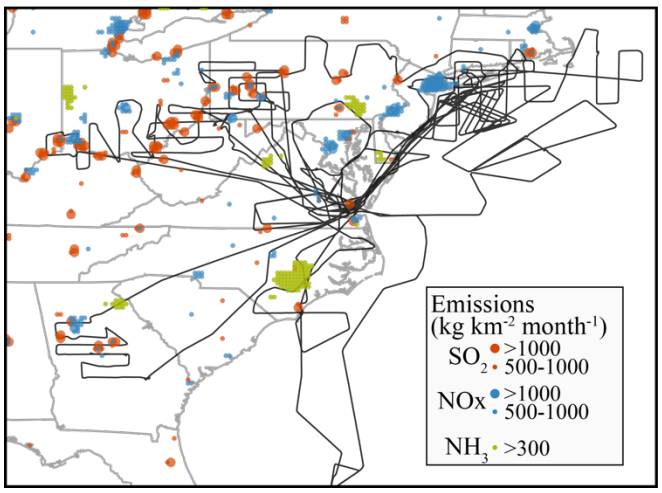

Figure 2A.2: Map of the flight tracks for the 13 research flights of the WINTER campaign. The overlay shows the largest SO_2, NOx and NH_3 emissions sources for 2015 (U.S. Environmental Protection Agency, 2017b).

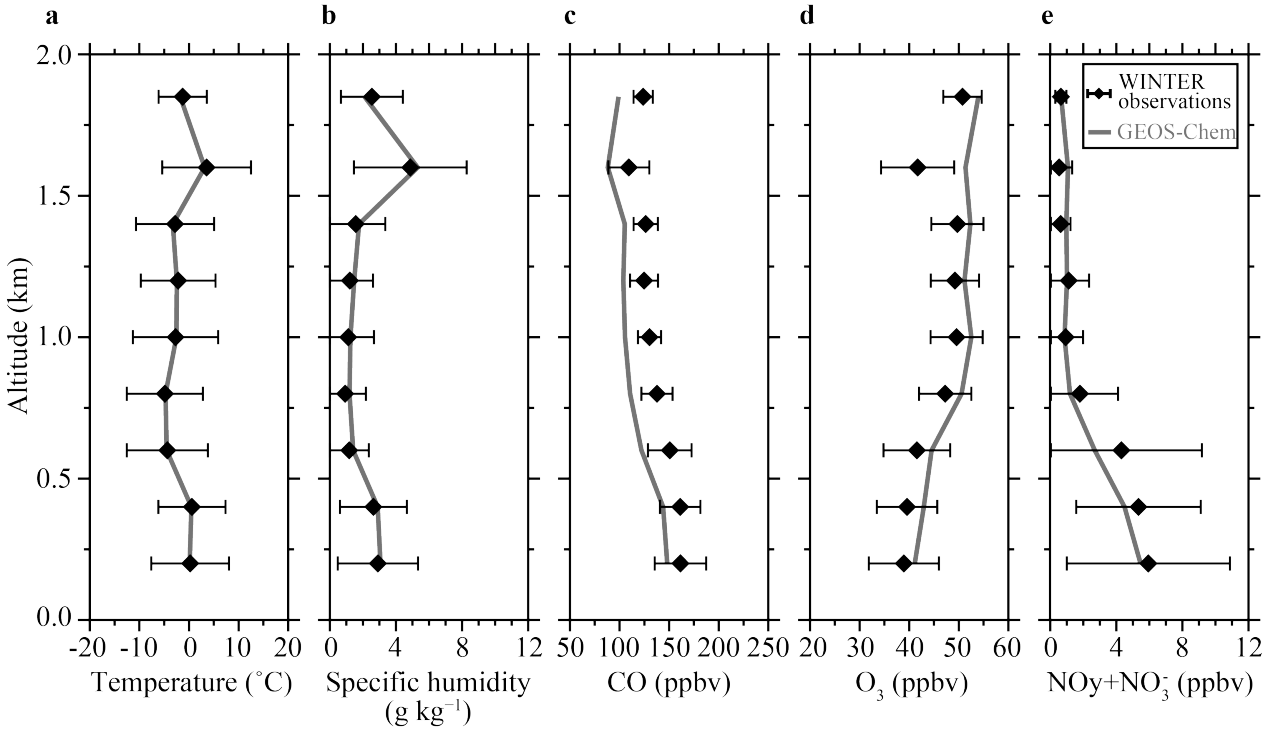

Figure 2A.3: Observed and simulated vertical profiles of (a) temperature, (b) specific humidity, (c) CO, (d) O_3, and (e) sum of NOy and NO_3^- for the WINTER campaign. For the observations, the mean (filled diamond) ± standard deviations (error bars) for measurements in each altitude bin are shown.

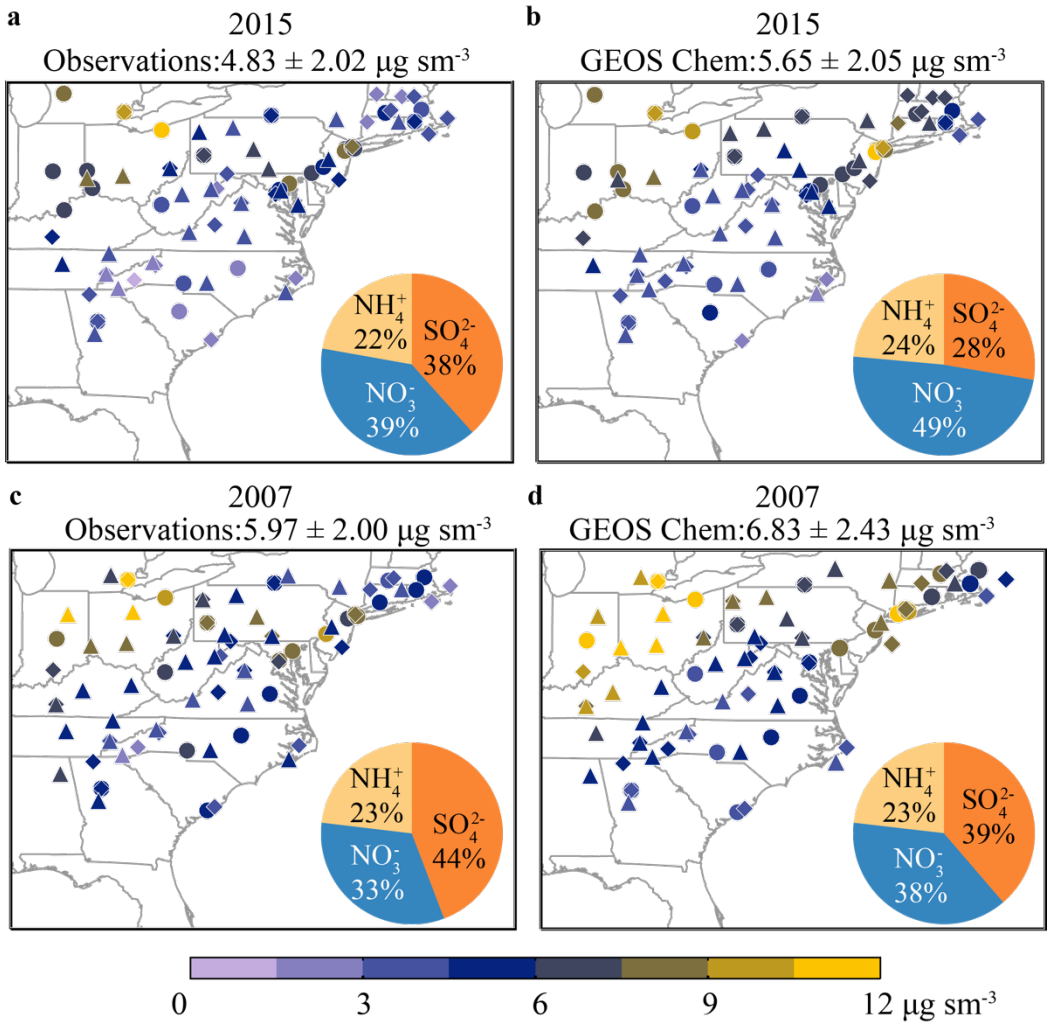

Figure 2A.4: Observed and GEOS-Chem simulated concentrations of total SO_4^{2-}-NO_3^--NH_4^+ mass concentrations at the CSN, IMPROVE and CASTNET sites for Feb. 1–Mar. 15, 2015 (a,b) and 2007 (c,d). The text shows the observed and modeled mean ± standard deviation for all sites. The inset pie charts show the observed and modeled composition.

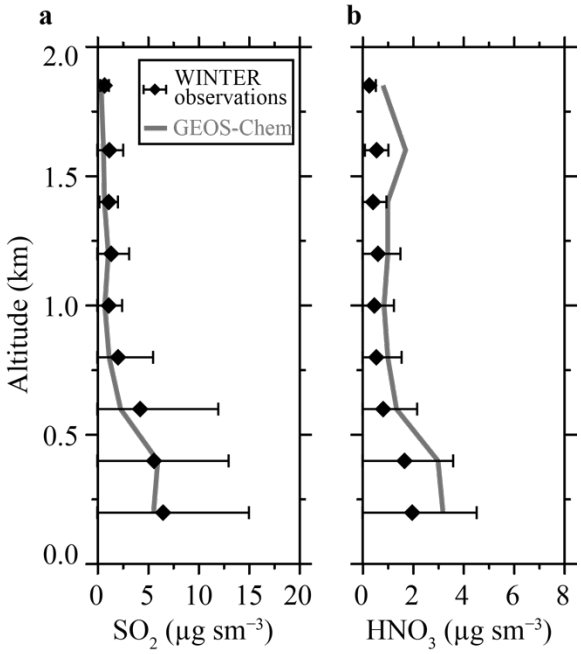

Figure 2A.5: Observed and simulated vertical profiles of (a) SO_2 and (b) HNO_3 for the WINTER campaign. For the observations, the mean (diamond) ± standard deviation (error bars) for measurements in each altitude bin are shown.

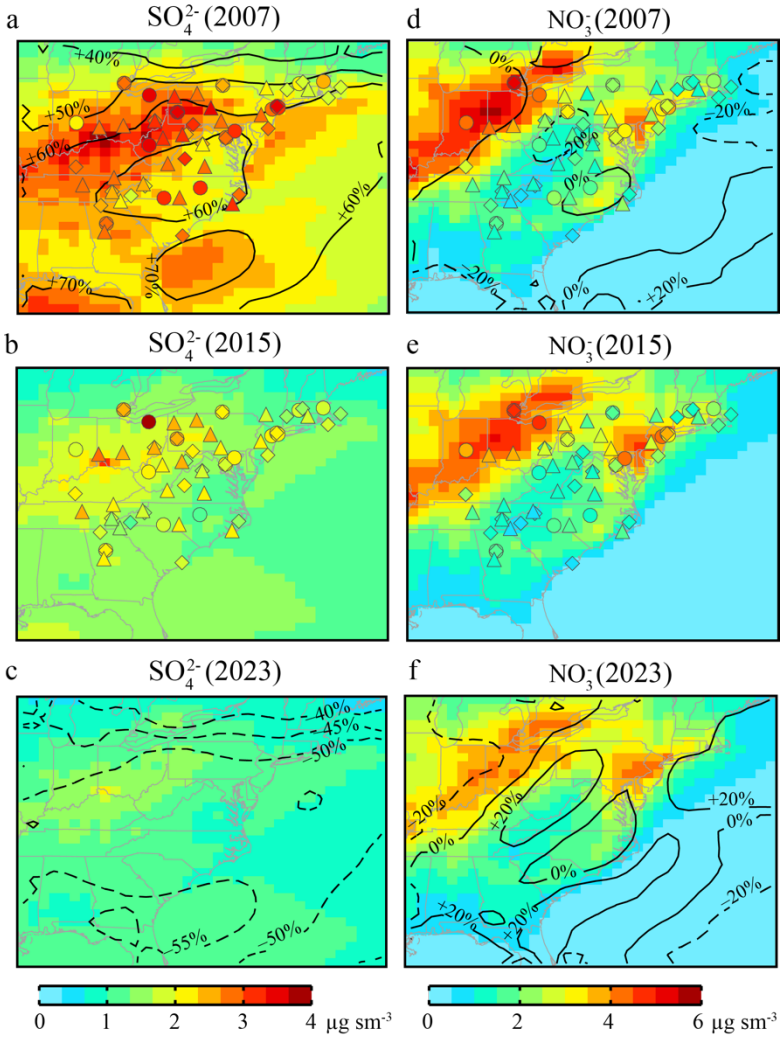

Figure 2A.6: Mean surface [SO_4^{2-}] and [NO_3^-] for Feb.1–Mar. 15, 2007 (a,d), 2015 (b,e) and 2023 (c,f). Background colors show the GEOS-Chem model concentrations, while observed concentrations at CSN (circles), IMPROVE (diamonds), and CASTNET (triangles) sites are indicated with color-coded symbols. The contour lines show the percent change with respect to 2015 concentrations.

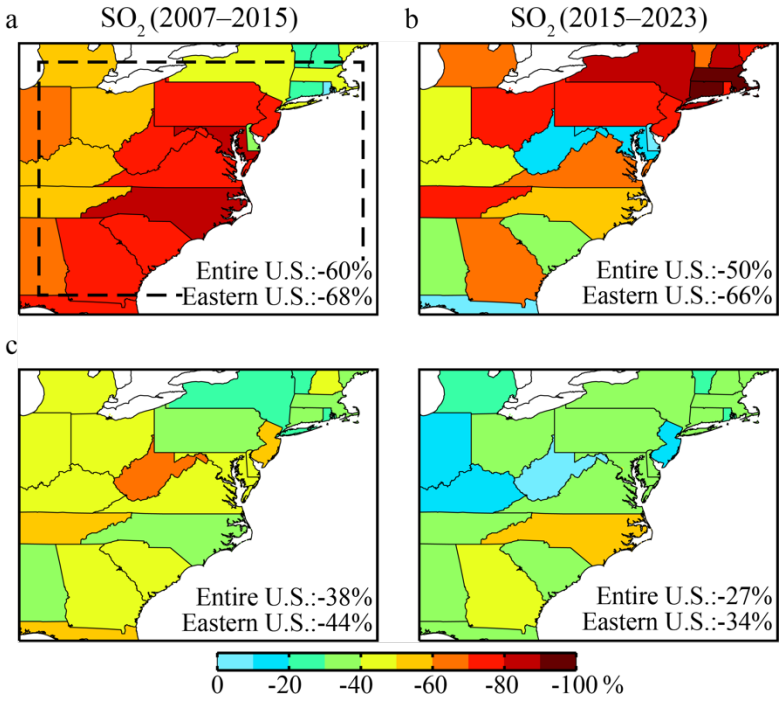

Figure 2A.7: Percent change in anthropogenic SO_2 (a,b) and NOx (c.d) emissions for Feb. and Mar. for 2007–2015 and 2015–2023. The change is calculated as (([2015]-[2007])/[2007]×100) and (([2023]-[2015])/[2015]×100). Also noted in each panel are the average percent change in the national emissions and in the emissions over the eastern U.S. (area enclosed by dashed lines in panel a) for Feb. and Mar. In comparison, the annual emissions changes for 2007–2015 are -58% (SO_2) and -35% (NOx), and for 2015–2023 are -47% (SO_2) and -25% (NOx).

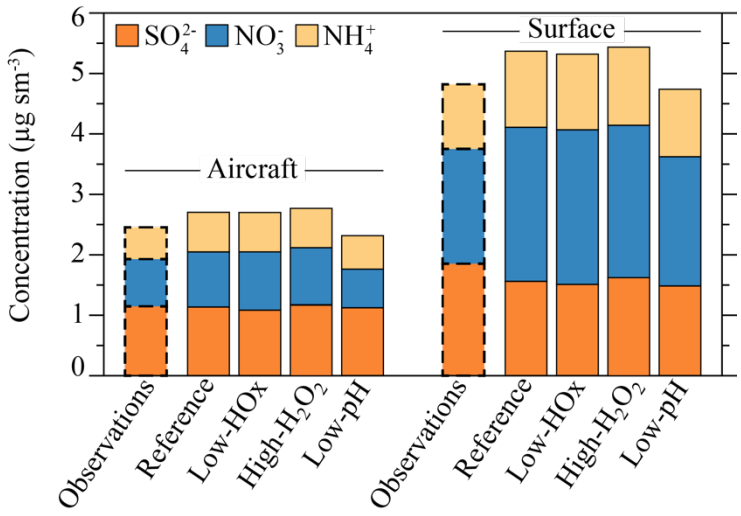

Figure 2A.8: Observed and simulated concentrations of SO_4^{2-}-NO_3^--NH_4^+ along the WINTER flight tracks and at the CSN, IMPROVE and CASTNET surface sites for Feb. 1–Mar. 15, 2015 with the sensitivity simulations. "Reference" denotes our primary simulation discussed in the main text and "Low-HOx", "High-H_2O_2", and "Low-pH" denote sensitivity simulations as described in Section 2.

Chapter 3. ORGANIC AEROSOLS OVER THE NORTHEASTERN U.S. DURING WINTER

3.1 INTRODUCTION

Organic aerosol particles (OA) constitute about half of the fine particulate matter in densely populated areas worldwide (Zhang et al., 2007; Snider et al., 2016). Over the northeastern U.S. (NE US) they account for 25–40% of the fine particulate matter observed at ground-based sites year-round (Hand et al., 2012; Malm et al., 2017). Biogenic and fire sources of OA are dominant globally, but anthropogenic emissions from fossil-fuel and biofuel use, hereafter called urban sources, become more important over the NE US during winter (Bond et al., 2004; de Gouw and Jimenez, 2009; Spracklen et al., 2011). These urban sources produce OA by direct emissions (primary organic aerosol, POA) and through atmospheric processing of organic compounds (secondary organic aerosol, SOA). During summer, the secondary urban sources are estimated to be larger than the primary urban sources, based on source apportionment of OA observations within and downwind of cities in the NE US (de Gouw et al., 2005; Sullivan et al., 2006; Kleinman et al., 2007; de Gouw et al., 2008). However, during winter, the distribution of urban POA and SOA sources over the NE US and other mid-latitude polluted regions is not well-understood because of a lack of observations. Tsigaridis et al. (2014) intercompare 31 global models, finding a systematic underestimate in observed urban OA concentrations especially during winter, which they hypothesize is due to missing urban sources of both POA and SOA in models. This issue extends to regional and urban scale models (e.g. Koo et al., 2014; Fountoukis et al., 2016), which are widely used in making policies to mitigate the health burden of fine particulate matter.

Wintertime OA concentrations at ground-based sites in the NE US are about a factor of 2 lower than summertime concentrations (Hand et al., 2012). In summer, emissions of biogenic volatile organic compounds (VOCs), such as monoterpenes and isoprene, are at their peak, and so too are the concentrations of biogenic SOA. In winter, loss of deciduous foliage, less insolation, and cold temperatures lower the emissions of biogenic VOCs and, consequently, the concentrations of biogenic SOA. Open-fire sources are typically small in the NE US, especially in winter (Giglio et al., 2013). Emissions from residential wood combustion (RWC) become important during winter in the NE US. RWC is estimated to account for 61% of the POA emissions over the region during winter (U.S. Environmental Protection Agency, 2017b), and several source apportionment studies have inferred that 10–44% of the wintertime OA over cities in NE US and the Midwest are from RWC sources (Brown et al., 2006; Robinson et al., 2006; Jaeckels et al., 2007). These OA source apportionment studies use receptor models such as the molecular marker based chemical mass balance, when the emission sources of the markers are known (Schauer et al., 1996), or multivariate factor analysis, when the nature of the sources is unknown (Lanz et al., 2007; Zhang et al., 2011). The lower insolation and water vapor concentrations during winter reduce the source of OH radicals and slow the formation of SOA from oxidation of urban emissions. Despite this, 24–54% of the wintertime OA over cities in the NE US is apportioned to SOA (Polidori et al., 2006; Subramanian et al., 2007; Jimenez et al., 2009; Rattigan et al., 2010). Similarly high winter fractions of SOA are estimated for cities in East Asia (Takegawa et al., 2006; Kondo et al., 2007; Hu et al., 2016; Sun et al., 2016) and western Europe (Sciare et al., 2011; Crippa et al., 2013; Xu et al., 2016). These observations suggest efficient formation of SOA from urban VOC emissions, even during winter.

The primary and secondary sources of OA in urban environments and at regional scales remian poorly constrained, and varying approaches are used to represent them in chemical transport models. Most chemical transport models use one of two following approaches to model OA from urban sources: (i) POA is assumed to be nonvolatile and inert and SOA forms only from the oxidation of specific VOCs, or (ii) POA is assumed to be co-emitted in equilibrium with organic compounds of low volatility, which are treated as additional SOA precursors. Models using the first approach significantly underestimate urban SOA concentrations (Volkamer et al., 2006; Dzepina et al., 2009; Hodzic et al., 2009; Heald et al., 2011; Baker et al., 2015). But the second approach has many remaining uncertainties relating to the sources, volatility distribution, and aging of low-volatility species and SOA (Heald et al., 2011; Hodzic and Jimenez, 2011; Bergström et al., 2012; Hayes et al., 2015; Ma et al., 2017). As a result, models using the second approach can reproduce the urban OA and SOA observations under certain assumptions (Hodzic et al., 2010; Tsimpidi et al., 2010; Shrivastava et al., 2011), but not under others (e.g. Woody et al., 2016; Tsimpidi et al., 2016; Fountoukis et al., 2016). A simpler third approach is to use an empirical parameterization based on the observed evolution of OA and SOA during field campaigns. Such a parameterization was developed based on observations in Mexico City and Pasadena, CA (Hodzic and Jimenez, 2011; Hayes et al., 2015), and has shown promising results when applied to simulate observations in the southeastern U.S. (Kim et al., 2015). The fidelity of these three OA modeling approaches has not yet been fully evaluated during winter over the NE US because of a lack of observations of the distribution and evolution of OA within and downwind of the pollution sources.

The 2015 Wintertime Investigation of Transport, Emissions, and Reactivity (WINTER) campaign provides the first regional-scale dataset of high time-resolution airborne measurements

of OA and other related chemical constituents over the NE US during winter. Here I use the WINTER aircraft observations and ground-based observations to evaluate the three aforementioned approaches of modeling urban OA with the GEOS-Chem chemical transport model. I use the GEOS-Chem simulations to characterize the wintertime OA distribution and quantify their sources and contribution to the burden of fine particulate matter in the NE US.

My study complements two other studies that have also analyzed the sources of OA during WINTER. Schroder et al. (2018) used multivariate factor analysis to determine the sources of OA during WINTER and found that 60% of the OA was SOA, and 40% POA. They examined SOA formation in an urban outflow and found that the winter SOA formation rate was similar to summer after accounting for difference in OH concentrations. Sullivan et al. (2018) used levoglucosan as a molecular marker to estimate that ~30–100% of the carbon in OA is from RWC sources during WINTER. The GEOS-Chem WINTER simulations are also used by Jaeglé et al. (2018) to analyze the budget of reactive nitrogen (NOy) over the NE US, and by Shah et al. (2018) to investigate the wintertime formation of SO_4^{2-}, NO_3^-, and NH_4^+ particles in NE U.S.

3.2 OBSERVATIONS AND MODELS USED IN THIS STUDY

The WINTER aircraft campaign took place between Feb. 1 and Mar. 15, 2015. The NSF/NCAR C-130 aircraft was used to conduct 13 research flights (RF) from the NASA Langley Research Center, Hampton, VA (Fig. 3.1) covering a large area in the NE US. The measurements were carried out during both daytime and nighttime, and the majority (71%) of measurements were made below an altitude of 1 km. The plane was equipped with an extensive payload measuring atmospheric gas and aerosol composition. Here I use measurements of aerosol composition (Sect. 2.1), CO and C_6-C_8 aromatic VOCs. CO was measured by Vacuum UV fluorescence (Aero-Laser

AL-5002), and the VOCs were measured with the Trace Organic Gas Analyzer instrument (Apel et al., 2010; Hornbrook et al., 2011).

3.2.1 *Aerosol composition measurements*

A high-resolution time of flight aerosol mass spectrometer (HR-ToF-AMS, Aerodyne Research Inc.) was used to measure the concentration of OA, SO_4^{2-}, NO_3^-, and NH_4^+ in PM_1 (particulate matter with aerodynamic diameter < 1 μm) (DeCarlo et al., 2006; Canagaratna et al., 2007; Dunlea et al., 2009; Kimmel et al., 2011). The instrument setup, operation, and calibration during the WINTER campaign is described in detail by Schroder et al. (2018). Briefly, the instrument samples ambient air through a custom inlet; it passes through the high-vacuum region of the mass spectrometer to the detection chamber, where non-refractory species are flash vaporized at 600°C and ionized with 70 eV electron impact ionization. The ions are orthogonally extracted and analyzed by time-of-flight mass spectrometry. Collection efficiencies were estimated with the composition-dependent algorithm of Middlebrook et al. (2012). Measurements were reported at 1 s and 1 min periods. The 1-min measurements are used in my analysis. Detection limits for the 1-min measurements were 194 ng sm^{-3} (OA), 57 ng sm^{-3} (SO_4^{2-}), 30 ng sm^{-3} (NO_3^-), and 5 ng sm^{-3} (NH_4^+). (1 sm^3 equals 1 m^3 at 273.15 K and 1013.25 hPa.) The instrument accuracy was 38% (OA) and 35% (inorganics) (Bahreini et al., 2009). The instrument was operational on 12 of 13 flights during the campaign.

POA and SOA concentrations were inferred from the positive matrix factorization (PMF) of the AMS 1-min observations for flights RF01–07 as described by Schroder et al. (2018). PMF is a form of multivariate factor analysis that is commonly applied to the AMS measurements to characterize the sources and properties of OA (Ulbrich et al., 2009; Zhang et al., 2011). The PMF decomposes the observed time series of the OA mass spectra into a linear combination of a small

number of factors and their time-varying concentrations. Each factor is composed of several co-varying chemical species and each factor represents specific sources and chemical processes. The PMF analysis of the WINTER OA data yields four factors: hydrocarbon-like OA (HOA), biomass burning OA (BBOA), less-oxidized oxidized OA (LO-OOA), and more-oxidized oxidized OA (MO-OOA). HOA is composed of reduced hydrocarbons emitted mainly by vehicles and correlates well with primary VOCs and NOx during WINTER (Schroder et al., 2018). BBOA is associated with emissions from wood combustion and is correlated with CO, benzene, and the AMS ions dominant in biomass burning OA (Schroder et al., 2018). The LO-OOA factor has a mix of oxidized and hydrocarbon-like species, and the MO-OOA factor is composed almost entirely of oxidized species. LO-OOA and MO-OOA are correlated with formaldehyde (HCHO), SO_4^{2-}, CO, and AMS ions associated with oxidized OA (Schroder et al., 2018). Hereafter I refer to the sum of the HOA and BBOA concentrations as the observed POA, and the sum of LO-OOA and MO-OOA concentrations as the observed SOA.

3.2.2 *Surface measurements*

The Chemical Speciation Network (CSN) and the Interagency Monitoring of Protected Visual Environments (IMPROVE) are ground-based $PM_{2.5}$ monitoring networks (Solomon et al., 2014; Hand et al., 2012). The networks use a filter-based approach for measuring the concentration and composition of $PM_{2.5}$. Both networks use the URG 3000N sampler to collect OA particles on quartz-fiber filters, which are subsequently analyzed using thermal optical methods to determine the amount of organic carbon (OC). The networks report 24-hour mean OC concentrations every third or sixth day. Given my 6-week long simulation period, I include only sites that report every third day, and have at least 70% temporal coverage for Feb. 1–Mar. 15, 2015. The NE US (defined here as the region between 35–45˚N and 65–89˚W, Fig. 3.1a) had 30 CSN and 26 IMPROVE sites

matching the above criteria. I use an OA/OC multiplier of 1.8 to determine OA concentrations from the OC measurements (Hand et al., 2012).

Filter-based measurements are subject to both positive and negative biases, due to collection of organic gases or volatilization of semivolatile particles, during sample collection, transport, storage, and laboratory analysis. The IMPROVE measurements partly account for these OC artifacts by reporting blank-corrected concentrations, but the CSN measurements are not blank-corrected. Following Hand et al. (2012), I apply a uniform correction to the CSN measurements of –0.3 μgC sm^{-3}, equivalent to 16% of the OC concentrations observed at the CSN sites in NE U.S. during WINTER.

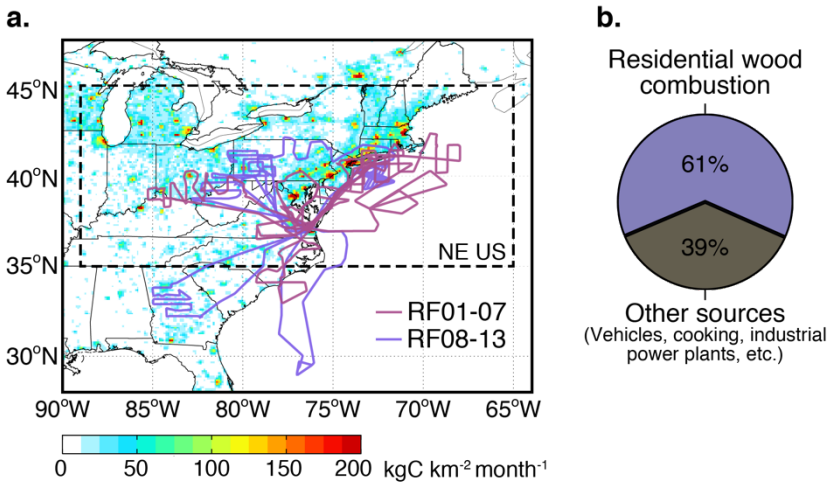

Figure 3.1: WINTER flight tracks and organic carbon emissions. (a) Map of the WINTER flight tracks overlaid onto the primary organic carbon (OC) emission flux from the U.S. EPA's National Emissions Inventory (NEI) 2011 for 1 Feb–15 Mar. The area defined as the northeastern US in this study (35–45˚N and 65–89˚W) is enclosed by the dashed lines (b) Primary OC emission source distribution for the northeastern US.

3.2.3 *GEOS-Chem model*

I use the GEOS-Chem chemical transport model v10-01 (www.geos-chem.org) driven by assimilated meteorological fields from NASA Global Modeling and Assimilation Office's GEOS-5 Forward Processing (FP) system (Reinecker et al., 2008; Molod et al., 2015). I use the one-way

nested-grid configuration with a resolution of 0.5˚ latitude by 0.625˚ longitude over North America (130˚W–60˚W, 10˚N–60˚N) with initial and boundary conditions from a 4˚×5˚ global simulation (Kim et al., 2015; Wang et al., 2004). The model has 47 levels in the vertical with 8 levels within 1 km of the surface. GEOS-Chem includes gas-phase chemistry of HOx-NOx-VOC-O_3-SO_2-BrOx (Bey et al., 2001; Mao et al., 2010; Parrella et al., 2012; Travis et al., 2016; Fisher et al., 2016) coupled with the chemistry of SO_4^{2-}, nitrate (NO_3^-), ammonium (NH_4^+) (Park et al., 2004; Alexander et al., 2005; Pye et al., 2009; Alexander et al., 2012; Kim et al., 2015) and OA (Park et al., 2003; Heald et al., 2006, 2011; Pye et al., 2010; Kim et al., 2015). GEOS-Chem simulates the process of advection with a flux-form semi-Lagrangian scheme (Lin and Rood, 1996), boundary layer mixing using a non-local scheme (Lin and McElroy, 2010), and convective transport using archived convective mass fluxes from GEOS-5 FP (Wu et al., 2007). The wet deposition scheme includes scavenging of gases and particles in wet convective updrafts and in large-scale precipitation (Liu et al., 2001; Wang et al., 2011; Amos et al., 2012). The dry deposition scheme is based on the standard resistance-in-series model (Wesely, 1989; Wang et al., 1998; Zhang et al., 2001). Emissions are calculated with the Harvard-NASA Emission Component (HEMCO) v1.1 (Keller et al., 2014). U.S. anthropogenic emissions are from the U.S. EPA's National Emissions Inventory (NEI) 2011 (Travis et al., 2016). For the WINTER simulations, I have scaled the 2011 U.S. emissions to 2015 levels based on the U.S. EPA emissions trend report (U.S. Environmental Protection Agency, 2015a) (scaling factors SO_2: 0.72, NOx: 0.80, CO: 0.83, and VOCs: 0.93). Fire emissions from the Global Fire Emissions Database (GFED) v4 (Giglio et al., 2013; Randerson et al., 2012; van der Werf et al., 2017), and biogenic emissions from Model of Emissions of Gases and Aerosols from Nature (MEGAN) v2.1 (Guenther et al., 2012).

I have a made several modifications to the GEOS-Chem model for my WINTER simulations, which are described in Jaeglé et al. (2018) and Shah et al. (2018). In particular, I increase surface emissions of HCHO by a factor of 5 to bring the GEOS-Chem predictions in better agreement with the WINTER observations. I decrease emissions of toluene by 60% based on Hu et al. (2015), who reported that GEOS-Chem simulations with the NEI emissions overpredicted toluene in the Midwest by a factor of 2.5. I have updated the heterogeneous chemistry of NOy, implemented transition-metal catalyzed SO_2 oxidation, and added a simple $ClNO_2$ chemical pathway. I have also updated the GEOS-Chem's dry deposition scheme at cold temperatures and corrected for an underestimate of wet scavenging under cold temperatures (<268 K).

I perform four simulations using three modeling approaches for OA from urban sources (Table 3.1). All simulations are performed for Feb 1–Mar 15, with a spin-up period of 6 months for the global simulation and 15 days for the high-resolution North America simulation. For comparison to observations, the model is sampled at the time and location of the measurements. GEOS-Chem simulates the emissions of POA from urban and fire sources, and SOA formation from biogenic, urban, and fire emissions (Park et al., 2003; Pye et al., 2010; Heald et al., 2011; Kim et al., 2015). Marine biogenic POA sources are not included in my version of GEOS-Chem. The spatial distribution of the NEI 2011 POA emissions for Feb 1–Mar 15 is shown in Fig. 3.1a. For the WINTER simulations, the NEI 2011 POA emissions are reduced by 1.7% based on the U.S. EPA emissions trend for $PM_{2.5}$ emissions (U.S. Environmental Protection Agency, 2015a). During Feb 1–Mar 15, 2015, the total POA emissions over the NE US (defined as 35–45˚N and 65–89˚W) was 470 Mg C d^{-1}. The majority (61%) of the wintertime POA emissions in the NE US are from RWC sources (Fig. 3.1b). The rest of the POA emissions are from vehicles, cooking, industrial units, and power plants. Urban emissions of C_6-C_8 aromatics (represented by benzene,

toluene, and xylene respectively) are mainly from vehicular sources, surface coating and solvent use, gas stations, and RWC. The total emissions of benzene, toluene, and xylene over the NE US for Feb 1–Mar 15 were 184, 326, and 714 Mg C d^{-1}. Over the NE US, biogenic emissions of isoprene were 93 Mg C d^{-1} and of monoterpenes were 1243 Mg C d^{-1}. Biogenic emissions were concentrated near the southern edge of the region and decreased sharply northwards, reflecting the gradient in temperature and sunlight. While the emissions of monoterpenes seem large compared to POA emissions, a typical SOA yield from monoterpenes is about 5–15% (Griffin et al., 1999; Chung and Seinfeld, 2002; Shilling et al., 2008).

I use the three OA modeling approaches which have been implemented in GEOS-Chem in previous work (Table 3.1). Each makes different assumptions about the properties and chemistry of POA and SOA. The first approach ("traditional" approach, denoted here as TRAD) follows the POA model of Park et al. (2003) and the urban SOA parameterization of Henze et al. (2008) with updates from Pye at al. (2010). In the second approach (Semivolatile POA, denoted here as SVPOA), urban POA and SOA are modeled as components of one dynamic organic gas-particle system, following the parameterization of Pye and Seinfeld (2010). The parameters used in the above two approaches are primarily based on laboratory studies of the chemical properties of POA and SOA from urban emissions (Shrivastava et al., 2006; Grieshop et al., 2009; Ng et al., 2007; Chan et al., 2009). The third approach (Simple approach, denoted here by the prefix SMPL), was described in Hodzic and Jimenez (2011) and implemented in GEOS-Chem by Kim et al. (2015). POA and urban SOA are assumed to be nonvolatile. SOA forms from the oxidation of POA and an unspeciated VOC surrogate gas. I perform two simulations using this approach: one without any modifications to POA emissions from the NEI inventory (SMPL_A) and the other with POA

emissions from the NEI inventory scaled down by a factor of 2 (SMPL_B). Further details of the three simulations are in the Section 3.9.

Table 3.1: Overview of the GEOS-Chem OA simulations performed for this study.

Urban POA	Urban SOA
TRAD simulation (Park et al., 2003; Pye et al., 2010)	
1) Species: 2 nonvolatile (hydrophobic and hydrophilic) 2) Source: NEI POA emissions (50% to each specie) 3) Aging: hydrophobic to hydrophilic ($k=1\times10^{-5}$ s^{-1})	1) Species: 1 nonvolatile, 3 semivolatile gas-aerosol pairs (C* of 1, 10, 100 μg m^{-3}). 2) Source: oxidation of peroxy radicals of C_6-C_8 aromatics with HO_2 and NO
SVPOA simulation (Pye and Seinfeld, 2010; Pye et al., 2010)	
1) Species: 2 semivolatile gas-aerosol pairs (C*=20,1600 μg sm^{-3}) 2) Source: NEI POA emissions (~50% to each specie) 3) Aging: Oxidizes in gas phase with OH	1) Species: 1 nonvolatile, 3 semivolatile gas-aerosol pairs (C*=1, 10, 100 μg m^{-3}) from C_6-C_8 aromatic and P-IVOC oxidation, 2 semivolatile gas-aerosol pairs (C*=0.2, 16 μg m^{-3}) from P-SVOC oxidation 2) Sources: C_6-C_8 aromatics oxidation (similar to TRAD), P-SVOC oxidation P-IVOC oxidation. Naphthalene (C*=10^5 μg m^{-3}) as surrogate, scaling factor of 66. Naphthalene co-emitted with benzene (0.041 mol mol^{-1})
SMPL_A & SMPL_B simulations (Hodzic and Jimenez, 2011; Kim et al., 2015)	
1) Species: 2 nonvolatile species, one from RWC and one from non-RWC sources 2) Source: NEI POA emissions. POA emissions halved in SMPL_B simulation. Separation of RWC sources based on U.S. EPA estimates. 3) Aging: POA oxidizes in gas phase with OH	1) Species: 2 nonvolatile species: one from RWC and one from non-RWC sources 2) Source: Oxidation with OH of surrogate VOC co-emitted with CO (0.069 g g^{-1} for non-RWC sources, 0.013 g g^{-1} for RWC sources)

POA: Primary organic aerosol
SOA: Secondary organic aerosol
SVOC: Semivolatile organic compounds
IVOC: Intermediate-volatility organic compounds
P-SVOC: Primary SVOC
P-IVOC: Primary IVOC
C*: saturation concentration

3.3 OBSERVED AND MODELED DISTRIBUTION OF OA DURING WINTER

The campaign-average concentration of OA observed below 1 km altitude was 1.48 ± 0.93 μg sm^{-3} (mean ± standard deviation) (Fig. 3.2a). OA concentrations of 3–4 μg sm^{-3} were measured downwind of the heavily urbanized area between Washington D.C. and New York City and along the Ohio River Valley between Cincinnati and Pittsburgh. This is similar to the urban OA enhancement of ~2 μg sm^{-3} observed at NE US CSN and IMPROVE sites during winter (Hand et al., 2012). Aircraft observations of OA concentrations upwind of urban regions or over the ocean far off the coast were lower (Fig. 3.2a). OA concentrations were highest within 0.5 km of the surface (1.9 μg sm^{-3}) and decreased to below 0.5 μg sm^{-3} above 2 km altitude (Fig. 3.2b). The WINTER vertical profile is consistent with most previous aircraft campaign observations over polluted regions not impacted by fires (Heald et al., 2011).

The observed mean POA and SOA concentrations below 1 km altitude for flights RF01–07 are 0.74 μg sm^{-3} and 1.1 μg sm^{-3}, respectively (Fig. 3.3a). Of the POA, 70% is composed of BBOA (28% of the OA). RWC is expected to be the dominant source of wintertime POA over NE US (Fig. 3.1b), which explains the abundance of BBOA during WINTER (Schroder et al., 2018). Sullivan et al. (2018) used levoglucosan measurements to estimate that ~30–100% of the OC observed during WINTER is from RWC sources. The WINTER RWC source contribution is within the range of previous observations in the NE and Midwest US (10–44%) and in Central and Northern Europe (17–49%) (Brown et al., 2006; Glasius et al., 2018; Jaeckels et al., 2007; Lanz et al., 2010; Robinson et al., 2006).

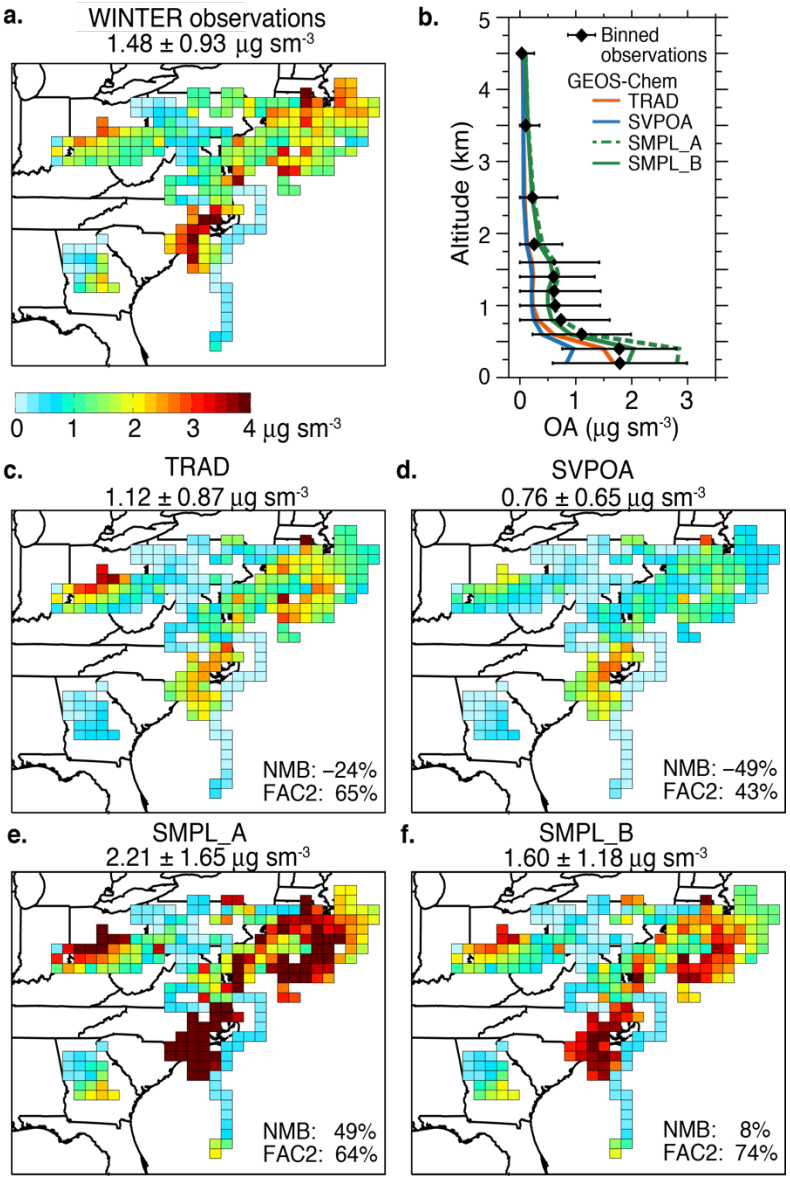

Figure 3.2: Observed and simulated OA concentrations during WINTER. (a) Maps of the OA concentrations observed along the WINTER flight tracks below the altitude of 1 km for RF01-13, and the corresponding modeled concentrations for the (c) TRAD, (d) SVPOA, (e) SMPL_A, and (f) SMPL_B simulations. The observations and the modeled concentrations are binned into a 0.5º latitude × 0.625º longitude GEOS-Chem grid. The mean ± standard deviation of the observed and modeled OA is shown above. The inset has the normalized mean bias (NMB) and the FAC2 index. (b) Vertical profile of the observed OA and the OA predicted by the TRAD (orange), SVPOA (blue), SMPL_A (green dashed), and SMPL_B (green solid) simulations. GEOS-Chem simulations. The observed means (black diamonds) ± standard deviations (error bars) and the modeled mean OA concentrations in each altitude bin are shown.

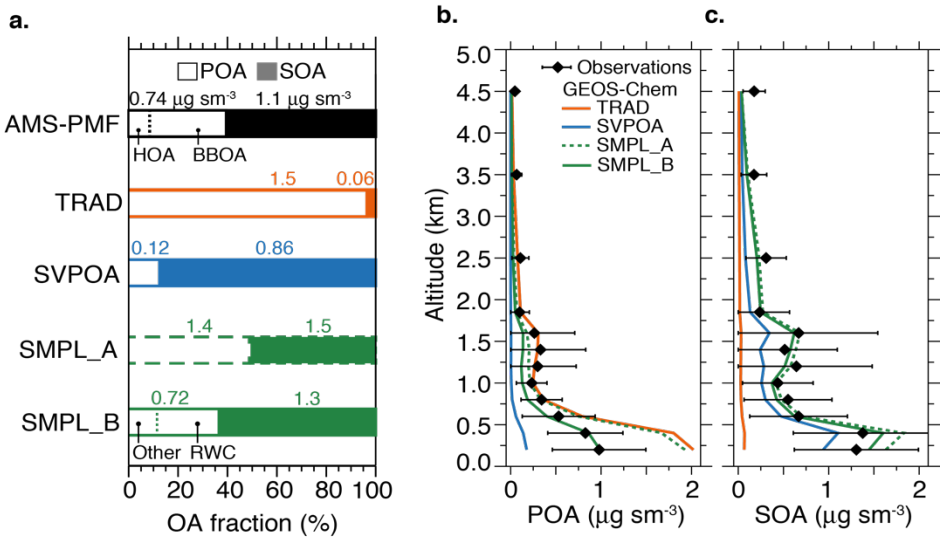

Figure 3.3: Observed and simulated POA and SOA during WINTER. (a) POA and SOA fractions of OA below 1 km altitude for flights RF01–RF07 inferred from the positive matrix factorization (PMF) analysis of the observations (black) and for the TRAD (orange), SVPOA (blue), SMPL_A (green, dashed), and SMPL_B (green, solid) simulations. The hydrocarbon-like (HOA) and biomass burning (BBOA) fractions of POA and the fractions of modeled POA from residential wood combustion (BB) and all remaining sources (Other) for the SMPL_B simulation are also shown. Vertical profiles of (b) POA and (c) SOA and the corresponding modeled POA and SOA. The observation-inferred POA and SOA means (black diamonds) ± standard deviations (error bars) in each altitude bin and the modeled means from the TRAD (orange line), SVPOA (blue line), SMPL_A (green dashed line), and SMPL_B (green solid line) simulations are shown.

The WINTER SOA/OA fraction (60%) is also consistent with the SOA fraction inferred from source apportionment of past wintertime surface measurements in New York City (54%), Pittsburgh (~50%) and several European cities (36–60%) influenced by RWC sources (Weimer et al., 2006; Subramanian et al., 2007; Jimenez et al., 2009; Lanz et al., 2010). POA and SOA concentrations decrease from below 0.5 km to above 2 km (Fig. 3.3b, c), but the vertical gradient of POA is steeper than that of SOA in the 0.5–2 km layer. This layer is the so-called residual layer, which during winter remains detached from the surface for much of day and contains more aged emissions.

The TRAD simulation reproduces the observed total OA reasonably well, but overestimates POA, and substantially underestimates SOA (Fig. 3.2c, 3.3a). Compared to observed OA concentrations, the TRAD simulation has a normalized mean bias (NMB) of –24% and a FAC2 index of 64%. (NMB=$(\overline{M_i} / \overline{O_i} - 1)\times 100\%$, where O_i and M_i are the paired observed and modeled OA concentrations and the overbar represents the mean, and FAC2 is the percent of model-observation pairs such that $0.5 \leq M_i / O_i \leq 2$). This simulation predicts POA concentrations that are a factor of 2 higher than the observations. It predicts almost no SOA formation during WINTER, in stark contrast to the observations. The TRAD OA agrees well with the observations below 0.5 km, because of cancellation of errors in POA and SOA (Fig. 3.2b). At higher altitudes (between 0.5 and 2 km), the TRAD OA is a factor 2 lower than the observations, because of the underestimate in SOA formation aloft. Urban SOA in the TRAD simulation is formed from the condensation of the oxidation products of C_6-C_8 aromatics. GEOS-Chem tends to overestimate these VOCs (Fig. 3A.2), which suggests that there are other SOA precursors missing from the TRAD simulation.

The SVPOA simulation underestimates OA concentrations by about a factor of 2 (NMB= –49%), underestimates POA by about of factor of 5, but simulates SOA concentrations (0.86 μg sm^{-3}) in better agreement with the observations (Fig. 3.2d, 3.3a). The same patterns are seen in the SVPOA vertical profiles (Fig. 3.2b, 3.3b, 3.3c). The SVPOA simulation treats POA as semivolatile. A significant fraction of the emitted POA evaporates to low-volatility gases, resulting in lower POA concentrations. The oxidation of the low-volatility gases to lower volatilities followed by condensation is the main source of SOA in this simulation.

The SMPL_B simulation reproduces the OA observations well (NMB=8%, FAC2=74%), while the SMPL_A overestimates OA by a factor of 2 (NMB=49%) (Fig. 3.2d, e). The lower OA

in SMPL_B than in SMPL_A is due to the factor of 2 decrease in the NEI POA emissions (Sect. 2.3). The SMPL_B POA concentrations (0.72 μg sm^{-3}) and the contribution of BBOA to POA (67%) are in good agreement with the observations (Fig. 3.3a). This suggests that NEI 2011 captures the fraction of POA emissions from RWC sources over the NE US, but the total POA emissions may be a factor of 2 too high. The SMPL_A and SMPL_B SOA concentrations below 1 km (1.3–1.5 μg sm^{-3}) are within 35% of the observations (Fig. 3.3a). The small difference in the SMPL_A and SMPL_B SOA concentrations is due to the difference in POA and thus the amount of SOA formed from POA aging. The SMPL_B simulation captures the vertical profiles of the observed OA, POA, and SOA well (Fig. 3.2b, 3.3b, 3.3c).

Among the four simulations, I find that the SMPL_B simulation has the most realistic representation of the observed concentrations of POA and SOA during WINTER. The parameters for SOA formation in this simulation are based on observations in Mexico City and Pasadena, CA (Hodzic and Jimenez, 2011; Hayes et al., 2013), and I find that they also are suitable for simulating the NE US wintertime conditions. I performed 10 additional runs of the SMPL_B simulation to test the sensitivity to the two SOA parameters: AVOC/CO emissions ratio and AVOC+OH oxidation rate. I find that 5 of the sensitivity simulations generate OA and SOA concentrations within ±20% of the observations (Fig. 3A.3). For example, the simulation with 25% higher AVOC emissions and 35% lower AVOC oxidation rate than SMPL_B, and the simulation with 50% lower AVOC emissions and 2 times the AVOC oxidation rate result in OA and SOA concentrations close to the observations. Extrapolation of the results of the sensitivity simulations indicates that if the AVOC+OH rate is close to its theoretical upper limit (~1×10^{-10} cm^3 $molec^{-1}$ s^{-1}), then the minimum AVOC/CO emissions ratio is ~20 g/kg. The SOA parameter combination of the SMPL_B simulation is not unique in reproducing the WINTER OA. The two parameters could be resolved

further using a technique like the oxidation flow reactor that artificially oxidizes SOA precursors in an ambient air sample in real-time (Ortega et al., 2016).

3.4 TIME EVOLUTION OF OA

Past studies have shown OA concentrations to increase rapidly with atmospheric processing of urban emissions because of the photochemical formation of SOA from urban VOC precursors (de Gouw et al., 2008; Kleinman et al., 2008; DeCarlo et al., 2010; Hayes et al., 2013; de Gouw and Jimenez, 2009; Kleinman et al., 2007). The evolution of OA with time depends on the timescales and efficiency of SOA formation, but also on the magnitude of emissions and loss by dilution and removal. Following previous studies, I minimize the effect of variability of emissions and dilution by considering the enhancement in OA normalized to enhancement in CO (ΔOA/ΔCO). The degree of photochemical processing is usually represented by an OH equivalent age, which is a measure of the time exposure of the emissions to a particular [OH] (Parrish et al., 1992; Kleinman et al., 2007).

The OH equivalent age is usually estimated using ratios of NOx to NOy, or ratios of two VOCs that react with OH at different rates (Parrish et al., 1992; Kleinman et al., 2007). The NOx/NOy method is subject to inaccuracies arising from the mixing of emissions of different ages, differences in wet and dry deposition efficiencies of NOx and NOy species, and conversion of NOx to NOy by pathways other than reaction with OH. During WINTER only 33% of the NOx to NOy conversion happens through the daytime NO_2+OH pathway (Jaeglé et al., 2018), which limits the application of the NOx/NOy method to estimate the OH equivalent age to the entire WINTER dataset. There are inaccuracies in the age calculated from the ratio of two VOCs because of uncertainties in their emission ratios and mixing of emissions of different ages. Besides, VOC measurements are not available for WINTER flights RF09–13. Schroder et al. (2018) applied both

these methods to determine the age of an urban plume encountered on a daytime WINTER flight. To extend this analysis to the full WINTER dataset, I use an OH equivalent age calculated by GEOS-Chem. It is derived from the simulated concentrations of two species (X and Y) along the WINTER flight tracks. Species X is emitted from urban sources and reacts with OH with a rate constant k (k=1.25×10^{-11} cm^3 molec^{-1} s^{-1}) to form species Y. The OH equivalent age, Δt, is calculated from the simulated concentrations of X and Y (Eq. 3.1–3.3)

$$[X]_{\Delta t} = [X]_0 \exp(-k[OH]\,\Delta t) \quad (3.1)$$

$$[Y]_{\Delta t} = [X]_0\left(1 - \exp(-k[OH]\,\Delta t)\right) \quad (3.2)$$

$$\Delta t = \frac{1}{k[OH]} \ln\left(1 + \frac{[Y]_{\Delta t}}{[X]_{\Delta t}}\right) \quad (3.3)$$

where, $[X]_0$ is the concentration of X at the source, $[X]_{\Delta t}$ and $[Y]_{\Delta t}$ are the concentrations after time Δt. For comparison to previous studies, I use [OH] = 1.5×10^6 molec cm^{-3}. I calculate a median OH equivalent age of 6.5 hours along the WINTER flight tracks. The OH equivalent age is better correlated with simulated –log(NOx/NOy) for daytime flights than nighttime flights (Fig. 3A.4a). The OH equivalent age is smaller than the GEOS-Chem derived transport time of emissions (Fig. 3A.4b), as [OH] is lower than 1.5×10^6 molec cm^{-3} in winter. An OH equivalent age of 12 hours corresponds to a transport time of ~1 day for daytime samples and ~1.4 days for nighttime samples.

I analyze the observed aging of OA by grouping observations below 1 km altitude into OH equivalent age bins and then calculating ΔOA/ΔCO from the ordinary least squares bisector regression (Isobe et al., 1990) slope between OA and CO in each OH equivalent age bin (Fig. 3A.5). I repeat this calculation for the observed ΔSOA/ΔCO for flights RF01–07, for which POA and SOA concentrations were calculated from PMF analysis. The observed ΔPOA/ΔOA is calculated without separating the observations into age bins (Fig. 3A.6). I apply the same

procedure to the GEOS-Chem simulations. I exclude the SMPL_A simulation from further analysis since it is not different from the SMPL_B simulation except for the POA emissions.

The average observed ΔOA/ΔCO is 41 μg sm^{-3} $ppmv^{-1}$, and the observed ΔPOA/ΔCO and ΔSOA/ΔCO for flights RF01–07 are equal to each other (~21 μg sm^{-3} $ppmv^{-1}$). I find that the observed ΔOA/ΔCO and ΔSOA/ΔCO increase substantially with OH equivalent age (Fig. 3.4a, b), as a result of photochemical formation of SOA. Observed ΔOA/ΔCO doubles from 39 μg sm^{-3} $ppmv^{-1}$ to 85 μg sm^{-3} $ppmv^{-1}$ as OH equivalent age increases to from 2 hours to 1 day. This implies an observed growth in ΔSOA/ΔCO of 46 μg sm^{-3} $ppmv^{-1}$ in aged air. The RF01–07 observed ΔSOA/ΔCO shows a similar increase from 13 to 62 μg sm^{-3} $ppmv^{-1}$ between OH equivalent ages of 2 and 20 hours (Fig. 3.4b).

The observed photochemical evolution of OA and SOA observed during the WINTER campaign is consistent with summertime observations in the NE US and other urban regions (Kleinman et al., 2007, 2008; de Gouw and Jimenez, 2009; DeCarlo et al., 2010; Hayes et al., 2013), even though there is presumably a significant shift in the types of VOC contributing to SOA formation between winter and summer in the NE part of the domain. The observed ΔOA/ΔCO for aged air falls within the range reported by de Gouw and Jimenez (2009) (45–90 μg sm^{-3} $ppmv^{-1}$). I find that the WINTER observed ΔPOA/ΔCO (21 μg sm^{-3} $ppmv^{-1}$) is a factor of 2-3 higher than the summertime values summarized in de Gouw & Jimenez (2009) because of the large contribution of RWC sources to POA during winter.

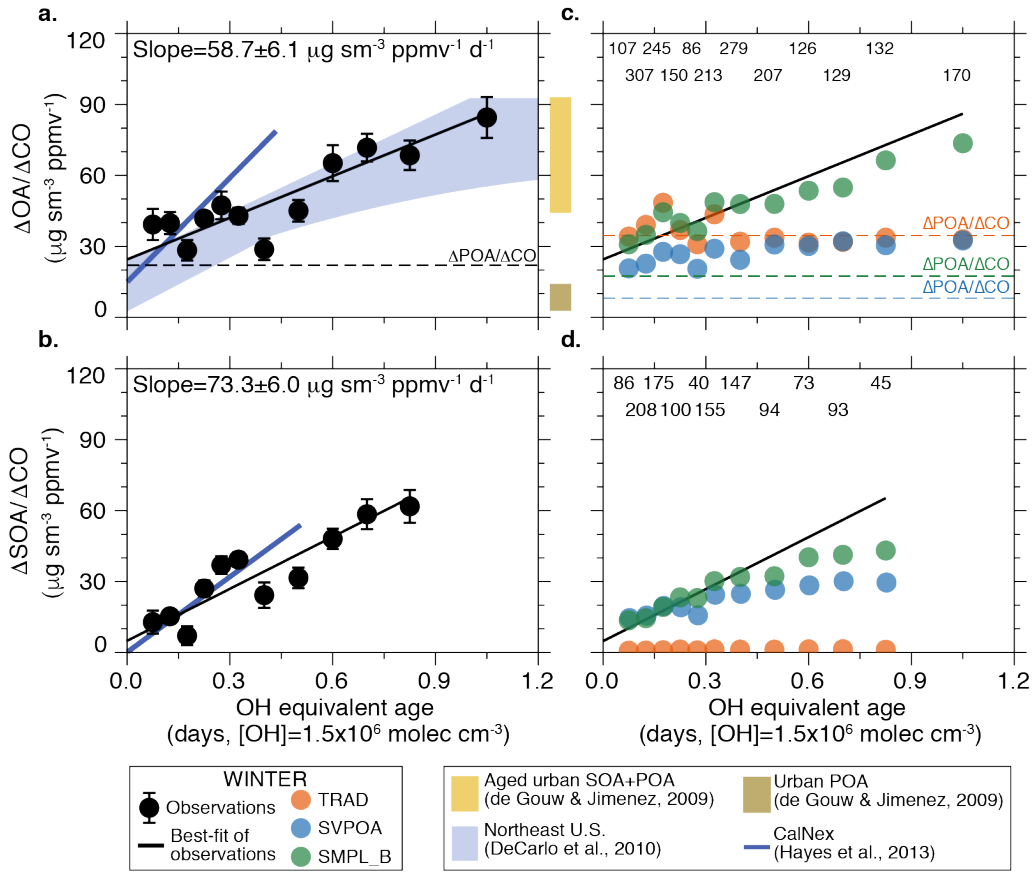

Figure 3.4: Observed and simulated time evolution of OA and SOA. (a) ΔOA/ΔCO and (b) ΔSOA/ΔCO as function of OH equivalent age for the WINTER observations below 1 km altitude. Panel a includes observations from all WINTER flights (RF01–13), and panel b includes observations from flights RF01–07. ΔOA/ΔCO and ΔSOA/ΔCO are calculated using linear regression of the observations grouped by their OH equivalent age as described in the text (Fig. 3A.4, 3A.5). The regression slopes (filled circles) ± their 95% confidence intervals (error bars) for each age bin are shown. The slope of the best-fit line (solid black) is indicated. The ΔPOA/ΔCO is calculated without binning the observations by age. Also shown are the range of observed urban POA/ΔCO (dark blue bar) and (POA+SOA)/ΔCO in aged urban emissions (yellow bar) (de Gouw and Jimenez, 2009), the range of ΔOA/ΔCO observed over the NE U.S. at different OH equivalent ages (light blue shaded area), and the increase in ΔOA/ΔCO with OH equivalent age observed in Pasadena, CA during the 2010 CalNex campaign. (c) ΔOA/ΔCO and (d) ΔSOA/ΔCO from the TRAD (orange), SVPOA (blue) and SMPL_B (green) simulations. The number of points in each age bin is shown at the top in panels c and d.

The TRAD simulation, which has almost no SOA formation, shows no change in the modeled ΔOA/ΔCO with age (Fig. 3.4c, d). The TRAD ΔOA/ΔCO is within about 20% of the observations in the first 10 hours after emissions, but it is a factor of 2 too low at the age of 1 day.

Since the median OH equivalent age of the WINTER observations was 6.5 hours, the large discrepancy in TRAD OA in more aged air was not apparent when the campaign-average OA concentrations was compared to the observations (Sect. 3.1). The modeled ΔOA/ΔCO in the SVPOA simulation are lower than the observations at all OH equivalent ages (Fig. 3.4c, d), because of the underestimate in the modeled ΔPOA/ΔCO (8 μg sm^{-3} $ppmv^{-1}$), and the smaller growth in ΔSOA/ΔCO. This suggests that the SOA formation potential of the SVPOA parametrization is too low.

The SMPL_B simulation is best able to capture the time evolution of OA observed during WINTER. The SMPL_B simulation reproduces the mean ΔOA/ΔCO (40 μg sm^{-3} $ppmv^{-1}$) and its growth (43 μg sm^{-3} $ppmv^{-1}$) at a OH equivalent age of 1 day (Fig. 3.4c). The RF01–07 ΔSOA/ΔCO in SMPL_B also reaches 43 μg sm^{-3} $ppmv^{-1}$ in aged air, and is a little lower than the observations (Fig. 3.4d).

3.5 FLIGHTS RF02 AND RF04

I now analyze the OA observations on two of the WINTER flights and evaluate the performance of the TRAD, SVPOA, and SMPL_B simulations for these flights. Both flights sampled air downwind of urban areas at low altitudes (below 0.5 km) and were both day-into-night flights. The first flight, RF02, sampled fresh emissions with OH equivalent ages of 3–5 hours. While the second flight, RF04, sampled aged pollution with OH equivalent ages of 7–20 hours. Thus, these two flights together represent the range of OH equivalent ages observed during the WINTER campaign.

RF02

RF02 took place on February 6, 2015. The C-130 aircraft sampled air over the Ohio River Valley, downwind of the cities of Cincinnati, OH and Columbus, OH (Fig. 3.5). Sampling in the boundary layer at ~0.3 km altitude, took place between 12:45 and 17:45 pm (EST) (Fig. 3.5a). Mean CO concentrations of 0.18 ppm were observed during this period. GEOS-Chem predicts mean CO concentrations of 0.16 ppm and captures the observed variability. The observed OA concentrations vary between 1 and 4 μg sm^{-3} (Fig. 3.5b), closely tracking the CO timeseries. The observed POA and SOA concentrations are 1.0 and 0.9 μg sm^{-3}, respectively (Fig. 3.5c, d). The observed SOA/OA ratio of 0.47 is consistent with the low OH equivalent age of the sampled emissions (Fig. 3.4a). The mean OA concentrations predicted by the TRAD (2.1 μg sm^{-3}) and the SMPL_B (2.0 μg sm^{-3}) simulations are within 15% of observed concentrations (1.8 μg sm^{-3}), but the SVPOA simulation (1.1 μg sm^{-3}) is a factor of 2 too low. The SMPL_B POA (1.1 μg sm^{-3}) and SOA (0.98 μg sm^{-3}) concentrations are also close to the observations, and the SOA/OA ratio (0.49) is well-reproduced. The TRAD simulation POA concentrations (2.1 μg sm^{-3}) are too high, and the OA in the TRAD simulation is almost entirely composed of POA. In the SVPOA simulation, most of the OA is made up of SOA (SOA/OA=0.81), in disagreement with the observations.

RF04

Flight RF04 took place on February 11, 2015, when a wide slow-moving pollution plume originating from Washington D.C. and Baltimore was sampled. The aircraft flew between Maryland and South Carolina making several transects across the plume at an altitude of about 0.35 km. CO concentrations of 0.17 ppm were measured, with little variation within the plume (Fig. 3.6a). CO concentrations dropped to background levels (~0.1 ppm) whenever the plane climbed above the boundary layer. GEOS-Chem captures the observed CO concentrations in the plume. The mean observed OA concentration below 0.5 km was 2.5 μg sm^{-3}, with lower

concentrations closer to the source region (15:15–16:30 EST) than further downwind (Fig. 3.6b).

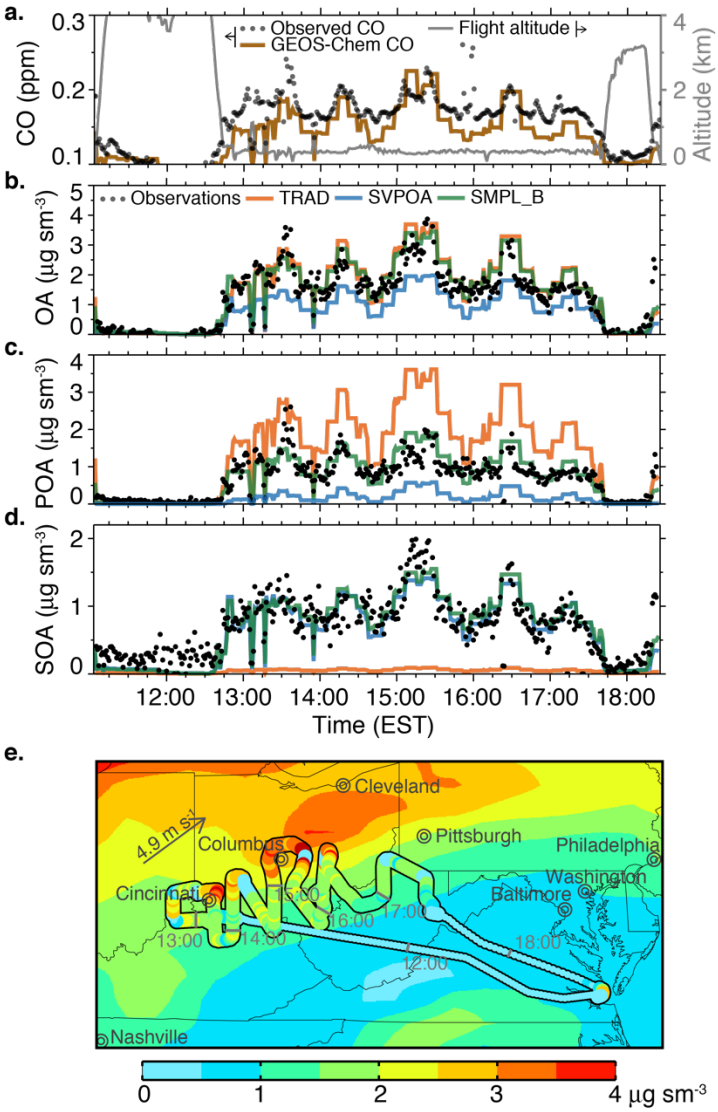

Figure 3.5: Comparison of observations and simulations for flight RF02. Observed and modeled concentrations of CO (a), OA (b), POA (c), and SOA (d) for flight RF-02. Observations are in black and the modeled concentrations from the three simulations are in solid lines (TRAD: orange, SVPOA: blue, and SMPL_B: green). Panel a also shows the flight altitude. Panel e shows the flight track colored by observed OA concentrations and overlaid onto the modeled OA concentrations at the surface-level in the SMPL_B simulation. The observed wind speed and direction is also shown.

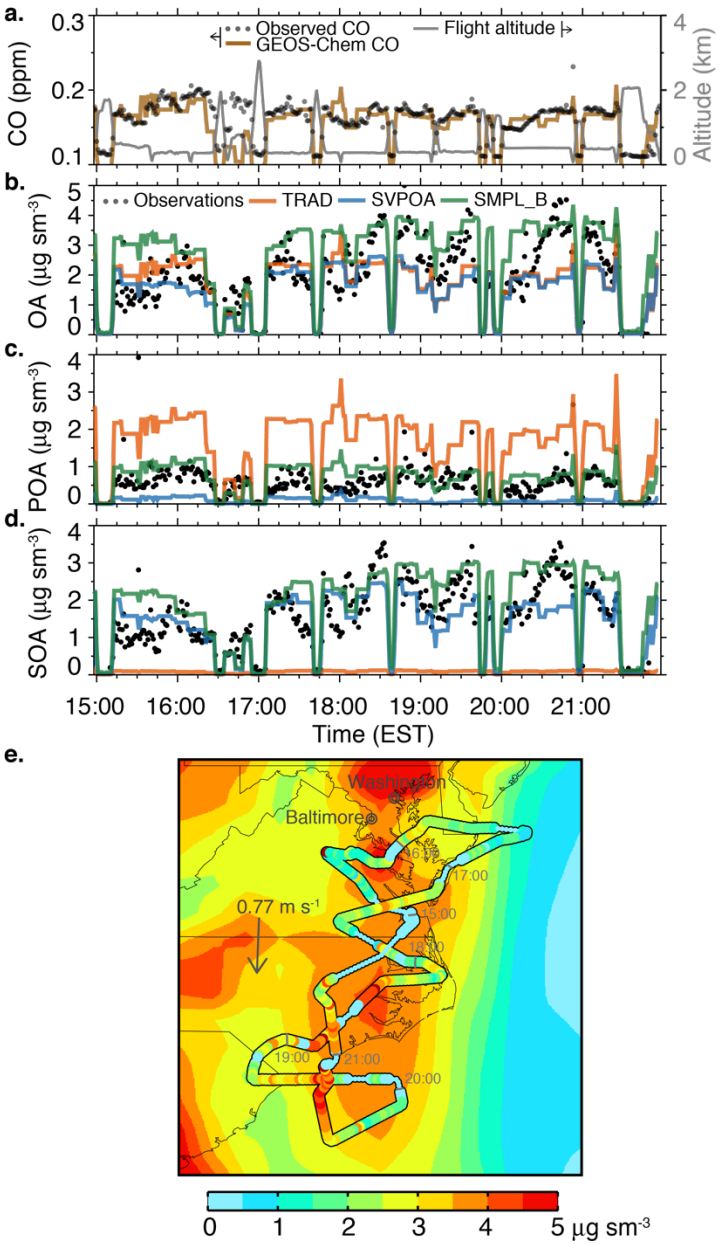

Figure 3.6 Comparison of observations and simulations for flight RF04. Same as Fig. 3.5 otherwise.

For most of the flight, observed SOA (mean: 1.9 μg sm^{-3}) was considerably higher than POA (0.65 μg sm^{-3}), with a mean SOA/OA ratio of 0.75 (Fig. 3.6c, d). The high contribution of SOA to the OA mass is due to the longer period of atmospheric processing of urban emissions (Fig. 3.4a). The total OA concentrations from the three simulations are within ±30% of the

observations for this flight, but display very different SOA/OA ratios. The TRAD simulation significantly underestimates SOA (SOA/OA=0.04), while the SVPOA simulation overestimates SOA (SOA/OA=0.94). The SMPL_B simulation SOA (2.4 μg sm^{-3}) is close to the observations and reproduces the SOA/OA ratio (SMPL_B: 0.74).

3.6 COMPARISON WITH GROUND-BASED OBSERVATIONS

The ground-based OA measurements of the CSN and IMPROVE networks provide an independent constraint on the modeled OA. The model, in turn, provides a link to assess the consistency between the ground-based and the WINTER aircraft measurements. Figure 3.6a shows the measured OA concentrations at these 56 ground-based sites over the NE US for Feb 1–Mar 15, 2015, with a mean of 2.77 ± 1.12 μg sm^{-3} (Fig. 3.8a). Higher OA concentrations are seen at sites between Washington D.C. and New York City and in cities like Pittsburgh, PA and Cleveland, OH.

The TRAD and the SMPL_B simulations predict mean OA concentrations in reasonable agreement with the observations (NMB=-8% and -11% respectively), while the SVPOA simulation is 65% too low (Fig. 3.6b–d, 3A.7). The TRAD simulation overestimates OA at sites between New York City and Boston, where POA emissions are larger (Fig. 3.1a), but underestimates OA elsewhere. The SMPL_B simulation shows modest skill in reproducing the spatial variability observed at the CSN sites and little skill for the IMPROVE sites. This could be because the horizontal resolution of the model (~50 km) is too coarse to simulate finer-scale spatial gradients in the vicinity of ground-based sites or because the local variations in POA emissions are not fully captured by the NEI. At the regional scale, the overall agreement of SMPL_B simulation with the ground-based OA measurements indicates broad consistency between the ground-based and WINTER aircraft measurements.

Overall, my results demonstrate the skill of the SMPL_B simulation in reproducing the OA concentrations, the fractions of POA and SOA, and growth of OA with OH equivalent age observed during the WINTER campaign. In the next section, I focus on the implications of the results of the SMPL_B simulation on the sources and distribution of OA and PM_1 over the NE US during winter.

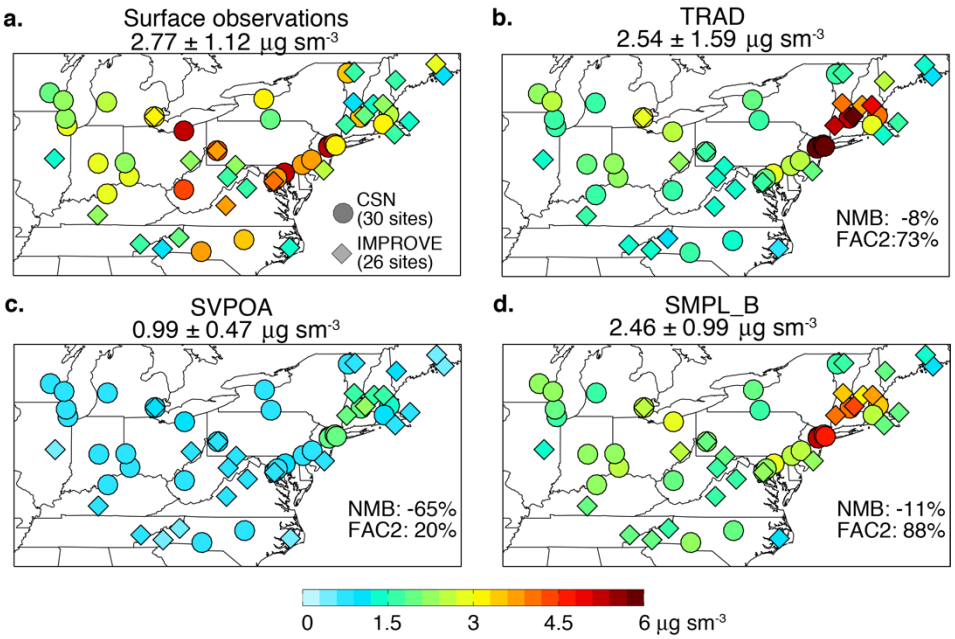

Figure 3.7: Observed and simulated OA concentrations at ground-bsaed sites. (a) OA concentrations observed at the CSN and IMPROVE sites for Feb 1–Mar 15, 2015 and the corresponding modeled OA concentrations in the (b) TRAD, (c) SVPOA, and (d) SMPL_B simulations. Scatterplots of the observed and modeled concentrations are shown in Fig. 3A.6.

3.7 WINTERTIME SOURCES, DISTRIBUTION AND BURDEN OF OA AND PM_1

Figure 3.8 shows the distribution of POA, SOA and OA below 1 km altitude over the NE US for Feb 1–Mar 15, 2015 as calculated in the SMPL_B simulation. The mean POA concentration over land in the NE US is 0.5 µg sm^{-3}, with higher concentrations (0.6–1.0 µg sm^{-3}) near the urban

source regions in the Northeast Corridor between Washington D.C. and Boston, and over western Pennsylvania and Ohio (Fig. 3.8a). I calculate that 0.33 μg sm^{-3} (66%) of POA over land in the NE US is from RWC sources (Fig. 3.9a). SOA concentrations (0.80 μg sm^{-3}) are more evenly distributed over the region, and account for 60-80% of OA (Fig. 3.8b, c). While VOCs are largely emitted in urban areas, their slow photochemical oxidation during winter extends the influence of urban SOA to the regional scale. I find that only 35% of the VOCs are oxidized to SOA over the NE US, with the rest being exported out of the region. The fraction of SOA precursor that gets oxidized increases southward with increasing OH production, which along with higher biogenic VOCs emissions, results in higher SOA concentrations over the southeastern U.S. (black contours in Fig. 3.9b). The oxidized fraction of the AVOC also increases over the ocean as the urban emissions undergo longer photochemical processing. Further photochemical processing can lead to fragmentation and volatilization of SOA (Jimenez et al., 2009; Henry and Donahue, 2012; Epstein et al., 2014; Hodzic et al., 2015), but these processes are not included in my model.

The distribution of OA is largely driven by the distribution of SOA and shows a nearly uniform distribution over the region (Fig. 3.8c). In the SMPL_B simulation, urban SOA accounts for 63% of the OA in the NE US (Fig. 3.9a). The SOA contribution is high over the ocean with continuing SOA formation from the oxidation of AVOC and POA. The distribution of OA in the TRAD and the SVPOA simulations are considerably different. OA in the TRAD simulation is centered around urban areas with high POA emissions, while OA in the SVPOA simulation shows a sharp north-south gradient reflecting the spatial gradient in urban SOA production (Fig. 3A.8). Figure 3.9 contrasts my WINTER results to the Kim et al. (2015) GEOS-Chem simulations for the $SEAC^4RS$ campaign over the southeastern (SE) US in Aug–Sept 2013. The version of GEOS-Chem used for the $SEAC^4RS$ simulation is similar to my SMPL_A simulation for WINTER.

Higher summertime biogenic VOC and fire emissions in the SE US and faster photochemical formation of SOA from biogenic and urban VOCs result in the SEAC^{4}RS OA concentrations to be 5 times higher than the WINTER concentrations (Fig. 3.9a, b). During SEAC^{4}RS, urban POA and fire POA each account for 6–10% of OA. During WINTER, POA account for 35% of OA, with a large contribution from RWC sources. The amplitude of the seasonal cycle in the OA concentrations and sources in urban areas of the NE US is likely smaller than what the WINTER to SEAC^{4}RS comparison suggests. Measurements in Queens, NY during the PMTACS-NY campaign show that winter OA concentration (4.8 μg m^{-3}) are similar to summer OA concentrations (5.9 μg m^{-3}) (Drewnick et al., 2004; Jimenez et al., 2009; Weimer et al., 2006). During the PMTACS-NY campaign, the SOA/OA ratio decreased from 81% in summer to 54% in winter, consistent with the seasonal change seen between the SEAC^{4}RS (SOA/OA=81%) and WINTER (SOA/OA=65%) campaigns.

I now examine the contribution of OA to the total PM_1 concentrations (OA, SO_4^{2-}, NO_3^- and NH_4^+) during WINTER (Fig. 3.10). A detailed comparison between GEOS-Chem and WINTER observations of SO_4^{2-}, NO_3^-, and NH_4^+ is presented in Shah et al. (2018). The GEOS-Chem simulation predicts PM_1 concentrations of ~5 μg sm^{-3} over most of the region, with 20–35% of the PM_1 from OA (Fig. 3.10a). The regional extent of PM_1 stems from the predominance of secondary sources over direct emissions. Overall, GEOS-Chem calculates that ~85% of the PM_1 during WINTER is from secondary sources, with 35% of OA originating from primary emissions of POA and 4% of SO_4^{2-}- NO_3^-- NH_4^+ aerosol due to primary SO_4^{2-} emissions (Shah et al., 2018). The mean PM_1 concentration observed below 1 km altitude during WINTER was 3.94 μg sm^{-3}, composed of 38% OA, 29% SO_4^{2-}, 20% NO_3^-, and 13% NH_4^+. GEOS-Chem reproduces the mean observed PM_1 concentration and composition well (Fig. 3.10b). GEOS-Chem also reproduces the mean PM_1

concentration observed at the CSN and IMPROVE sites for Feb 1–Mar 15, 2015 (8.0 μg sm^{-3}) and PM_1 composition (35% OA, 22% SO_4^{2-}, 28% NO_3^-, and 15% NH_4^+) (Fig. 3.10c).

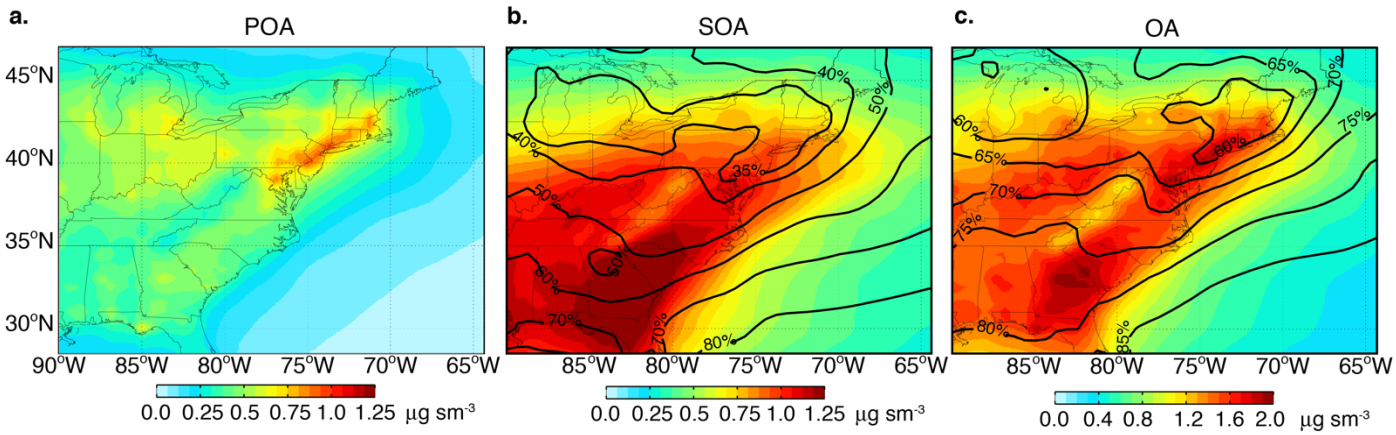

Figure 3.8: Modeled concentrations of (a) POA, (b) SOA, and (c) OA (POA+SOA) below 1 km altitude for Feb 1–Mar 15, 2015. (SMPL_B simulation) The contour lines in panel b show the percent of the AVOC oxidized to SOA. The contour lines in panel c show the percent of OA that is present as SOA. Note the different color scale for panel c.

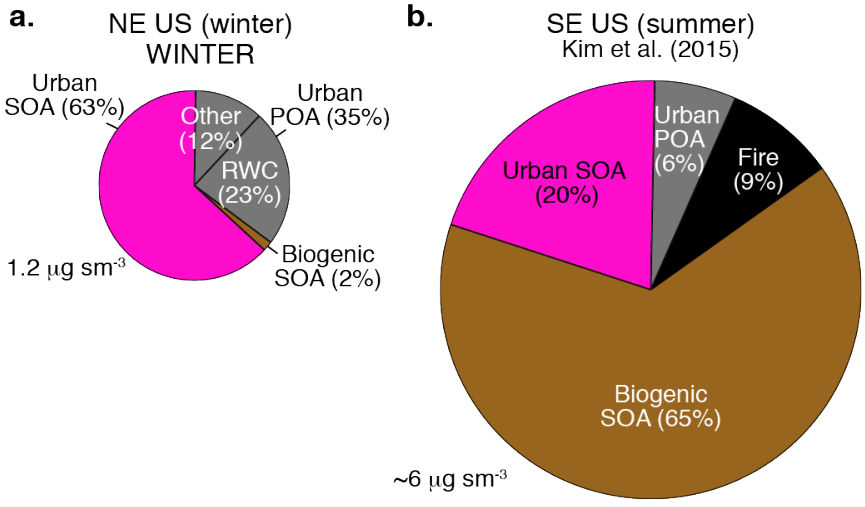

Figure 3.9: Comparison of sources of OA in winter and summer. (a) Contribution of urban, biogenic, and fire primary and secondary sources to the OA simulated for the WINTER campaign. (b) The GEOS-Chem simulated OA sources for the 2013 SEAC^{4}RS campaign (Kim et al., 2015).

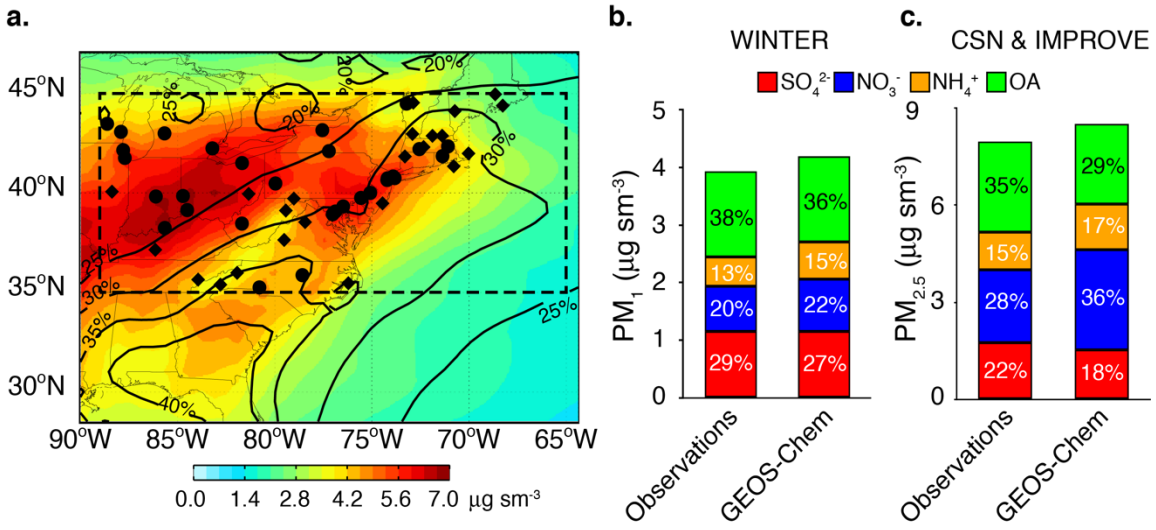

Figure 3.10: Distribution and compostion of PM_1 over the eastern U.S. in winter. (a) Modeled PM_1 concentrations of below 1 km altitude for Feb 1–Mar 15, 2015 in the SMPL_B simulation. The contour lines show the contribution of OA to PM_1. The location of the CSN (circles) and IMPROVE (diamonds) sites in the NE US are shown. (b) The WINTER campaign-average composition of PM_1 observed and modeled (SMPL_B simulation) for flight altitudes below 1 km. (c) The composition of PM_1 observed at the CSN and IMPROVE surface sites for Feb 1–Mar 15, 2015 and the corresponding modeled PM_1 composition (SMPL_B simulation).

3.8 CONCLUSIONS

We have analyzed observations of OA made during the WINTER aircraft campaign over NE US during Feb 1–Mar 15, 2015. The observed OA concentrations below 1 km altitude was 1.48 ± 0.93 µg sm^{-3}. Positive matrix factorization of the OA measurements on the first 7 flights showed comparable magnitude of POA (0.74 µg sm^{-3}) and SOA (1.1 µg sm^{-3}) concentrations. Three-quarters of the POA was composed of BBOA emitted by residential wood combustion sources. SOA was efficiently formed via oxidation of urban VOCs, with near-absent VOC emissions from biogenic and fire sources. I find that the WINTER ΔOA/ΔCO more than doubled (39 to 85 µg sm^{-3} $ppmv^{-1}$) as the OH equivalent age increased from 2 hours to ~1 day, similar to published results for summertime observations over the NE US.

I find that the GEOS-Chem simulation with halved POA emissions and an empirical SOA parameterization (SMPL_B) reproduces the horizontal and vertical distribution of OA, POA, and SOA observed during the WINTER campaign. This simulation displays an NMB of 8% and a FAC2 index of 74% with respect to OA observations below 1 km. It simulates POA (0.74 μg sm^{-3}) and SOA (1.3 μg sm^{-3}) in agreement with observations. It also captures the observed growth in ΔOA/ΔCO and ΔSOA/ΔCO with photochemical processing. The related simulation that used unscaled POA emissions (SMPL_A), overestimates POA by a factor of 2. The TRAD simulation, which has SOA formation only from C_6–C_8 aromatics, predicts OA concentrations with a small bias (NMB: –24%), but overestimates POA by a factor of 2, predicts almost no SOA, and therefore shows no growth in ΔOA/ΔCO with age. The SVPOA simulation, with semivolatile POA and SOA from low-volatility organic compounds, underestimates SOA by ~20%, but POA by a factor of 5, and thus OA by a factor of 2. Its simulated growth in ΔOA/ΔCO with age is a factor of 2 lower than the observations. Flights RF02 and RF04, which sampled emissions of different OH equivalent ages, further illustrated these differences in the three approaches. I compared the simulations with ground-based observations of OA from the CSN and IMPROVE networks, and found that SMPL_B simulation agrees with observations better than the other simulations.

My results of the TRAD and SVPOA simulation are consistent with those of Pye and Seinfeld (2010), who also found that the TRAD simulation underestimates observed OA concentrations at ground-based sites in in the US during winter by 22%, while the SVPOA simulation underestimates them by 63%. Other models with SOA parameterizations similar to the TRAD simulation have also been unable to explain the SOA observed in polluted areas (Volkamer et al., 2006; Dzepina et al., 2009; Hodzic et al., 2009; Heald et al., 2011; Baker et al., 2015). Models that include SOA from the oxidation of low-volatility gases, and are similar to my SVPOA

simulation, simulate substantially higher SOA concentrations (Hodzic et al., 2010; Tsimpidi et al., 2010; Shrivastava et al., 2011; Woody et al., 2016). However, many of these models are also able to reproduce the observed POA, while my SVPOA simulation underestimates WINTER POA by a factor of 5. This is due to different modeling assumptions in the parameters related to the emissions, volatility, and aging of primary and secondary organic compounds. For example, some models include large emissions of low-volatility organic gases in addition to the inventoried POA emissions (e.g. Hodzic et al., 2010), while my SVPOA simulation does not.

My results highlight the challenges in modeling OA using bottom-up approaches and shows that the simple empirical parameterization developed by Hodzic & Jimenez (2011) and Hayes et al. (2015), based on *summertime* observations in Mexico City and Pasadena, CA, can successfully simulate *wintertime* POA and SOA concentrations over the NE US. This is despite the large seasonal differences in the emissions of POA and SOA precursors, oxidation rates of organic gases, and the temperature-dependent partitioning of semivolatile species. This simulation (SMPL_B) shows nearly uniform distribution of OA (1–1.5 $\mu g\ sm^{-3}$) over the NE US for Feb 1–Mar 15, 2015. I find that 63% of the OA is composed of urban SOA and only 2% from biogenic SOA. The remaining 35% OA, is from urban POA with RWC contributing to 2/3 of urban POA emissions. Overall, OA account for 35% of PM_1 observed during the WINTER campaign.

In contrast to summer, which is dominated by biogenic SOA, winter OA over the NE US is almost entirely from anthropogenic emissions. Shah et al. (2018) show that large SO_2 and NOx emissions reductions over the past decade have had limited success in reducing wintertime PM_1 concentrations. They found that despite reductions of 58% and 35% in SO_2 and NOx emissions, respectively, SO_4^{2-} concentrations decreased by 40% and NO_3^- concentrations changed little. This weak response of wintertime PM_1 concentrations to further SO_2 and NOx emissions is likely to

continue in the near future as a result of chemical feedbacks forming PM_1 more efficiently at lower emissions. OA makes up a substantial fraction of the PM_1 and could be a viable policy target for continuing improvements in wintertime air quality. Past decreases in OA over the NE US have likely been driven by decreases in POA emissions (Ridley et al., 2018), but the large contribution of SOA observed during WINTER suggest that further decrease in wintertime OA will need identification, quantification, and reductions in emissions of the SOA precursors.

3.9 Appendix 1: Detailed description of the GEOS-Chem OA simulation

TRAD simulation

The modeling approach of the TRAD simulation follows the POA model of Park et al. (2003) and the urban SOA parameterization of Henze et al. (2008) with updates from Pye at al. (2010). POA is treated as nonvolatile and separated into two species: hydrophobic and hydrophilic. Both species are emitted in equal fractions. Their emissions are calculated by multiplying the NEI's OC emissions by an OA/OC factor. Earlier GEOS-Chem studies used an OA/OC multiplication factor of 2.1 for POA (e.g. Pye and Seinfeld, 2010; Heald et al., 2011), which is much higher than the observed OA/OC ratios (Canagaratna et al., 2015). I therefore use a lower OA/OC factor of 1.4 for POA. The hydrophobic POA converts to hydrophilic POA with atmospheric aging at a rate of 1×10^{-5} s^{-1}. POA is lost by wet and dry deposition. Hydrophobic POA is insoluble in water and is not removed by in-cloud scavenging, but is removed by below-cloud scavenging through impaction.

The SOA parametrization uses the volatility basis set (VBS) framework (Donahue et al., 2006). Urban SOA is formed from the oxidation of benzene, toluene, xylene (Table 3A.1: R1–R9). These VOCs react with OH to form a bicyclic peroxy radical, which is oxidized by HO_2 or NO to form a mixture of nonvolatile and secondary semi-volatile organic compounds (SVOC are organic

compounds with saturation concentrations, C*, between 0.3 and 300 μg m^{-3}). I refer to secondary SVOC as S-SVOC and distinguish from primary SVOC (P-SVOC). The S-SVOC are lumped into three volatility bins (C* at 298 K of 1, 10, and 100 μg m^{-3}). The distribution of the oxidation products of peroxy radicals into the SVOC and nonvolatile bins depends on the VOC and the peroxy oxidation pathway. SOA forms from the gas-particle partitioning of S-SVOC (Table 3A.1: R16)., which is based on absorptive partitioning theory (Eq. 1).

$$\xi_i = \left(1 + \frac{C_i^*}{C_{OA}}\right)^{-1} \qquad (3.4)$$

where, ξ_i is the particle-phase fraction of an SVOC with saturation concentration C_i^* and C_{OA} is the OA concentration (including POA). The method used by GEOS-Chem to solve the partitioning equations is described in Chung and Seinfeld (2002). The temperature dependence of C* follows the van't Hoff equation, with an assumed enthalpy of vaporization of 42 kJ mol^{-1}. The S-SVOC and SOA deposit by dry and wet deposition. The Henry's law coefficient for S-SVOC is 10^5 M atm^{-1} (298 K). SOA is considered less-soluble, and its in-cloud scavenging efficiency is assumed to be 80%. The deposition of aromatic VOCs is assumed as negligible. Biogenic SOA from the oxidation of terpenes and isoprene is described by Pye et al. (2010).

SVPOA simulation

The SVPOA simulation follows the modeling approach of Pye and Seinfeld (2010). In this approach POA and SOA are considered as two components of one dynamic organic gas-particle system. Primary organic compounds are emitted as SVOC, IVOC ($300 < C^* < 3\times10^6$ μg m^{-3}), and VOCs, which undergo gas-particle partitioning and gas-phase oxidation to lower volatilities and further partitioning. POA is formed from the partitioning of P-SVOC (Table 3A.1: R15), while SOA is formed from the condensation of secondary gases formed by the oxidation of primary gases. P-SVOC are lumped into 2 bins of C* at 300 K of 1600 μg m^{-3} (49% of emissions) and 20

μg m^{-3} (51% of emissions). POA emissions inventories may miss some of the P-SVOC emitted in the gas phase, depending on the conditions under which the emission factors were calculated. Pye and Seinfeld (2010) assumed that P-SVOC emissions are 27% higher than that captured in the global POA inventories, based on the laboratory studies of wood combustion. Here, I assume that the NEI captures all urban P-SVOC emissions as POA, and do not consider any additional P-SVOC emissions, following Shrivastava et al. (2008) and Koo et al. (2014). The OA/OC ratio of the P-SVOC emissions is assumed to be 1.4, similar to the TRAD simulation. P-SVOC oxidize by OH (Table 3A.1: R13, R14) to produce SVOC with 100 times lower volatilities (C* at 300 K of 16 and 0.2 μg m^{-3}) and 50% higher mass due to the addition of oxygen (OA/OC=2.1). The S-SVOC partition to the particle phase forming SOA (Eq. 3.4).

Primary IVOC (P-IVOC) are represented using naphthalene as a surrogate species. Naphthalene is emitted from urban sources with emission ratios of 0.041 mol (mol benzene)$^{-1}$ with a C* of 10^5 μg m^{-3} at 299 K. Naphthalene emissions are scaled up by a factor of 66 to account for other P-IVOC species. P-IVOC oxidation is based on chamber studies of naphthalene oxidation and is parameterized similar to the oxidation of C_6-C_8 aromatics in the TRAD simulation (Table 3A.1: R10–12). The oxidation of C_6-C_8 aromatic VOCs and biogenic VOCs is the same as in the TRAD simulation. SOA is formed from the gas-particle partitioning of S-SVOC (Eq. 3.4). The enthalpy of vaporization of all SVOC species is assumed to 42 kJ mol^{-1}. SOA, P-SVOC and S-SVOC deposit by wet and dry deposition, and POA by dry deposition. The Henry's law coefficient for P-SVOC is much lower (9.5 M atm^{-1}) than that of S-SVOC (10^5 M atm^{-1}). The in-cloud scavenging efficiency of SOA is 80%. The deposition of P-IVOC is considered negligible.

The implementation of this approach in GEOS-Chem is fully described in Pye and Seinfeld (2010). An alternate VBS scheme has been implemented in GEOS-Chem (Jo et al., 2013), but it

is not currently included in the public release of the model and I do not use it here. Pye and Seinfeld (2010) compared the OA concentrations predicted by the TRAD and the SVPOA approaches to surface observations in the U.S. during winter, and found that the TRAD simulation underestimates the observations by 22%, but the SVPOA by 63% due to evaporation of POA to the gas phase. They found that a 2-fold increase in P-SVOC emissions, 10-fold decrease in C* of P-SVOC, or a 2-fold increase in the enthalpy of vaporization of SVOC species reduces the discrepancy with the observations. The WINTER observations do not provide any new constraints on these parameters and I keep them at their original values.

SMPL_A and SMPL_B simulations

The third approach (denoted here as SMPL_A and SMPL_B) was first proposed by Hodzic and Jimenez (2011) and implemented in GEOS-Chem by Kim et al. (2015). Urban POA is assumed to be nonvolatile and is separated into two species by source: one emitted by urban sources excluding RWC, and the other emitted form RWC sources. To separate POA from RWC sources, I use the county-level source-resolved POA emissions reported in the U.S. EPA 2011v6 emissions platform (U.S. Environmental Protection Agency, 2017b). An OA/OC multiplier of 1.34 and 1.64 is used to convert the NEI OC emissions to POA emissions from non-RWC urban sources and RWC sources, respectively (Canagaratna et al., 2015). The average OA/OA for POA is 1.55, 10% higher than that in the TRAD and SVPOA simulations. POA reacts with OH to form SOA (Table 3A.1: R17), which is also considered a nonvolatile specie. SOA largely forms from a surrogate VOC (AVOC) emitted by urban sources mainly from vehicles. AVOC does not correspond to any particular SOA precursor, but represents the combined SOA formation potential of VOCs, P-SVOC, and P-IVOC. AVOC emissions are scaled to CO emissions from surface sources using an emission ratio of 0.069 g AVOC (g CO)$^{-1}$ for non-RWC urban sources and 0.013 g AVOC (g

CO)$^{-1}$ for biomass burning sources (Cubison et al., 2011; Hayes et al., 2015; Kim et al., 2015). The separation of CO emissions from RWC sources is also based on the county-level source-resolved CO emissions reported in the U.S. EPA 2011v6 emissions platform (U.S. Environmental Protection Agency, 2017b). I assume that point sources do not emit AVOC. AVOC oxidizes by OH to form SOA (Table 3A.1: R18). POA and SOA are lost by dry and wet deposition. The in-cloud scavenging efficiency of POA is lower (50%) than that of SOA (80%). The loss of AVOC by deposition is assumed to be negligible. Biogenic SOA is assumed to form with fixed yields of 3% and 5% from isoprene and monoterpenes, respectively, following Kim et al. (2015). I perform two simulations using this parameterization: one without any modifications to POA emissions from the NEI inventory (SMPL_A) and the other with POA emissions from the NEI inventory scaled down by a factor of 2 (SMPL_B).

Table 3A.1. Reactions of POA and SOA precursors from urban sources

Reaction	Rate (cm^3 $molec^{-1}$ s^{-1})
VOC oxidation (TRAD and SVPOA simulations)	
1. $BENZ+OH \xrightarrow{O_2} BRO_2$	$2.33\times10^{-12}\times\exp(-193/T)$
2. $TOLU+OH \xrightarrow{O_2} TRO_2$	$1.81\times10^{-12}\times\exp(338/T)$
3. $XYLE+OH \xrightarrow{O_2} XRO_2$	2.31×10^{-11}
4. $BRO_2+NO \rightarrow 0.078$ S-$SVOC_1 + 0.793$ S-$SVOC_{100}$	$2.6\times10^{-12}\times\exp(350/T)$
5. $TRO_2+NO \rightarrow 0.032$ S-$SVOC_1 +$ 0.094 S-$SVOC_{10}+0.08$ S-$SVOC_{100}$	$2.6\times10^{-12}\times\exp(350/T)$
6. $XRO_2+NO \rightarrow 0.025$ S-$SVOC_1 +$ 0.036 S-$SVOC_{10}+0.09$ S-$SVOC_{100}$	$2.6\times10^{-12}\times\exp(350/T)$
7. $BRO_2+HO_2 \rightarrow 0.37\ SOA_N$	$1.4\times10^{-12}\times\exp(700/T)$
8. $TRO_2+HO_2 \rightarrow 0.36\ SOA_N$	$1.4\times10^{-12}\times\exp(700/T)$
9. $XRO_2+HO_2 \rightarrow 0.30\ SOA_N$	$1.4\times10^{-12}\times\exp(700/T)$
P-IVOC oxidation (NAP as surrogate, SVPOA simulation)	
10. $NAP+OH \xrightarrow{O_2} NRO_2$	$1.56\times10^{-11}\times\exp(117/T)$
11. $NRO_2+NO \rightarrow 0.039$ S-$SVOC_1 + 0.296$ S-$SVOC_{10} +$ 0.235 S-$SVOC_{100}$	$2.6\times10^{-12}\times\exp(350/T)$
12. $NRO_2+HO_2 \rightarrow 0.73\ SOA_N$	$1.4\times10^{-12}\times\exp(700/T)$
P-SVOC oxidation (SVPOA simulation)	
13. P-$SVOC_{20}$(g)+OH $\rightarrow$ S-$SVOC_{0.2}$	2×10^{-11}
14. P-$SVOC_{1600}$(g)+OH $\rightarrow$ S-$SVOC_{16}$	2×10^{-11}
Gas-particle partitioning (TRAD and SVPOA simulations)	
15. P-$SVOC_i$ (g) $\leftrightarrow$ POA_i (i=20,1600)	–
16. S-$SVOC_i$ (g) $\leftrightarrow$ SOA_i (i=0.2,1,10,16,100)	–
POA and AVOC oxidation (SMPL simulations)	
17. POA+OH $\rightarrow$ SOA_N	3×10^{-12}
18. AVOC+OH $\rightarrow$ SOA_N	1.25×10^{-11}

BENZ: benzene; TOLU: toluene; XYLE: xylene; NAP: naphthalene;
BRO_2, TRO_2, XRO_2, NRO_2: peroxy radicals from benzene, toluene, xylene, and naphthalene, respectively;
AVOC: surrogate VOC;
SOA_N: nonvolatile SOA;
P/S-$SVOC_i$: primary or secondary SVOC in volatility bin of saturation concentration of i μg m^{-3}.

3.10 ADDITIONAL FIGURES FOR CHAPTER 3

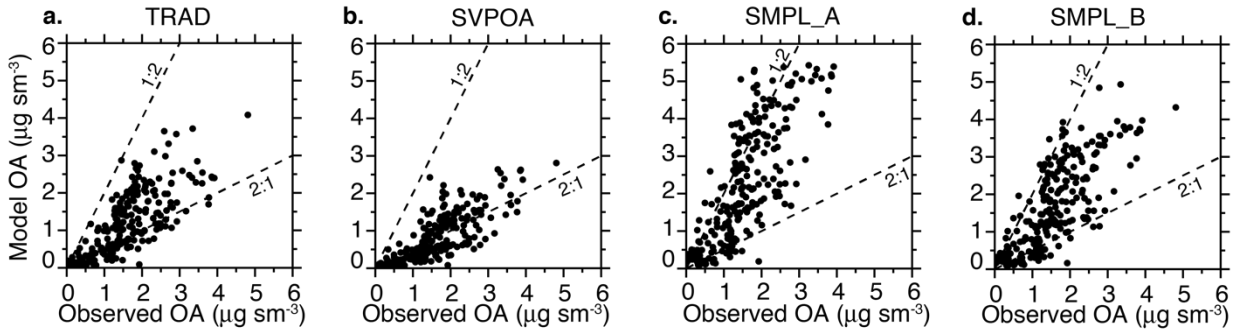

Figure 3A.1: Scatterplots comparing the OA observations shown in Fig. 3.2 and the corresponding modeled concentrations. (a) TRAD, (b) SVPOA, (c) SMPL_A, and (d) SMPL_B simulations.

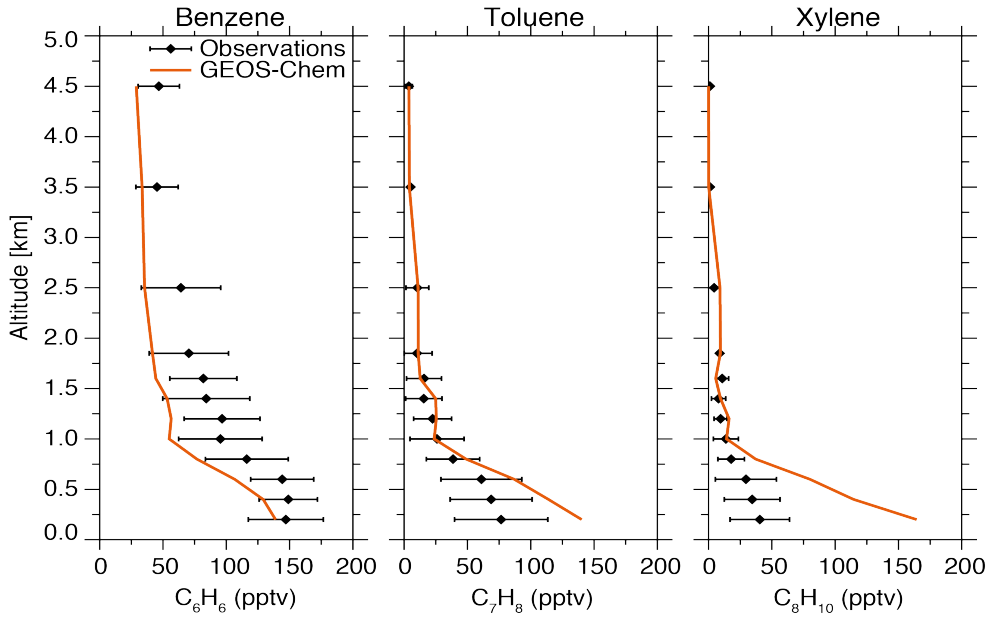

Figure 3A.2:Vertical profiles of the observed and GEOS-Chem simulated (a) benzene, (b) toluene, and (c) xylene. The measured xylene includes ethyl benzene too.

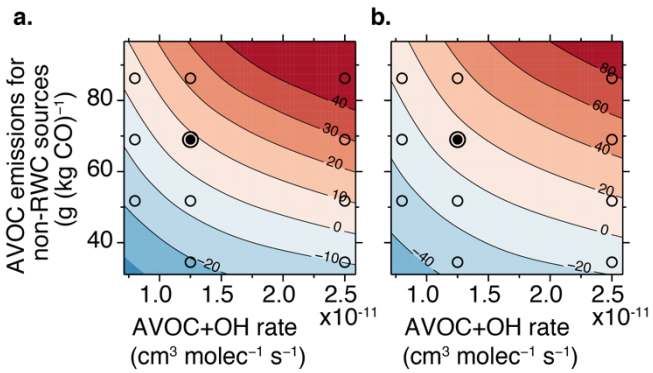

Figure 3A.3:. Normalized mean bias (NMB) with respect to the WINTER observations of (a) OA and (b) SOA for sensitivity runs of the SMPL_B simulation with varying AVOC emissions and AVOC+OH oxidation rate. The parameter values used in the sensitivity runs are shown with the open circles, and the parameter values of the SMPL_B simulation are shown with the filled circle. The NMB contours are calculated by interpolation.

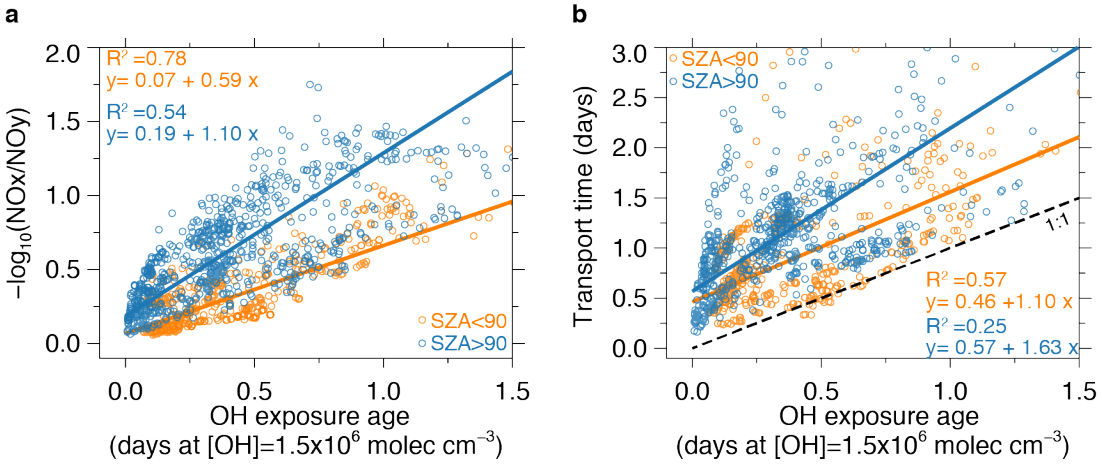

Figure 3A.4. Scatterplot of the OH equivalent age vs. –log$_{10}$(NOx/NOy) and transport time. The OH equivalent age is normalized to an OH concentration of 1.5×10^6 molec cm^{-3}. The inset shows the square of the correlation coefficient (R^2) and the equation for the best-fit line (red line) calculated using ordinary least squares bisector regression.

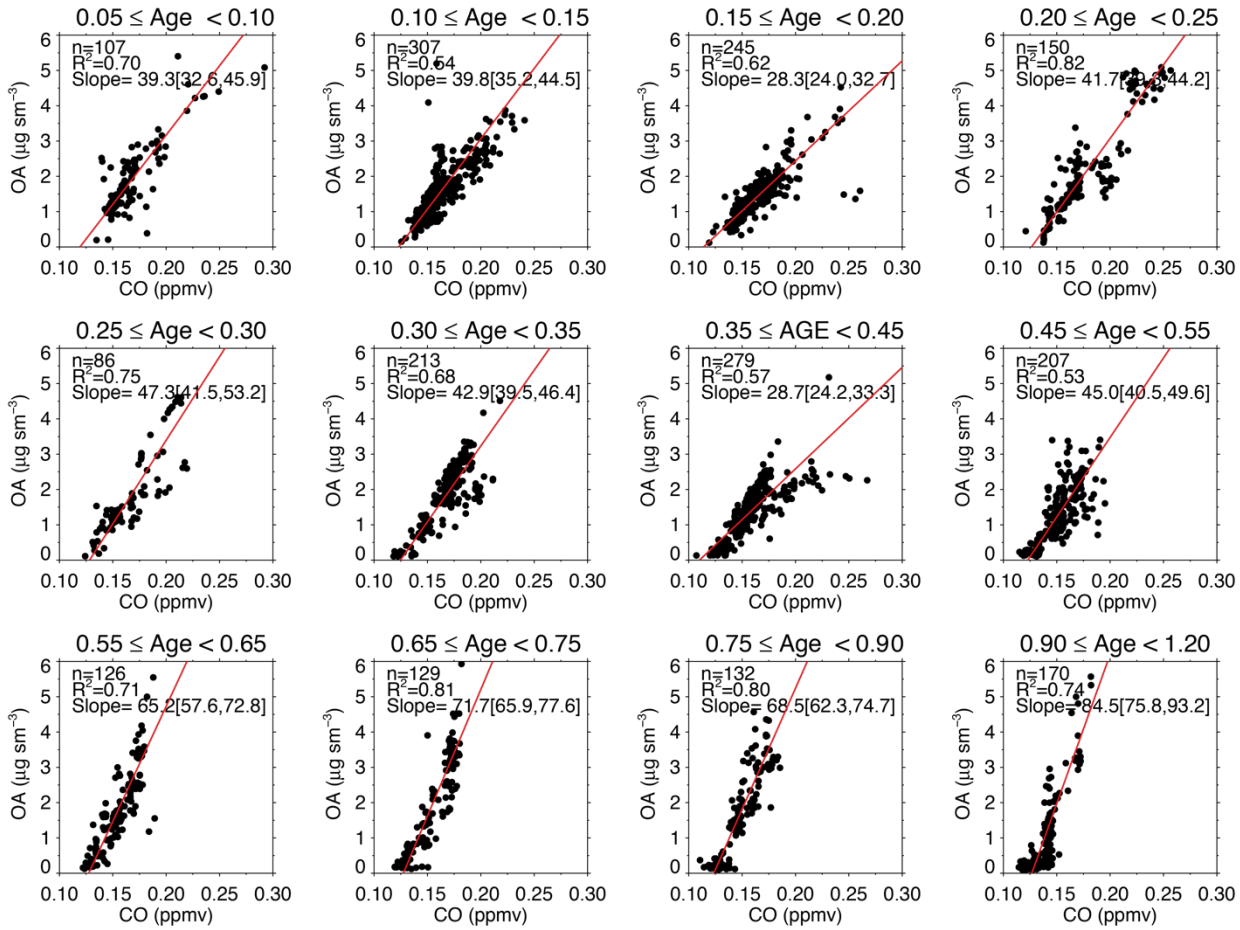

Figure 3A.5.Scatterplots of the observed OA vs. observed CO along the WINTER flights for different ranges of OH equivalent age values. Each panel shows the number of points (n), the square of the correlation coefficient (R^2), and the slope and its 95% confidence interval (in square brackets) calculated using ordinary least squares bisector regression. The best-fit lines are shown in red.

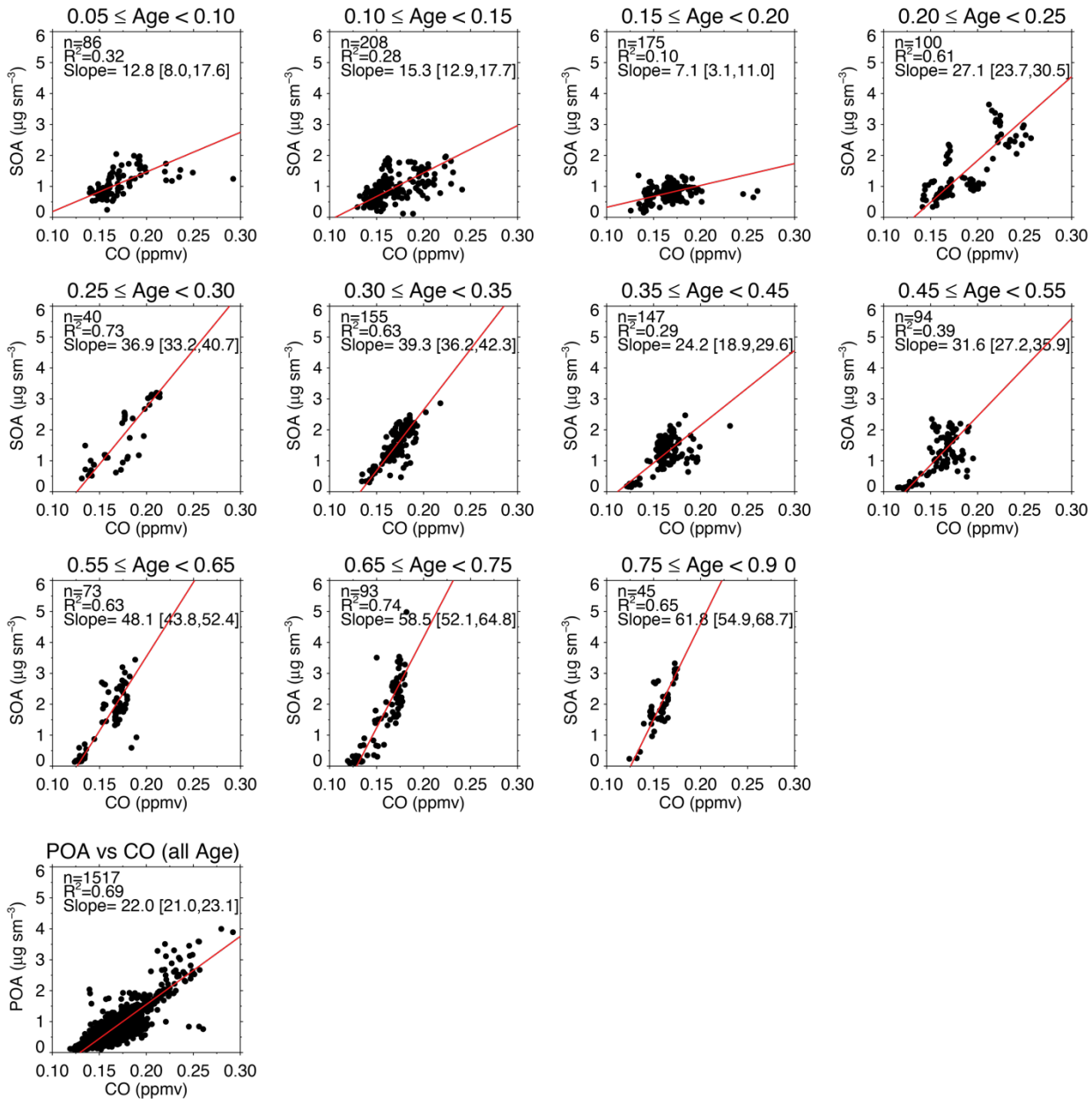

Figure 3A.6: Scatterplots of the observed SOA and POA vs. observed CO along the WINTER flights RF01–07.

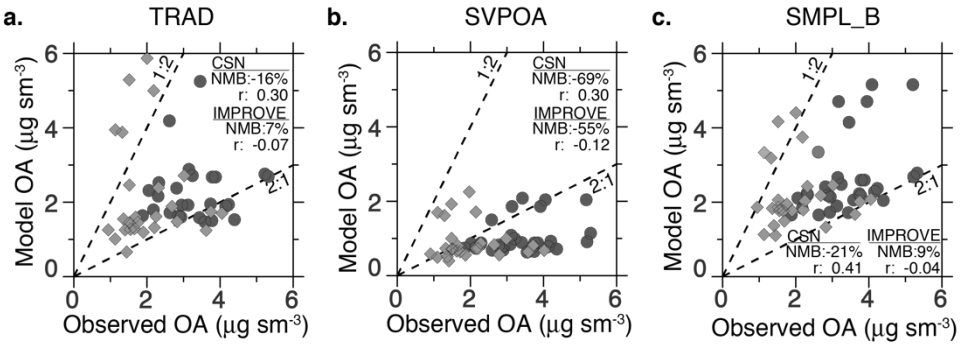

Figure 3A.7. Scatterplots comparing the OA concentrations observed at the CSN (circles) and IMPROVE (diamonds) sites with the modeled OA concentrations. (a) TRAD, (b) SVPOA, and (c) SMPL_B simulations.

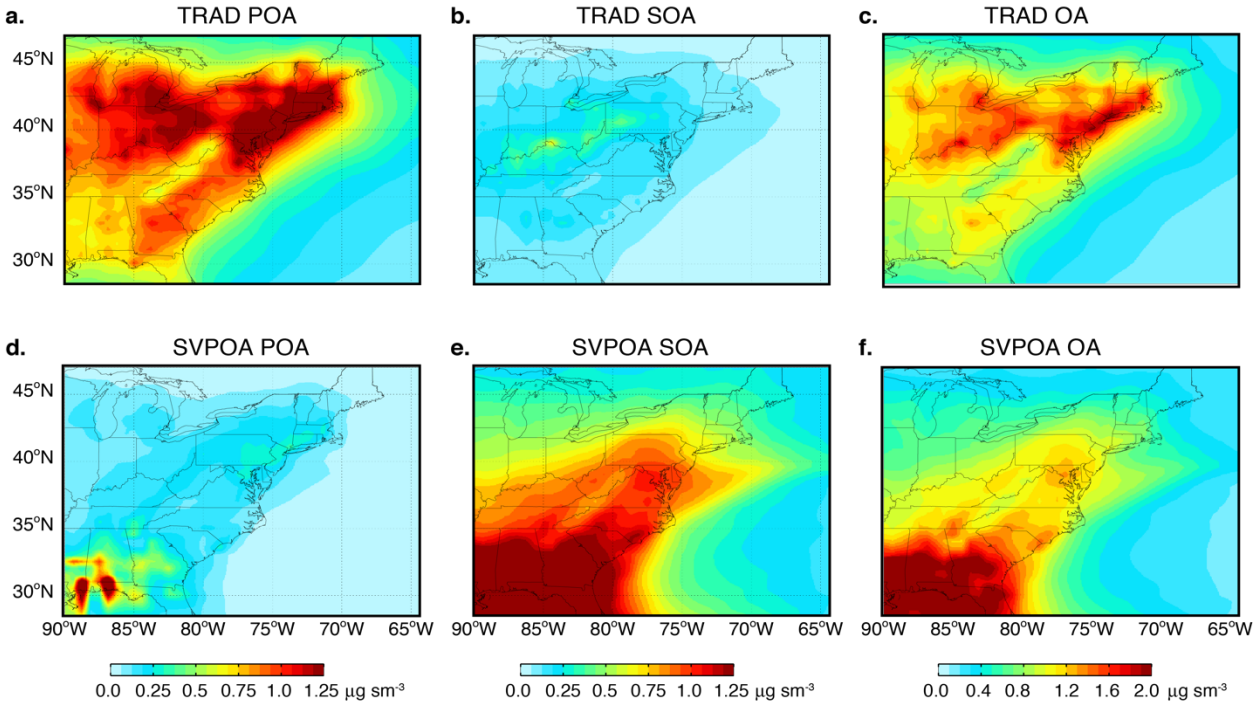

Figure 3A.8. Modeled POA, SOA, and OA below 1 km for Feb 1–Mar 15, 2015 for the (a–c) TRAD and (d–f) SVPOA simulations.

Chapter 4. GLOBAL PRODUCTION AND DISTRIBUTION OF OXIDIZED MERCURY

This chapter has been published as: Shah, V. and Jaeglé, L.: Subtropical subsidence and surface deposition of oxidized mercury produced in the free troposphere, Atmospheric Chemistry and Physics, 17(14), 8999–9017, doi:10.5194/acp-17-8999-2017, 2017.

4.1 INTRODUCTION

Atmospheric deposition of mercury (Hg) is the main source of Hg to most aquatic ecosystems. Methylmercury concentrations in fish in an ecosystem are strongly linked to the local Hg deposition rate (Hammerschmidt and Fitzgerald, 2006; Harris et al., 2007). Dry deposition and wet deposition are both significant contributors to the global deposition flux of Hg (Bergan et al., 1999; Seigneur et al., 2001; Dastoor and Larocque, 2004; Jung et al., 2009; Amos et al., 2012). Models suggest that the global dry deposition fluxes of gaseous elemental mercury (Hg(0)) and oxidized mercury in the gas and particle phases (Hg(II)) are comparable (Seigneur et al., 2001; Amos et al., 2012). Wet deposition of Hg occurs almost entirely through precipitation scavenging of Hg(II). Hg(II) is co-emitted with Hg(0) from several anthropogenic sources, but the predominant source of Hg(II) in the atmosphere is in situ oxidation of Hg(0) (Pirrone et al., 2010; Selin and Jacob, 2008; Holmes et al., 2010). Br is likely the main oxidant of Hg(0) (Ebinghaus et al., 2002; Laurier et al., 2003; Donohoue et al., 2006; Obrist et al., 2011; Gratz et al., 2015), but the importance of O_3 and OH is unclear (Hynes et al., 2009; Sprovieri et al., 2010; Subir et al., 2011; Ariya et al., 2015).

Hg(II) concentrations in the planetary boundary layer are typically about 50 pg m^{-3} (Valente et al., 2007; Gay et al., 2013), but could be as high as 1000 pg m^{-3} in urban areas with large anthropogenic sources (Poissant et al., 2005; Fu et al., 2012) and in the Arctic during springtime

Mercury Depletion Events (Cobbett et al., 2007). The free troposphere is thought to hold a global pool of elevated Hg(II) (Selin, 2009), but few Hg(II) observations have been made in the free troposphere. At high-elevation ground sites, back-trajectory analysis and simultaneous measurements of H_2O and O_3 were used to identify free-tropospheric air masses which contained higher Hg(II) concentrations compared to air masses transported from the planetary boundary layer (Swartzendruber et al., 2006; Faïn et al., 2009; Lyman and Gustin, 2009; Sheu et al., 2010; Timonen et al., 2013; Weiss-Penzias et al., 2015; Fu et al., 2016a). Lyman and Jaffe (2012) conducted aircraft-based measurements of Hg(II) in the upper troposphere and lower stratosphere and inferred that Hg(II) concentrations are highest at the tropopause. Other aircraft-based studies have also found increasing Hg(II) concentrations at 2-5 km altitude in the free troposphere (Sillman et al., 2007; Swartzendruber et al., 2009; Brooks et al., 2014). During the Nitrogen, Oxidants, Mercury, and Aerosol Distributions, Sources, and Sinks (NOMADSS) aircraft campaign, the highest Hg(II) concentrations (300–680 pg m^{-3}) were observed in clean and dry air (CO < 75 ppbv and RH < 35%) originating in the subsiding air masses of the Pacific and the Atlantic subtropical anticyclones (Gratz et al., 2015; Shah et al., 2016). Furthermore, higher concentrations of Hg in precipitation are observed in thunderstorms reaching higher altitudes (Guentzel et al., 2001; Shanley et al., 2015; Holmes et al., 2016; Kaulfus et al., 2017), and higher Hg wet and dry deposition fluxes are associated with transport from the free troposphere (Weiss-Penzias et al., 2011; Gustin et al., 2012; Huang and Gustin, 2012; Sheu and Lin, 2013).

The influence of free-tropospheric Hg on deposition has been evaluated with regional and global chemical transport models. Using the global GEOS-Chem model, Selin and Jacob (2008) estimated that 59% of the annual Hg(II) wet deposition over the U.S. is from Hg(II) scavenged from altitudes above 850 hPa. In another study (Myers et al., 2013), Hg present at the upper

boundary (5.4 km) of the regional CMAQ model was found to contribute about 40% to dry deposition and about 80% to wet deposition in July over the U.S. Coburn et al. (2016) estimated that most of the surface Hg(II) over Florida in April 2010 was produced above 700 hPa. However, these model estimates are limited to specific regions and seasons.

In this study, I use the GEOS-Chem global chemical transport model to quantify the regional contributions of Hg(II) produced at different heights in the atmosphere to the annual deposition of Hg(II). I have added a tagging method to the GEOS-Chem model to track Hg(II) produced in the lower (surface–750 hPa), middle (750–400 hPa) and upper troposphere (400 hPa–tropopause), Hg(II) produced in the stratosphere, and Hg(II) emitted by anthropogenic activities. This simulation is described and evaluated with ground-based observations of Hg(II) concentrations and wet deposition (Sect. 4.2). In Sect. 4.3, I present the distribution of the tagged Hg(II) and calculate their contributions to wet and dry deposition fluxes in different regions of the world. I also examine the sensitivity of my results to different model assumptions for Hg chemistry and anthropogenic emission speciation. I use my simulation to examine the role of the subtropical anticyclones as global reservoirs of Hg(II)-rich air (Sect. 4.4) and evaluate the role of tagged Hg(II) tracers in explaining the observed variability of Hg(II) concentrations and wet deposition fluxes (Sect. 4.5). Finally, I discuss the implications of my study in Sect. 4.6 and present conclusions in Sect. 4.7.

4.2 OBSERVATIONS AND MODEL USED IN THIS STUDY

4.2.1 *Observations of Hg wet deposition and atmospheric concentrations of Hg(II)*

Hg wet deposition fluxes over North America and Europe are measured by the Mercury Deposition Network (MDN; http://nadp.sws.uiuc.edu/mdn/) and the European Monitoring and Evaluation Programme (EMEP; http://www.nilu.no/projects/ccc/index.html), respectively. These networks

measure precipitation depth and Hg concentrations in precipitation weekly (MDN), biweekly (EMEP) or monthly (EMEP). In this study, I use the 2013–2014 monthly-mean and annual-mean wet deposition flux and volume-weighted mean (VWM) Hg concentrations. The VWM concentration for any period is the total Hg wet deposition flux for that period divided by the total precipitation depth. All sites in the MDN network use standard instruments and protocols, and all samples are analyzed at the same laboratory (Prestbo and Gay, 2009). The measurement precision in MDN observations, estimated from collocated sampling, is less than 15% (Wetherbee et al., 2007). A field inter-comparison of instruments and methods used in the EMEP network found the measurement precision for the EMEP network to be about 40% (Aas, 2006).

To calculate monthly means, I discard sites with fewer than 3 weeks of measurements in any given month. For annual means I require at least 8 months of valid measurements. The MDN network had 80 stations over the continental U.S. that met the above data completeness criteria during 2013–2014, whereas the EMEP network had 9 stations over Europe (Table 4A.1).

The Atmospheric Mercury Network (AMNet; http://nadp.sws.uiuc.edu/amn/) monitors surface concentrations of Hg(0), reactive gaseous mercury (RGM) and particle-bound mercury (PBM). The sum of RGM and PBM is considered to represent Hg(II). RGM and PBM measurements are made on a 2- or 3-hour cycle, depending on the site. All AMNet stations use the Tekran® 2537-1130-1135 speciation system, and follow operational procedures described in Gay et al. (2013). There is no standard calibration method for Tekran RGM and PBM measurements, and the uncertainties in these measurements are not fully quantified. A few studies have found that the AMNet instruments underestimate RGM by a factor of 2–3 in the presence of ambient water vapor and O_3 (Lyman et al., 2010; Ambrose et al., 2013; McClure et al., 2014). Here, I use the 2009–2012 AMNet observations, as this data is publicly available. AMNet had 23 sites over the

continental U.S. and eastern Canada (Nova Scotia) operational during this period (Table 4A.2). The annual and monthly statistics for each station are calculated by aggregating 2- or 3-hour measurements made during 2009–2012.

Ground-based measurements of Hg wet deposition and Hg(II) surface concentration have been made as part of the Global Mercury Observations System (GMOS) network (Angot et al., 2014; Wängberg et al., 2016; Sprovieri et al., 2016, 2017; Travnikov et al., 2017), and at sites in Europe (Weigelt et al., 2013), Canada, and East Asia (Sheu et al., 2010; Sheu and Lin, 2013; Fu et al., 2015, 2016b). I use the 2013-2014 measurements wherever available, but use all sites with one year or more of observations. I exclude sites in China classified as urban, because of proximity to large Hg(II) sources. I include 14 sites with annual-mean measurements of Hg wet deposition (Table 4A.1), and 14 sites with annual-mean measurements of surface Hg(II) (Table 4A.2).

The NOMADSS aircraft campaign took place over the eastern U.S. from June 1 to July 15, 2013. Total Hg and Hg(II) observations were made with the University of Washington Detector of Oxidized Hg Species (DOHGS) instrument (Ambrose et al., 2015; Swartzendruber et al., 2009; Lyman and Jaffe, 2012). The detection limit of the DOHGS instrument for Hg(II) measurements during the campaign was between 57 and 228 pg m^{-3}, and I use the robust Regression on Order Statistics (ROS) to estimate values for measurements below detection limit, as described by Shah et al. (2016). I also include aircraft-based measurements of Hg(II) carried out near Tullahoma, Tennessee, USA from August 2012 to June 2013 (Brooks et al., 2014).

4.2.2 *GEOS-Chem model*

GEOS-Chem is a global chemical transport model that simulates the emissions, transport, chemistry, and deposition of Hg(0), gas-phase Hg(II), and particle-phase Hg(II) (Selin et al., 2007). The model is driven by meteorological fields from the NASA Global Modeling and Assimilation

Office (GMAO) Goddard Earth Observing System Model Forward Processing (GEOS-FP) modeling system. The GEOS-FP system consists of a general circulation model coupled with a data assimilation system (Reinecker et al., 2008), and has a native horizontal resolution of 0.25° latitude × 0.3125° longitude with 72 vertical levels up to 0.01 hPa. I average the meteorological fields to a coarser resolution of 2° latitude × 2.5° longitude and 47 vertical levels for the GEOS-Chem simulations in this study. I use GEOS-Chem v9-02 (http://acmg.seas.harvard.edu/geos/). Global anthropogenic emissions of Hg are from the global United Nations Environment Programme (UNEP) / Arctic Monitoring and Assessment Programme (AMAP) 2010 inventory (http://www.amap.no/mercury-emissions/datasets). I assume that stack emissions (emission height > 50m) of Hg consist of 90% Hg(0) and 10% Hg(II) (see Sect 2.2.1). Natural emissions are simulated using a slab ocean model (Strode et al., 2007; Soerensen et al., 2010) and a land emissions model (Selin et al., 2008). Emissions from biomass burning and geogenic activity are prescribed as in Holmes et al. (2010). Transport processes simulated in the GEOS-Chem model include advection (Lin and Rood, 1996), convective transport (Wu et al., 2007), and turbulent mixing in the boundary layer (Lin and McElroy, 2010).

The redox chemistry of Hg consists of oxidation of Hg(0) by Br, as described below, and aqueous phase reduction in the presence of sunlight (Holmes et al., 2010). Gas / particle partitioning of Hg(II) on sea-salt aerosols is simulated as a kinetic process (Holmes et al., 2010), while partitioning on other aerosols is simulated as an equilibrium process (Amos et al., 2012). The oxidation of Hg(0) to Hg(II) is simulated as follows (Goodsite et al., 2004; Balabanov et al., 2005; Dibble et al., 2012):

$$\mathrm{Hg(0) + Br \xleftrightarrow{M} HgBr} \quad \text{(R4.1)}$$

$$\mathrm{HgBr + Br \longrightarrow Hg(0) + Br_2} \quad \text{(R4.2)}$$

$$\mathrm{HgBr + X \longrightarrow Hg(II)} \quad \text{(R4.3)}$$

$$\mathrm{(X = NO_2, HO_2, BrO, Br, OH)}$$

with the following reaction rates:

$$k_{1f} = 1.46 \times 10^{-32} \times \left(\frac{T}{298}\right)^{-1.86} \times [M] \quad cm^3 \text{ molecule}^{-1} \text{ s}^{-1}$$

$$k_{1r} = 2.67 \times 10^{41} \times \exp\left(\frac{-7292}{T}\right) \times \left(\frac{T}{298}\right)^{1.76} \times k_{1f} \quad s^{-1}$$

$$k_2 = 3.9 \times 10^{-11} \quad cm^3 \text{ molecule}^{-1} \text{ s}^{-1}$$

$$k_3 = 2.5 \times 10^{-10} \times \left(\frac{T}{298}\right)^{-0.57} \quad cm^3 \text{ molecule}^{-1} \text{ s}^{-1}$$

Concentrations of Br, BrO, NO_2, HO_2, and OH are obtained from the archived monthly-mean output of the 4° latitude × 5° longitude HOx-NOx-O_3-VOC-Br GEOS-Chem simulation for 2013 (Bey et al., 2001; Parrella et al., 2012). In my previous work (Shah et al., 2016), I found that the GEOS-Chem Br concentrations simulated by Parrella et al. (2012) were insufficient in explaining Hg(II) concentrations observed during the NOMADSS aircraft campaign at 5–7 km altitude. I found improved agreement with NOMADSS Hg(II) observations when I increased Br concentrations by a factor of 3 between 45°S and 45°N and between 750 hPa and the tropopause. Schmidt et al. (2016) have recently updated the GEOS-Chem bromine simulation by expanding the multiphase chemistry of bromine to include reactions with chlorine and ozone. These updates result in faster recycling of HBr to BrO_x and a factor of 2.5 increase in tropospheric Br concentrations for 45°S–45°N above 2.5 km, improving agreement with satellite and in situ observations of BrO. This is consistent with my assumption that Br concentrations are 3 times higher than those simulated with the previous mechanism. In addition, these updates by Schmidt et al. (2016) have resulted in a factor of 2.3 increase in free tropospheric Br concentrations at higher latitudes (45°N–90°N). To maintain consistency with my previous work, I continue to use the Parrella et al. (2012) Br fields with the factor of 3 scaling in this study too, but note that Br concentrations north of 45°N may be too low.

The GEOS-Chem model includes wet deposition of Hg(II) and dry deposition of Hg(0) and Hg(II). Wet deposition includes in-cloud scavenging (rainout) and below-cloud scavenging (washout) in convective and large-scale precipitation (Liu et al., 2001). Within clouds, the dissolution of gas-phase Hg(II) in liquid droplets is modeled as an equilibrium process, while particle-phase Hg(II) is assumed to be fully dissolved (Amos et al., 2012). I assume that rainout of gas-phase Hg(II) does not occur during ice nucleation ($T < 248$ K). Below clouds, gas-phase Hg(II) is washed out by dissolving in falling raindrops ($T > 268$K), but not in falling snow and ice (Amos et al., 2012). Particle-phase Hg(II) is washed out in collisions in falling rain, snow, and ice with different efficiencies (Wang et al., 2011). Dry deposition of gas-phase Hg(II) and particle-phase Hg(II) on particles other than sea-salt aerosols is based on the resistance-in-series model (Wesely, 1989; Wang et al., 1998; Zhang et al., 2001). The surface resistance of gas-phase Hg(II) is assumed to be negligibly small (Selin et al., 2007; Amos et al., 2012). The dry deposition of particle-phase Hg(II) present on sea-salt aerosols is parameterized using results of a box model simulating the chemistry and deposition of Hg(II) in the marine boundary layer (Holmes et al., 2009, 2010).

4.2.2.1 Model uncertainties

Uncertainties in mercury modeling and chemistry have been recently reviewed by Gustin et al. (2015), Ariya et al. (2015), and Kwon and Selin (2016). Here I briefly discuss uncertainties which are pertinent to my study: uncertainties in the assumption of Br as the sole oxidant of Hg(0), in reduction kinetics of Hg(II), and in the assumed speciation of Hg(0) and Hg(II) in anthropogenic emissions.

While Br, O_3, and OH have been identified as possibly important oxidants of Hg(0), there is growing evidence from theoretical (Goodsite et al., 2004; Dibble et al., 2012), laboratory (Ariya et al., 2002; Donohoue et al., 2006) and field studies (Ebinghaus et al., 2002; Lindberg et al., 2002;

Laurier et al., 2003; Obrist et al., 2011; Gratz et al., 2015) that Br may be the most relevant oxidant of Hg(0) in the atmosphere. Ab-initio calculations have suggested that HgO, the product of gas-phase oxidation of Hg(0) by O_3 and OH, is a weakly-bound molecule, and that oxidation of Hg(0) by O_3 and OH is an endothermic reaction of little importance in the atmosphere (Hynes et al., 2009).

The pathways for reduction of Hg(II) to Hg(0) in the atmosphere are poorly characterized. Laboratory experiments suggest that photoreduction of Hg(II) can occur in the aqueous-phase in the presence of organic compounds or on dry aerosol surfaces at atmospherically relevant rates (Si and Ariya, 2008; Tong et al., 2013), and field studies have found some evidence for in situ reduction of Hg(II) (Edgerton et al., 2006; Landis et al., 2014; de Foy et al., 2016). Most global atmospheric mercury models include at least one pathway of Hg(II) reduction in order to simulate realistic Hg(0) concentrations (Ariya et al., 2015). The reduction rate of aqueous-phase Hg(II) in GEOS-Chem is parameterized based on the simulated NO_2 photolysis rate (Holmes et al., 2010). I adjust the reduction rate to best match aircraft- and ground-based observations of Hg(0) over the mid-latitudes.

I have assumed an emissions speciation of 90% Hg(0) and 10% Hg(II) for anthropogenic emissions from stacks, as opposed to the UNEP/AMAP speciation of 55% Hg(0) : 45% Hg(II) for stack sources. Zhang et al. (2012b) and Kos et al. (2013) found that a speciation scheme with 10–15% of Hg(II), and the rest Hg(0), best explains the spatial variability in Hg(II) wet deposition observed over the U.S. However, the speciation of Hg emissions can vary considerably based on the type of source, type of pollution control devices, and the availability of oxidants in the flue gas (Kim et al., 2010).

4.2.2.2 Simulations performed for this study

I have added a tagging technique to the GEOS-Chem model to identify the production regions of Hg(II). I divide the atmosphere vertically into lower troposphere (LT: surface–750 hPa), middle troposphere (MT: 750–400 hPa), upper troposphere (UT: 400 hPa–tropopause) and stratosphere (STRAT), to track the Hg(II) produced in each of these regions as separate Hg(II) tracers. Hg(II) emitted directly to the atmosphere is also tagged separately (E–Hg(II)). Each of these tagged tracers undergo the same physical and chemical processes as the total Hg(II) tracer. Hg(II) loss by deposition or reduction in a model grid cell is divided among all tagged tracers present in the grid cell in proportion to their masses. I perform a simulation with the tagged tracers for the years 2013 and 2014 following a model spin-up period of 15 years.

I perform an additional simulation to quantify the role of the dry subsidence regions of the subtropical anticyclones in the global transport of Hg(II). I identify the dry subtropical subsidence areas as those that lie between 45°S and 45°N and between 750 hPa and the tropopause and where the monthly-mean relative humidity is less than 20%. The relative humidity threshold is based on the definition of dry subtropical areas of Cau et al. (2007). I introduce duplicate Hg(II) tracers that are produced and lost exactly as the original Hg(II) tracers, but at each time step I set to zero the concentrations of these tracers within the dry subtropical areas. The amount of Hg(II) originating in the dry areas (dry-Hg(II)) is then calculated by difference between the original and the duplicate Hg(II) tracers. This simulation is performed for the years 2013-2016.

In addition, I perform three one-year (2013) sensitivity simulations with the tagged tracers addressing uncertainties in mercury oxidation and Hg(0):Hg(II) partitioning in anthropogenic emissions (Sect. 4.2.2.1).

4.2.3 *Comparison of modeled and measured Hg(II)*

Figures 4.1–4.3 compare the modeled Hg(II) concentrations and wet deposition fluxes to observations from the MDN, EMEP, and AMNet networks. The modeled annual wet deposition flux at the MDN sites (10.4 ± 4.2 μg m^{-2} a^{-1}; mean ± standard deviation) is in close agreement with observations (10.2 ± 4.0 μg m^{-2} a^{-1}) (Fig. 4.1a). The model reproduces the observed spatial pattern in annual wet deposition fluxes (r^2=0.67). Wet deposition is lowest in western U.S. (MDN: 6.9 μg m^{-2} a^{-1}, GEOS-Chem: 6.2 μg m^{-2} a^{-1}), higher in the northeast U.S. (MDN: 8.5 μg m^{-2} a^{-1}, GEOS-Chem: 8.4 μg m^{-2} a^{-1}) and in the central U.S. (MDN: 11.2 μg m^{-2} a^{-1}, GEOS-Chem: 13.2 μg m^{-2} a^{-1}), and largest in the southeast U.S. (MDN: 15.4 μg m^{-2} a^{-1}, GEOS-Chem: 15.2 μg m^{-2} a^{-1}). The observed monthly-mean wet deposition fluxes exhibit a seasonal maximum in summer, particularly in the central, northeast, and southeast regions (Fig. 4.1c). This seasonality is driven by an increase in precipitation and an increase in mercury concentrations in precipitation (Prestbo and Gay, 2009; Selin and Jacob, 2008). The model reproduces the observed seasonal variations in the central and northeast regions, but underestimates the summer deposition fluxes in the southeast because of a factor of 2 underestimate in summertime precipitation by the GEOS-FP meteorological fields (not shown). Overall, 66–88% of the modeled wet deposition fluxes are within a factor of 2 of the observations (FAC2; FAC2=percentage of points where $0.5 \le M_i / O_i \le 2$ where O_i and M_i are observed and simulated values, respectively) for the four regions, and the normalized mean bias (NMB; $\mathrm{NMB}=\sum_i (M_i - O_i) \Big/ \sum_i O_i \times 100\%$) ranges between -7% and +20%.

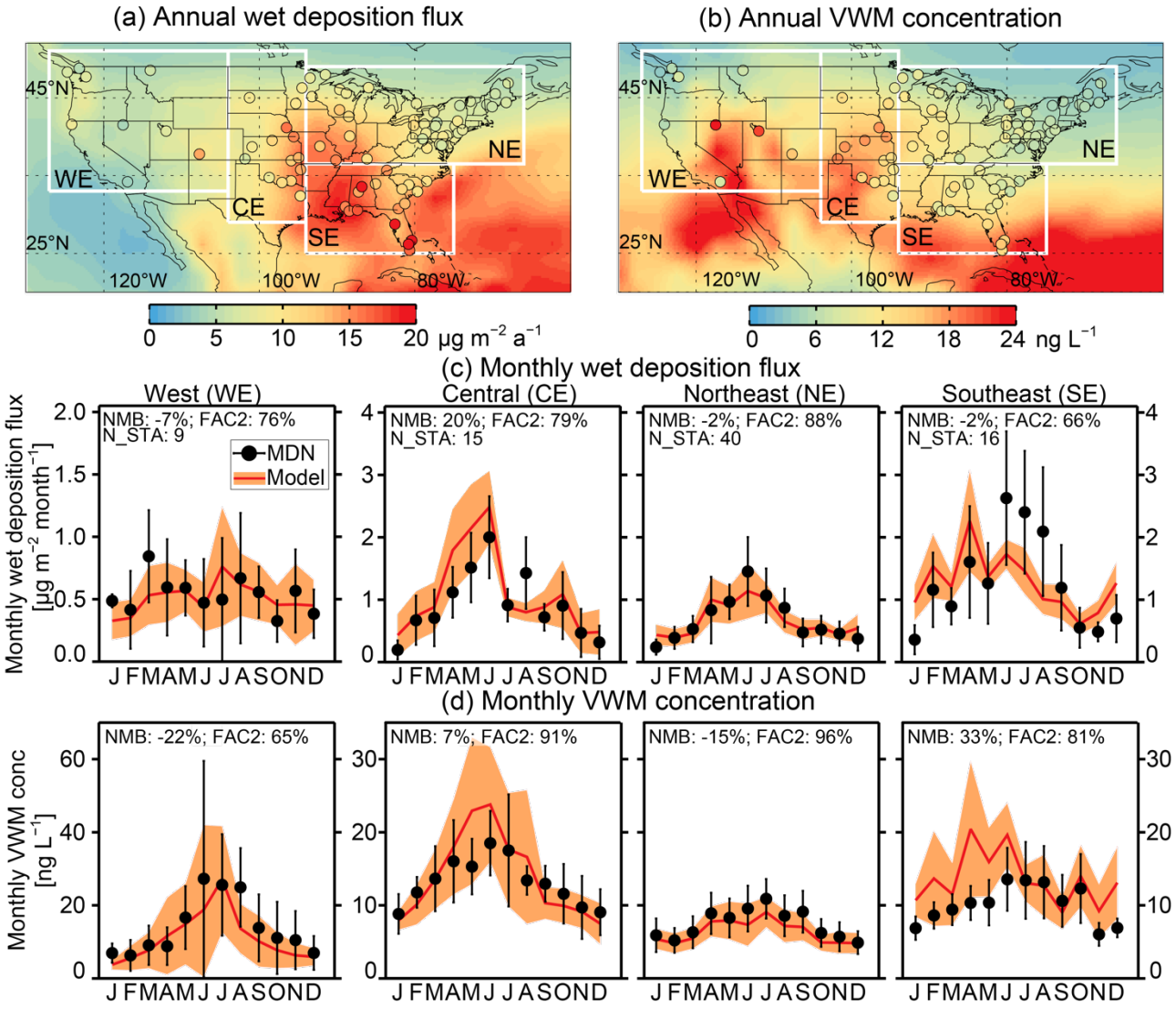

Figure 4.1: Comparison of observed and modeled Hg wet deposition over the U.S. (a) Annual Hg(II) wet deposition fluxes and (b) volume-weighted mean (VWM) mercury concentrations over the U.S. for 2013–2014. The map backgrounds show the GEOS-Chem results and the filled circles show the Mercury Deposition Network (MDN) measurements. The bottom two rows (c and d) show the seasonal variations in wet deposition and VWM concentrations for the four regions marked by white boxes in (a) and (b): west (WE), central (CE), northeast (NE), and southeast (SE). Black circles and error bars show the observed means and standard deviations. The red lines and orange shading are for the modeled means and standard deviations. Each panel displays the Normalized Mean Bias (NMB) and the percentage of model-observation pairs within a factor of 2 of each other (FAC2). The number of stations in each region (N_STA) is also shown. Note the different scales on the y-axis for the WE region relative to the other regions (panels c and d).

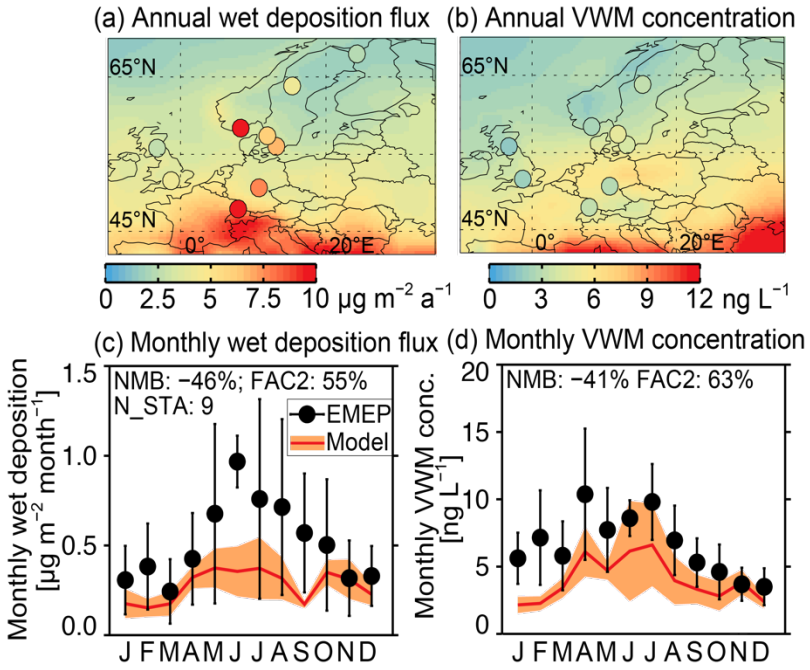

Figure 4.2: Comparison of observed and modeled Hg wet deposition over the Europe. Same as Fig. 4.1, but for European Monitoring and Evaluation Programme (EMEP) sites.

The model also captures the observed annual VWM concentrations (MDN: 10.0 ± 4.3 ng L^{-1}; GEOS-Chem: 9.7 ± 4.7 ng L^{-1}) (Fig. 4.1d). Higher VWM concentrations are observed in the western and central U.S. (11.6 and 14.1 ng L^{-1} respectively) compared to the northeast and southeast (7.9 and 10.6 ng L^{-1} respectively), indicating the presence of higher atmospheric concentrations of Hg(II) over these regions. Modeled VWM concentrations show a spatial pattern similar to observations: higher values in western (8.7 ng L^{-1}) and central (14.4 ng L^{-1}) U.S. and lower values in northeast (6.7 ng L^{-1}) and southeast (13.6 ng L^{-1}). In western and central U.S., the observed and modeled VWM concentrations show a pronounced summer maximum (Fig. 4.1d), while in northeast and southeast the seasonal cycle is weaker. I find that 65–96% of the modeled monthly VWM concentrations are within a factor of 2 of the observations, with an NMB ranging

between -22% and +33%. Over southeast U.S., modeled VWM concentrations are higher than observations during winter and spring, suggesting a model overestimate in atmospheric Hg(II) concentrations in that region, or an overestimate in the amount of Hg(II) scavenged by precipitation.

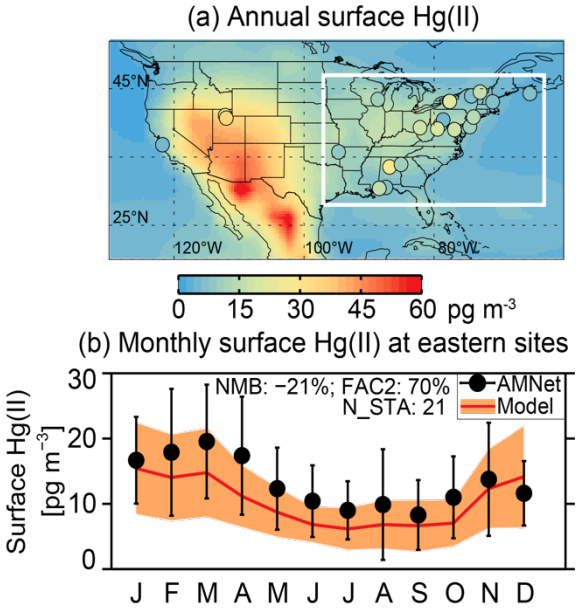

Figure 4.3: Comparison of observed and modeled Hg(II) surface concentrations over the U.S. (a) Annual surface Hg(II) concentrations over the U.S. The map backgrounds show the GEOS-Chem concentrations (2013–2014), and the filled circles show the observations at Atmospheric Mercury Network (AMNet) sites (2009–2012). (b) Monthly surface Hg(II) concentrations at the AMNet sites in the eastern U.S. (white box in panel a). Black circles and error bars show the mean and standard deviation of the monthly-mean observations. Red lines and orange shading indicate the modelled means and standard deviations.

Over Europe (Fig. 4.2a), the modeled wet deposition flux (3.5 ± 1.4 μg m^{-2} a^{-1}) underestimates observations at EMEP sites (6.1 ± 3.1 μg m^{-2} a^{-1}). Similarly, modeled VWM concentrations (3.6 ± 1.0 ng L^{-1}) are significantly lower than observations (6.0 ± 1.8 ng L^{-1}) (Fig. 4.2b). The summertime underestimate is partially explained by a 40% underestimate of observed summertime precipitation by the GEOS-FP meteorological fields, but the discrepancy exists year-round. The remaining discrepancy could indicate an underestimate in the modeled Hg(II)

concentrations over the region, likely because the upward scaling of the Br concentrations in my simulation did not extend north of 45°N and covered only parts of southern Europe (Sect. 2.2). The modeled seasonal cycle in wet deposition shows higher fluxes from April to August, following qualitatively the observed seasonal cycle (Fig. 4.2c). I find that 55% of the modeled monthly-mean wet deposition fluxes are within a factor of 2 of the observations, with an NMB of -46%. Model and observations display a similar seasonal cycle in VWM, with higher concentrations in April through August (Fig. 4.2d). The FAC2 and NMB statistics for the modeled VWM concentrations are 63% and -41% respectively, suggesting that the modeled oxidation rate is too slow over this region.

In Fig. 4.3 I present a comparison of modeled surface Hg(II) concentrations with observations at AMNet sites. Modeled Hg(II) surface concentrations (11.7 ± 8.3 pg m^{-3}) are comparable to observations (15.0 ± 8.2 pg m^{-3}) (Fig. 4.3a). The fact that the observations and the simulations are for different periods adds additional uncertainty from inter-annual variations. From four years of model simulation (2013-16), I estimate this uncertainty at ±30%. The model simulates enhanced Hg(II) surface concentrations (25–40 pg m^{-3}) over the intermountain region of the western U.S., consistent with AMNet observations in Utah. During summer, observed and modeled Hg(II) concentrations reach a minimum in the eastern U.S. (Fig. 4.3b). This is due to multiple factors: larger losses of Hg(II) by wet deposition and reduction induced by increasing low cloud coverage and precipitation, as well as decrease in Hg(II) production following the seasonal cycle in Hg(0) concentrations (Amos et al., 2012; Zhang et al., 2012b). Overall, I find that 70% of monthly-mean modeled concentrations are within a factor of 2 of AMNet observations in the eastern U.S., with an NMB of -21%. If I assume that the reported RGM is underestimated by factor of 3 due to interferences (see Sect. 2.1), I find a model NMB of -57%.

Figs. 4A.1–4A.3 present further evaluation of the model with observations at other ground-based sites as well as with aircraft observations. The modeled Hg wet deposition fluxes and VWM concentrations are in reasonable agreement with the observations (NMB: 48–52%, FAC2: 64–78%), and show a high correlation (r = 0.86–0.93) (Fig. 4A.1a,b). This suggests that the model is able to capture patterns of Hg deposition observed at sites in different parts of the world. The comparison of the model with Hg(II) surface concentrations also shows moderate agreement (NMB: -9%, FAC2: 50%, r: 0.46) (Fig. 4A.2). The model is also able to broadly capture the increase in Hg(II) concentrations with altitude observed in aircraft measurements over Tullahoma, TN, U.S. (Fig. 4A.3a) and during the NOMADSS campaign (Fig. 4A.3b). The NMB at higher altitudes (>3 km for Tullahoma, TN and >4 km for NOMADSS) is between -29% and 14%, and a FAC2 of about 50%. The model is unable to capture the higher Hg(II) concentrations in the 1-3 km region that were observed during one flight of the NOMADSS campaign as previously discussed in Shah et al. (2016).

4.3 TAGGED SIMULATION RESULTS

4.3.1 *Global distribution of tagged Hg(II) tracers*

The annual zonal mean distribution of modeled Hg(II) concentrations is shown in Fig. 4.4a. Hg(II) concentrations increase from 10 pg m^{-3} near the surface to 1000 pg m^{-3} in the upper troposphere, and exhibit local maxima in the subtropical middle troposphere, within the descending Hadley branches. The chemical production rate of Hg(II) (via reactions R4.1–R4.3, Fig. 4.4b) increases by an order of magnitude between the lower and upper troposphere. This increase is driven by increasing Br concentrations coupled with colder temperatures (hence slower thermal decomposition of HgBr in R4.1) (Holmes et al., 2010). Regions of high Hg(II) production rates also occur near the surface in the Arctic due to springtime release of Br in bromine explosion

events (Holmes et al., 2010). The elevated Southern Ocean production rates are associated with high emissions of sea-salt aerosol, which are assumed to release bromine (Parrella et al., 2012). Note that the sharp gradients in Hg(II) production rates at 45°N and 45°S reflect the boundaries of the Br scaling in the model.

The lifetime of Hg(II) increases from less than 1 day in the lower troposphere to over 3 years in the tropical upper troposphere. Hg(II) in the lower troposphere is subject to dry deposition, and in-cloud reduction and scavenging by precipitation in the lower and middle troposphere. Thus, despite higher production rates, Hg(II) concentrations over the Arctic and the Southern Ocean are low. The long lifetimes of Hg(II) in the upper troposphere and in the descending branches of the Hadley circulation are due to infrequent occurrence of reduction within clouds and wet scavenging. As summarized in Table 4.1, I find that the tropospheric lifetime of Hg(II) decreases from 43 days for the STRAT tracer and 22 days for the UT tracer down to 0.6 days for the LT tracer. This is consistent with expectations, as most of the UT tracer, for example, resides in the upper troposphere, where deposition is slower.

The large production rates of Hg(II) in the upper and middle troposphere combined with a longer lifetime result in the large contributions of the UT and MT tracers to the tropospheric mass and deposition of Hg(II). Overall, the tropospheric burden of Hg(II) is dominated by Hg(II) produced in the UT (84%), with contribution of 8% from the stratosphere (STRAT) and the MT, and less than 1% from the LT and direct emissions (Table 4.1). The UT and MT tracers each contribute 35-40% of the Hg(II) burden in the lower troposphere (Table 4.1 and Fig. 4.4d and e). The contribution of the LT tracer increases to >50% near the surface over the Arctic and the Southern Ocean (Fig. 4.4f), where local production of Hg(II) in the polar and marine boundary layers is larger. I also find that most of the Hg(II) in the lowermost stratosphere is comprised of

the UT tracer (Fig. 4.4d), because Hg(0) is rapidly oxidized in the upper troposphere and is almost completely depleted before reaching the stratosphere, as shown by observations (Talbot et al., 2007; Lyman and Jaffe, 2012). The E-Hg(II) tracer accounts for 5% of the Hg(II) burden in the lower troposphere (Table 4.1), but its contribution increases to >10% over the northern mid-latitudes (Fig. 4.4h).

81% of the tropospheric Hg(II) production happens in the upper and middle troposphere (Table 4.1). Together, the UT and MT tracers account of 91% of global surface wet deposition (60% from UT and 31% from MT) and 52% of dry deposition (24% from UT and 28% from MT). Their higher contributions to wet deposition is because precipitation scavenging can directly remove these tracers from higher altitudes, while dry deposition requires the transport of these tracers to the planetary boundary layer.

Table 4.1: Tropospheric budgets of Hg(II) and individual tagged Hg(II) tracers.

	Total Hg(II)	Tagged Hg(II) tracers[a]				
		UT	MT	LT	STRAT	E-Hg(II)
Tropospheric mass of Hg(II)[b] [Mg]	618	517	48	4	48	1
Mass located in UT [Mg]	480	432	3	0	45	0
Mass located in MT [Mg]	118	79	36	0	3	0
Mass located in LT [Mg]	20	7	8	4	0	1
Hg(II) production[b] [Mg a^{-1}]	15,790	8,560	4,190	2,460	410	170
Hg(II) reduction [Mg a^{-1}]	9,740	5,750	2,390	1,260	290	50
Hg(II) wet deposition [Mg a^{-1}]	3,740	2,250	1,150	230	80	30
Hg(II) dry deposition [Mg a^{-1}]	2,310	570	640	970	40	90
Hg(II) tropospheric lifetime [days]	14	22	4.1	0.6	43	2.2

(a) Regions are defined as follows: UT (upper troposphere: 400hPa–tropopause), MT (middle troposphere: 750–400hPa), LT (lower troposphere: surface–750hPa), STRAT (stratosphere), E-Hg(II) (directly emitted anthropogenic Hg(II)).
(b) 1 Mg = 10^6 g, and 1 Mg a^{-1} = 10^6 g per year.

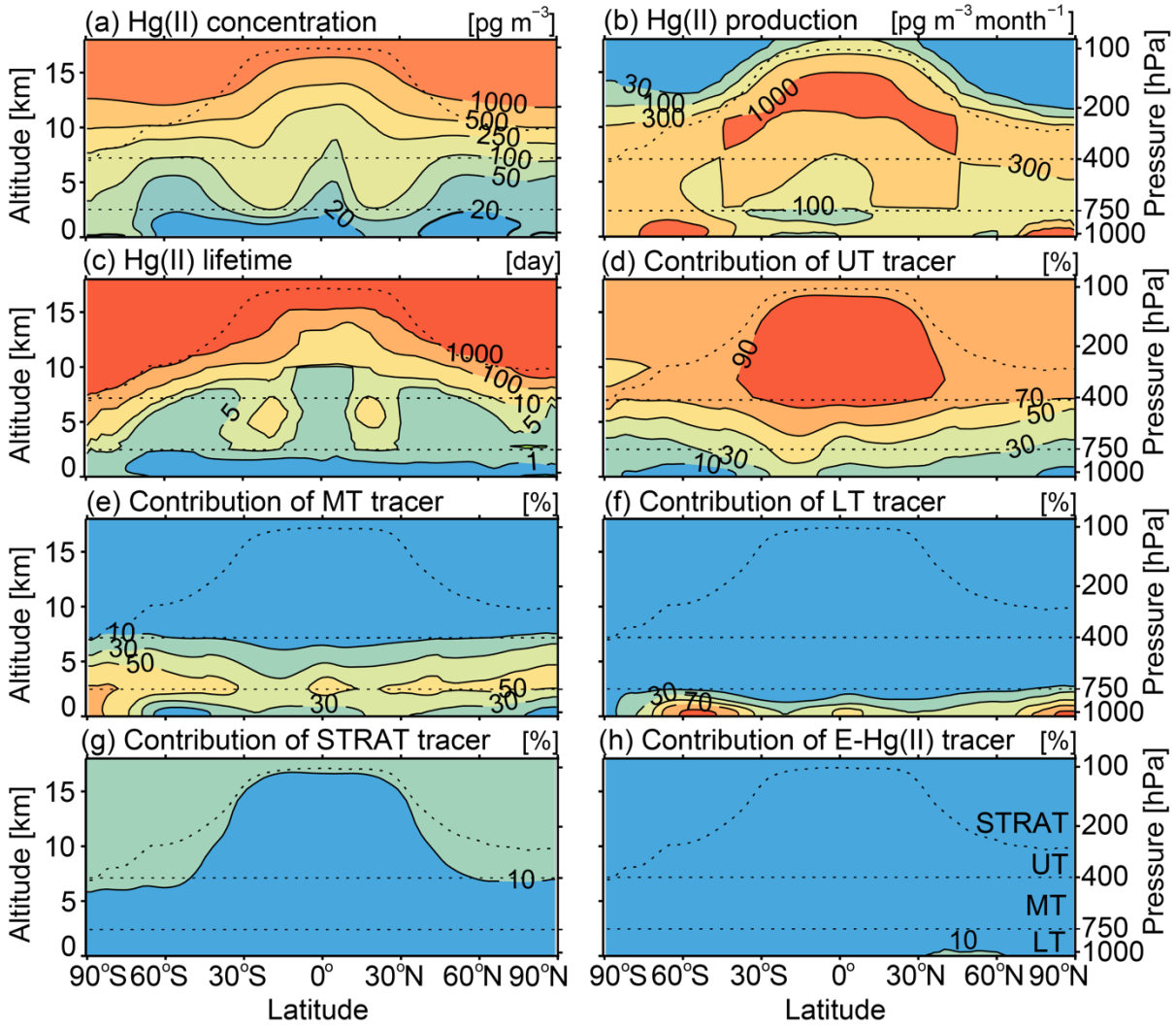

Figure 4.4: Modeled zonal mean Hg(II) distribution, production, and loss. Modeled zonal mean (a) Hg(II) concentrations (pg m^{-3}), (b) Hg(II) production rates (pg m^{-3} month^{-1}), and (c) lifetime (days) for 2013-2014. Panels (d-h) show the percent contributions of Hg(II) tagged tracers produced in the upper troposphere (UT), middle troposphere (MT), lower troposphere (LT), stratosphere (STRAT), and directly emitted (E-Hg(II)). Dotted lines indicate my boundaries for STRAT, UT, MT, and LT.

4.3.2 *Origin of Hg(II) in surface deposition and concentrations*

As shown in Fig. 4.5a, the highest surface Hg(II) concentrations (>50 pg m^{-3}) are simulated over high-elevation areas (e.g., western U.S., the Andes, and the Tibetan plateau), in polar regions, near emission sources (e.g., East Asia), and in dry subtropical areas (e.g., the Sahara Desert, southern Africa, and Australia). Modeled Hg(II) concentrations are generally low over the oceans because of fast removal by sea-salt aerosols. Together, the UT and MT tracers account for 63% of surface Hg(II) over the continents (Fig. 4.5e and 4.6b). Hg(II) over most of the oceans is predominantly from the LT tracer (Fig. 4.5e). In the subtropical anticyclones, free-tropospheric air is entrained in the marine boundary layer due to large-scale subsidence causing higher contributions from the MT. For western U.S., South America, Africa, and Australia, UT and MT each make a contribution of about 40% to surface Hg(II), whereas for the Pacific and the North Atlantic Oceans 57% of surface Hg(II) is from the LT tracer (Fig. 4.6b). The contribution of E-Hg(II) to surface Hg(II) concentrations is limited to regions with high anthropogenic emissions. I calculate that 27–69% of surface Hg(II) in eastern U.S., Europe, East and South Asia consists of E-Hg(II) (Fig. 4.6b). The contribution of E-Hg(II) is >80% in areas close to emission sources (Fig. 4.5e), and is likely to be higher within tens of kilometers of the sources. However, the near-source contribution of emitted Hg(II) cannot be estimated with my 2° latitude × 2.5° longitude global model.

The global distribution of the Hg(II) wet deposition flux (Fig. 4.5b) largely follows the spatial distribution of precipitation, with high wet deposition along the Intertropical Convergence Zone (ITCZ) and in the mid-latitude storm tracks. Globally, the UT tracer accounts for 60% of Hg(II) in wet deposition, but in some areas over South America, Africa, and Asia it exceeds 70% (Fig. 4.5f). The MT tracer makes up most of the remaining fraction of wet deposition, with a global

average contribution of 31% (Table 4.1). The contribution from the LT tracer is significant only at high latitudes, while the contribution from E-Hg(II) reaches values greater than 10% mainly over East Asia. The relative wet deposition contributions of the tagged Hg(II) tracers remain fairly uniform across the ten regions summarized in Fig. 4.6c.

Table 4.2: Contribution of tagged Hg(II) tracers to the tropospheric mass and total deposition of Hg(II) for the base case and the sensitivity simulations.

	Simulation	Tagged Hg(II) tracer contribution [%]				
		UT	MT	LT	STRAT	E-Hg(II)
Contribution to Hg(II) tropospheric mass [%]	Base	84	8	<1	8	<1
	Lower UT+MT Br[a]	71	7	1	21	<1
	O_3/OH oxidation[b]	61	18	4	17	<1
	Higher Hg(II) emissions[c]	84	8	<1	8	<1
Contribution to Hg(II) deposition [%]	Base	47	30	19	2	2
	Lower UT+MT Br[a]	43	21	27	6	3
	O_3/OH oxidation[b]	20	38	38	2	2
	Higher Hg(II) emissions[c]	49	28	17	2	4

(a) Simulation using the original GEOS-Chem Br concentrations instead of the 3 times Br concentrations in the base simulation,
(b) Simulation using O_3 and OH as the Hg(0) oxidants instead of Br as in the base simulation,
(c) Simulation using the default UNEP/AMAP Hg(0):Hg(II) emission speciation of 55%:45% instead of the 90%:10% speciation as in the base simulation.

The Hg(II) dry deposition flux (Fig. 4.5c) maximizes in the subtropical anticyclones, where subsidence provides a source of free-tropospheric Hg(II) to the planetary boundary layer. In addition, local maxima occur downwind of the emissions regions of the eastern US and East Asia, over high-elevation regions in western U.S. and the Himalayas, and over the Southern Ocean. In terms of the tagged tracers, their spatial contribution to dry deposition (Fig. 4.5g) is similar to their

contribution to surface Hg(II) concentrations (Fig. 4.5e). I find that 79–82% of the Hg(II) dry deposition over western U.S., South America, Africa, and Australia is from the UT and MT tracers. The E-Hg(II) tracer contributes 21–62% to dry deposition over eastern U.S., Europe and South and East Asia (Fig. 4.6d). Over the Pacific and North Atlantic Oceans, the UT, MT, and LT tracers each contribute about 30% to the dry deposition flux (Fig. 4.6d).

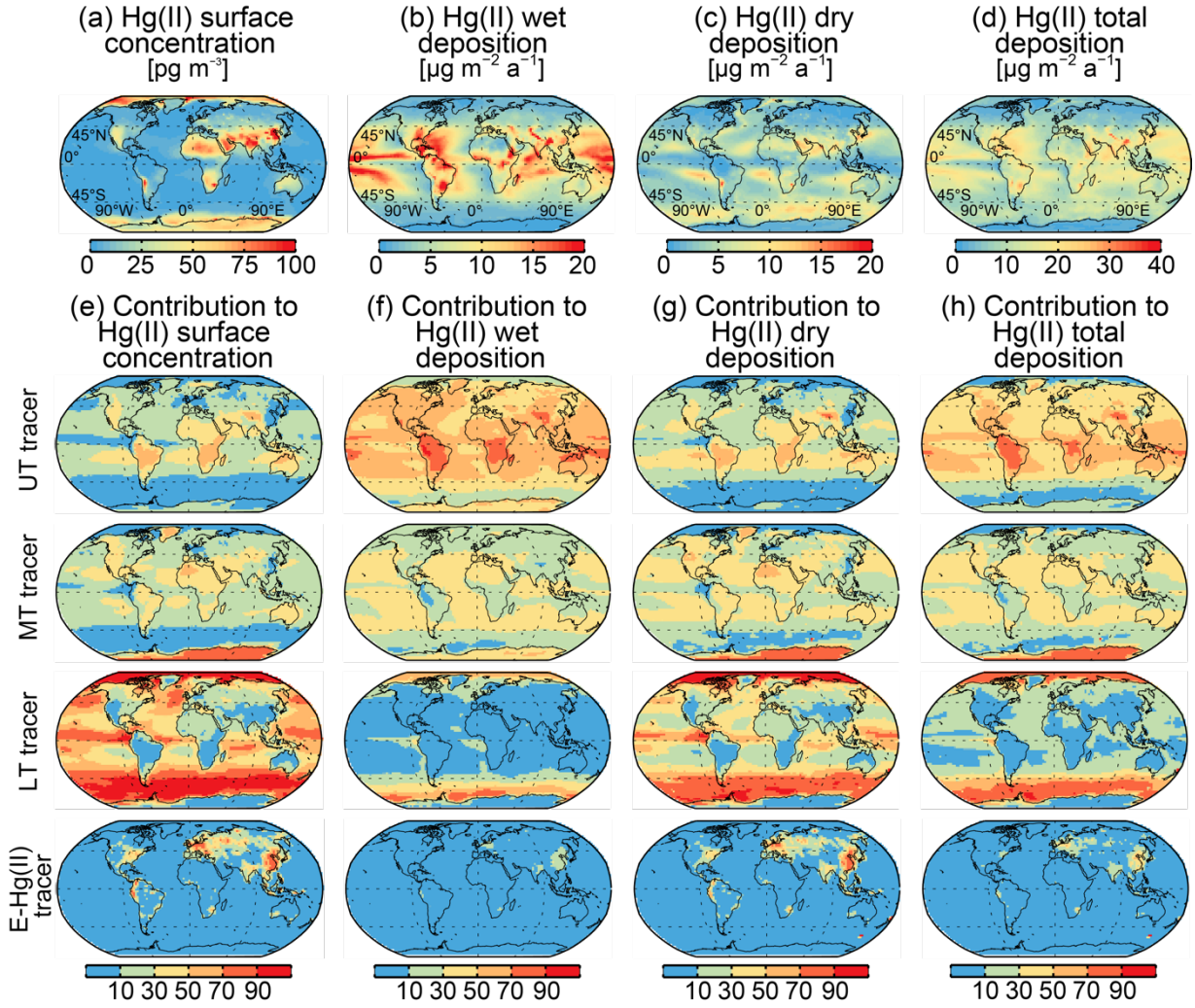

Figure 4.5:Simulated distribution of Hg(II) surface concentrations and deposition flux. (a) Annual-mean surface Hg(II) concentration, (b) wet deposition flux, (c) Hg(II) dry deposition flux, and (d) total (wet+dry) deposition flux simulated for 2013-2014. Contributions from tagged Hg(II) tracers to (e) surface Hg(II) concentrations, (f) wet deposition flux, (g) dry deposition flux, and (h) total deposition flux.

In Sect. 4.2.2.3 we saw that the model overestimated observed wet deposition of Hg(II) over southeast U.S. during winter and spring. As a result, my estimate of the contribution of UT and MT tracers is likely an overestimate for this region and season. From my model evaluation, I had also concluded that my free-tropospheric Hg(II) production was too slow over Europe and, possibly, other regions north of 45°N. This suggests an underestimate of the concentrations of modeled UT and MT tracers in these regions.

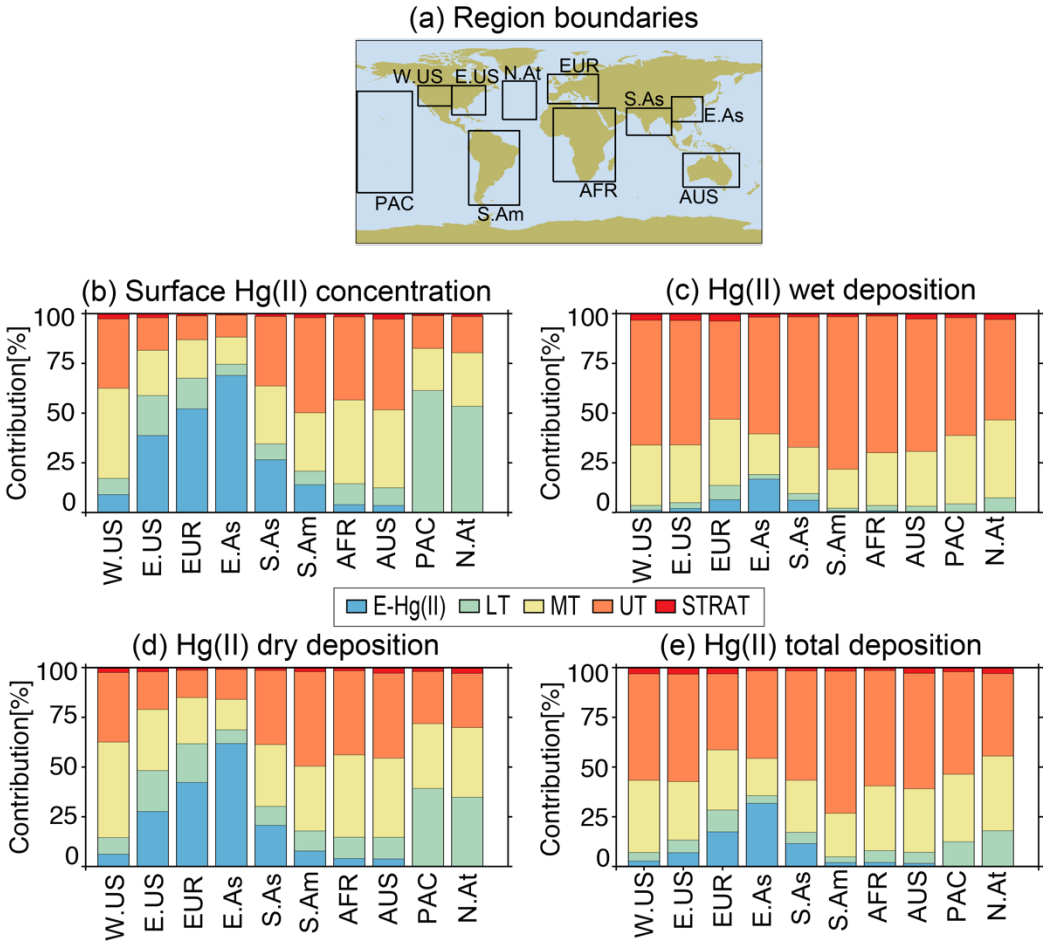

Figure 4.6: Regional contribution of tagged Hg(II) tracers. (a) Boundaries and names for regions used in panels b-e. Regional contributions of tagged Hg(II) tracers to (b) Hg(II) surface concentrations, (c) Hg(II) wet deposition, (d) Hg(II) dry deposition, (e) Hg(II) total (wet+dry) deposition. For continental regions the averages are calculated over land only.

My estimate that 92% of Hg(II) wet deposition and 73% of dry deposition over the U.S. is contributed by production in the upper and middle troposphere is qualitatively consistent with the estimates of Selin and Jacob (2008). They calculated that 59% of the Hg(II) wet deposited over the U.S. was scavenged above 1.5 km, and that 70% of the Hg(II) below 1.5 km was transported from elsewhere. For comparison, with my simulation I find that 85% of the Hg(II) wet deposited over the U.S. is scavenged above 1.5 km (note that to be consistent with Selin and Jacob (2008), we are comparing here the contribution of Hg(II) *present* above 1.5 km, and not the Hg(II) *produced* above 1.5 km). While Selin and Jacob (2008) also used the GEOS-Chem model, their simulation was based on Hg(0) oxidation by OH and O_3, while ours is based on oxidation by Br. In Sect. 3.3, we quantify the sensitivity of my results to the oxidation pathway assumed.

4.3.3 *Model sensitivity to oxidation chemistry and emission speciation*

We now assess the sensitivity of my results to my assumptions about mercury oxidation and Hg(0):Hg(II) partitioning in anthropogenic emissions. I perform three additional one-year (2013) sensitivity simulations with the following changes with respect to the base simulation: (i) use of the original GEOS-Chem Br concentrations instead of the 3 times Br concentrations in the base simulation, (ii) use of O_3 and OH as the Hg(0) oxidants (rate constants of Hall (1995) and Sommar et al. (2001)) instead of Br, and (iii) with the default UNEP/AMAP Hg(0):Hg(II) emission speciation of 55%:45% instead of the modified speciation. I summarize the results of these three sensitivity simulations relative to the base simulation in Table 4.2.

When I use the original GEOS-Chem Br concentration, the contribution of the UT and MT tracers to the tropospheric Hg(II) burden decreases to 78% (base: 92%), while the contribution to total deposition decreases to 64% (base: 77%, see Table 4.2). In the O_3 and OH oxidation simulation, I find that Hg(II) production shifts to lower altitudes, leading to an increase in the

contributions of the LT and MT tracers to tropospheric Hg(II) mass (base: 8%; O_3/OH: 22%) and deposition flux (base: 49%; O_3/OH: 76%). The change in the Hg(0):Hg(II) emission speciation results in a doubling of the contribution of E-Hg(II) tracer to total deposition, but the contribution of the UT and MT tracers to deposition remains nearly unchanged (Table 4.2). In all three sensitivity simulations, I find that the UT+MT tracers together contribute significantly to the tropospheric mass (78–90%) and the surface deposition flux (57–76%) of Hg(II), thus my overall conclusions remain robust.

4.4 ROLE OF THE SUBTROPICAL DRY REGIONS

In this section, I focus on the specific role of subtropical anticyclones as a global reservoir of Hg(II). The large-scale sinking motion in the subtropical anticyclones transports Hg(II) produced in the upper and middle troposphere downwards, and suppresses cloud formation and precipitation, thereby inhibiting Hg(II) loss of by reduction and wet deposition. The subtropical anticyclones, therefore, act as global reservoirs of Hg(II), as were presented in Shah et al. (2016). Here, we further quantify how much Hg(II) is transported from the subtropical anticyclones (dry-Hg(II) tracer) with a simulation where I artificially set to zero the Hg(II) present in the subtropical dry areas (defined as RH < 20% and latitude < 45°). Figure 4.7 shows the means and the anomaly of the contributions of dry-Hg(II) to surface Hg(II), 500 hPa Hg(II), and Hg(II) wet deposition for 2013-2016. The anomaly is defined here as the maximum deviation of the contribution of dry-Hg(II) for individual years from the 4-year mean. Areas at 500 hPa where the 2013-2016 monthly mean RH was less than 20% for minimum of four months out of twelve are shown in Fig. 4.7c and d. Based on this definition, I find that the dry areas contain 8% of the tropospheric mass of air.

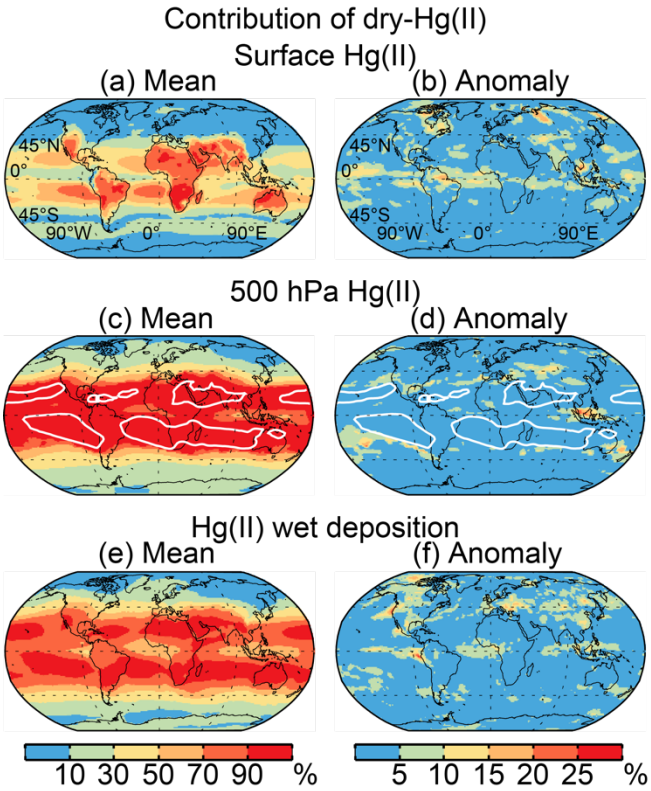

Figure 4.7: Contribution of dry-Hg(II) to global Hg(II) concentrations and deposition. Mean and anomaly (maximum deviation from the mean) of the contributions of dry-Hg(II) to (a,b) surface Hg(II) concentrations, (c,d) 500 hPa Hg(II) concentrations, and (e,f) Hg(II) wet deposition flux for 2013-2016. The white contours in (c,d) show the boundaries at 500 hPa for areas with RH less than 20% for a minimum of four months of the year.

We see from Fig. 4.7a that dry-Hg(II) exerts a disproportionate influence on surface Hg(II) concentrations between 40°S and 40°N, where its contribution is 45 ± 25%. The influence is higher over the continents (64%) than over the oceans, where the local production of Hg(II) in the marine boundary layer is larger. More than 80% of the surface Hg(II) over dry areas in Africa, the Middle East, and Australia, and in the high-elevation regions of western U.S., Tibetan Plateau, and South America consists of dry-Hg(II). The influence of dry-Hg(II) on surface Hg(II) concentrations is <20% in anthropogenic Hg(II) source regions such as eastern U.S. and East Asia, and in regions that experience deep convection such as the ITCZ in the Pacific, Atlantic, and Indian Oceans, South Asia, the Maritime Continent. The inter-annual variation of the dry-Hg(II) contribution is

generally less than 5% (Fig. 4.7b). Hg(II) can also be transported to the surface from higher altitudes in transient large-scale eddies in the mid-latitudes. Over Canada and Russia, for example, the UT+MT tracer contribution to surface Hg(II) is 50%, but the influence of dry-Hg(II) is <10% (Figs. 4.5e and 4.7a).

90% of the mass of Hg(II) present at 500 hPa in the 40°S–40°N band is made up of dry-Hg(II) (Fig. 4.7c), with little inter-annual variation (Fig. 4.7d). The contribution of dry-Hg(II) extends far beyond the boundaries of the dry areas, suggesting that these regions act as global suppliers of Hg(II). My model simulation suggests that 74% of the Hg(II) present at 500 hPa over the continental U.S. is transported from the dry subsidence band over the Pacific Ocean. The contribution of dry-Hg(II) decreases north of 40°N, but is still larger than 25% over most parts of Canada, Europe, and northern Asia. The contribution of dry-Hg(II) to Hg(II) wet deposition falls in-between the contributions of dry-Hg(II) to the surface and 500 hPa concentrations (Fig. 4.7e), as most precipitation scavenging of Hg(II) occurs between the surface and 500 hPa. The inter-annual variability reaches 10-20% over the western and SE U.S., Eastern Europe, and Eastern Asia (Fig. 4.7f). In areas of the globe with large deposition fluxes (the ITCZ and the mid-latitude storm tracks) at least 50% of the deposition consists of dry-Hg(II). Globally, dry-Hg(II) accounts for 78% to the tropospheric Hg(II) mass, and 61% of the total Hg(II) deposition (wet: 69% and dry: 48%).

During the 2013 NOMADSS aircraft campaign, high Hg(II) concentrations were observed and simulated above 5 km altitude (observations: 189 ± 103 pg m^{-3}; model: 165 ± 104 pg m^{-3}) (Shah et al., 2016). Back trajectory calculations indicated that these air masses were transported from even higher altitudes within the Pacific and the Atlantic anticyclones (Gratz et al., 2015; Shah et al., 2016). I sample the GEOS-Chem model along the NOMADSS flight tracks to determine the

contribution of dry-Hg(II) to the Hg(II) concentrations measured during the campaign. I find that dry-Hg(II) accounted for 75% of Hg(II) when observed Hg(II) concentrations exceeded 250 pg m^{-3}(Fig. 4.8). The dry-Hg(II) contribution decreased for observations with lower Hg(II) concentrations: 58% for 200–250 pg m^{-3} and 10–20% for concentrations below 200 pg m^{-3}. The association between NOMADSS observations of high Hg(II) concentrations and higher contribution of dry-Hg(II) adds support to my finding that the subsidence regions act as a large source of Hg(II) present and deposited over the U.S.

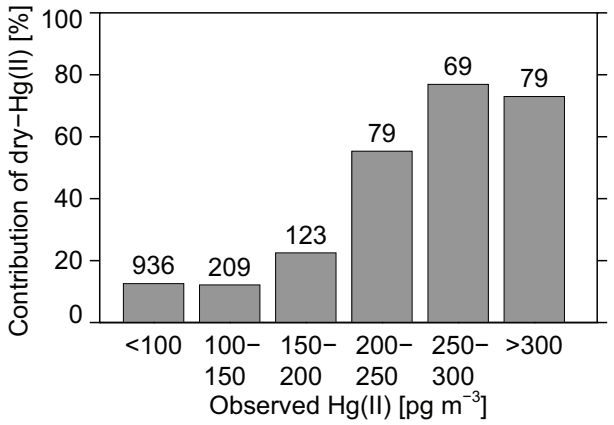

Figure 4.8: Modeled contribution of the dry-Hg(II) tracer to observed Hg(II) concentrations during the NOMADSS aircraft campaign. The number of 2.5-minute observations points in each concentration bin is shown on top of the bars.

My finding is consistent with ground-based Hg(II) observations in western U.S., an area heavily influenced (>60%) by Hg(II) present in the dry subtropical regions (Fig. 4.7). Weiss-Penzias et al. (2009) reported that occurrence of higher (~50 pg m^{-3}) RGM concentrations in Nevada during June–August were associated with subsiding air in the anticyclone located over the Pacific Ocean, and Huang and Gustin (2012) found higher than mean Hg(II) deposition in Nevada under similar patterns of air transport. Timonen et al. (2013) showed that the highest

concentrations of RGM (700 pg m^{-3}) observed at the Mt. Bachelor Observatory in Oregon (2.7 km altitude) corresponded to air masses transported from the subtropical Pacific Ocean.

4.5 TAGGED TRACER CONTRIBUTIONS AT MDN AND AMNET SITES

My tagged simulation show that the upper and middle troposphere are the predominant regions of production of Hg(II). Thus, areas where wet deposition is strongly influenced by Hg(II) produced in these regions can be expected to have higher wet deposition flux of Hg(II). We now examine whether such an enhancement in Hg wet deposition flux is indeed observed at MDN sites. Figure 4.9 shows the relationship between observed MDN annual Hg wet deposition fluxes to precipitation and modeled contribution of the UT and MT tracers to the wet deposition flux at the site locations. As expected, we see that Hg wet deposition fluxes increase with increasing precipitation (e.g. Prestbo and Gay, 2009; Selin and Jacob, 2008). In addition, I find that the Hg wet deposition fluxes increase with increasing contribution of the UT and MT tracers to the wet deposition flux. Using multiple linear regression, I derive the following relationship between the observed Hg flux [μg m^{-2} a^{-1}], precipitation amount [mm a^{-1}], and contribution of UT+MT [%]:

$$\text{Flux} = a_1 \times \text{Precipitation} + a_2 \times \text{UT+MT contribution} + a_3 \quad (4.4)$$

Where, $a_1 = 0.004$ μg L^{-1}, $a_2 = 0.8 \times 10^{-2}$ μg $m^{-2}a^{-1}$, and $a_3 = -68$. The regression parameters are statistically significant ($p<0.001$, 2-sided t-test, N=80), implying that both higher precipitation amounts and higher contribution of UT+MT tracers to wet deposition result in higher Hg flux. Precipitation amounts and the contribution of UT and MT together explain 55% of the spatial variation in the observed Hg flux, while individually they explain 25% and 42% of the spatial variation, respectively. This is consistent with previous studies that have shown higher Hg wet deposition flux in convective thunderstorms that can scavenge Hg(II) present at high altitudes (Guentzel et al., 2001; Shanley et al., 2015; Holmes et al., 2016; Kaulfus et al., 2017).

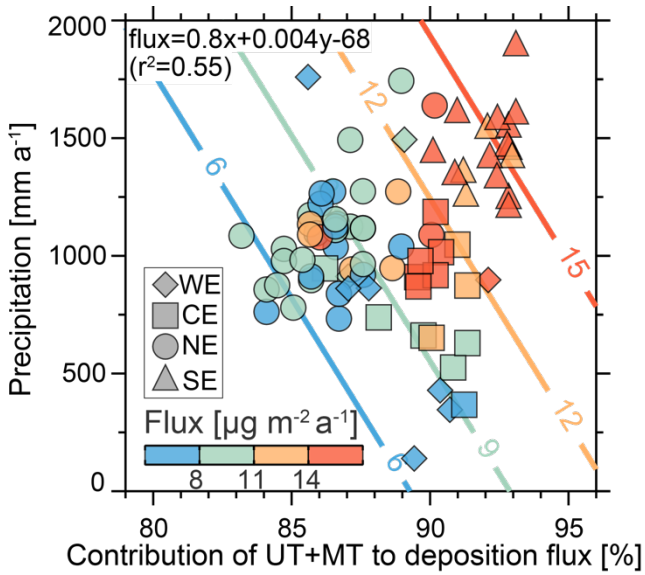

Figure 4.9: Relationship of observed MDN Hg wet deposition flux to observed precipitation and modeled contribution of UT and MT tracers to the Hg(II) wet deposition flux. The symbols identify MDN sites for each region in Fig. 4.1 (WE: diamonds, CE: squares, NE: circles, and SE: triangles), with color-coding according to observed wet deposition flux. Also shown is the multiple linear regression equation relating flux to the contribution of UT+MT tracers (x) and the observed precipitation (y), and the square of the correlation coefficient (r^2). Colored contours correspond to deposition fluxes calculated with the regression equation.

AMNet sites in the eastern U.S. are close to regional Hg(II) emission sources, and are thus more likely to be influenced by Hg(II) directly emitted rather than by Hg(II) produced aloft. Figure 4.10 shows that the 2009–2012 median Hg(II) concentrations observed at the AMNet sites in the eastern U.S. are higher at sites where the contribution of E-Hg(II) tracer is higher. For example, the surface Hg(II) concentrations at sites NY06, WV99, and MD08 are ~10 pg m^{-3}, with 60–65% of the Hg(II) due to the E-Hg(II) tracer. On the other hand, at the remote site NS01, Hg(II) concentration are 3 pg m^{-3} and the contribution of E-Hg(II) tracer is less than 10%. I find that spatial variation in the contribution of the E-Hg(II) tracer explains 27% of the variation in observed surface Hg(II) concentrations at the AMNet sites (excluding the outlier NY95) in the eastern U.S. (Fig. 4.10b). A statistically significant linear relationship (p=0.018, 2-sided t-test, N=20, NY95

excluded) between Hg(II) concentrations and the contribution of the E-Hg(II) tracer is obtained from ordinary least squares regression. This suggests that although Hg(II) produced in the free troposphere makes up a large part of Hg(II) in the planetary boundary layer, spatial variations in Hg(II) concentrations in areas close to Hg(II) sources reflect variations in the amount of directly emitted Hg(II).

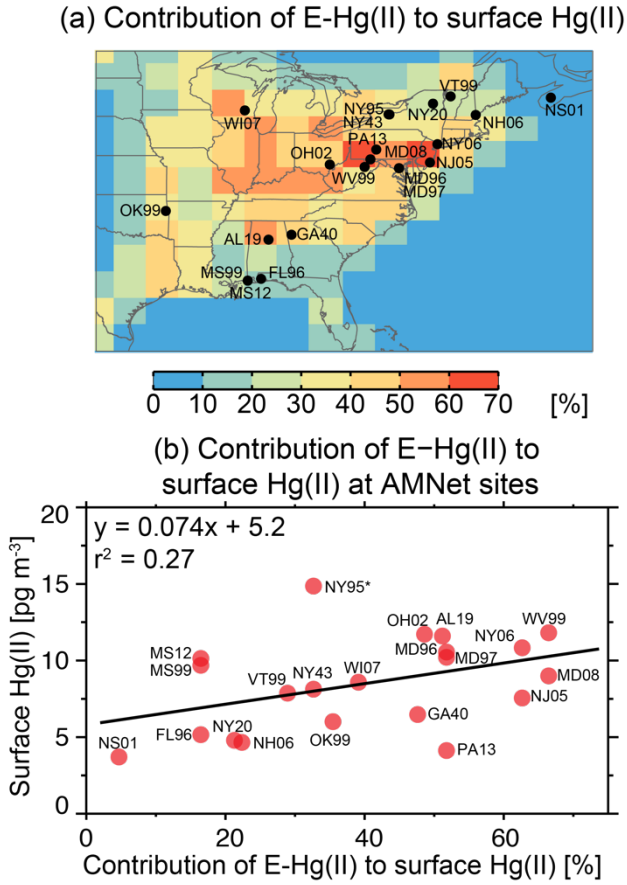

Figure 4.10: Influence of E-Hg(II) tracer at the surface over the eastern U.S. (a) Simulated surface concentration of Hg(II) for 2013–2014. Also shown are the locations of the AMNet stations mapped to the model grid. (b) Relationship between the 2009–2012 median Hg(II) concentrations observed at the AMNet sites and the contribution of E-Hg(II) tracer to surface Hg(II) concentrations. The black line is the best-fit line from ordinary least squares regression. The text displays the regression equation and the square of the correlation coefficient (r^2). The outlier NY95 is excluded from the regression calculation.

4.6 IMPLICATIONS

My modeling study indicates that even in areas with large anthropogenic sources of Hg(II) most of the mercury wet deposition flux consists of Hg(II) produced in the upper and middle troposphere. This implies that regional decreases in anthropogenic Hg emissions do not lead to a proportional regional decrease in wet deposition. Indeed, numerous studies have demonstrated the importance of intercontinental transport to mercury wet deposition (Pirrone and Keating, 2010). For example, Jaeglé et al. (2009) found that a 20% decrease in regional anthropogenic mercury emissions in the GEOS-Chem model leads to between 3% (North America) and 12% (East Asia) decrease in mercury deposition. Moreover, observed long-term temporal trends in mercury wet deposition reflect trends in the global emissions of Hg(0) (Zhang et al., 2016; Weiss-Penzias et al., 2016; Zhang and Jaeglé, 2013). My study shows that oxidation of Hg(0) in the upper and middle troposphere is the key to linking global emissions to deposition of mercury.

I also find that a large fraction of the upper and middle tropospheric Hg(II) over the U.S. is transported from the subsiding subtropical anticyclone over the Pacific Ocean. Thus, we expect that variability in the location of the Pacific anticyclone, the synoptic wind patterns transporting Hg(II) to the U.S., the heights of the precipitating clouds, in addition to the amount and type of precipitation can affect Hg wet deposition flux over a particular area. These meteorological conditions vary in response to natural variability associated with multiyear phenomena, such as the El Niño-La Niña cycle (Gratz et al., 2009), and can confound the interpretation of spatial and temporal trends in wet deposition at MDN sites.

My results support the idea of a global pool of Hg(II) in the free troposphere. I find that this global pool of Hg(II) is concentrated in the upper troposphere (above 7 km) and extends to lower altitudes in the subsidence areas of the subtropical anticyclones. These regions of the

atmosphere are where most of the production of Hg(II) takes place, and where the lifetime of Hg(II) against reduction and deposition is the longest, making them ideal target regions for future aircraft-based campaigns to understand the chemistry of mercury in the atmosphere.

4.7 CONCLUSIONS

I have added to the GEOS-Chem mercury model a Hg(II) tagging method following regions where Hg(II) is produced. I have performed a two-year simulation (2013–2014) with the tagged Hg(II) tracers, and have found that Hg(II) produced in the upper and middle troposphere constitutes 91% of the tropospheric mass of Hg(II), 91% of the annual Hg(II) wet deposition flux, and 52% of the annual Hg(II) dry deposition flux. The disproportionately high contribution of the Hg(II) produced in these regions is the result of higher production of Hg(II) in the upper and middle troposphere combined with a longer lifetime of Hg(II) and the large-scale subsidence of Hg(II) in the troposphere. Hg(II) produced in the upper and middle troposphere contributes 63% to surface Hg(II) over the continents, and 74–82% over western U.S, South America, Africa, and Australia. Over the oceans, however, surface Hg(II) is formed locally in the marine boundary layer because of Br released from sea-salt aerosols. Directly emitted anthropogenic Hg(II) makes up a significant fraction (27–69%) of surface Hg(II) concentrations near source regions in eastern U.S., Europe and South and East Asia. However, the wet deposition flux in these regions is largely (~90%) the result of Hg(II) produced in the upper and middle troposphere. The contribution of directly emitted Hg(II) can be higher within tens of kilometers of a source, but cannot be quantified by my coarse-resolution global model. We examined the sensitivity of my results by performing additional simulations with lower Br concentrations, different oxidants (O_3 and OH), and different Hg(0):Hg(II) anthropogenic emission speciation. In these simulations, too, I found that Hg(II)

produced in the upper and middle troposphere together contribute significantly to the tropospheric Hg(II) mass (78–90%) and the global Hg(II) surface deposition flux (57–76%).

I examined the consistency of my modeling results with measurements at the MDN, EMEP, and AMNet sites. I found reasonable agreement between the modeled and observed Hg wet deposition flux at the MDN sites (NMB: -7 to +20%, FAC2: 66 to 88%), and surface Hg(II) concentration at AMNet sites in the eastern U.S. (NMB: -21%, FAC2: 70%), but poorer agreement for Hg wet deposition flux at EMEP observations (NMB: -46%, FAC2: 55%). I also found that the Hg wet deposition flux at the MDN sites increases with increase in precipitation and the contribution of Hg(II) produced in the upper and middle troposphere. Together, they explain 55% of the spatial variation in the wet deposition flux across the MDN network. For AMNet sites in the eastern U.S., I find that 27% of the spatial variation is explained by the contribution of emitted Hg(II) to surface Hg(II) concentrations.

I quantified the role of Hg(II) in dry subtropical anticyclones and found it exerts a strong influence on Hg(II) concentrations at the surface (44% contribution) and 500 hPa (90% contribution) between 40°S and 40°N. Globally, dry-Hg(II) accounts for 78% to the tropospheric Hg(II) mass, and 61% of the total Hg(II) deposition. About >60% of the surface Hg(II) over dry areas, such as the western U.S., is transported from these subtropical regions, while 74% of Hg(II) at 500 hPa over the continental U.S. originated in the subtropical anticyclones. I also found that 75% of the observations with Hg(II) concentrations greater than 250 pg m^{-3} observed during the NOMADSS aircraft campaign were transported from the subsidence regions, compared to only 10% for samples with Hg(II) concentrations less than 100 pg m^{-3}. My results highlight the importance of the subtropical anticyclones as the primary conduits for the production and export of Hg(II) in the global atmosphere.

4.8 APPENDIX: ADDITIONAL TABLES AND FIGURES FOR CHAPTER 4

Table 4A.1: List of stations with observations of Hg wet deposition used in this study

Site ID	Site Name	Latitude	Longitude	Elevation (m.a.s.l.)	Measurement period	Network/ Region
CO96	Molas Pass	37.75	-107.69	3248	2013-2014	MDN[a]
FL11	Everglades National Park-Research Center	25.39	-80.68	2	2013-2014	MDN
WA18	Seattle/NOAA	47.68	-122.26	11	2013-2014	MDN
TX21	Longview	32.38	-94.71	103	2013-2014	MDN
VT99	Underhill	44.53	-72.87	399	2013-2014	MDN
VA28	Shenandoah National	38.52	-78.43	1072	2013-2014	MDN
WI36	Trout Lake	46.05	-89.65	509	2013-2014	MDN
WI99	Lake Geneva	42.58	-88.50	288	2013-2014	MDN
PA29	Kane Experimental Forest	41.60	-78.77	618	2013-2014	MDN
PA42	Leading Ridge	40.66	-77.94	287	2013-2014	MDN
PA72	Milford	41.33	-74.82	212	2013-2014	MDN
TN11	Great Smoky Mountains	35.66	-83.59	640	2013-2014	MDN
MN18	Fernberg	47.95	-91.50	524	2013-2014	MDN
ME02	Bridgton	44.11	-70.73	222	2013-2014	MDN
ME96	Casco Bay-Wolfe's Neck	43.83	-70.06	15	2013-2014	MDN
NC08	Waccamaw State Park	34.26	-78.48	10	2013-2014	MDN
PA13	Allegheny Portage Historic	40.46	-78.56	739	2013-2014	MDN
PA90	Hills Creek State Park	41.80	-77.19	476	2013-2014	MDN
SC19	Congaree Swamp	33.81	-80.78	34	2013-2014	MDN
IL11	Bondville	40.05	-88.37	212	2013-2014	MDN
FL34	Everglades Nutrient	26.66	-80.40	10	2013-2014	MDN
FL05	Chassahowitzka National Wildlife Refuge	28.75	-82.56	3	2013-2014	MDN
GA09	Okefenokee National Wildlife Refuge	30.74	-82.13	45	2013-2014	MDN
PA00	Arendtsville	39.92	-77.31	269	2013-2014	MDN
KS32	Lake Scott State Park	38.67	-100.92	863	2013-2014	MDN
ME98	Acadia National Park-McFarland Hill	44.38	-68.26	150	2013-2014	MDN
ME00	Caribou	46.87	-68.01	191	2013-2014	MDN
ME09	Greenville Station	45.49	-69.66	322	2013-2014	MDN
MN16	Marcell Experimental Forest	47.53	-93.47	431	2013-2014	MDN

Table 4A.1 continued

Site ID	Site Name	Latitude	Longitude	Elevation (m.a.s.l.)	Measurement period	Network/ Region
MN23	Camp Ripley	46.25	-94.50	410	2013-2014	MDN
MN27	Lamberton	44.24	-95.30	367	2013-2014	MDN
MO03	Ashland Wildlife Area	38.75	-92.20	257	2013-2014	MDN
MT05	Glacier National Park-Fire Weather Station	48.51	-114.00	964	2013-2014	MDN
NE15	Mead	41.15	-96.49	352	2013-2014	MDN
NY20	Huntington Wildlife	43.97	-74.22	500	2013-2014	MDN
NY68	Biscuit Brook	41.99	-74.50	634	2013-2014	MDN
PA37	Waynesburg	39.82	-80.29	452	2013-2014	MDN
MI48	Seney National Wildlife Refuge-Headquarters	46.29	-85.95	220	2013-2014	MDN
SC05	Cape Romain National	32.94	-79.66	1	2013-2014	MDN
SC03	Savannah River	33.25	-81.65	90	2013-2014	MDN
PA60	Valley Forge	40.12	-75.88	46	2013-2014	MDN
PA30	Erie	42.16	-80.11	177	2013-2014	MDN
AL03	Centreville	32.90	-87.25	135	2013-2014	MDN
GA40	Yorkville	33.93	-85.05	395	2013-2014	MDN
MO46	Mingo National Wildlife Refuge	36.97	-90.14	105	2013-2014	MDN
KY10	Mammoth Cave National Park	37.13	-86.15	236	2013-2014	MDN
MS22	Oak Grove	30.98	-88.93	100	2013-2014	MDN
WI31	Devil's Lake	43.44	-89.68	389	2013-2014	MDN
PA47	Millersville	39.99	-76.39	84	2013-2014	MDN
GA33	Sapelo Island	31.40	-81.28	3	2013-2014	MDN
OK99	Stilwell	35.75	-94.67	299	2013-2014	MDN
NV02	Lesperance Ranch	41.50	-117.50	1388	2013-2014	MDN
MD99	Beltsville	39.03	-76.82	46	2013-2014	MDN
MD08	Piney Reservoir	39.71	-79.01	769	2013-2014	MDN
NJ30	New Brunswick	40.47	-74.42	21	2013-2014	MDN
ON07	Egbert	44.23	-79.79	196	2013-2014	MDN
WI10	Potawatomi	45.56	-88.81	570	2013-2014	MDN
WA03	Makah National Fish	48.29	-124.65	6	2013-2014	MDN
CA94	Converse Flats	34.19	-116.91	1724	2013-2014	MDN
CA20	Yurok Tribe-Requa	41.56	-124.09	110	2013-2014	MDN
OK01	McGee Creek	34.32	-95.89	195	2013-2014	MDN
OK31	Copan	36.91	-95.88	255	2013-2014	MDN
SD18	Eagle Butte	44.99	-101.24	742	2013-2014	MDN
MD00	Smithsonian	38.89	-76.56	20	2013-2014	MDN
FL97	Everglades-Western Broward County	26.17	-80.82	4	2013-2014	MDN

Table 4A.1 continued

Site ID	Site Name	Latitude	Longitude	Elevation (m.a.s.l.)	Measurement period	Network/ Region
UT97	Salt Lake City	40.71	-111.96	1297	2013-2014	MDN
OK04	Lake Murray	34.10	-97.07	245	2013-2014	MDN
PA52	Little Pine State Park	41.36	-77.36	228	2013-2014	MDN
KS03	Reserve	39.98	-95.57	265	2013-2014	MDN
KS24	Glen Elder State Park	39.51	-98.34	456	2013-2014	MDN
KS99	Cimarron National Grassland	37.13	-101.82	1021	2013-2014	MDN
OK06	Wichita Mountains	34.73	-98.71	492	2013-2014	MDN
KS04	West Mineral	37.27	-94.94	274	2013-2014	MDN
NY43	Rochester	43.15	-77.55	136	2013-2014	MDN
NY06	Bronx	40.87	-73.88	68	2013-2014	MDN
MN98	Blaine	45.14	-93.22	275	2013-2014	MDN
MS12	Grand Bay NERR	30.43	-88.43	2	2013-2014	MDN
PA21	Goddard State Park	41.43	-80.15	385	2013-2014	MDN
FL96	Pensacola	30.55	-87.38	45	2013-2014	MDN
AL19	Birmingham	33.55	-86.81	200	2013-2014	MDN
DE0008R	Schmücke	50.65	10.77	937	2013-2014	EMEP[b]
FI0036R	Pallas (Matorova)	68.00	24.24	340	2013-2014	EMEP
GB0036R	Harwell	51.57	-1.32	137	2013-2014	EMEP
GB0048R	Auchencorth Moss	55.79	-3.24	260	2013-2014	EMEP
NO0001R	Birkenes	58.38	8.25	190	2013-2014	EMEP
SE0005R	Bredkälen	63.85	15.33	404	2013-2014	EMEP
SE0011R	Vavihill	56.02	13.15	175	2013-2014	EMEP
SE0014R	Råö	57.39	11.91	5	2013-2014	EMEP
NYA	Ny-Ålesund	78.90	11.88	12	2013-2014	GMOS[c]
MHE	Mace Head	53.33	-9.91	5	2013	GMOS
ISK	Iskrba	45.56	14.86	520	2013-2014	GMOS
SIS	Sisal	21.16	-90.05	7	2013-2014	GMOS
AMS	Amsterdam Island	-37.80	77.55	3	2013-2014	GMOS
CGR	Cape Grim	-40.68	144.69	94	2013-2014	GMOS
MCB	Mt. Changbai	42.41	128.11	736	2011-2014	China[d]
MDM	Mt. Damei	29.63	121.57	550	2012-2014	China
MLG	Mt. Leigong	26.39	108.20	2176	2008-2009	China
MAL	Mt. Ailao	24.53	101.11	2450	2011-2014	China
MWA	Mt. Waliguan	36.29	100.90	3816	2012-2014	China
BYB	Bayinbuluk	42.89	83.72	2500	2013-2014	China
PEN	Pengjiayu	25.63	122.07	102	2009	Taiwan[e]
PR20	El Verde	18.32	-65.82	380	2015	MDN[a]

(a) http://nadp.sws.uiuc.edu/mdn/; (b) http://www.nilu.no/projects/ccc/index.html
(c) Sprovieri et al. (2017); (d) Fu et al. (2016b)
(e) Sheu and Lin (2013)

Table 4A.2: List of ground stations with observations of Hg(II) surface concentrations used in this study.

Site ID	Site Name	Latitude	Longitude	Elevation (m.a.s.l.)	Measurement period	Network/ Region
AL19	Birmingham	33.55	-86.81	177	2009-2012	AMNet[a]
CA48	Elkhorn Slough	36.81	-121.78	10	2010-2011	AMNet
FL96	Pensacola	30.55	-87.38	44	2009-2012	AMNet
GA40	Yorkville	33.93	-85.05	394	2009-2012	AMNet
MD08	Piney Reservoir	39.71	-79.01	761	2009-2012	AMNet
MD96	Beltsville_B	39.03	-76.82	47	2009-2012	AMNet
MD97	Beltsville	39.03	-76.82	47	2009-2012	AMNet
MS12	Grand Bay NERR	30.41	-88.40	1	2009-2012	AMNet
MS99	Grand Bay NERR_B	30.41	-88.40	1	2009-2012	AMNet
NH06	Thompson Farm	43.11	-70.95	25	2009-2011	AMNet
NJ05	Brigantine	39.46	-74.45	8	2009-2012	AMNet
NS01	Kejimkujik	44.43	-65.20	158	2009-2012	AMNet
NY06	New York City	40.87	-73.88	26	2009-2012	AMNet
NY20	Huntington Wildlife Forest	43.97	-74.22	502	2009-2012	AMNet
NY43	Rochester	43.15	-77.62	154	2009	AMNet
NY95	Rochester_B	43.15	-77.55	154	2009-2012	AMNet
OH02	Athens	39.31	-82.12	274	2009-2012	AMNet
OK99	Stilwell	35.75	-94.67	300	2009-2012	AMNet
PA13	Allegheny Portage	40.46	-78.56	739	2009-2012	AMNet
UT96	Antelope Island	41.09	-112.12	1285	2009-2011	AMNet
UT97	Salt Lake City	40.71	-111.96	1099	2009-2012	AMNet
VT99	Underhill	44.53	-72.87	397	2009-2012	AMNet
WI07	Horicon	43.46	-88.62	272	2009-2012	AMNet
WV99	Canaan Valley Institute	39.12	-79.45	985	2009-2012	AMNet
AMS	Amsterdam Island	-37.80	77.55	70	2012-13	GMOS[b]
RAO	Råö	57.39	11.91	7	2012-15	GMOS[c]
LON	Longobucco	39.39	16.61	1379	2013	GMOS[d]
MAN	Manaus	-2.89	-59.97	110	2013	GMOS[d]
WAL	Waldhof	52.80	10.76	74	2009-2011	Germany[e]
MCH	Mt. Changbai	42.40	128.11	740	2013-2014	China[f]
MWA	Mt. Waliguan	36.29	100.90	3816	2007-2008	China
MAL	Mt. Ailao	24.53	101.02	2450	2011-2012	China
SLA	Shangri-La	28.02	99.73	3580	2009-2010	China
MYU	Miyun	40.48	116.76	220	2008-2009	China
MDA	Mt. Damei	29.63	121.57	550	2011-2013	China
MGO	Mt. Gongga	29.65	102.12	1640	2005-2007	China
LABS	Lulin Atmospheric Background Station	23.51	120.92	2862	2006-2007	Taiwan[g]
ALE	Alert	82.49	-62.34	210	2009-2011	Canada[h]

(a) http://nadp.sws.uiuc.edu/amn/; (b) Angot et al. (2014); (c) Wängberg et al. (2016)
(d) Travnikov et al. (2017); (e) Weigelt et al. (2013); (f) Fu et al. (2015); (g) Sheu et al. (2010)

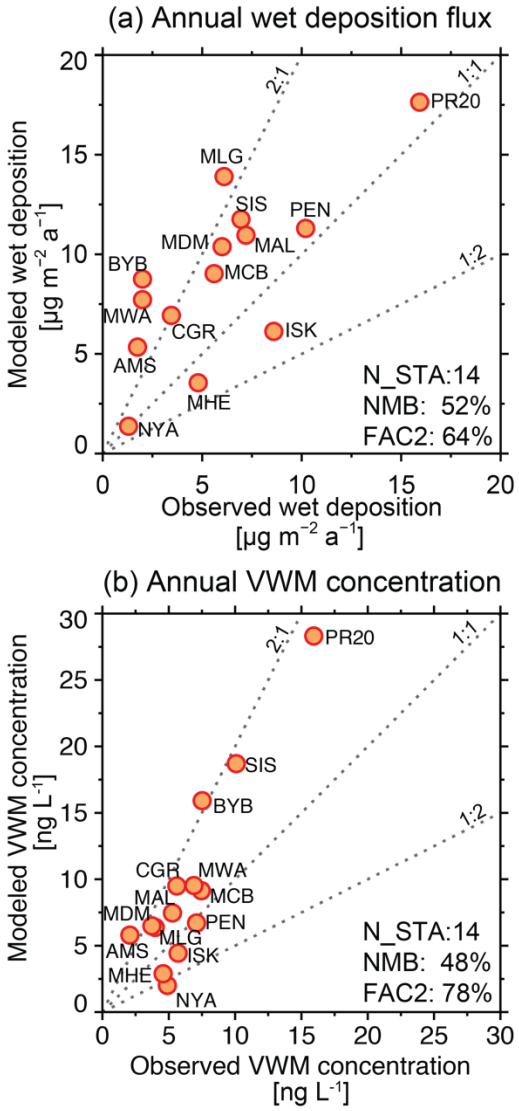

Figure 4A.1: Simulated and observed Hg wet deposition at worldwide sites. (a) Simulated and observed Hg wet deposition flux for GMOS and other stations listed in Table 4A.1. (b) Simulated and observed annual volume-weighted mean (VWM) Hg concentration for GMOS and other stations listed in Table 4A.1. The number of stations (N_STA), normalized mean bias (NMB; $\mathrm{NMB} = \sum_i (M_i - O_i) \Big/ \sum_i O_i \times 100\%$), and FAC2 (percentage of points where $0.5 \le M_i/O_i \le 2$ and O_i and M_i are observed and simulated values, respectively) is included in both panels.

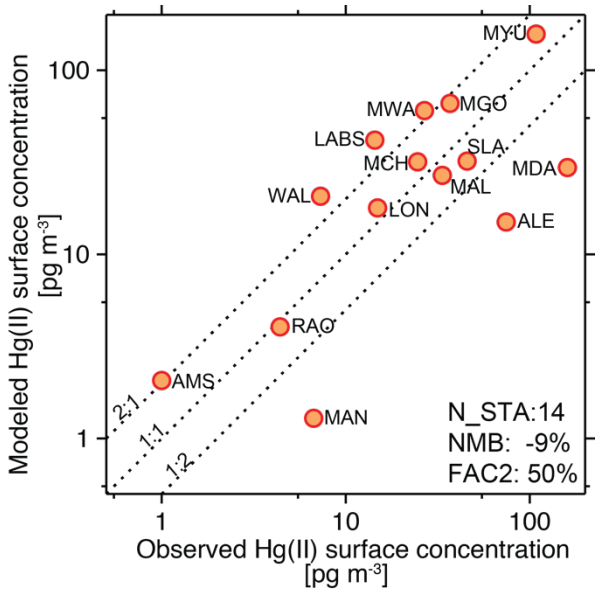

Figure 4A.2: Simulated and observed surface Hg(II) concentrations at worldwide sites. Stations are listed in Table 4A.2. Note the logarithmic scale on both axes.

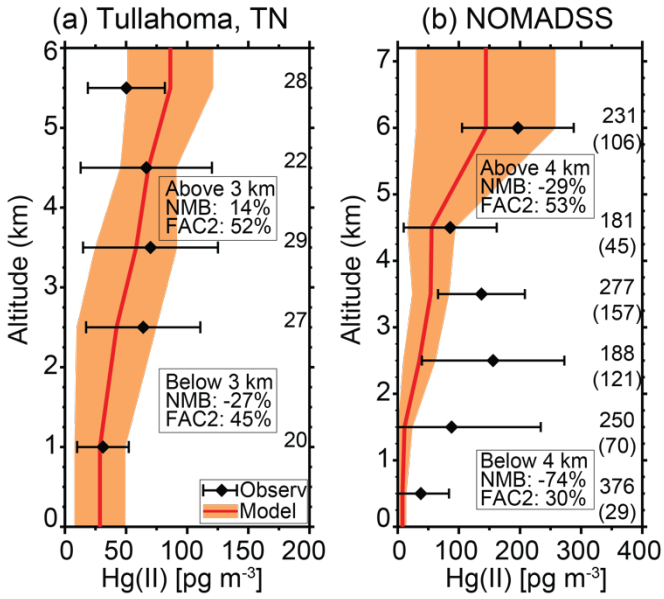

Figure 4A.3: Simulated and observed Hg(II) concentrations for two aircraft campaigns over the U.S. (a) Simulated and observed Hg(II) concentrations for aircraft-based campaign over Tullahoma, TN, USA (2012-2013) (Brooks et al., 2014). (b) Simulated and observed Hg(II) concentrations for the NOMADSS aircraft-based campaign (2013) (Shah et al., 2016). The number of model-observation pairs in each height bin is shown in panel (a). In panel (b), the number of model-observation pairs in each height bin, and, in parentheses, the number of model-observation pairs where the observations were above the instrument detection limit, are shown.

Chapter 5. SUMMARY AND FUTURE WORK

Aerosol particles and mercury have adverse effects on human health and impact the Earth's physical and biological systems. The origin and fate of these pollutants is governed by a web of complex physical and chemical processes, which are not fully understood. In my Ph.D. thesis, I have examined the sources, chemistry, and transport of aerosols and oxidized mercury compounds in the atmosphere. I have done this using a combination of aircraft- and ground-based observations and results from the GEOS-Chem chemical transport model.

Two chapters have focused on wintertime air pollution from fine aerosol particles in the eastern U.S. I used aircraft-based observations from the Wintertime INvestigation of Transport, Emissions, and Reactivity (WINTER) campaign (1 Feb–15 Mar 2015), ground-based observations from monitoring sites and the GEOS-Chem model to investigate the sources and chemistry of SO_4^{2-}, NO_3^-, NH_4^+ and OA. In Chapter 2, I have tried to understand why concentrations of wintertime SO_4^{2-}, NO_3^- and NH_4^+ in the eastern U.S. have displayed a weak or non-existent response to strong reductions in emissions of SO_2 and NOx. Between 2007 and 2015, SO_2 and NOx emissions have decreased by 58% and 35%, SO_4^{2-}, respectively, but SO_4^{2-} concentrations have decreased by 31% and NO_3^- concentrations have not changed much. I have first evaluated the GEOS-Chem simulations against aircraft- and ground-based observations. I show that GEOS-Chem can simulate the concentrations of SO_4^{2-}, NO_3^-, and NH_4^+ in good agreement with observations from the WINTER campaign. The observed concentration of SO_4^{2-}-NO_3^--NH_4^+, combined, below 1 km altitude was 2.45 μg sm^{-3}, with 47% SO_4^{2-}, 32% NO_3^-, and 21% NH_4^+. I found that the GEOS-Chem predicted mean concentrations (2.79 μg sm^{-3}) and composition (42% SO_4^{2-}; 34% NO_3^-; 24% NH_4^+) match the observations. Using the simulation results, I have analyzed the chemical controls on the formation

of SO_4^{2-} and NO_3^- in winter. NH_4^+ concentrations are covary with SO_4^{2-} and NO_3^-. I found that during the WINTER campaign only 18% of the SO_2 is regionally oxidized to SO_4^{2-} in winter over the eastern U.S. SO_2 oxidation happens mostly through the aqueous-phase H_2O_2 (46%) and gas-phase OH (35%) pathways. The efficiency of oxidation through these pathways is low in winter because of low concentrations of the oxidants. NO_3^- is formed from the partitioning of nitric acid to the particle phase. The fraction that partitions depends strongly on the particle pH. The observations and GEOS-Chem simulations showed that particle pH was low (~1.3) during WINTER, which allowed only about 45% of the total nitrate (gas + particle) to partition to the particle phase. Thus, I showed that there are chemical limitations on the formation of both SO_4^{2-} and NO_3^- during winter resulting from low oxidant concentrations and low particle pH. I next examined how these limitations may have evolved with changing emissions of SO_2 and NOx, by analyzing recent trends in the concentration of SO_4^{2-} and NO_3^-.

SO_4^{2-} concentrations at ground-based monitoring sites in the eastern U.S. decreased by only 31%, despite a 58% decrease in SO_2 emissions between 2007 and 2015. The GEOS-Chem simulations reproduced this relatively small change in SO_4^{2-} concentrations for 2007–2015. I showed that the weak response of SO_4^{2-} concentrations to decreasing SO_2 emissions was caused by an increase in the SO_4^{2-} formation efficiency. This is because the simulated H_2O_2 concentrations did not change between 2007 and 2015, but as SO_2 emissions decrease, the amount of H_2O_2 available for oxidation of each unit of SO_2 emissions increases. Between 2007 and 2015, NOx emissions decreased by 35%, but the concentrations of NO_3^- remained unchanged, appearing to not respond to NOx emissions. I show that the NOx emissions did decrease nitric acid formation, but the concurrent decrease in concentrations of SO_4^{2-} increased the particle pH, which in turn pushed

more nitric acid to the particle phase. I project that these chemical feedbacks will persist into the near future. Between 2015 and 2023, I predict a 24% decrease in SO_4^{2-} concentrations and little to no change in NO_3^- despite an expected 47% decrease in SO_2 emissions and 25% decrease in NOx emissions. My findings have bearing on air quality management policies in the eastern U.S.

In Chapter 3, I have used the GEOS-Chem model to determine the sources of OA observed during the WINTER campaign. The chemistry of OA in polluted environments is poorly understood, and models of OA have had limited success in reproducing the observations. The WINTER OA observations served as a touchstone to evaluate different OA modeling approaches. I conducted three simulations with the GEOS-Chem model: (i) TRAD, in which POA is considered as nonvolatile and SOA from only known aromatic VOCs is included, (ii) SVPOA, in which POA is treated as semivolatile and SOA from the oxidation of primary S/IVOCs is also included, and (iii) SMPL_A and SMPL_B, which treat POA as nonvolatile and the SOA chemistry uses an empirical parameterization based on past field studies. The EPA NEI POA emissions are scaled down by a factor of 2 in the SMPL_B simulation compared to the other simulations.

The OA concentrations observed on the WINTER flights below 1 km altitude was 1.48 ± 0.93 μg sm^{-3}. OA was composed of higher fractions of SOA (60%) than POA (40%). I found that OA concentrations, normalized by enhancement in CO (ΔOA/ΔCO), grew from 39 μg sm^{-3} $ppmv^{-1}$ in fresh emissions to 85 μg sm^{-3} $ppmv^{-1}$ at an OH equivalent age of 1 day driven by SOA formation. This was consistent with past summertime observations over the NE US. I showed that the SMPL_B simulation captured the observed OA, POA, and SOA well. It showed a mean bias of -8%, and simulated SOA (63%) and POA (37%) fractions in agreement with the observations. It also reproduced the observed growth in ΔOA/ΔCO and ΔSOA/ΔCO with photochemical processing. The SMPL_B simulation also predicted OA concentration at the ground-based

monitoring sites with a mean bias of -11%. I showed that the other simulations were unable to capture OA observations. The TRAD simulation was found to overestimate POA by a factor of 2 but predicted almost no SOA, whereas the SVPOA simulation predicted reasonable SOA concentrations but underestimated POA by a factor of 5. The SMPL_B simulation results show that OA is nearly uniform distributed over the eastern US in the winter season and constitutes about 35% of fine particulates near the surface. 65% of the OA over the region is from secondary formation, which implies that continuing reduction in wintertime OA levels will require decreases in the emissions of gaseous precursors of OA.

In Chapter 4, we looked at the influence of oxidized mercury produced in the middle and upper troposphere and its transport in the subtropical anticyclones. My previous work on the NOMADSS aircraft campaign had suggested that the subtropical anticyclones are reservoirs of Hg(II) because of the subsidence that transported Hg(II)-rich air from the upper troposphere and the lack of precipitation that prolonged the lifetime of Hg(II) in the region. I have implemented a tagging technique in GEOS-Chem to track the effect of Hg(II) produced at different altitudes in the atmosphere. I found that Hg(II) produced above 750 hPa accounted for 91% of the tropospheric Hg(II) mass, 91% of the annual Hg wet deposition flux, and 52% of the dry deposition flux. The Hg(II) produced at these altitudes contributes up to 82% to the Hg(II) present over the surface in the western U.S., South America, Africa, and Australia. Direct Hg(II) emissions make the highest contribution (up to 69%) in East and South Asia. The GEOS-Chem simulations were consistent with observations of Hg wet deposition and Hg(II) surface concentrations at the MDN and AMNet sites, where the model mean bias was about 20%. The Hg wet deposition flux at the MDN sites was found to increase with precipitation and the contribution of Hg(II) produced above 750 hPa. These two factors explained 55% of the variance in observations at the MDN sites.

I have quantified the role of Hg(II) in the subtropical anticyclones by conducting a simulation in which the Hg(II) present in the anticyclones was artificially set to zero. I found that between 40°S and 40°N, 44% of the Hg(II) at the surface and 90% of the Hg(II) at 500 hPa comes from the anticyclones. Globally, Hg(II) in the anticyclones accounts for 78% to the tropospheric Hg(II) mass, and 61% of the total Hg(II) deposition. I also found that 75% of the observations with Hg(II) concentrations greater than 250 pg m^{-3} observed during the NOMADSS aircraft campaign were transported from the anticyclones. These results further highlighted the importance of the subtropics in the atmospheric cycling of Hg(II).

Recommendations for future work

Below I have listed some outstanding questions that could be addressed in future work.

i. <u>How strong are the chemical feedbacks that control the formation of wintertime SO_4^{2-} and NO_3^- for other regions of the U.S, and how do the reductions in SO_2 and NOx emissions effect the concentrations of SO_4^{2-}, NO_3^- and NH_4^+ particles?</u> My work has focused on the eastern U.S. which is typically the most polluted region in the country. But other regions may be under a different chemical regime, and the factors that are important for the eastern U.S. may not be as important elsewhere. For example, California has large urban sources of NOx in close proximity to large agricultural sources of NH_3, but few sources of SO_2 (Heald et al., 2012; Walker et al., 2012). The chemistry of SO_4^{2-}, NO_3^- and NH_4^+ particles there would be considerably different from the eastern U.S. My GEOS-Chem simulations for the WINTER campaign could be useful to study other regions of the U.S.

ii. <u>Which factors are important in the wintertime chemistry of SO_4^{2-}, NO_3^- and NH_4^+ over Europe and other areas of the world?</u> Most parts of Europe have seen reductions in SO_2

and NOx emissions similar to the eastern U.S., but still regularly have unhealthy concentrations of fine particulates in the winter (European Environment Agency, 2017). The urban areas in China and India experience some of their worst particulate pollution episodes in winter (Dey and Di Girolamo, 2011; Guttikunda et al., 2014; Huang et al., 2014; Ma et al., 2016). Regional models are not always able to reproduce the observed concentration, composition, or trends of particulates (Colette et al., 2011). My GEOS-Chem simulations for WINTER have showed significant improvement in our ability to model wintertime chemistry in polluted areas. The improved GEOS-Chem model can be applied beneficially to Europe and other areas of the world.

iii. What are the wintertime concentrations of OH and H_2O_2 and other oxidants over the U.S.? What factors control the emissions and concentrations of NH_3 over the U.S. in winter? The amounts of oxidants and NH_3 are among the main uncertainties in modeling wintertime chemistry in polluted mid-latitude regions. There are very few measurements of oxidants and NH_3 available to properly constrain models. Besides, the magnitude of NH_3 emissions and their seasonal variation are not well-constrained. These questions should be considered by future field-intensive studies over polluted regions, which should include state-of-the-art measurements of oxidant concentrations, especially those of OH and H_2O_2, and concentrations of NH_3.

iv. What factors drive wintertime trends in sulfur and nitrogen species deposition? How will these trends change with changing emissions in the future? The trends in sulfur and nitrogen deposition are thought to be largely determined by trends in the emissions of SO_2, NOx, and NH_3. For example, Li et al. (2016) report that the deposition of NO_3^- has decreased while that of NH_4^+ has increased in the past three decades in the U.S., and

attribute it solely to trends in NOx, and NH_3 emissions. It would be useful to investigate what role the coupled chemistry of SO_4^{2-}, NO_3^- and NH_4^+ particles plays in modulating these deposition trends.

v. How consistent is the GEOS-Chem OA simulation with surface observations in other areas of the U.S. and in other seasons? What is the mix of urban, biogenic and fire sources of POA and SOA in the U.S? The GEOS-Chem simulation with the simple SOA parameterization performs well for the WINTER campaign, and has been shown to perform well for the SEAC^{4}RS campaign in the southeastern U.S. summer in a previous study (Kim et al., 2015). Given this success, such a simulation can be applied further to study the sources of OA in other areas of U.S. and on an annual scale.

vi. How sensitive are the results of the complex OA modeling approach (SVPOA) to different assumptions and parameter values? Which modifications or updates to the parameterization are most consistent with WINTER observations? The SVPOA approach is physically more realistic than the other OA modeling approaches. The SVPOA includes a representation of the processes of POA evaporation, oxidation, and re-condensation to SOA. These processes are strongly temperature-dependent, which can lead to seasonal differences in the SOA yields. However, the parameters in the SVPOA approach for the emissions, volatility distribution, and aging of low-volatility gases and SOA are inadequately constrained. The WINTER observations can be used to determine a set of assumptions and parameter values that produce results most consistent with the observations. Recent studies (e.g. Ma et al., 2017) have proposed updates to the OA parameterizations that can be implemented in GEOS-Chem and tested against the WINTER observations.

vii. What are the sources, chemical properties, and abundance of anthropogenic SOA precursors in urban environments? I have shown that the secondary formation of OA from oxidation of anthropogenic VOC precursors exceeds direct OA emissions over the eastern U.S. in winter. But there are still critical outstanding questions about the speciation, sources, and SOA formation potential of these VOC precursors. For example, motor vehicles are a large source of chain, branched and cycloalkanes and single-ring and polycyclic aromatic compounds of 8–25 carbon atoms, which are key SOA precursors. But it not clear whether the SOA formation potential of the mixture of emissions from gasoline or diesel vehicles is higher (Gentner et al., 2017), nor how the formation potential would change with temperature. Answering these kinds of questions will need additional field-intensive campaigns and laboratory studies focused on SOA in polluted areas.

viii. How does the contribution of Hg(II) produced in the free troposphere vary among different models? Does this difference explain the inter-model spread in the simulated Hg vertical profiles and wet deposition? Comparisons of different Hg models have shown about a factor of 5 difference in the simulated Hg(II) concentrations in the free troposphere (Bieser et al., 2017), and about a factor of 2 difference in Hg wet deposition (Travnikov et al., 2017), due to different assumptions about Hg(II) production pathways. It would be useful to test differences among models on the basis of the primary region(s) of production of Hg(II) in each model. A tagging approach similar to what I used can be applied for this purpose.

ix. How much does the production and transport of oxidized mercury vary inter-annually? How does this variability affect the trend in Hg deposition in the U.S. and in other areas?

Weiss-Penzias et al. (2016) found that Hg wet deposition over the U.S. has generally decreased for the 1997–2013 period, but for 2007–2013 the Central and Western U.S. have seen a reversal in this trend. They attribute this to rising Hg emissions in East Asia and long-range transport. My work shows that a large fraction of the spatial variability in Hg wet deposition over the U.S. is due to spatial variability in precipitation and the influence of oxidation in the free troposphere. It would be useful to employ my GEOS-Chem tagged simulation to investigate the combined effects of emission changes and meteorological variability on the observed Hg wet deposition trends.

x. Are the subtropical anticyclones reservoirs of oxidized mercury? My analysis of aircraft- and ground-based Hg observations and the GEOS-Chem simulations strongly suggest the presence of an Hg(II)-rich pool at high altitudes and in subtropical anticyclones. Other observation-based studies have also suggested this (e.g. Weiss-Penzias et al., 2011; Lyman and Jaffe, 2012; Gratz et al., 2015), but there haven't been large-scale direct speciated measurements of Hg at altitudes of 8–12 km and in the subtropical anticyclones. Future aircraft-based measurements of Hg could focus on these areas, and include high time resolution speciated Hg measurements, along with measurements of the key Hg oxidants: Br/BrO and other halogen species, OH, and O_3.

BIBLIOGRAPHY

Aas, W.: Data quality 2004, quality assurance, and field comparisons. EMEP/CCC Report 4/2006, NILU, Norway, [online] Available from: http://www.nilu.no/projects/ccc/reports/cccr4-2006.pdf, 2006.

Ailshire, J. A. and Crimmins, E. M.: Fine Particulate Matter Air Pollution and Cognitive Function Among Older US Adults, Am. J. Epidemiol., 180(4), 359–366, doi:10.1093/aje/kwu155, 2014.

Alexander, B., Park, R. J., Jacob, D. J., Li, Q., Yantosca, R. M., Savarino, J., Lee, C. and Thiemens, M.: Sulfate formation in sea-salt aerosols: Constraints from oxygen isotopes, J. Geophys. Res. Atmospheres, 110(D10), D10307, doi:10.1029/2011JD016773, 2005.

Alexander, B., Hastings, M. G., Allman, D. J., Dachs, J., Thornton, J. A. and Kunasek, S. A.: Quantifying atmospheric nitrate formation pathways based on a global model of the oxygen isotopic composition ($\Delta^{17}O$) of atmospheric nitrate, Atmospheric Chem. Phys., 9(14), 5043–5056, doi:10.5194/acp-9-5043-2009, 2009a.

Alexander, B., Park, R. J., Jacob, D. J. and Gong, S.: Transition metal-catalyzed oxidation of atmospheric sulfur: Global implications for the sulfur budget, J. Geophys. Res. Atmospheres, 114(D2), D02309, doi:10.1029/2008JD010486, 2009b.

Alexander, B., Allman, D. J., Amos, H. M., Fairlie, T. D., Dachs, J., Hegg, D. A. and Sletten, R. S.: Isotopic constraints on the formation pathways of sulfate aerosol in the marine boundary layer of the subtropical northeast Atlantic Ocean, J. Geophys. Res. Atmospheres, 117(D6), D06304, doi:10.1029/2011JD016773, 2012.

Ambrose, J. L., Lyman, S. N., Huang, J., Gustin, M. S. and Jaffe, D. A.: Fast Time Resolution Oxidized Mercury Measurements during the Reno Atmospheric Mercury Intercomparison Experiment (RAMIX), Environ. Sci. Technol., 47(13), 7285–7294, doi:10.1021/es303916v, 2013.

Ambrose, J. L., Gratz, L. E., Jaffe, D. A., Campos, T., Flocke, F. M., Knapp, D. J., Stechman, D. M., Stell, M., Weinheimer, A. J., Cantrell, C. A. and Mauldin, R. L.: Mercury Emission Ratios from Coal-Fired Power Plants in the Southeastern United States during NOMADSS, Environ. Sci. Technol., 49(17), 10389–10397, doi:10.1021/acs.est.5b01755, 2015.

Amos, H. M., Jacob, D. J., Holmes, C. D., Fisher, J. A., Wang, Q., Yantosca, R. M., Corbitt, E. S., Galarneau, E., Rutter, A. P., Gustin, M. S., Steffen, A., Schauer, J. J., Graydon, J. A., Louis, V. L. S., Talbot, R. W., Edgerton, E. S., Zhang, Y. and Sunderland, E. M.: Gas-particle partitioning of atmospheric Hg(II) and its effect on global mercury deposition, Atmospheric Chem. Phys., 12(1), 591–603, doi:10.5194/acp-12-591-2012, 2012.

Amos, H. M., Jacob, D. J., Streets, D. G. and Sunderland, E. M.: Legacy impacts of all-time anthropogenic emissions on the global mercury cycle, Glob. Biogeochem. Cycles, 27(2), 410–421, doi:10.1002/gbc.20040, 2013.

Aneja, V. P., Chauhan, J. P. and Walker, J. T.: Characterization of atmospheric ammonia emissions from swine waste storage and treatment lagoons, J. Geophys. Res. Atmospheres, 105(D9), 11535–11545, doi:10.1029/2000JD900066, 2000.

Anenberg, S. C., Horowitz, L. W., Tong, D. Q. and West, J. J.: An estimate of the global burden of anthropogenic ozone and fine particulate matter on premature human mortality using atmospheric modeling, Environ. Health Perspect., 118(9), 1189–1195, doi:10.1289/ehp.0901220, 2010.

Angot, H., Barret, M., Magand, O., Ramonet, M. and Dommergue, A.: A 2-year record of atmospheric mercury species at a background Southern Hemisphere station on Amsterdam Island, Atmospheric Chem. Phys., 14(20), 11461–11473, doi:10.5194/acp-14-11461-2014, 2014.

Apel, E. C., Emmons, L. K., Karl, T., Flocke, F., Hills, A. J., Madronich, S., Lee-Taylor, J., Fried, A., Weibring, P., Walega, J., Richter, D., Tie, X., Mauldin, L., Campos, T., Weinheimer, A., Knapp, D., Sive, B., Kleinman, L., Springston, S., Zaveri, R., Ortega, J., Voss, P., Blake, D., Baker, A., Warneke, C., Welsh-Bon, D., de Gouw, J., Zheng, J., Zhang, R., Rudolph, J., Junkermann, W. and Riemer, D. D.: Chemical evolution of volatile organic compounds in the outflow of the Mexico City Metropolitan area, Atmospheric Chem. Phys., 10(5), 2353–2375, doi:10.5194/acp-10-2353-2010, 2010.

Ariya, P. A., Khalizov, A. and Gidas, A.: Reactions of gaseous mercury with atomic and molecular halogens: kinetics, product studies, and atmospheric implications, J. Phys. Chem. A, 106(32), 7310–7320, doi:10.1021/jp020719o, 2002.

Ariya, P. A., Amyot, M., Dastoor, A., Deeds, D., Feinberg, A., Kos, G., Poulain, A., Ryjkov, A., Semeniuk, K., Subir, M. and Toyota, K.: Mercury Physicochemical and Biogeochemical Transformation in the Atmosphere and at Atmospheric Interfaces: A Review and Future Directions, Chem. Rev., 115(10), 3760–3802, doi:10.1021/cr500667e, 2015.

Badger, C. L., Griffiths, P. T., George, I., Abbatt, J. P. D. and Cox, R. A.: Reactive Uptake of N_2O_5 by Aerosol Particles Containing Mixtures of Humic Acid and Ammonium Sulfate, J. Phys. Chem. A, 110(21), 6986–6994, doi:10.1021/jp0562678, 2006.

Bahreini, R., Dunlea, E. J., Matthew, B. M., Simons, C., Docherty, K. S., DeCarlo, P. F., Jimenez, J. L., Brock, C. a. and Middlebrook, A. M.: Design and Operation of a Pressure-Controlled Inlet for Airborne Sampling with an Aerodynamic Aerosol Lens, Aerosol Sci. Technol., 42(6), 465–471, doi:10.1080/02786820802178514, 2008.

Bahreini, R., Ervens, B., Middlebrook, A. M., Warneke, C., de Gouw, J. A., DeCarlo, P. F., Jimenez, J. L., Brock, C. a., Neuman, J. A., Ryerson, T. B., Stark, H., Atlas, E., Brioude, J., Fried, A., Holloway, J. S., Peischl, J., Richter, D., Walega, J., Weibring, P., Wollny, a. G. and Fehsenfeld, F. C.: Organic aerosol formation in urban and industrial plumes near Houston and Dallas, Texas, J. Geophys. Res., 114(D00F16), D00F16, doi:10.1029/2008JD011493, 2009.

Baker, K. R., Carlton, A. G., Kleindienst, T. E., Offenberg, J. H., Beaver, M. R., Gentner, D. R., Goldstein, A. H., Hayes, P. L., Jimenez, J. L., Gilman, J. B., de Gouw, J. A., Woody, M. C., Pye, H. O. T., Kelly, J. T., Lewandowski, M., Jaoui, M., Stevens, P. S., Brune, W. H., Lin, Y.-H.,

Rubitschun, C. L. and Surratt, J. D.: Gas and aerosol carbon in California: comparison of measurements and model predictions in Pasadena and Bakersfield, Atmospheric Chem. Phys., 15(9), 5243–5258, doi:10.5194/acp-15-5243-2015, 2015.

Balabanov, N. B., Shepler, B. C. and Peterson, K. A.: Accurate Global Potential Energy Surface and Reaction Dynamics for the Ground State of $HgBr_2$, J. Phys. Chem. A, 109(39), 8765–8773, doi:10.1021/jp053415l, 2005.

Bergan, T., Gallardo, L. and Rodhe, H.: Mercury in the global troposphere: a three-dimensional model study, Atmos. Environ., 33(10), 1575–1585, doi:10.1016/S1352-2310(98)00370-7, 1999.

Bergström, R., Denier van der Gon, H. A. C., Prévôt, A. S. H., Yttri, K. E. and Simpson, D.: Modelling of organic aerosols over Europe (2002–2007) using a volatility basis set (VBS) framework: application of different assumptions regarding the formation of secondary organic aerosol, Atmospheric Chem. Phys., 12(18), 8499–8527, doi:10.5194/acp-12-8499-2012, 2012.

Bertram, A. K., Martin, S. T., Hanna, S. J., Smith, M. L., Bodsworth, A., Chen, Q., Kuwata, M., Liu, A., You, Y. and Zorn, S. R.: Predicting the relative humidities of liquid-liquid phase separation, efflorescence, and deliquescence of mixed particles of ammonium sulfate, organic material, and water using the organic-to-sulfate mass ratio of the particle and the oxygen-to-carbon elemental ratio of the organic component, Atmospheric Chem. Phys., 11(21), 10995–11006, doi:10.5194/acp-11-10995-2011, 2011.

Bertram, T. H. and Thornton, J. A.: Toward a general parameterization of N_2O_5 reactivity on aqueous particles: the competing effects of particle liquid water, nitrate and chloride, Atmospheric Chem. Phys., 9(21), 8351–8363, doi:10.5194/acp-9-8351-2009, 2009.

Bey, I., Jacob, D. J., Yantosca, R. M., Logan, J. A., Field, B. D., Fiore, A. M., Li, Q., Liu, H. Y., Mickley, L. J. and Schultz, M. G.: Global modeling of tropospheric chemistry with assimilated meteorology: Model description and evaluation, J. Geophys. Res. Atmospheres, 106(D19), 23073–23095, doi:10.1029/2001JD000807, 2001.

Bian, H., Chin, M., Hauglustaine, D. A., Schulz, M., Myhre, G., Bauer, S. E., Lund, M. T., Karydis, V. A., Kucsera, T. L., Pan, X., Pozzer, A., Skeie, R. B., Steenrod, S. D., Sudo, K., Tsigaridis, K., Tsimpidi, A. P. and Tsyro, S. G.: Investigation of global particulate nitrate from the AeroCom phase III experiment, Atmospheric Chem. Phys., 17(21), 12911–12940, doi:10.5194/acp-17-12911-2017, 2017.

Bieser, J., Slemr, F., Ambrose, J., Brenninkmeijer, C., Brooks, S., Dastoor, A., DeSimone, F., Ebinghaus, R., Gencarelli, C. N., Geyer, B., Gratz, L. E., Hedgecock, I. M., Jaffe, D., Kelley, P., Lin, C.-J., Jaegle, L., Matthias, V., Ryjkov, A., Selin, N. E., Song, S., Travnikov, O., Weigelt, A., Luke, W., Ren, X., Zahn, A., Yang, X., Zhu, Y. and Pirrone, N.: Multi-model study of mercury dispersion in the atmosphere: vertical and interhemispheric distribution of mercury species, Atmospheric Chem. Phys., 17(11), 6925–6955, doi:10.5194/acp-17-6925-2017, 2017.

Bond, T. C., Streets, D. G., Yarber, K. F., Nelson, S. M., Woo, J.-H. and Klimont, Z.: A technology-based global inventory of black and organic carbon emissions from combustion, J. Geophys. Res. Atmospheres, 109(D14), D14203, doi:10.1029/2003JD003697, 2004.

Boucher, O., Randall, D., Artaxo, P., Bretherton, C., Feingold, G., Forster, P., Kerminen, V.-M., Kondo, Y., Liao, H., Lohmann, U., Rasch, P., Satheesh, S. K., Sherwood, S., Stevens, B. and Zhang, X. Y.: Clouds and Aerosols, in Climate Change 2013: The Physical Science Basis. Contribution of Working Group I to the Fifth Assessment Report of the Intergovernmental Panel on Climate Change, edited by T. F. Stocker, D. Qin, G.-K. Plattner, M. Tignor, S. K. Allen, J. Boschung, A. Nauels, Y. Xia, V. Bex, and P. M. Midgley, pp. 571–658, Cambridge University Press, Cambridge, United Kingdom and New York, NY, USA., 2013.

Bouwman, A. F., Lee, D. S., Asman, W. A. H., Dentener, F. J., Van Der Hoek, K. W. and Olivier, J. G. J.: A global high-resolution emission inventory for ammonia, Glob. Biogeochem. Cycles, 11(4), 561–587, doi:10.1029/97GB02266, 1997.

Brooks, S., Ren, X., Cohen, M., Luke, W. T., Kelley, P., Artz, R., Hynes, A., Landing, W. and Martos, B.: Airborne Vertical Profiling of Mercury Speciation near Tullahoma, TN, USA, Atmosphere, 5(3), 557, doi:10.3390/atmos5030557, 2014.

Brown, S., Hafner, H., Roberts, P., Sheesley, R. and Schauer, J.: Integration of results for the upper Midwest urban organics study. [online] Available from: http://www.ladco.org/reports/rpo/monitoring/urban_organics_study_integration_final_report_sti_uw.pdf (Accessed 9 March 2018), 2006.

Canagaratna, M. R., Jayne, J. T., Jimenez, J. L., Allan, J. D., Alfarra, M. R., Zhang, Q., Onasch, T. B., Drewnick, F., Coe, H., Middlebrook, A. M., Delia, A., Williams, L. R., Trimborn, A. M., Northway, M. J., DeCarlo, P. F., Kolb, C. E., Davidovits, P. and Worsnop, D. R.: Chemical and microphysical characterization of ambient aerosols with the Aerodyne Aerosol Mass Spectrometer, Mass Spectrom. Rev., 26(2), 185–222, doi:10.1002/mas, 2007.

Canagaratna, M. R., Jimenez, J. L., Kroll, J. H., Chen, Q., Kessler, S. H., Massoli, P., Hildebrandt Ruiz, L., Fortner, E., Williams, L. R., Wilson, K. R., Surratt, J. D., Donahue, N. M., Jayne, J. T. and Worsnop, D. R.: Elemental ratio measurements of organic compounds using aerosol mass spectrometry: characterization, improved calibration, and implications, Atmospheric Chem. Phys., 15(1), 253–272, doi:10.5194/acp-15-253-2015, 2015.

Cau, P., Methven, J. and Hoskins, B.: Origins of Dry Air in the Tropics and Subtropics, J. Clim., 20(12), 2745–2759, doi:10.1175/JCLI4176.1, 2007.

Chan, A. W. H., Kautzman, K. E., Chhabra, P. S., Surratt, J. D., Chan, M. N., Crounse, J. D., Kürten, A., Wennberg, P. O., Flagan, R. C. and Seinfeld, J. H.: Secondary organic aerosol formation from photooxidation of naphthalene and alkylnaphthalenes: implications for oxidation of intermediate volatility organic compounds (IVOCs), Atmospheric Chem. Phys., 9(9), 3049–3060, doi:10.5194/acp-9-3049-2009, 2009.

Christian, K. E., Brune, W. H. and Mao, J.: Global sensitivity analysis of the GEOS-Chem chemical transport model: ozone and hydrogen oxides during ARCTAS (2008), Atmospheric Chem. Phys., 17(5), 3769–3784, doi:10.5194/acp-17-3769-2017, 2017.

Chung, S. H. and Seinfeld, J. H.: Global distribution and climate forcing of carbonaceous aerosols, J. Geophys. Res. Atmospheres, 107(D19), AAC 14-1, doi:10.1029/2001JD001397, 2002.

Cobbett, F. D., Steffen, A., Lawson, G. and Heyst, B. J. V.: GEM fluxes and atmospheric mercury concentrations (GEM, RGM and PBM) in the Canadian Arctic at Alert, Nunavut, Canada (February–June 2005), Atmos. Environ., 41(31), 6527–6543, doi:10.1016/j.atmosenv.2007.04.033, 2007.

Coburn, S., Dix, B., Edgerton, E., Holmes, C. D., Kinnison, D., Liang, Q., ter Schure, A., Wang, S. and Volkamer, R.: Mercury oxidation from bromine chemistry in the free troposphere over the southeastern US, Atmospheric Chem. Phys., 16(6), 3743–3760, doi:10.5194/acp-16-3743-2016, 2016.

Cohen, A. J., Brauer, M., Burnett, R., Anderson, H. R., Frostad, J., Estep, K., Balakrishnan, K., Brunekreef, B., Dandona, L., Dandona, R., Feigin, V., Freedman, G., Hubbell, B., Jobling, A., Kan, H., Knibbs, L., Liu, Y., Martin, R., Morawska, L., Pope, C. A., Shin, H., Straif, K., Shaddick, G., Thomas, M., van Dingenen, R., van Donkelaar, A., Vos, T., Murray, C. J. L. and Forouzanfar, M. H.: Estimates and 25-year trends of the global burden of disease attributable to ambient air pollution: an analysis of data from the Global Burden of Diseases Study 2015, The Lancet, 389(10082), 1907–1918, doi:10.1016/S0140-6736(17)30505-6, 2017.

Colette, A., Granier, C., Hodnebrog, Ø., Jakobs, H., Maurizi, A., Nyiri, A., Bessagnet, B., D'Angiola, A., D'Isidoro, M., Gauss, M., Meleux, F., Memmesheimer, M., Mieville, A., Rouïl, L., Russo, F., Solberg, S., Stordal, F. and Tampieri, F.: Air quality trends in Europe over the past decade: a first multi-model assessment, Atmospheric Chem. Phys., 11(22), 11657–11678, doi:10.5194/acp-11-11657-2011, 2011.

Crippa, M., DeCarlo, P. F., Slowik, J. G., Mohr, C., Heringa, M. F., Chirico, R., Poulain, L., Freutel, F., Sciare, J., Cozic, J., Di Marco, C. F., Elsasser, M., Nicolas, J. B., Marchand, N., Abidi, E., Wiedensohler, A., Drewnick, F., Schneider, J., Borrmann, S., Nemitz, E., Zimmermann, R., Jaffrezo, J.-L., Prévôt, A. S. H. and Baltensperger, U.: Wintertime aerosol chemical composition and source apportionment of the organic fraction in the metropolitan area of Paris, Atmospheric Chem. Phys., 13(2), 961–981, doi:10.5194/acp-13-961-2013, 2013.

Croft, B., Martin, R. V., Leaitch, W. R., Tunved, P., Breider, T. J., D'Andrea, S. D. and Pierce, J. R.: Processes controlling the annual cycle of Arctic aerosol number and size distributions, Atmospheric Chem. Phys., 16(6), 3665–3682, doi:10.5194/acp-16-3665-2016, 2016.

Cubison, M. J., Ortega, A. M., Hayes, P. L., Farmer, D. K., Day, D., Lechner, M. J., Brune, W. H., Apel, E., Diskin, G. S., Fisher, J. A., Fuelberg, H. E., Hecobian, A., Knapp, D. J., Mikoviny, T., Riemer, D., Sachse, G. W., Sessions, W., Weber, R. J., Weinheimer, A. J., Wisthaler, A. and Jimenez, J. L.: Effects of aging on organic aerosol from open biomass burning smoke in aircraft and laboratory studies, Atmospheric Chem. Phys., 11(23), 12049–12064, doi:10.5194/acp-11-12049-2011, 2011.

Dastoor, A. P. and Larocque, Y.: Global circulation of atmospheric mercury: a modelling study, Atmos. Environ., 38(1), 147–161, doi:10.1016/j.atmosenv.2003.08.037, 2004.

DeCarlo, P. F., Kimmel, J. R., Trimborn, A., Northway, M. J., Jayne, J. T., Aiken, A. C., Gonin, M., Fuhrer, K., Horvath, T., Docherty, K. S., Worsnop, D. R. and Jimenez, J. L.: Field-Deployable, High-Resolution, Time-of-Flight Aerosol Mass Spectrometer, Anal. Chem., 78(24), 8281–8289, doi:10.1021/ac061249n, 2006.

DeCarlo, P. F., Ulbrich, I. M., Crounse, J., de Foy, B., Dunlea, E. J., Aiken, A. C., Knapp, D., Weinheimer, A. J., Campos, T., Wennberg, P. O. and Jimenez, J. L.: Investigation of the sources and processing of organic aerosol over the Central Mexican Plateau from aircraft measurements during MILAGRO, Atmospheric Chem. Phys., 10(12), 5257–5280, doi:10.5194/acp-10-5257-2010, 2010.

Dey, S. and Di Girolamo, L.: A decade of change in aerosol properties over the Indian subcontinent, Geophys. Res. Lett., 38(14), L14811, doi:10.1029/2011GL048153, 2011.

Dibble, T. S., Zelie, M. J. and Mao, H.: Thermodynamics of reactions of ClHg and BrHg radicals with atmospherically abundant free radicals, Atmospheric Chem. Phys., 12(21), 10271–10279, doi:10.5194/acp-12-10271-2012, 2012.

Dominici, F., Peng RD, Bell ML and et al: Fine particulate air pollution and hospital admission for cardiovascular and respiratory diseases, JAMA, 295(10), 1127–1134, doi:10.1001/jama.295.10.1127, 2006.

Donahue, N. M., Robinson, A. L., Stanier, C. O. and Pandis, S. N.: Coupled Partitioning, Dilution, and Chemical Aging of Semivolatile Organics, Environ. Sci. Technol., 40(8), 2635–2643, doi:10.1021/es052297c, 2006.

Donohoue, D. L., Bauer, D., Cossairt, B. and Hynes, A. J.: Temperature and pressure dependent rate coefficients for the reaction of Hg with Br and the reaction of Br with Br: A pulsed laser photolysis-pulsed laser induced fluorescence study, J. Phys. Chem. A, 110(21), 6623–6632, doi:10.1021/jp054688j, 2006.

Drewnick, F., Schwab, J. J., Jayne, J. T., Canagaratna, M., Worsnop, D. R. and Demerjian, K. L.: Measurement of Ambient Aerosol Composition During the PMTACS-NY 2001 Using an Aerosol Mass Spectrometer. Part I: Mass Concentrations Special Issue of Aerosol Science and Technology on Findings from the Fine Particulate Matter Supersites Program, Aerosol Sci. Technol., 38(sup1), 92–103, doi:10.1080/02786820390229507, 2004.

Dunlea, E. J., Decarlo, P. F., Aiken, A. C., Kimmel, J. R., Peltier, R. E., Weber, R. J., Tomlinson, J., Collins, D. R., Shinozuka, Y., McNaughton, C. S., Howell, S. G., Clarke, A. D., Emmons, L. K., Apel, E. C., Pfister, G. G., van Donkelaar, A., Martin, R. V, Millet, D. B., Heald, C. L., Jimenez, J. L. and Tomlison, J.: Evolution of Asian aerosols during transpacific transport in INTEX-B, Atmospheric Chem. Phys., 8(19), 15375–15461, 2009.

Dzepina, K., Volkamer, R. M., Madronich, S., Tulet, P., Ulbrich, I. M., Zhang, Q., Cappa, C. D., Ziemann, P. J. and Jimenez, J. L.: Evaluation of recently-proposed secondary organic aerosol models for a case study in Mexico City, Atmospheric Chem. Phys., 9(15), 5681–5709, doi:10.5194/acp-9-5681-2009, 2009.

Earth Observing Laboratory: HIAPER Modular Inlet, [online] Available from: https://www.eol.ucar.edu/instruments/hiaper-modular-inlet (Accessed 2 January 2018), 2018.

Ebinghaus, R., Kock, H. H., Temme, C., Einax, J. W., Löwe, A. G., Richter, A., Burrows, J. P. and Schroeder, W. H.: Antarctic Springtime Depletion of Atmospheric Mercury, Environ. Sci. Technol., 36(6), 1238–1244, doi:10.1021/es015710z, 2002.

Edgerton, E. S., Hartsell, B. E. and Jansen, J. J.: Mercury Speciation in Coal-fired Power Plant Plumes Observed at Three Surface Sites in the Southeastern U.S., Environ. Sci. Technol., 40(15), 4563–4570, doi:10.1021/es0515607, 2006.

Epstein, S. A., Blair, S. L. and Nizkorodov, S. A.: Direct Photolysis of α-Pinene Ozonolysis Secondary Organic Aerosol: Effect on Particle Mass and Peroxide Content, Environ. Sci. Technol., 48(19), 11251–11258, doi:10.1021/es502350u, 2014.

European Environment Agency: Air quality in Europe — 2017 report. [online] Available from: https://www.eea.europa.eu/publications/air-quality-in-europe-2017 (Accessed 16 April 2018), 2017.

Evans, M. and Jacob, D. J.: Impact of new laboratory studies of N_2O_5 hydrolysis on global model budgets of tropospheric nitrogen oxides, ozone, and OH, Geophys. Res. Lett., 32(9), L09813, doi:10.1029/2005GL022469, 2005.

Faïn, X., Obrist, D., Hallar, A. G., Mccubbin, I. and Rahn, T.: High levels of reactive gaseous mercury observed at a high elevation research laboratory in the Rocky Mountains, Atmospheric Chem. Phys., 9(20), 8049–8060, doi:10.5194/acp-9-8049-2009, 2009.

Fann, N., Lamson, A. D., Anenberg, S. C., Wesson, K., Risley, D. and Hubbell, B. J.: Estimating the national public health burden associated with exposure to ambient $PM_{2.5}$ and ozone, Risk Anal., 32(1), 81–95, doi: 10.1111/j.1539-6924.2011.01630.x, 2012.

Fisher, J. A., Jacob, D. J., Travis, K. R., Kim, P. S., Marais, E. A., Chan Miller, C., Yu, K., Zhu, L., Yantosca, R. M., Sulprizio, M. P., Mao, J., Wennberg, P. O., Crounse, J. D., Teng, A. P., Nguyen, T. B., St. Clair, J. M., Cohen, R. C., Romer, P., Nault, B. A., Wooldridge, P. J., Jimenez, J. L., Campuzano-Jost, P., Day, D. A., Hu, W., Shepson, P. B., Xiong, F., Blake, D. R., Goldstein, A. H., Misztal, P. K., Hanisco, T. F., Wolfe, G. M., Ryerson, T. B., Wisthaler, A. and Mikoviny, T.: Organic nitrate chemistry and its implications for nitrogen budgets in an isoprene- and monoterpene-rich atmosphere: constraints from aircraft (SEAC^{4}RS) and ground-based (SOAS) observations in the Southeast US, Atmospheric Chem. Phys., 16(9), 5969–5991, doi:10.5194/acp-16-5969-2016, 2016.

Fitzgerald, W. F., Lamborg, C. H. and Hammerschmidt, C. R.: Marine Biogeochemical Cycling of Mercury, Chem. Rev., 107(2), 641–662, doi:10.1021/cr050353m, 2007.

Fountoukis, C. and Nenes, A.: ISORROPIA II: a computationally efficient thermodynamic equilibrium model for K^+–Ca^{2+}–Mg^{2+}–NH_4^+–Na^+–SO_4^{2-}–NO_3^-–Cl^-–H_2O aerosols, Atmospheric Chem. Phys., 7(17), 4639–4659, doi:10.5194/acp-7-4639-2007, 2007.

Fountoukis, C., Megaritis, A. G., Skyllakou, K., Charalampidis, P. E., Denier van der Gon, H. A. C., Crippa, M., Prévôt, A. S. H., Fachinger, F., Wiedensohler, A., Pilinis, C. and Pandis, S. N.: Simulating the formation of carbonaceous aerosol in a European Megacity (Paris) during the MEGAPOLI summer and winter campaigns, Atmospheric Chem. Phys., 16(6), 3727–3741, doi:10.5194/acp-16-3727-2016, 2016.

de Foy, B., Tong, Y., Yin, X., Zhang, W., Kang, S., Zhang, Q., Zhang, G., Wang, X. and Schauer, J. J.: First field-based atmospheric observation of the reduction of reactive mercury driven by sunlight, Atmos. Environ., 134, 27–39, doi:10.1016/j.atmosenv.2016.03.028, 2016.

Fu, X., Feng, X., Sommar, J. and Wang, S.: A review of studies on atmospheric mercury in China, Sci. Total Environ., 421–422, 73–81, doi:10.1016/j.scitotenv.2011.09.089, 2012.

Fu, X., Marusczak, N., Heimbürger, L.-E., Sauvage, B., Gheusi, F., Prestbo, E. M. and Sonke, J. E.: Atmospheric mercury speciation dynamics at the high-altitude Pic du Midi Observatory, southern France, Atmospheric Chem. Phys., 16(9), 5623–5639, doi:10.5194/acp-16-5623-2016, 2016a.

Fu, X., Yang, X., Lang, X., Zhou, J., Zhang, H., Yu, B., Yan, H., Lin, C.-J. and Feng, X.: Atmospheric wet and litterfall mercury deposition at urban and rural sites in China, Atmospheric Chem. Phys., 16(18), 11547–11562, doi:10.5194/acp-16-11547-2016, 2016b.

Fu, X. W., Zhang, H., Yu, B., Wang, X., Lin, C.-J. and Feng, X. B.: Observations of atmospheric mercury in China: a critical review, Atmospheric Chem. Phys., 15(16), 9455–9476, doi:10.5194/acp-15-9455-2015, 2015.

Gay, D. A., Schmeltz, D., Prestbo, E., Olson, M., Sharac, T. and Tordon, R.: The Atmospheric Mercury Network: measurement and initial examination of an ongoing atmospheric mercury record across North America, Atmospheric Chem. Phys., 13(22), 11339–11349, doi:10.5194/acp-13-11339-2013, 2013.

Gentner, D. R., Jathar, S. H., Gordon, T. D., Bahreini, R., Day, D. A., El Haddad, I., Hayes, P. L., Pieber, S. M., Platt, S. M., de Gouw, J., Goldstein, A. H., Harley, R. A., Jimenez, J. L., Prévôt, A. S. H. and Robinson, A. L.: Review of Urban Secondary Organic Aerosol Formation from Gasoline and Diesel Motor Vehicle Emissions, Environ. Sci. Technol., 51(3), 1074–1093, doi:10.1021/acs.est.6b04509, 2017.

Giglio, L., Randerson, J. T. and van der Werf, G. R.: Analysis of daily, monthly, and annual burned area using the fourth-generation global fire emissions database (GFED4), J. Geophys. Res. Biogeosciences, 118(1), 317–328, doi:10.1002/jgrg.20042, 2013.

Glasius, M., Hansen, A. M. K., Claeys, M., Henzing, J. S., Jedynska, A. D., Kasper-Giebl, A., Kistler, M., Kristensen, K., Martinsson, J., Maenhaut, W., Nøjgaard, J. K., Spindler, G., Stenström, K. E., Swietlicki, E., Szidat, S., Simpson, D. and Yttri, K. E.: Composition and sources of carbonaceous aerosols in Northern Europe during winter, Atmos. Environ., 173, 127–141, doi:10.1016/j.atmosenv.2017.11.005, 2018.

Goodsite, M. E., Plane, J. M. C. and Skov, H.: A Theoretical Study of the Oxidation of Hg0 to $HgBr_2$ in the Troposphere, Environ. Sci. Technol., 38(6), 1772–1776, doi:10.1021/es034680s, 2004.

de Gouw, J. A. and Jimenez, J. L.: Organic Aerosols in the Earth's Atmosphere, Environ. Sci. Technol., 43(20), 7614–7618, doi:10.1021/es9006004, 2009.

de Gouw, J. A., Middlebrook, A. M., Warneke, C., Goldan, P. D., Kuster, W. C., Roberts, J. M., Fehsenfeld, F. C., Worsnop, D. R., Canagaratna, M. R., Pszenny, A. A. P., Keene, W. C., Marchewka, M., Bertman, S. B. and Bates, T. S.: Budget of organic carbon in a polluted atmosphere: Results from the New England Air Quality Study in 2002, J. Geophys. Res. Atmospheres, 110(D16), doi:10.1029/2004JD005623, 2005.

de Gouw, J. A., Brock, C. A., Atlas, E. L., Bates, T. S., Fehsenfeld, F. C., Goldan, P. D., Holloway, J. S., Kuster, W. C., Lerner, B. M., Matthew, B. M., Middlebrook, A. M., Onasch, T. B., Peltier, R. E., Quinn, P. K., Senff, C. J., Stohl, A., Sullivan, A. P., Trainer, M., Warneke, C., Weber, R. J. and Williams, E. J.: Sources of particulate matter in the northeastern United States in summer: 1. Direct emissions and secondary formation of organic matter in urban plumes, J. Geophys. Res. Atmospheres, 113(D8), D08301, doi:10.1029/2007JD009243, 2008.

Gratz, L. E., Keeler, G. J. and Miller, E. K.: Long-term relationships between mercury wet deposition and meteorology, Atmos. Environ., 43(39), 6218–6229, doi:10.1016/j.atmosenv.2009.08.040, 2009.

Gratz, L. E., Ambrose, J. L., Jaffe, D. A., Shah, V., Jaeglé, L., Stutz, J., Festa, J., Spolaor, M., Tsai, C., Selin, N. E., Song, S., Zhou, X., Weinheimer, A. J., Knapp, D. J., Montzka, D. D., Flocke, F. M., Campos, T. L., Apel, E., Hornbrook, R., Blake, N. J., Hall, S., Tyndall, G. S., Reeves, M., Stechman, D. and Stell, M.: Oxidation of mercury by bromine in the subtropical Pacific free troposphere, Geophys. Res. Lett., 42(23), 10,494–10,502, doi:10.1002/2015GL066645, 2015.

Grieshop, A. P., Logue, J. M., Donahue, N. M. and Robinson, A. L.: Laboratory investigation of photochemical oxidation of organic aerosol from wood fires 1: measurement and simulation of organic aerosol evolution, Atmospheric Chem. Phys., 9(4), 1263–1277, doi:10.5194/acp-9-1263-2009, 2009.

Griffin, R. J., Cocker David R., Seinfeld John H. and Dabdub Donald: Estimate of global atmospheric organic aerosol from oxidation of biogenic hydrocarbons, Geophys. Res. Lett., 26(17), 2721–2724, doi:10.1029/1999GL900476, 1999.

Guenther, A. B., Jiang, X., Heald, C. L., Sakulyanontvittaya, T., Duhl, T., Emmons, L. K. and Wang, X.: The Model of Emissions of Gases and Aerosols from Nature version 2.1 (MEGAN2.1): an extended and updated framework for modeling biogenic emissions, Geosci. Model Dev., 5(6), 1471–1492, doi:10.5194/gmd-5-1471-2012, 2012.

Guentzel, J. L., Landing, W. M., Gill, G. A. and Pollman, C. D.: Processes Influencing Rainfall Deposition of Mercury in Florida, Environ. Sci. Technol., 35(5), 863–873, doi:10.1021/es001523+, 2001.

Guo, H., Sullivan, A. P., Campuzano-Jost, P., Schroder, J. C., Lopez-Hilfiker, F. D., Dibb, J. E., Jimenez, J. L., Thornton, J. A., Brown, S. S., Nenes, A. and Weber, R. J.: Fine particle pH and the partitioning of nitric acid during winter in the northeastern United States, J. Geophys. Res. Atmospheres, 121(17), 10,355–10,376, doi:10.1002/2016JD025311, 2016.

Guo, H., Liu, J., Froyd, K. D., Roberts, J. M., Veres, P. R., Hayes, P. L., Jimenez, J. L., Nenes, A. and Weber, R. J.: Fine particle pH and gas–particle phase partitioning of inorganic species in Pasadena, California, during the 2010 CalNex campaign, Atmospheric Chem. Phys., 17(9), 5703–5719, doi:10.5194/acp-17-5703-2017, 2017a.

Guo, H., Weber, R. J. and Nenes, A.: High levels of ammonia do not raise fine particle pH sufficiently to yield nitrogen oxide-dominated sulfate production, Sci. Rep., 7(1), 12109, doi:10.1038/s41598-017-11704-0, 2017b.

Gustin, M. S., Weiss-Penzias, P. S. and Peterson, C.: Investigating sources of gaseous oxidized mercury in dry deposition at three sites across Florida, USA, Atmospheric Chem. Phys., 12(19), 9201–9219, doi:10.5194/acp-12-9201-2012, 2012.

Gustin, M. S., Amos, H. M., Huang, J., Miller, M. B. and Heidecorn, K.: Measuring and modeling mercury in the atmosphere: a critical review, Atmospheric Chem. Phys., 15(10), 5697–5713, doi:10.5194/acp-15-5697-2015, 2015.

Guttikunda, S. K., Goel, R. and Pant, P.: Nature of air pollution, emission sources, and management in the Indian cities, Atmos. Environ., 95(Supplement C), 501–510, doi:10.1016/j.atmosenv.2014.07.006, 2014.

Hall, B.: The Gas Phase Oxidation of Elemental Mercury by Ozone, in Mercury as a Global Pollutant: Proceedings of the Third International Conference held in Whistler, British Columbia, July 10–14, 1994, edited by D. B. Porcella, J. W. Huckabee, and B. Wheatley, pp. 301–315, Springer Netherlands, Dordrecht., 1995.

Hammerschmidt, C. R. and Fitzgerald, W. F.: Methylmercury in Freshwater Fish Linked to Atmospheric Mercury Deposition, Environ. Sci. Technol., 40(24), 7764–7770, doi:10.1021/es061480i, 2006.

Hand, J., Schichtel, B., Pitchford, M., Malm, W. and Frank, N.: Seasonal composition of remote and urban fine particulate matter in the United States, J. Geophys. Res. Atmospheres, 117(D5), D05209, doi:10.1029/2011JD017122, 2012.

Hanson, P. J. and Lindberg, S. E.: Dry deposition of reactive nitrogen compounds: A review of leaf, canopy and non-foliar measurements, Atmospheric Environ. Part Gen. Top., 25(8), 1615–1634, doi:10.1016/0960-1686(91)90020-8, 1991.

Harris, R. C., Rudd, J. W. M., Amyot, M., Babiarz, C. L., Beaty, K. G., Blanchfield, P. J., Bodaly, R. A., Branfireun, B. A., Gilmour, C. C., Graydon, J. A., Heyes, A., Hintelmann, H., Hurley, J. P., Kelly, C. A., Krabbenhoft, D. P., Lindberg, S. E., Mason, R. P., Paterson, M. J., Podemski, C. L., Robinson, A., Sandilands, K. A., Southworth, G. R., St. Louis, V. L. and Tate,

M. T.: Whole-ecosystem study shows rapid fish-mercury response to changes in mercury deposition, Proc. Natl. Acad. Sci., 104(42), 16586–16591, doi:10.1073/pnas.0704186104, 2007.

Hatch, L. E., Creamean, J. M., Ault, A. P., Surratt, J. D., Chan, M. N., Seinfeld, J. H., Edgerton, E. S., Su, Y. and Prather, K. A.: Measurements of Isoprene-Derived Organosulfates in Ambient Aerosols by Aerosol Time-of-Flight Mass Spectrometry - Part 1: Single Particle Atmospheric Observations in Atlanta, Environ. Sci. Technol., 45(12), 5105–5111, doi:10.1021/es103944a, 2011a.

Hatch, L. E., Creamean, J. M., Ault, A. P., Surratt, J. D., Chan, M. N., Seinfeld, J. H., Edgerton, E. S., Su, Y. and Prather, K. A.: Measurements of Isoprene-Derived Organosulfates in Ambient Aerosols by Aerosol Time-of-Flight Mass Spectrometry—Part 2: Temporal Variability and Formation Mechanisms, Environ. Sci. Technol., 45(20), 8648–8655, doi:10.1021/es2011836, 2011b.

Hayes, P. L., Ortega, A. M., Cubison, M. J., Froyd, K. D., Zhao, Y., Cliff, S. S., Hu, W. W., Toohey, D. W., Flynn, J. H., Lefer, B. L., Grossberg, N., Alvarez, S., Rappenglück, B., Taylor, J. W., Allan, J. D., Holloway, J. S., Gilman, J. B., Kuster, W. C., de Gouw, J. A., Massoli, P., Zhang, X., Liu, J., Weber, R. J., Corrigan, A. L., Russell, L. M., Isaacman, G., Worton, D. R., Kreisberg, N. M., Goldstein, A. H., Thalman, R., Waxman, E. M., Volkamer, R., Lin, Y. H., Surratt, J. D., Kleindienst, T. E., Offenberg, J. H., Dusanter, S., Griffith, S., Stevens, P. S., Brioude, J., Angevine, W. M. and Jimenez, J. L.: Organic aerosol composition and sources in Pasadena, California, during the 2010 CalNex campaign, J. Geophys. Res. Atmospheres, 118(16), 9233–9257, doi:10.1002/jgrd.50530, 2013.

Hayes, P. L., Carlton, A. G., Baker, K. R., Ahmadov, R., Washenfelder, R. A., Alvarez, S., Rappenglück, B., Gilman, J. B., Kuster, W. C., de Gouw, J. A., Zotter, P., Prévôt, A. S. H., Szidat, S., Kleindienst, T. E., Offenberg, J. H., Ma, P. K. and Jimenez, J. L.: Modeling the formation and aging of secondary organic aerosols in Los Angeles during CalNex 2010, Atmospheric Chem. Phys., 15(10), 5773–5801, doi:10.5194/acp-15-5773-2015, 2015.

Heald, C., Jacob, D. J., Turquety, S., Hudman, R. C., Weber, R. J., Sullivan, A. P., Peltier, R. E., Atlas, E. L., de Gouw, J. A., Warneke, C., Holloway, J. S., Neuman, J. A., Flocke, F. M. and Seinfeld, J. H.: Concentrations and sources of organic carbon aerosols in the free troposphere over North America, J. Geophys. Res. Atmospheres, 111(D23), D23S47, doi:10.1029/2006JD007705, 2006.

Heald, C., Coe, H., Jimenez, J. L., Weber, R. J., Bahreini, R., Middlebrook, A. M., Russell, L. M., Jolleys, M., Fu, T.-M., Allan, J. D., Bower, K. N., Capes, G., Crosier, J., Morgan, W. T., Robinson, N. H., Williams, P. I., Cubison, M. J., DeCarlo, P. F. and Dunlea, E. J.: Exploring the vertical profile of atmospheric organic aerosol: comparing 17 aircraft field campaigns with a global model, Atmospheric Chem. Phys., 11(24), 12673–12696, doi:10.5194/acp-11-12673-2011, 2011.

Heald, C., Collett Jr, J., Lee, T., Benedict, K., Schwandner, F., Li, Y., Clarisse, L., Hurtmans, D., Van Damme, M., Clerbaux, C., Coheur, P.-F. and Pye, H. O. T.: Atmospheric ammonia and

particulate inorganic nitrogen over the United States, Atmospheric Chem. Phys., 12(21), 10295–10312, doi:10.5194/acp-12-10295-2012, 2012.

Helsel, D. R. and Hirsch, R. M.: Statistical methods in water resources. Techniques of Water Resources Investigations, Book 4, chapter A3, U.S. Geological Survey. [online] Available from: https://pubs.usgs.gov/twri/twri4a3/pdf/twri4a3-new.pdf (Accessed 24 August 2014), 2002.

Henry, K. M. and Donahue, N. M.: Photochemical Aging of α-Pinene Secondary Organic Aerosol: Effects of OH Radical Sources and Photolysis, J. Phys. Chem. A, 116(24), 5932–5940, doi:10.1021/jp210288s, 2012.

Henze, D., Seinfeld, J., Ng, N., Kroll, J., Fu, T.-M., Jacob, D. J. and Heald, C.: Global modeling of secondary organic aerosol formation from aromatic hydrocarbons: high-vs. low-yield pathways, Atmospheric Chem. Phys., 8(9), 2405–2420, doi:10.5194/acp-8-2405-2008, 2008.

Hodzic, A. and Jimenez, J. L.: Modeling anthropogenically controlled secondary organic aerosols in a megacity: a simplified framework for global and climate models, Geosci. Model Dev., 4(4), 901–917, doi:10.5194/gmd-4-901-2011, 2011.

Hodzic, A., Jimenez, J. L., Madronich, S., Aiken, A. C., Bessagnet, B., Curci, G., Fast, J., Lamarque, J.-F., Onasch, T. B., Roux, G., Schauer, J. J., Stone, E. A. and Ulbrich, I. M.: Modeling organic aerosols during MILAGRO: importance of biogenic secondary organic aerosols, Atmospheric Chem. Phys., 9(18), 6949–6981, doi:10.5194/acp-9-6949-2009, 2009.

Hodzic, A., Jimenez, J. L., Madronich, S., Canagaratna, M. R., DeCarlo, P. F., Kleinman, L. and Fast, J.: Modeling organic aerosols in a megacity: potential contribution of semi-volatile and intermediate volatility primary organic compounds to secondary organic aerosol formation, Atmospheric Chem. Phys., 10(12), 5491–5514, doi:10.5194/acp-10-5491-2010, 2010.

Hodzic, A., Madronich, S., Kasibhatla, P. S., Tyndall, G., Aumont, B., Jimenez, J. L., Lee-Taylor, J. and Orlando, J.: Organic photolysis reactions in tropospheric aerosols: effect on secondary organic aerosol formation and lifetime, Atmospheric Chem. Phys., 15(16), 9253–9269, doi:10.5194/acp-15-9253-2015, 2015.

Holmes, C. D., Jacob, D. J., Mason, R. P. and Jaffe, D. A.: Sources and deposition of reactive gaseous mercury in the marine atmosphere, Atmos. Environ., 43(14), 2278–2285, doi:10.1016/j.atmosenv.2009.01.051, 2009.

Holmes, C. D., Jacob, D. J., Corbitt, E. S., Mao, J., Yang, X., Talbot, R. and Slemr, F.: Global atmospheric model for mercury including oxidation by bromine atoms, Atmospheric Chem. Phys., 10(24), 12037–12057, doi:10.5194/acp-10-12037-2010, 2010.

Holmes, C. D., Krishnamurthy, N. P., Caffrey, J. M., Landing, W. M., Edgerton, E. S., Knapp, K. R. and Nair, U. S.: Thunderstorms Increase Mercury Wet Deposition, Environ. Sci. Technol., 50(17), 9343–9350, doi:10.1021/acs.est.6b02586, 2016.

Holt, J., Selin, N. E. and Solomon, S.: Changes in Inorganic Fine Particulate Matter Sensitivities to Precursors Due to Large-Scale US Emissions Reductions, Environ. Sci. Technol., 49(8), 4834–4841, doi:10.1021/acs.est.5b00008, 2015.

Hornbrook, R. S., Blake, D. R., Diskin, G. S., Fried, A., Fuelberg, H. E., Meinardi, S., Mikoviny, T., Richter, D., Sachse, G. W., Vay, S. A., Walega, J., Weibring, P., Weinheimer, A. J., Wiedinmyer, C., Wisthaler, A., Hills, A., Riemer, D. D. and Apel, E. C.: Observations of nonmethane organic compounds during ARCTAS − Part 1: Biomass burning emissions and plume enhancements, Atmospheric Chem. Phys., 11(21), 11103–11130, doi:10.5194/acp-11-11103-2011, 2011.

Hu, L., Millet Dylan B., Baasandorj Munkhbayar, Griffis Timothy J., Travis Katherine R., Tessum Christopher W., Marshall Julian D., Reinhart Wesley F., Mikoviny Tomas, Müller Markus, Wisthaler Armin, Graus Martin, Warneke Carsten and Gouw Joost: Emissions of C6–C8 aromatic compounds in the United States: Constraints from tall tower and aircraft measurements, J. Geophys. Res. Atmospheres, 120(2), 826–842, doi:10.1002/2014JD022627, 2015.

Hu, W., Hu, M., Hu, W., Jimenez, J. L., Yuan, B., Chen, W., Wang, M., Wu, Y., Chen, C., Wang, Z., Peng, J., Zeng, L. and Shao, M.: Chemical composition, sources, and aging process of submicron aerosols in Beijing: Contrast between summer and winter, J. Geophys. Res. Atmospheres, 121(4), 1955–1977, doi:10.1002/2015JD024020, 2016.

Huang, J. and Gustin, M. S.: Evidence for a Free Troposphere Source of Mercury in Wet Deposition in the Western United States, Environ. Sci. Technol., 46(12), 6621–6629, doi:10.1021/es3005915, 2012.

Huang, R.-J., Zhang, Y., Bozzetti, C., Ho, K.-F., Cao, J.-J., Han, Y., Daellenbach, K. R., Slowik, J. G., Platt, S. M., Canonaco, F., Zotter, P., Wolf, R., Pieber, S. M., Bruns, E. A., Crippa, M., Ciarelli, G., Piazzalunga, A., Schwikowski, M., Abbaszade, G., Schnelle-Kreis, J., Zimmermann, R., An, Z., Szidat, S., Baltensperger, U., Haddad, I. E. and Prévôt, A. S. H.: High secondary aerosol contribution to particulate pollution during haze events in China, Nature, 514(7521), 218–222, doi:10.1038/nature13774, 2014.

Hynes, A. J., Donohoue, D. L., Goodsite, M. E. and Hedgecock, I. M.: Our current understanding of major chemical and physical processes affecting mercury dynamics in the atmosphere and at the air-water/terrestrial interfaces, in Mercury Fate and Transport in the Global Atmosphere: Emissions, Measurements and Models, edited by R. Mason and N. Pirrone, pp. 427–457, Springer US, Boston, MA., 2009.

Isobe, T., Feigelson, E. D., Akritas, M. G. and Babu, G. J.: Linear regression in astronomy I, Astrophys. J., 364(1), 104–113, 1990.

Jacob, D. J.: Heterogeneous chemistry and tropospheric ozone, Atmos. Environ., 34(12), 2131–2159, doi:10.1016/S1352-2310(99)00462-8, 2000.

Jaeckels, J. M., Bae, M.-S. and Schauer, J. J.: Positive Matrix Factorization (PMF) Analysis of Molecular Marker Measurements to Quantify the Sources of Organic Aerosols, Environ. Sci. Technol., 41(16), 5763–5769, doi:10.1021/es062536b, 2007.

Jaeglé, L., Strode, S. A., Selin, N. E. and Jacob, D. J.: The Geos-Chem model, in Mercury Fate and Transport in the Global Atmosphere: Emissions, Measurements and Models, edited by R. Mason and N. Pirrone, pp. 533–545, Springer US, Boston, MA., 2009.

Jaeglé, L., Shah, V., Lopez-Hilfiker, F. D., Lee, B. H., Thornton, J. A., McDuffie, E. E., Fibiger, D. L., Brown, S. S., Veres, P. R., Sparks, T., Ebben, C., Wooldridge, P. J., Cohen, R. C., Weinheimer, A. J., Campos, T. L., Hall, S. R., Ullmann, K., Montzka, D. D., DiGangi, J., Wolfe, G. M., Hansico, T., Schroder, J. C., Campuzano Jost, P., Day, D. A., Jimenez, J. L., Sullivan, A. P., Guo, H. and Weber, R. J.: Reactive nitrogen emissions, chemistry, and deposition over the Northeast United States during the WINTER aircraft campaign, J. Geophys. Res. Atmospheres, In preparation, 2018.

Jaffe, D. A., Lyman, S., Amos, H. M., Gustin, M. S., Huang, J., Selin, N. E., Levin, L., ter Schure, A., Mason, R. P., Talbot, R., Rutter, A., Finley, B., Jaeglé, L., Shah, V., McClure, C., Ambrose, J., Gratz, L., Lindberg, S., Weiss-Penzias, P., Sheu, G.-R., Feddersen, D., Horvat, M., Dastoor, A., Hynes, A. J., Mao, H., Sonke, J. E., Slemr, F., Fisher, J. A., Ebinghaus, R., Zhang, Y. and Edwards, G.: Progress on Understanding Atmospheric Mercury Hampered by Uncertain Measurements, Environ. Sci. Technol., 48(13), 7204–7206, doi:10.1021/es5026432, 2014.

Jimenez, J. L., Canagaratna, M. R., Donahue, N. M., Prévôt, A. S. H., Zhang, Q., Kroll, J. H., DeCarlo, P. F., Allan, J. D., Coe, H., Ng, N. L., Aiken, A. C., Docherty, K. S., Ulbrich, I. M., Grieshop, A. P., Robinson, A. L., Duplissy, J., Smith, J. D., Wilson, K. R., Lanz, V. A., Hueglin, C., Sun, Y. L., Tian, J., Laaksonen, A., Raatikainen, T., Rautiainen, J., Vaattovaara, P., Ehn, M., Kulmala, M., Tomlinson, J. M., Collins, D. R., Cubison, M. J., Dunlea, J., Huffman, J. A., Onasch, T. B., Alfarra, M. R., Williams, P. I., Bower, K., Kondo, Y., Schneider, J., Drewnick, F., Borrmann, S., Weimer, S., Demerjian, K., Salcedo, D., Cottrell, L., Griffin, R., Takami, A., Miyoshi, T., Hatakeyama, S., Shimono, A., Sun, J. Y., Zhang, Y. M., Dzepina, K., Kimmel, J. R., Sueper, D., Jayne, J. T., Herndon, S. C., Trimborn, A. M., Williams, L. R., Wood, E. C., Middlebrook, A. M., Kolb, C. E., Baltensperger, U. and Worsnop, D. R.: Evolution of Organic Aerosols in the Atmosphere, Science, 326(5959), 1525, doi:10.1126/science.1180353, 2009.

Jo, D. S., Park, R. J., Kim, M. J. and Spracklen, D. V.: Effects of chemical aging on global secondary organic aerosol using the volatility basis set approach, Atmos. Environ., 81, 230–244, doi:10.1016/j.atmosenv.2013.08.055, 2013.

Jung, G., Hedgecock, I. M. and Pirrone, N.: ECHMERIT V1.0 - a new global fully coupled mercury-chemistry and transport model, Geosci. Model Dev., 2(2), 175–195, doi:10.5194/gmd-2-175-2009, 2009.

Kaulfus, A. S., Nair, U., Holmes, C. D. and Landing, W. M.: Mercury Wet Scavenging and Deposition Differences by Precipitation Type, Environ. Sci. Technol., 51(5), 2628–2634, doi:10.1021/acs.est.6b04187, 2017.

Keller, C. A., Long, M. S., Yantosca, R. M., Da Silva, A. M., Pawson, S. and Jacob, D. J.: HEMCO v1.0: a versatile, ESMF-compliant component for calculating emissions in atmospheric models, Geosci. Model Dev., 7(4), 1409–1417, doi:10.5194/gmd-7-1409-2014, 2014.

Kim, J.-H., Park, J.-M., Lee, S.-B., Pudasainee, D. and Seo, Y.-C.: Anthropogenic mercury emission inventory with emission factors and total emission in Korea, Atmos. Environ., 44(23), 2714–2721, doi:http://dx.doi.org/10.1016/j.atmosenv.2010.04.037, 2010.

Kim, P. S., Jacob, D. J., Fisher, J. A., Travis, K., Yu, K., Zhu, L., Yantosca, R. M., Sulprizio, M. P., Jimenez, J. L., Campuzano-Jost, P., Froyd, K. D., Liao, J., Hair, J. W., Fenn, M. A., Butler, C. F., Wagner, N. L., Gordon, T. D., Welti, A., Wennberg, P. O., Crounse, J. D., St. Clair, J. M., Teng, A. P., Millet, D. B., Schwarz, J. P., Markovic, M. Z. and Perring, A. E.: Sources, seasonality, and trends of southeast US aerosol: an integrated analysis of surface, aircraft, and satellite observations with the GEOS-Chem chemical transport model, Atmospheric Chem. Phys., 15(18), 10411–10433, doi:10.5194/acp-15-10411-2015, 2015.

Kimmel, J. R., Farmer, D. K., Cubison, M. J., Sueper, D., Tanner, C., Nemitz, E., Worsnop, D. R., Gonin, M. and Jimenez, J. L.: Real-time aerosol mass spectrometry with millisecond resolution, Int. J. Mass Spectrom., 303(1), 15–26, doi:10.1016/j.ijms.2010.12.004, 2011.

Kinne, S., Schulz, M., Textor, C., Guibert, S., Balkanski, Y., Bauer, S. E., Berntsen, T., Berglen, T. F., Boucher, O., Chin, M., Collins, W., Dentener, F., Diehl, T., Easter, R., Feichter, J., Fillmore, D., Ghan, S., Ginoux, P., Gong, S., Grini, A., Hendricks, J., Herzog, M., Horowitz, L., Isaksen, I., Iversen, T., Kirkev\a ag, A., Kloster, S., Koch, D., Kristjansson, J. E., Krol, M., Lauer, A., Lamarque, J. F., Lesins, G., Liu, X., Lohmann, U., Montanaro, V., Myhre, G., Penner, J., Pitari, G., Reddy, S., Seland, O., Stier, P., Takemura, T. and Tie, X.: An AeroCom initial assessment â€“ optical properties in aerosol component modules of global models, Atmospheric Chem. Phys., 6(7), 1815–1834, doi:10.5194/acp-6-1815-2006, 2006.

Kleffmann, J., Becker, K. H. and Wiesen, P.: Heterogeneous NO_2 conversion processes on acid surfaces: possible atmospheric implications, Atmos. Environ., 32(16), 2721–2729, doi:10.1016/S1352-2310(98)00065-X, 1998.

Kleinman, L. I., Daum, P. H., Lee, Y.-N., Senum, G. I., Springston, S. R., Wang, J., Berkowitz, C., Hubbe, J., Zaveri, R. A., Brechtel, F., Jayne, J., Onasch, T. B. and Worsnop, D.: Aircraft observations of aerosol composition and ageing in New England and Mid-Atlantic States during the summer 2002 New England Air Quality Study field campaign, J. Geophys. Res. Atmospheres, 112(D9), doi:10.1029/2006JD007786, 2007.

Kleinman, L. I., Springston, S. R., Daum, P. H., Lee, Y.-N., Nunnermacker, L. J., Senum, G. I., Wang, J., Weinstein-Lloyd, J., Alexander, M. L., Hubbe, J., Ortega, J., Canagaratna, M. R. and Jayne, J.: The time evolution of aerosol composition over the Mexico City plateau, Atmospheric Chem. Phys., 8(6), 1559–1575, doi:10.5194/acp-8-1559-2008, 2008.

Kondo, Y., Miyazaki, Y., Takegawa, N., Miyakawa, T., Weber, R. J., Jimenez, J. L., Zhang, Q. and Worsnop, D. R.: Oxygenated and water-soluble organic aerosols in Tokyo, J. Geophys. Res. Atmospheres, 112(D1), D01203, doi:10.1029/2006JD007056, 2007.

Koo, B., Knipping, E. and Yarwood, G.: 1.5-Dimensional volatility basis set approach for modeling organic aerosol in CAMx and CMAQ, Atmos. Environ., 95, 158–164, doi:10.1016/j.atmosenv.2014.06.031, 2014.

Kos, G., Ryzhkov, A., Dastoor, A., Narayan, J., Steffen, A., Ariya, P. A. and Zhang, L.: Evaluation of discrepancy between measured and modelled oxidized mercury species, Atmospheric Chem. Phys., 13(9), 4839–4863, doi:10.5194/acp-13-4839-2013, 2013.

Krotkov, N. A., McLinden, C. A., Li, C., Lamsal, L. N., Celarier, E. A., Marchenko, S. V., Swartz, W. H., Bucsela, E. J., Joiner, J., Duncan, B. N., Boersma, K. F., Veefkind, J. P., Levelt, P. F., Fioletov, V. E., Dickerson, R. R., He, H., Lu, Z. and Streets, D. G.: Aura OMI observations of regional SO_2 and NO_2 pollution changes from 2005 to 2015, Atmospheric Chem. Phys., 16(7), 4605–4629, doi:10.5194/acp-16-4605-2016, 2016.

Kwon, S. Y. and Selin, N. E.: Uncertainties in Atmospheric Mercury Modeling for Policy Evaluation, Curr. Pollut. Rep., 2(2), 103–114, doi:10.1007/s40726-016-0030-8, 2016.

Landis, M. S., Ryan, J. V., ter Schure, A. F. H. and Laudal, D.: Behavior of Mercury Emissions from a Commercial Coal-Fired Power Plant: The Relationship between Stack Speciation and Near-Field Plume Measurements, Environ. Sci. Technol., 48(22), 13540–13548, doi:10.1021/es500783t, 2014.

Lanz, V. A., Alfarra, M. R., Baltensperger, U., Buchmann, B., Hueglin, C. and Prévôt, A. S. H.: Source apportionment of submicron organic aerosols at an urban site by factor analytical modelling of aerosol mass spectra, Atmospheric Chem. Phys., 7(6), 1503–1522, doi:10.5194/acp-7-1503-2007, 2007.

Lanz, V. A., Prévôt, A. S. H., Alfarra, M. R., Weimer, S., Mohr, C., DeCarlo, P. F., Gianini, M. F. D., Hueglin, C., Schneider, J., Favez, O., D'Anna, B., George, C. and Baltensperger, U.: Characterization of aerosol chemical composition with aerosol mass spectrometry in Central Europe: an overview, Atmospheric Chem. Phys., 10(21), 10453–10471, doi:10.5194/acp-10-10453-2010, 2010.

Laurier, F. J. G., Mason, R. P., Whalin, L. and Kato, S.: Reactive gaseous mercury formation in the North Pacific Ocean's marine boundary layer: A potential role of halogen chemistry, J. Geophys. Res. Atmospheres, 108(D17), 4529, doi:10.1029/2003JD003625, 2003.

Lee, B. H., Lopez-Hilfiker, F. D., Mohr, C., Kurtén, T., Worsnop, D. R. and Thornton, J. A.: An Iodide-Adduct High-Resolution Time-of-Flight Chemical-Ionization Mass Spectrometer: Application to Atmospheric Inorganic and Organic Compounds, Environ. Sci. Technol., 48(11), 6309–6317, doi:10.1021/es500362a, 2014.

Lelieveld, J., Evans, J., Fnais, M., Giannadaki, D. and Pozzer, A.: The contribution of outdoor air pollution sources to premature mortality on a global scale, Nature, 525(7569), 367–371, doi:10.1038/nature15371, 2015.

Li, Y., Schichtel, B. A., Walker, J. T., Schwede, D. B., Chen, X., Lehmann, C. M. B., Puchalski, M. A., Gay, D. A. and Collett, J. L.: Increasing importance of deposition of reduced nitrogen in the United States, Proc. Natl. Acad. Sci., 113(21), 5874, doi:10.1073/pnas.1525736113, 2016.

Lin, J.-T. and McElroy, M.: Impacts of boundary layer mixing on pollutant vertical profiles in the lower troposphere: Implications to satellite remote sensing, Atmos. Environ., 44(14), 1726–1739, doi:10.1016/j.atmosenv.2010.02.009, 2010.

Lin, S.-J. and Rood, R.: Multidimensional flux-form semi-Lagrangian transport schemes, Mon. Weather Rev., 124(9), 2046–2070, doi:10.1175/1520-0493(1996)124<2046:MFFSLT>2.0.CO;2, 1996.

Lindberg, S. E., Brooks, S., Lin, C.-J., Scott, K. J., Landis, M. S., Stevens, R. K., Goodsite, M. and Richter, A.: Dynamic Oxidation of Gaseous Mercury in the Arctic Troposphere at Polar Sunrise, Environ. Sci. Technol., 36(6), 1245–1256, doi:10.1021/es0111941, 2002.

Liu, D.-Y., Wenzel, R. J. and Prather, K. A.: Aerosol time-of-flight mass spectrometry during the Atlanta Supersite Experiment: 1. Measurements, J. Geophys. Res. Atmospheres, 108(D7), 8426, doi:10.1029/2001JD001562, 2003.

Liu, H., Jacob, D. J., Bey, I. and Yantosca, R. M.: Constraints from ^{210}Pb and ^{7}Be on wet deposition and transport in a global three-dimensional chemical, J. Geophys. Res., 106(D11), 12109--12128, doi:10.1029/2000JD900839, 2001.

Lyman, S. N. and Gustin, M. S.: Determinants of atmospheric mercury concentrations in Reno, Nevada, U.S.A., Sci. Total Environ., 408(2), 431–438, doi:10.1016/j.scitotenv.2009.09.045, 2009.

Lyman, S. N. and Jaffe, D. A.: Formation and fate of oxidized mercury in the upper troposphere and lower stratosphere, Nat. Geosci, 5(2), 114–117, doi:10.1038/ngeo1353, 2012.

Lyman, S. N., Jaffe, D. A. and Gustin, M. S.: Release of mercury halides from KCl denuders in the presence of ozone, Atmospheric Chem. Phys., 10(17), 8197–8204, doi:10.5194/acp-10-8197-2010, 2010.

Ma, P. K., Zhao, Y., Robinson, A. L., Worton, D. R., Goldstein, A. H., Ortega, A. M., Jimenez, J. L., Zotter, P., Prévôt, A. S. H., Szidat, S. and Hayes, P. L.: Evaluating the impact of new observational constraints on P-S/IVOC emissions, multi-generation oxidation, and chamber wall losses on SOA modeling for Los Angeles, CA, Atmospheric Chem. Phys., 17(15), 9237–9259, doi:10.5194/acp-17-9237-2017, 2017.

Ma, Z., Hu, X., Sayer, A. M., Levy, R., Zhang, Q., Xue, Y., Tong, S., Bi, J., Huang, L. and Liu, Y.: Satellite-based spatiotemporal trends in PM2. 5 concentrations: China, 2004–2013, Environ. Health Perspect., 124(2), 184, doi:10.1289/ehp.1409481, 2016.

Mahowald, N., Ward, D. S., Kloster, S., Flanner, M. G., Heald, C. L., Heavens, N. G., Hess, P. G., Lamarque, J.-F. and Chuang, P. Y.: Aerosol Impacts on Climate and Biogeochemistry, Annu. Rev. Environ. Resour., 36(1), 45–74, doi:10.1146/annurev-environ-042009-094507, 2011.

Malm, W. C., Schichtel, B. A., Hand, J. L. and Collett, J. L.: Concurrent Temporal and Spatial Trends in Sulfate and Organic Mass Concentrations Measured in the IMPROVE Monitoring Program, J. Geophys. Res. Atmospheres, 122(19), 10,462–10,476, doi:10.1002/2017JD026865, 2017.

Mao, J., Jacob, D. J., Evans, M. J., Olson, J. R., Ren, X., Brune, W. H., Clair, J. M. S., Crounse, J. D., Spencer, K. M., Beaver, M. R., Wennberg, P. O., Cubison, M. J., Jimenez, J. L., Fried, A., Weibring, P., Walega, J. G., Hall, S. R., Weinheimer, A. J., Cohen, R. C., Chen, G., Crawford, J. H., McNaughton, C., Clarke, A. D., Jaeglé, L., Fisher, J. A., Yantosca, R. M., Le Sager, P. and Carouge, C.: Chemistry of hydrogen oxide radicals (HO_x) in the Arctic troposphere in spring, Atmospheric Chem. Phys., 10(13), 5823–5838, doi:10.5194/acp-10-5823-2010, 2010.

McClure, C. D., Jaffe, D. A. and Edgerton, E. S.: Evaluation of the KCl Denuder Method for Gaseous Oxidized Mercury using $HgBr_2$ at an In-Service AMNet Site, Environ. Sci. Technol., 48(19), 11437–11444, doi:10.1021/es502545k, 2014.

Mergler, D., Anderson, H. A., Chan, L. H. M., Mahaffey, K. R., Murray, M., Sakamoto, M. and Stern, A. H.: Methylmercury exposure and health effects in humans: a worldwide concern, AMBIO J. Hum. Environ., 36(1), 3–11, 2007.

Middlebrook, A. M., Murphy, D. M., Lee, S.-H., Thomson, D. S., Prather, K. A., Wenzel, R. J., Liu, D.-Y., Phares, D. J., Rhoads, K. P., Wexler, A. S., Johnston, M. V., Jimenez, J. L., Jayne, J. T., Worsnop, D. R., Yourshaw, I., Seinfeld, J. H. and Flagan, R. C.: A comparison of particle mass spectrometers during the 1999 Atlanta Supersite Project, J. Geophys. Res. Atmospheres, 108(D7), 8424, doi:10.1029/2001JD000660, 2003.

Middlebrook, A. M., Bahreini, R., Jimenez, J. L. and Canagaratna, M. R.: Evaluation of Composition-Dependent Collection Efficiencies for the Aerodyne Aerosol Mass Spectrometer using Field Data, Aerosol Sci. Technol., 46(3), 258–271, doi:10.1080/02786826.2011.620041, 2012.

Molod, A., Takacs, L., Suarez, M. and Bacmeister, J.: Development of the GEOS-5 atmospheric general circulation model: evolution from MERRA to MERRA2, Geosci. Model Dev., 8(5), 1339–1356, doi:10.5194/gmd-8-1339-2015, 2015.

Morel, F. M. M., Kraepiel, A. M. L. and Amyot, M.: The Chemical Cycle and Bioaccumulation of Mercury, Annu. Rev. Ecol. Syst., 29(1), 543–566, doi:10.1146/annurev.ecolsys.29.1.543, 1998.

Murphy, D. M., Cziczo, D. J., Froyd, K. D., Hudson, P. K., Matthew, B. M., Middlebrook, A. M., Peltier, R. E., Sullivan, A., Thomson, D. S. and Weber, R. J.: Single-particle mass spectrometry of tropospheric aerosol particles, J. Geophys. Res. Atmospheres, 111(D23), D23S32, doi:10.1029/2006JD007340, 2006.

Myers, T., Atkinson, R. D., Bullock Jr., O. R. and Bash, J. O.: Investigation of effects of varying model inputs on mercury deposition estimates in the Southwest US, Atmospheric Chem. Phys., 13(2), 997–1009, doi:10.5194/acp-13-997-2013, 2013.

Ng, N. L., Kroll, J. H., Chan, A. W. H., Chhabra, P. S., Flagan, R. C. and Seinfeld, J. H.: Secondary organic aerosol formation from m-xylene, toluene, and benzene, Atmospheric Chem. Phys., 7(14), 3909–3922, doi:10.5194/acp-7-3909-2007, 2007.

Obrist, D., Tas, E., Peleg, M., Matveev, V., Fain, X., Asaf, D. and Luria, M.: Bromine-induced oxidation of mercury in the mid-latitude atmosphere, Nat. Geosci, 4(1), 22–26, doi:10.1038/ngeo1018, 2011.

Obrist, D., Kirk, J. L., Zhang, L., Sunderland, E. M., Jiskra, M. and Selin, N. E.: A review of global environmental mercury processes in response to human and natural perturbations: Changes of emissions, climate, and land use, Ambio, 47(2), 116–140, doi:10.1007/s13280-017-1004-9, 2018.

Ortega, A. M., Hayes, P. L., Peng, Z., Palm, B. B., Hu, W., Day, D. A., Li, R., Cubison, M. J., Brune, W. H., Graus, M., Warneke, C., Gilman, J. B., Kuster, W. C., de Gouw, J., Gutiérrez-Montes, C. and Jimenez, J. L.: Real-time measurements of secondary organic aerosol formation and aging from ambient air in an oxidation flow reactor in the Los Angeles area, Atmospheric Chem. Phys., 16(11), 7411–7433, doi:10.5194/acp-16-7411-2016, 2016.

Pandis, S. N. and Seinfeld, J. H.: Sensitivity analysis of a chemical mechanism for aqueous-phase atmospheric chemistry, J. Geophys. Res. Atmospheres, 94(D1), 1105–1126, doi:10.1029/JD094iD01p01105, 1989.

Park, R. J., Jacob, D. J., Chin, M. and Martin, R. V.: Sources of carbonaceous aerosols over the United States and implications for natural visibility, J. Geophys. Res. Atmospheres, 108(D12), 4355, doi:10.1029/2002JD003190, 2003.

Park, R. J., Jacob, D. J., Field, B. D., Yantosca, R. M. and Chin, M.: Natural and transboundary pollution influences on sulfate-nitrate-ammonium aerosols in the United States: Implications for policy, J. Geophys. Res. Atmospheres, 109(D15), D15204, doi:10.1029/2003JD004473, 2004.

Parrella, J. P., Jacob, D. J., Liang, Q., Zhang, Y., Mickley, L. J., Miller, B., Evans, M. J., Yang, X., Pyle, J. A., Theys, N. and Van Roozendael, M.: Tropospheric bromine chemistry: implications for present and pre-industrial ozone and mercury, Atmospheric Chem. Phys., 12(15), 6723–6740, doi:10.5194/acp-12-6723-2012, 2012.

Parrish, D. D., Hahn C. J., Williams E. J., Norton R. B., Fehsenfeld F. C., Singh H. B., Shetter J. D., Gandrud B. W. and Ridley B. A.: Indications of photochemical histories of Pacific air masses from measurements of atmospheric trace species at Point Arena, California, J. Geophys. Res. Atmospheres, 97(D14), 15883–15901, doi:10.1029/92JD01242, 1992.

Paulot, F., Fan, S. and Horowitz, L. W.: Contrasting seasonal responses of sulfate aerosols to declining SO_2 emissions in the Eastern U.S.: Implications for the efficacy of SO_2 emission controls, Geophys. Res. Lett., 44(1), 455–464, doi:10.1002/2016GL070695, 2017.

Pinder, R. W., Adams, P. J. and Pandis, S. N.: Ammonia Emission Controls as a Cost-Effective Strategy for Reducing Atmospheric Particulate Matter in the Eastern United States, Environ. Sci. Technol., 41(2), 380–386, doi:10.1021/es060379a, 2007.

Pirrone, N. and Keating, T., Eds.: Hemispheric transport of air pollution 2010 Part B: mercury, Task Force on Hemispheric Transport of Air Pollution, Geneva: UN-Economic Commission for Europe, [online] Available from: http://www.htap.org/publications/2010_report/2010_Final_Report/HTAP%202010%20Part%20B%20110408.pdf, 2010.

Pirrone, N., Cinnirella, S., Feng, X., Finkelman, R. B., Friedli, H. R., Leaner, J., Mason, R., Mukherjee, A. B., Stracher, G. B., Streets, D. G. and Telmer, K.: Global mercury emissions to the atmosphere from anthropogenic and natural sources, Atmospheric Chem. Phys., 10(13), 5951–5964, doi:10.5194/acp-10-5951-2010, 2010.

Poissant, L., Pilote, M., Beauvais, C., Constant, P. and Zhang, H. H.: A year of continuous measurements of three atmospheric mercury species (GEM, RGM and Hgp) in southern Québec, Canada, Atmos. Environ., 39(7), 1275–1287, doi:10.1016/j.atmosenv.2004.11.007, 2005.

Polidori, A., Turpin, B. J., Lim, H.-J., Cabada, J. C., Subramanian, R., Pandis, S. N. and Robinson, A. L.: Local and Regional Secondary Organic Aerosol: Insights from a Year of Semi-Continuous Carbon Measurements at Pittsburgh, Aerosol Sci. Technol., 40(10), 861–872, doi:10.1080/02786820600754649, 2006.

Pope, C. A. 3rd and Dockery, D. W.: Health effects of fine particulate air pollution: lines that connect., J. Air Waste Manag. Assoc. 1995, 56(6), 709–742, doi:10.1080/10473289.2006.10464485, 2006.

Prestbo, E. M. and Gay, D. A.: Wet deposition of mercury in the US and Canada, 1996–2005: Results and analysis of the NADP mercury deposition network (MDN), Atmos. Environ., 43(27), 4223–4233, doi:10.1016/j.atmosenv.2009.05.028, 2009.

Pryor, S. C. and Klemm, O.: Experimentally derived estimates of nitric acid dry deposition velocity and viscous sub-layer resistance at a conifer forest, Atmos. Environ., 38(18), 2769–2777, doi:10.1016/j.atmosenv.2004.02.038, 2004.

Pye, H. O. T. and Seinfeld, J. H.: A global perspective on aerosol from low-volatility organic compounds, Atmospheric Chem. Phys., 10(9), 4377–4401, doi:10.5194/acp-10-4377-2010, 2010.

Pye, H. O. T., Liao, H., Wu, S., Mickley, L. J., Jacob, D. J., Henze, D. K. and Seinfeld, J. H.: Effect of changes in climate and emissions on future sulfate-nitrate-ammonium aerosol levels in the United States, J. Geophys. Res. Atmospheres, 114(D1), D01205, doi:10.1029/2008JD010701, 2009.

Pye, H. O. T., Chan, A. W. H., Barkley, M. P. and Seinfeld, J. H.: Global modeling of organic aerosol: the importance of reactive nitrogen (NO_x and NO_3), Atmospheric Chem. Phys., 10(22), 11261–11276, doi:10.5194/acp-10-11261-2010, 2010.

Randerson, J. T., Chen Y., van der Werf G. R., Rogers B. M., and Morton D. C.: Global burned area and biomass burning emissions from small fires, J. Geophys. Res. Biogeosciences, 117(G4), doi:10.1029/2012JG002128, 2012.

Rattigan, O. V., Dirk Felton, H., Bae, M.-S., Schwab, J. J. and Demerjian, K. L.: Multi-year hourly PM2.5 carbon measurements in New York: Diurnal, day of week and seasonal patterns, Atmos. Environ., 44(16), 2043–2053, doi:10.1016/j.atmosenv.2010.01.019, 2010.

Reff, A., Bhave, P. V., Simon, H., Pace, T. G., Pouliot, G. A., Mobley, J. D. and Houyoux, M.: Emissions Inventory of PM2.5 Trace Elements across the United States, Environ. Sci. Technol., 43(15), 5790–5796, doi:10.1021/es802930x, 2009.

Reinecker, M., Suarez, M., Todling, R., Bacmeister, J., Takacs, L., Liu, H., Gu, W., Sienkiewicz, M., Koster, R., Gelaro, R., Stajner, I. and Nielsen, J. E.: The GEOS-5 data assimilation system-documentation of versions 5.0. 1, 5.1. 0, NASA Tech Rep TM-2007, 104606 [online] Available from: https://gmao.gsfc.nasa.gov/pubs/docs/Rienecker369.pdf, 2008.

Ridley, D. A., Heald, C. L., Ridley, K. J. and Kroll, J. H.: Causes and consequences of decreasing atmospheric organic aerosol in the United States, Proc. Natl. Acad. Sci., 115(2), 290, doi:10.1073/pnas.1700387115, 2018.

Robinson, A. L., Subramanian, R., Donahue, N. M., Bernardo-Bricker, A. and Rogge, W. F.: Source Apportionment of Molecular Markers and Organic Aerosol. 2. Biomass Smoke, Environ. Sci. Technol., 40(24), 7811–7819, doi:10.1021/es060782h, 2006.

Schauer, J. J., Rogge, W. F., Hildemann, L. M., Mazurek, M. A., Cass, G. R. and Simoneit, B. R. T.: Source apportionment of airborne particulate matter using organic compounds as tracers, Atmos. Environ., 30(22), 3837–3855, doi:10.1016/1352-2310(96)00085-4, 1996.

Scheuhammer, A. M., Meyer, M. W., Sandheinrich, M. B. and Murray, M. W.: Effects of Environmental Methylmercury on the Health of Wild Birds, Mammals, and Fish, AMBIO J. Hum. Environ., 36(1), 12–19, doi:10.1579/0044-7447(2007)36[12:EOEMOT]2.0.CO;2, 2007.

Schmidt, J. A., Jacob, D. J., Horowitz, H. M., Hu, L., Sherwen, T., Evans, M. J., Liang, Q., Suleiman, R. M., Oram, D. E., Le Breton, M., Percival, C. J., Wang, S., Dix, B. and Volkamer, R.: Modeling the observed tropospheric BrO background: Importance of multiphase chemistry and implications for ozone, OH, and mercury, J. Geophys. Res. Atmospheres, 121(19), 11,819–11,835, doi:10.1002/2015JD024229, 2016.

Schroder, J. C., Campuzano-Jost, P., Day, D. A., Shah, V., Larson, K., Sommers, J. M., Sullivan, A. P., Campos, T., Reeves, M., Hills, A. J., Hornbrook, R. S., Blake, N. J., Scheuer, E., Guo, H., Fibiger, D. L., McDuffie, E. E., Hayes, P. L., Weber, R. J., Dibb, J. E., Apel, E. C., Jaeglé, L., Brown, S. S., Thornton, J. A. and Jimenez, J. L.: Sources and secondary production of organic aerosols in the northeastern US during WINTER, J. Geophys. Res. Atmospheres, Submitted, 2018.

Sciare, J., d'Argouges, O., Sarda-Estève, R., Gaimoz, C., Dolgorouky, C., Bonnaire, N., Favez, O., Bonsang, B. and Gros, V.: Large contribution of water-insoluble secondary organic aerosols in the region of Paris (France) during wintertime, J. Geophys. Res. Atmospheres, 116(D22), D22203, doi:10.1029/2011JD015756, 2011.

Seigneur, C., Karamchandani, P., Lohman, K., Vijayaraghavan, K. and Shia, R.-L.: Multiscale modeling of the atmospheric fate and transport of mercury, J. Geophys. Res. Atmospheres, 106(D21), 27795–27809, doi:10.1029/2000JD000273, 2001.

Selin, N. E.: Global biogeochemical cycling of mercury: a review, Annu. Rev. Environ. Resour., 34(1), 43, doi:10.1146/annurev.environ.051308.084314, 2009.

Selin, N. E. and Jacob, D. J.: Seasonal and spatial patterns of mercury wet deposition in the United States: Constraints on the contribution from North American anthropogenic sources, Atmos. Environ., 42(21), 5193–5204, doi:10.1016/j.atmosenv.2008.02.069, 2008.

Selin, N. E., Jacob, D. J., Park, R. J., Yantosca, R. M., Strode, S., Jaeglé, L. and Jaffe, D.: Chemical cycling and deposition of atmospheric mercury: Global constraints from observations, J. Geophys. Res. Atmospheres, 112(D2), D02308, doi:10.1029/2006JD007450, 2007.

Selin, N. E., Jacob, D. J., Yantosca, R. M., Strode, S., Jaegle, L. and Sunderland, E. M.: Global 3-D land-ocean-atmosphere model for mercury: Present-day versus preindustrial cycles and anthropogenic enrichment factors for deposition, Glob. Biogeochem. Cycles, 22(2), GB2011, doi:10.1029/2007GB003040, 2008.

Shah, V., Jaeglé, L., Gratz, L. E., Ambrose, J. L., Jaffe, D. A., Selin, N. E., Song, S., Campos, T. L., Flocke, F. M., Reeves, M., Stechman, D., Stell, M., Festa, J., Stutz, J., Weinheimer, A. J., Knapp, D. J., Montzka, D. D., Tyndall, G. S., Apel, E. C., Hornbrook, R. S., Hills, A. J., Riemer, D. D., Blake, N. J., Cantrell, C. A. and MauldinÂ III, R. L.: Origin of oxidized mercury in the summertime free troposphere over the southeastern US, Atmospheric Chem. Phys., 16(3), 1511–1530, doi:10.5194/acp-16-1511-2016, 2016.

Shah, V., Jaeglé, L., Thornton, J. A., Lopez-Hilfiker, F. D., Lee, B. H., Schroder, J. C., Campuzano-Jost, P., Jimenez, J. L., Guo, H., Sullivan, A. P., Weber, R. J., Green, J. R., Fiddler, M. N., Bililign, S., Campos, T. L., Stell, M., Weinheimer, A. J., Montzka, D. D. and Brown, S. S.: Chemical Feedbacks Weaken The Wintertime Response of Particulate Sulfate And Nitrate To Emissions Reductions Over The Eastern U.S., Proc. Natl. Acad. Sci., Submitted, 2018.

Shanley, J. B., Engle, M. A., Scholl, M., Krabbenhoft, D. P., Brunette, R., Olson, M. L. and Conroy, M. E.: High Mercury Wet Deposition at a “Clean Air” Site in Puerto Rico, Environ. Sci. Technol., 49(20), 12474–12482, doi:10.1021/acs.est.5b02430, 2015.

Sheu, G.-R. and Lin, N.-H.: Characterizations of wet mercury deposition to a remote islet (Pengjiayu) in the subtropical Northwest Pacific Ocean, Atmos. Environ., 77, 474–481, doi:10.1016/j.atmosenv.2013.05.038, 2013.

Sheu, G.-R., Lin, N.-H., Wang, J.-L., Lee, C.-T., Yang, C.-F. O. and Wang, S.-H.: Temporal distribution and potential sources of atmospheric mercury measured at a high-elevation background station in Taiwan, Atmos. Environ., 44(20), 2393–2400, doi:10.1016/j.atmosenv.2010.04.009, 2010.

Shilling, J. E., Chen, Q., King, S. M., Rosenoern, T., Kroll, J. H., Worsnop, D. R., McKinney, K. A. and Martin, S. T.: Particle mass yield in secondary organic aerosol formed by the dark

ozonolysis of α-pinene, Atmospheric Chem. Phys., 8(7), 2073–2088, doi:10.5194/acp-8-2073-2008, 2008.

Shrivastava, M. K., Lipsky, E. M., Stanier, C. O. and Robinson, A. L.: Modeling Semivolatile Organic Aerosol Mass Emissions from Combustion Systems, Environ. Sci. Technol., 40(8), 2671–2677, doi:10.1021/es0522231, 2006.

Shrivastava, M. K., Lane, T. E., Donahue, N. M., Pandis, S. N. and Robinson, A. L.: Effects of gas particle partitioning and aging of primary emissions on urban and regional organic aerosol concentrations, J. Geophys. Res. Atmospheres, 113(D18), D18301, doi:10.1029/2007JD009735, 2008.

Shrivastava, M. K., Fast, J., Easter, R., Gustafson Jr., W. I., Zaveri, R. A., Jimenez, J. L., Saide, P. and Hodzic, A.: Modeling organic aerosols in a megacity: comparison of simple and complex representations of the volatility basis set approach, Atmospheric Chem. Phys., 11(13), 6639–6662, doi:10.5194/acp-11-6639-2011, 2011.

Si, L. and Ariya, P. A.: Reduction of Oxidized Mercury Species by Dicarboxylic Acids (C2−C4): Kinetic and Product Studies, Environ. Sci. Technol., 42(14), 5150–5155, doi:10.1021/es800552z, 2008.

Sickles II, J. E. and Shadwick, D. S.: Air quality and atmospheric deposition in the eastern US: 20 years of change, Atmospheric Chem. Phys., 15(1), 173–197, doi:10.5194/acp-15-173-2015, 2015.

Sillman, S., Marsik, F. J., Al-Wali, K. I., Keeler, G. J. and Landis, M. S.: Reactive mercury in the troposphere: Model formation and results for Florida, the northeastern United States, and the Atlantic Ocean, J. Geophys. Res. Atmospheres, 112(D23), D23305, doi:10.1029/2006JD008227, 2007.

Simon, H., Baker, K. R. and Phillips, S.: Compilation and interpretation of photochemical model performance statistics published between 2006 and 2012, Atmos. Environ., 61, 124–139, doi:10.1016/j.atmosenv.2012.07.012, 2012.

Slama, R., Darrow, L., Parker, J., Woodruff, T. J., Strickland, M., Nieuwenhuijsen, M., Glinianaia, S., Hoggatt, K. J., Kannan, S., Hurley, F., Kalinka, J., Šrám, R., Brauer, M., Wilhelm, M., Heinrich, J. and Ritz, B.: Meeting Report: Atmospheric Pollution and Human Reproduction, Environ. Health Perspect., 116(6), 791–798, doi:10.1289/ehp.11074, 2008.

Snider, G., Weagle, C. L., Murdymootoo, K. K., Ring, A., Ritchie, Y., Stone, E., Walsh, A., Akoshile, C., Anh, N. X., Balasubramanian, R., Brook, J., Qonitan, F. D., Dong, J., Griffith, D., He, K., Holben, B. N., Kahn, R., Lagrosas, N., Lestari, P., Ma, Z., Misra, A., Norford, L. K., Quel, E. J., Salam, A., Schichtel, B., Segev, L., Tripathi, S., Wang, C., Yu, C., Zhang, Q., Zhang, Y., Brauer, M., Cohen, A., Gibson, M. D., Liu, Y., Martins, J. V., Rudich, Y. and Martin, R. V.: Variation in global chemical composition of $PM_{2.5}$: emerging results from SPARTAN, Atmospheric Chem. Phys., 16(15), 9629–9653, doi:10.5194/acp-16-9629-2016, 2016.

Soerensen, A. L., Sunderland, E. M., Holmes, C. D., Jacob, D. J., Yantosca, R. M., Skov, H., Christensen, J. H., Strode, S. A. and Mason, R. P.: An improved global model for air-sea exchange of mercury: High concentrations over the North Atlantic, Environ. Sci. Technol., 44(22), 8574–8580, doi:10.1021/es102032g, 2010.

Solomon, P. A., Crumpler, D., Flanagan, J. B., Jayanty, R. K. M., Rickman, E. E. and McDade, C. E.: U.S. National PM2.5 Chemical Speciation Monitoring Networks—CSN and IMPROVE: Description of networks, J. Air Waste Manag. Assoc., 64(12), 1410–1438, doi:10.1080/10962247.2014.956904, 2014.

Sommar, J., Gårdfeldt, K., Strömberg, D. and Feng, X.: A kinetic study of the gas-phase reaction between the hydroxyl radical and atomic mercury, Atmos. Environ., 35(17), 3049–3054, doi:10.1016/S1352-2310(01)00108-X, 2001.

Sørensen, L. L., Pryor, S. C., de Leeuw, G. and Schulz, M.: Flux divergence of nitric acid in the marine atmospheric surface layer, J. Geophys. Res. Atmospheres, 110(D15), D15306, doi:10.1029/2004JD005403, 2005.

Spracklen, D. V., Jimenez, J. L., Carslaw, K. S., Worsnop, D. R., Evans, M. J., Mann, G. W., Zhang, Q., Canagaratna, M. R., Allan, J., Coe, H., McFiggans, G., Rap, A. and Forster, P.: Aerosol mass spectrometer constraint on the global secondary organic aerosol budget, Atmospheric Chem. Phys., 11(23), 12109–12136, doi:10.5194/acp-11-12109-2011, 2011.

Sprovieri, F., Hedgecock, I. M. and Pirrone, N.: An investigation of the origins of reactive gaseous mercury in the Mediterranean marine boundary layer, Atmospheric Chem. Phys., 10(8), 3985–3997, doi:10.5194/acp-10-3985-2010, 2010.

Sprovieri, F., Pirrone, N., Bencardino, M., D'Amore, F., Carbone, F., Cinnirella, S., Mannarino, V., Landis, M., Ebinghaus, R., Weigelt, A., Brunke, E.-G., Labuschagne, C., Martin, L., Munthe, J., Wängberg, I., Artaxo, P., Morais, F., Barbosa, H. D. M. J., Brito, J., Cairns, W., Barbante, C., Diéguez, M. D. C., Garcia, P. E., Dommergue, A., Angot, H., Magand, O., Skov, H., Horvat, M., Kotnik, J., Read, K. A., Neves, L. M., Gawlik, B. M., Sena, F., Mashyanov, N., Obolkin, V., Wip, D., Feng, X. B., Zhang, H., Fu, X., Ramachandran, R., Cossa, D., Knoery, J., Marusczak, N., Nerentorp, M. and Norstrom, C.: Atmospheric mercury concentrations observed at ground-based monitoring sites globally distributed in the framework of the GMOS network, Atmospheric Chem. Phys., 16(18), 11915–11935, doi:10.5194/acp-16-11915-2016, 2016.

Sprovieri, F., Pirrone, N., Bencardino, M., D'Amore, F., Angot, H., Barbante, C., Brunke, E.-G., Arcega-Cabrera, F., Cairns, W., Comero, S., Diéguez, M. D. C., Dommergue, A., Ebinghaus, R., Feng, X. B., Fu, X., Garcia, P. E., Gawlik, B. M., Hageström, U., Hansson, K., Horvat, M., Kotnik, J., Labuschagne, C., Magand, O., Martin, L., Mashyanov, N., Mkololo, T., Munthe, J., Obolkin, V., Ramirez Islas, M., Sena, F., Somerset, V., Spandow, P., Vardè, M., Walters, C., Wängberg, I., Weigelt, A., Yang, X. and Zhang, H.: Five-year records of mercury wet deposition flux at GMOS sites in the Northern and Southern hemispheres, Atmospheric Chem. Phys., 17(4), 2689–2708, doi:10.5194/acp-17-2689-2017, 2017.

Strode, S. A., Jaeglé, L., Selin, N. E., Jacob, D. J., Park, R. J., Yantosca, R. M., Mason, R. P. and Slemr, F.: Air-sea exchange in the global mercury cycle, Glob. Biogeochem. Cycles, 21(1), GB1017, doi:10.1029/2006GB002766, 2007.

Subir, M., Ariya, P. A. and Dastoor, A. P.: A review of uncertainties in atmospheric modeling of mercury chemistry I. Uncertainties in existing kinetic parameters – Fundamental limitations and the importance of heterogeneous chemistry, Atmos. Environ., 45(32), 5664–5676, doi:10.1016/j.atmosenv.2011.04.046, 2011.

Subramanian, R., Donahue, N. M., Bernardo-Bricker, A., Rogge, W. F. and Robinson, A. L.: Insights into the primary–secondary and regional–local contributions to organic aerosol and PM2.5 mass in Pittsburgh, Pennsylvania, Atmos. Environ., 41(35), 7414–7433, doi:10.1016/j.atmosenv.2007.05.058, 2007.

Sullivan, A. P., Peltier R. E., Brock C. A., de Gouw J. A., Holloway J. S., Warneke C., Wollny A. G. and Weber R. J.: Airborne measurements of carbonaceous aerosol soluble in water over northeastern United States: Method development and an investigation into water-soluble organic carbon sources, J. Geophys. Res. Atmospheres, 111(D23), doi:10.1029/2006JD007072, 2006.

Sullivan, A. P., Guo, H., Schroder, J. C., Campuzano Jost, P., Jimenez, J. L., Campos, T., Shah, V., Jaeglé, L., Lee, B. H., Lopez-Hilfiker, F. D., Thornton, J. A., Brown, S. S. and Weber, R. J.: The Role of Residential Burning on Ambient Fine Particles During the WINTER Campaign: A Comparison of Airborne Measurements of Biomass Burning Markers Levoglucosan and Aerosol Mass Spectrometer $\Delta C_2H_4O_2^+$ and m/z 60, J. Geophys. Res. Atmospheres, Submitted, 2018.

Sun, Y., Du, W., Fu, P., Wang, Q., Li, J., Ge, X., Zhang, Q., Zhu, C., Ren, L., Xu, W., Zhao, J., Han, T., Worsnop, D. R. and Wang, Z.: Primary and secondary aerosols in Beijing in winter: sources, variations and processes, Atmospheric Chem. Phys., 16(13), 8309–8329, doi:10.5194/acp-16-8309-2016, 2016.

Sutton, M. A., Reis, S., Riddick, S. N., Dragosits, U., Nemitz, E., Theobald, M. R., Tang, Y. S., Braban, C. F., Vieno, M., Dore, A. J., Mitchell, R. F., Wanless, S., Daunt, F., Fowler, D., Blackall, T. D., Milford, C., Flechard, C. R., Loubet, B., Massad, R., Cellier, P., Personne, E., Coheur, P. F., Clarisse, L., Van Damme, M., Ngadi, Y., Clerbaux, C., Skjøth, C. A., Geels, C., Hertel, O., Wichink Kruit, R. J., Pinder, R. W., Bash, J. O., Walker, J. T., Simpson, D., Horváth, L., Misselbrook, T. H., Bleeker, A., Dentener, F. and de Vries, W.: Towards a climate-dependent paradigm of ammonia emission and deposition, Philos. Trans. R. Soc. B Biol. Sci., 368(1621), 20130166, doi:10.1098/rstb.2013.0166, 2013.

Swartzendruber, P. C., Jaffe, D. A., Prestbo, E. M., Weiss-Penzias, P., Selin, N. E., Park, R., Jacob, D. J., Strode, S. and Jaeglé, L.: Observations of reactive gaseous mercury in the free troposphere at the Mount Bachelor Observatory, J. Geophys. Res. Atmospheres, 111(D24), D24301, doi:10.1029/2006JD007415, 2006.

Swartzendruber, P. C., Jaffe, D. A. and Finley, B.: Development and First Results of an Aircraft-Based, High Time Resolution Technique for Gaseous Elemental and Reactive (Oxidized) Gaseous Mercury, Environ. Sci. Technol., 43(19), 7484–7489, doi:10.1021/es901390t, 2009.

Tai, A. P. K., Mickley, L. J., Jacob, D. J., Leibensperger, E. M., Zhang, L., Fisher, J. A. and Pye, H. O. T.: Meteorological modes of variability for fine particulate matter ($PM_{2.5}$) air quality in the United States: implications for $PM_{2.5}$ sensitivity to climate change, Atmospheric Chem. Phys., 12(6), 3131–3145, doi:10.5194/acp-12-3131-2012, 2012.

Takegawa, N., Miyakawa, T., Kondo, Y., Jimenez, J. L., Zhang, Q., Worsnop, D. R. and Fukuda, M.: Seasonal and diurnal variations of submicron organic aerosol in Tokyo observed using the Aerodyne aerosol mass spectrometer, J. Geophys. Res. Atmospheres, 111(D11), D11206, doi:10.1029/2005JD006515, 2006.

Talbot, R., Mao, H., Scheuer, E., Dibb, J. and Avery, M.: Total depletion of Hg° in the upper troposphere–lower stratosphere, Geophys. Res. Lett., 34(23), L23804, doi:10.1029/2007GL031366, 2007.

Thornton, J. A., Brown, S. S., Jaeglé, L., Cohen, R. C., Jimenez, J. L., Weber, R. J., Dibb, J. and Roberts, J. M. : Wintertime INvestigation of Transport, Emissions, and Reactivity (WINTER): A C-130 Aircraft Investigation, [online] Available from: https://www.eol.ucar.edu/system/files/Wintertime_NE_US_C130_WHITEPAPER_final.pdf (Accessed 15 January 2016), 2014.

Thornton, J. A., Kercher, J. P., Riedel, T. P., Wagner, N. L., Cozic, J., Holloway, J. S., Dubé, W. P., Wolfe, G. M., Quinn, P. K., Middlebrook, A. M., Alexander, B. and Brown, S. S.: A large atomic chlorine source inferred from mid-continental reactive nitrogen chemistry, Nature, 464, 271, doi:10.1038/nature08905, 2010.

Timonen, H., Ambrose, J. L. and Jaffe, D. A.: Oxidation of elemental Hg in anthropogenic and marine airmasses, Atmospheric Chem. Phys., 13(5), 2827–2836, doi:10.5194/acp-13-2827-2013, 2013.

Tong, Y., Eichhorst, T., Olson, M. R., McGinnis, J. E., Turner, I., Rutter, A. P., Shafer, M. M., Wang, X. and Schauer, J. J.: Atmospheric photolytic reduction of Hg(II) in dry aerosols, Env. Sci Process. Impacts, 15(10), 1883–1888, doi:10.1039/C3EM00249G, 2013.

Tørseth, K., Aas, W., Breivik, K., Fjæraa, A. M., Fiebig, M., Hjellbrekke, A. G., Lund Myhre, C., Solberg, S. and Yttri, K. E.: Introduction to the European Monitoring and Evaluation Programme (EMEP) and observed atmospheric composition change during 1972–2009, Atmospheric Chem. Phys., 12(12), 5447–5481, doi:10.5194/acp-12-5447-2012, 2012.

Travis, K. R., Jacob, D. J., Fisher, J. A., Kim, P. S., Marais, E. A., Zhu, L., Yu, K., Miller, C. C., Yantosca, R. M., Sulprizio, M. P., Thompson, A. M., Wennberg, P. O., Crounse, J. D., St. Clair, J. M., Cohen, R. C., Laughner, J. L., Dibb, J. E., Hall, S. R., Ullmann, K., Wolfe, G. M., Pollack, I. B., Peischl, J., Neuman, J. A. and Zhou, X.: Why do models overestimate surface ozone in the Southeast United States?, Atmospheric Chem. Phys., 16(21), 13561–13577, doi:10.5194/acp-16-13561-2016, 2016.

Travnikov, O., Angot, H., Artaxo, P., Bencardino, M., Bieser, J., D'Amore, F., Dastoor, A., De Simone, F., Diéguez, M. D. C., Dommergue, A., Ebinghaus, R., Feng, X. B., Gencarelli, C. N., Hedgecock, I. M., Magand, O., Martin, L., Matthias, V., Mashyanov, N., Pirrone, N.,

Ramachandran, R., Read, K. A., Ryjkov, A., Selin, N. E., Sena, F., Song, S., Sprovieri, F., Wip, D., Wängberg, I. and Yang, X.: Multi-model study of mercury dispersion in the atmosphere: atmospheric processes and model evaluation, Atmospheric Chem. Phys., 17(8), 5271–5295, doi:10.5194/acp-17-5271-2017, 2017.

Tsigaridis, K., Daskalakis, N., Kanakidou, M., Adams, P. J., Artaxo, P., Bahadur, R., Balkanski, Y., Bauer, S. E., Bellouin, N., Benedetti, A., Bergman, T., Berntsen, T. K., Beukes, J. P., Bian, H., Carslaw, K. S., Chin, M., Curci, G., Diehl, T., Easter, R. C., Ghan, S. J., Gong, S. L., Hodzic, A., Hoyle, C. R., Iversen, T., Jathar, S., Jimenez, J. L., Kaiser, J. W., Kirkev\a ag, A., Koch, D., Kokkola, H., Lee, Y. H., Lin, G., Liu, X., Luo, G., Ma, X., Mann, G. W., Mihalopoulos, N., Morcrette, J.-J., Müller, J.-F., Myhre, G., Myriokefalitakis, S., Ng, N. L., O'Donnell, D., Penner, J. E., Pozzoli, L., Pringle, K. J., Russell, L. M., Schulz, M., Sciare, J., Seland, Ø., Shindell, D. T., Sillman, S., Skeie, R. B., Spracklen, D., Stavrakou, T., Steenrod, S. D., Takemura, T., Tiitta, P., Tilmes, S., Tost, H., van Noije, T., van Zyl, P. G., von Salzen, K., Yu, F., Wang, Z., Wang, Z., Zaveri, R. A., Zhang, H., Zhang, K., Zhang, Q. and Zhang, X.: The AeroCom evaluation and intercomparison of organic aerosol in global models, Atmospheric Chem. Phys., 14(19), 10845–10895, doi:10.5194/acp-14-10845-2014, 2014.

Tsimpidi, A. P., Karydis, V. A. and Pandis, S. N.: Response of Inorganic Fine Particulate Matter to Emission Changes of Sulfur Dioxide and Ammonia: The Eastern United States as a Case Study, J. Air Waste Manag. Assoc., 57(12), 1489–1498, doi:10.3155/1047-3289.57.12.1489, 2007.

Tsimpidi, A. P., Karydis, V. A., Zavala, M., Lei, W., Molina, L., Ulbrich, I. M., Jimenez, J. L. and Pandis, S. N.: Evaluation of the volatility basis-set approach for the simulation of organic aerosol formation in the Mexico City metropolitan area, Atmospheric Chem. Phys., 10(2), 525–546, doi:10.5194/acp-10-525-2010, 2010.

Tsimpidi, A. P., Karydis, V. A., Pandis, S. N. and Lelieveld, J.: Global combustion sources of organic aerosols: model comparison with 84 AMS factor-analysis data sets, Atmospheric Chem. Phys., 16(14), 8939–8962, doi:10.5194/acp-16-8939-2016, 2016.

Ulbrich, I. M., Canagaratna, M. R., Zhang, Q., Worsnop, D. R. and Jimenez, J. L.: Interpretation of organic components from Positive Matrix Factorization of aerosol mass spectrometric data, Atmospheric Chem. Phys., 9(9), 2891–2918, doi:10.5194/acp-9-2891-2009, 2009.

UNEP Chemicals Branch: The Global Atmospheric Mercury Assessment: Sources, Emissions and Transport, UNEP Chemicals, Geneva. [online] Available from: https://wedocs.unep.org/bitstream/handle/20.500.11822/11517/UNEP_GlobalAtmosphericMercuryAssessment_May2009.pdf, 2008.

U.S. Environmental Protection Agency: Air Pollutant Emissions Trends Data. [online] Available from: https://www.epa.gov/air-emissions-inventories/air-pollutant-emissions-trends-data (Accessed 2 May 2015), 2015a.

U.S. Environmental Protection Agency: PM2.5 2014 design values report, [online] Available from: http://www3.epa.gov/airtrends/values.html (Accessed 15 January 2016), 2015b.

U.S. Environmental Protection Agency: Air Markets Program Data. [online] Available from: https://ampd.epa.gov/ampd/ (Accessed 3 March 2017), 2017a.

U.S. Environmental Protection Agency: Emissions Modeling Platform, 2011 Version 6 Air Emiss. Model. Platf. [online] Available from: https://www.epa.gov/air-emissions-modeling/emissions-modeling-platforms (Accessed 3 March 2017), 2017b.

U.S. Environmental Protection Agency: Emissions Modeling Platform, 2007/2008 Version 5 Air Emiss. Model. Platf. [online] Available from: https://www.epa.gov/air-emissions-modeling/20072008-version-5-air-emissions-modeling-platforms (Accessed 15 June 2017), 2017c.

U.S. Environmental Protection Agency: Our nation's air. [online] Available from: https://gispub.epa.gov/air/trendsreport/2017/ (Accessed 2 October 2017), 2017d.

U.S. Environmental Protection Agency: Particulate Matter (PM2.5) Trends. [online] Available from: https://www.epa.gov/air-trends/particulate-matter-pm25-trends (Accessed 18 October 2017), 2017e.

U.S. Environmental Protection Agency: Clean Air Status and Trends (CASTNET), [online] Available from: https://www.epa.gov/castnet (Accessed 5 October 2017), 2017f

Valente, R. J., Shea, C., Humes, K. L. and Tanner, R. L.: Atmospheric mercury in the Great Smoky Mountains compared to regional and global levels, Atmos. Environ., 41(9), 1861–1873, doi:10.1016/j.atmosenv.2006.10.054, 2007.

VandenBoer, T. C., Brown, S. S., Murphy, J. G., Keene, W. C., Young, C. J., Pszenny, A. A. P., Kim, S., Warneke, C., de Gouw, J. A., Maben, J. R., Wagner, N. L., Riedel, T. P., Thornton, J. A., Wolfe, D. E., Dubé, W. P., Öztürk, F., Brock, C. A., Grossberg, N., Lefer, B., Lerner, B., Middlebrook, A. M. and Roberts, J. M.: Understanding the role of the ground surface in HONO vertical structure: High resolution vertical profiles during NACHTT-11, J. Geophys. Res. Atmospheres, 118(17), 10,155–10,171, doi:10.1002/jgrd.50721, 2013.

Volkamer, R., Jimenez, J. L., San Martini, F., Dzepina, K., Zhang, Q., Salcedo, D., Molina, L. T., Worsnop, D. R. and Molina, M. J.: Secondary organic aerosol formation from anthropogenic air pollution: Rapid and higher than expected, Geophys. Res. Lett., 33(17), L17811, doi:10.1029/2006GL026899, 2006.

Walker, J. M., Philip, S., Martin, R. V. and Seinfeld, J. H.: Simulation of nitrate, sulfate, and ammonium aerosols over the United States, Atmospheric Chem. Phys., 12(22), 11213–11227, doi:10.5194/acp-12-11213-2012, 2012.

Wang, Q., Jacob, D. J., Fisher, J. A., Mao, J., Leibensperger, E. M., Carouge, C. C., Le Sager, P., Kondo, Y., Jimenez, J. L., Cubison, M. J. and Doherty, S. J.: Sources of carbonaceous aerosols and deposited black carbon in the Arctic in winter-spring: implications for radiative forcing, Atmospheric Chem. Phys., 11(23), 12453–12473, doi:10.5194/acp-11-12453-2011, 2011.

Wang, Y., Jacob, D. J. and Logan, J. A.: Global simulation of tropospheric O_3-NOx-hydrocarbon chemistry: 1. Model formulation, J. Geophys. Res. Atmospheres, 103(D9), 10713–10725, doi:10.1029/98JD00158, 1998.

Wang, Y. X., McElroy, M. B., Jacob, D. J. and Yantosca, R. M.: A nested grid formulation for chemical transport over Asia: Applications to CO, J. Geophys. Res. Atmospheres, 109(D22), D22307, doi:10.1029/2004JD005237, 2004.

Wängberg, I., Nerentorp Mastromonaco, M. G., Munthe, J. and Gårdfeldt, K.: Airborne mercury species at the Råö background monitoring site in Sweden: distribution of mercury as an effect of long-range transport, Atmospheric Chem. Phys., 16(21), 13379–13387, doi:10.5194/acp-16-13379-2016, 2016.

Weber, R. J., Guo, H., Russell, A. G. and Nenes, A.: High aerosol acidity despite declining atmospheric sulfate concentrations over the past 15 years, Nat. Geosci, 9(4), 282–285, doi:10.1038/ngeo2665, 2016.

Weigelt, A., Temme, C., Bieber, E., Schwerin, A., Schuetze, M., Ebinghaus, R. and Kock, H. H.: Measurements of atmospheric mercury species at a German rural background site from 2009 to 2011 – methods and results, Environ. Chem., 10(2), 102–110, doi:10.1071/EN12107, 2013.

Weimer, S., Drewnick, F., Hogrefe, O., Schwab, J. J., Rhoads, K., Orsini, D., Canagaratna, M., Worsnop, D. R. and Demerjian, K. L.: Size-selective nonrefractory ambient aerosol measurements during the Particulate Matter Technology Assessment and Characterization Study–New York 2004 Winter Intensive in New York City, J. Geophys. Res. Atmospheres, 111(D18), D18305, doi:10.1029/2006JD007215, 2006.

Weiss-Penzias, P., Gustin, M. S. and Lyman, S. N.: Observations of speciated atmospheric mercury at three sites in Nevada: Evidence for a free tropospheric source of reactive gaseous mercury, J. Geophys. Res. Atmospheres, 114(D14), D14302, doi:10.1029/2008JD011607, 2009.

Weiss-Penzias, P., Amos, H. M., Selin, N. E., Gustin, M. S., Jaffe, D. A., Obrist, D., Sheu, G.-R. and Giang, A.: Use of a global model to understand speciated atmospheric mercury observations at five high-elevation sites, Atmospheric Chem. Phys., 15(3), 1161–1173, doi:10.5194/acp-15-1161-2015, 2015.

Weiss-Penzias, P. S., Gustin, M. S. and Lyman, S. N.: Sources of gaseous oxidized mercury and mercury dry deposition at two southeastern U.S. sites, Atmos. Environ., 45(27), 4569–4579, doi:10.1016/j.atmosenv.2011.05.069, 2011.

Weiss-Penzias, P. S., Gay, D. A., Brigham, M. E., Parsons, M. T., Gustin, M. S. and ter Schure, A.: Trends in mercury wet deposition and mercury air concentrations across the U.S. and Canada, Sci. Total Environ., 568, 546–556, doi:10.1016/j.scitotenv.2016.01.061, 2016.

van der Werf, G. R., Randerson, J. T., Giglio, L., van Leeuwen, T. T., Chen, Y., Rogers, B. M., Mu, M., van Marle, M. J. E., Morton, D. C., Collatz, G. J., Yokelson, R. J. and Kasibhatla, P. S.: Global fire emissions estimates during 1997–2016, Earth Syst. Sci. Data, 9(2), 697–720, doi:10.5194/essd-9-697-2017, 2017.

Wesely, M.: Parameterization of surface resistances to gaseous dry deposition in regional-scale numerical models, Atmospheric Environ. 1967, 23(6), 1293–1304, doi:10.1016/0004-6981(89)90153-4, 1989.

Wesely, M. L. and Hicks, B. B.: A review of the current status of knowledge on dry deposition, Atmos. Environ., 34(12), 2261–2282, doi:10.1016/S1352-2310(99)00467-7, 2000.

Wetherbee, G. A., Gay, D. A., Brunette, R. C. and Sweet, C. W.: Estimated Variability of National Atmospheric Deposition Program/Mercury Deposition Network Measurements Using Collocated Samplers, Environ. Monit. Assess., 131(1), 49–69, doi:10.1007/s10661-006-9456-6, 2007.

Willem A. H. Asman, Sutton, M. A. and Schjorring, J. K.: Ammonia: Emission, Atmospheric Transport and Deposition, New Phytol., 139(1), 27–48, 1998.

Woody, M. C., Baker, K. R., Hayes, P. L., Jimenez, J. L., Koo, B. and Pye, H. O. T.: Understanding sources of organic aerosol during CalNex-2010 using the CMAQ-VBS, Atmospheric Chem. Phys., 16(6), 4081–4100, doi:10.5194/acp-16-4081-2016, 2016.

World Health Organization: Air quality and Health, Fact sheet no 313, September 2016. [online] Available from: http://www.who.int/mediacentre/factsheets/fs313/en/ (Accessed 15 January 2018), 2016.

Wu, S., Mickley, L. J., Jacob, D. J., Logan, J. A., Yantosca, R. M. and Rind, D.: Why are there large differences between models in global budgets of tropospheric ozone?, J. Geophys. Res. Atmospheres, 112(D5), D05302, doi:10.1029/2006JD007801, 2007.

Xing, J., Mathur, R., Pleim, J., Hogrefe, C., Gan, C.-M., Wong, D. C., Wei, C., Gilliam, R. and Pouliot, G.: Observations and modeling of air quality trends over 1990–2010 across the Northern Hemisphere: China, the United States and Europe, Atmospheric Chem. Phys., 15(5), 2723–2747, doi:10.5194/acp-15-2723-2015, 2015.

Xu, L., Williams, L. R., Young, D. E., Allan, J. D., Coe, H., Massoli, P., Fortner, E., Chhabra, P., Herndon, S., Brooks, W. A., Jayne, J. T., Worsnop, D. R., Aiken, A. C., Liu, S., Gorkowski, K., Dubey, M. K., Fleming, Z. L., Visser, S., Prévôt, A. S. H. and Ng, N. L.: Wintertime aerosol chemical composition, volatility, and spatial variability in the greater London area, Atmospheric Chem. Phys., 16(2), 1139–1160, doi:10.5194/acp-16-1139-2016, 2016.

Zanobetti, A. and Schwartz, J.: The Effect of Fine and Coarse Particulate Air Pollution on Mortality: A National Analysis, Environ. Health Perspect., 117(6), 898–903, doi:10.1289/ehp.0800108, 2009.

Zhang, L., Gong, S., Padro, J. and Barrie, L.: A size-segregated particle dry deposition scheme for an atmospheric aerosol module, Atmos. Environ., 35(3), 549–560, doi: 10.1016/S1352-2310(00)00326-5, 2001.

Zhang, L., Brook, J. R. and Vet, R.: A revised parameterization for gaseous dry deposition in air-quality models, Atmospheric Chem. Phys., 3(6), 2067–2082, doi:10.5194/acp-3-2067-2003, 2003.

Zhang, L., Jacob, D. J., Knipping, E. M., Kumar, N., Munger, J. W., Carouge, C. C., van Donkelaar, A., Wang, Y. X. and Chen, D.: Nitrogen deposition to the United States: distribution, sources, and processes, Atmospheric Chem. Phys., 12(10), 4539–4554, doi:10.5194/acp-12-4539-2012, 2012a.

Zhang, Q., Jimenez, J. L., Canagaratna, M. R., Allan, J. D., Coe, H., Ulbrich, I., Alfarra, M. R., Takami, A., Middlebrook, A. M., Sun, Y. L., Dzepina, K., Dunlea, E., Docherty, K., DeCarlo, P. F., Salcedo, D., Onasch, T., Jayne, J. T., Miyoshi, T., Shimono, A., Hatakeyama, S., Takegawa, N., Kondo, Y., Schneider, J., Drewnick, F., Borrmann, S., Weimer, S., Demerjian, K., Williams, P., Bower, K., Bahreini, R., Cottrell, L., Griffin, R. J., Rautiainen, J., Sun, J. Y., Zhang, Y. M. and Worsnop, D. R.: Ubiquity and dominance of oxygenated species in organic aerosols in anthropogenically-influenced Northern Hemisphere midlatitudes, Geophys. Res. Lett., 34(13), L13801, doi:10.1029/2007GL029979, 2007.

Zhang, Q., Jimenez, J. L., Canagaratna, M. R., Ulbrich, I. M., Ng, N. L., Worsnop, D. R. and Sun, Y.: Understanding atmospheric organic aerosols via factor analysis of aerosol mass spectrometry: a review, Anal. Bioanal. Chem., 401(10), 3045–3067, doi:10.1007/s00216-011-5355-y, 2011.

Zhang, Y. and Jaeglé, L.: Decreases in Mercury Wet Deposition over the United States during 2004–2010: Roles of Domestic and Global Background Emission Reductions, Atmosphere, 4(2), doi:10.3390/atmos4020113, 2013.

Zhang, Y., Jaeglé, L., van Donkelaar, A., Martin, R. V., Holmes, C. D., Amos, H. M., Wang, Q., Talbot, R., Artz, R., Brooks, S., Luke, W., Holsen, T. M., Felton, D., Miller, E. K., Perry, K. D., Schmeltz, D., Steffen, A., Tordon, R., Weiss-Penzias, P. and Zsolway, R.: Nested-grid simulation of mercury over North America, Atmospheric Chem. Phys., 12(14), 6095–6111, doi:10.5194/acp-12-6095-2012, 2012b.

Zhang, Y., Jaeglé, L., Thompson, L. and Streets, D. G.: Six centuries of changing oceanic mercury, Glob. Biogeochem. Cycles, 28(11), 1251–1261, doi:10.1002/2014GB004939, 2014.

Zhang, Y., Jacob, D. J., Horowitz, H. M., Chen, L., Amos, H. M., Krabbenhoft, D. P., Slemr, F., St. Louis, V. L. and Sunderland, E. M.: Observed decrease in atmospheric mercury explained by global decline in anthropogenic emissions, Proc. Natl. Acad. Sci., 113(3), 526–531, doi:10.1073/pnas.1516312113, 2016.

Zhu, L., Jacob, D. J., Keutsch, F. N., Mickley, L. J., Scheffe, R., Strum, M., González Abad, G., Chance, K., Yang, K., Rappenglück, B., Millet, D. B., Baasandorj, M., Jaeglé, L. and Shah, V.: Formaldehyde (HCHO) As a Hazardous Air Pollutant: Mapping Surface Air Concentrations from Satellite and Inferring Cancer Risks in the United States, Environ. Sci. Technol., 51(10), 5650–5657, doi:10.1021/acs.est.7b01356, 2017.

VITA

Viral Shah grew up in Mumbai and came to the U.S. at the age of 24. He has received a bachelor's degree in civil engineering from the Indian Institute of Technology Bombay, a master's degree in Civil and Environmental Engineering from the University of Pittsburgh. He joined the graduate program in the Department of Atmospheric Sciences at the University of Washington in 2012 and received a master's degree in Atmospheric Sciences from the University of Washington in 2015. Viral has worked as a structural engineer and a construction manager.